PERMEABILITY OF FIBER REINFORCEMENTS FOR LIQUID COMPOSITE MOLDING: SEQUENTIAL MULTI-SCALE INVESTIGATIONS INTO NUMERICAL FLOW MODELING ON THE MICRO- AND MESO-SCALE

By

Timothy John Franklin Luchini

A DISSERTATION

Submitted to
Michigan State University
in partial fulfillment of the requirements
for the degree of

Mechanical Engineering – Doctor of Philosophy

2015

ABSTRACT

PERMEABILITY OF FIBER REINFORCEMENTS FOR LIQUID COMPOSITE MOLDING: SEQUENTIAL MULTI-SCALE INVESTIGATIONS INTO NUMERICAL FLOW MODELING ON THE MICRO- AND MESO-SCALE

By

Timothy John Franklin Luchini

Composites are complex material mixtures, known to have high amounts of variability, with unique properties at the micro-, meso-, and macro-scales. In the context of advanced textile composite reinforcements, micro-scale refers to aligned fibers and toughening agents in a disordered arrangement; meso-scale is the woven, braided, or stitched fabric geometry (which compacts to various volume fractions); and macro-scale is the component or sub-component being produced for a mechanical application.

The Darcy-based permeability is an important parameter for modeling and understanding the flow profile and fill times for liquid composite molding. Permeability of composite materials can vary widely from the micro- to macro-scales. For example, geometric factors like compaction and ply layup affect the component permeability at the meso- and macro-scales. On the micro-scale the permeability will be affected by the packing arrangement of the fibers and fiber volume fraction. On any scale, simplifications to the geometry can be made to treat the fiber reinforcement as a porous media. Permeability has been widely studied in both experimental and analytical frameworks, but less attention has focused on the ability of numerical tools to predict the permeability of reinforced composite materials.

This work aims at (1) predicting permeability at various scales of interest and (2) developing a sequential, multi-scale, numerical modeling approach on the micro- and meso-scales. First, a micro-scale modeling approach is developed, including a geometry generation

tool and a fluids-based numerical permeability solver. This micro-scale model included all physical fibers and derived the empirical permeability constant directly though numerical simulation. This numerical approach was compared with literature results for perfect packing arrangements, and the results were shown to be comparable with previous work. The numerical simulations described here also extended these previous investigations by including the ability to study binary mixtures of commingled fibers, random packing, particulate loadings, and permeability variation at a single volume fraction as a function of the mean inter-fiber spacing.

Extending this approach from the micro-scale to the meso-scale creates an opportunity to quantify the effect of dual-scale porous media. More specifically, direct numerical simulations of carbon fiber reinforcement on the micro-scale were compared to measurements of unidirectional carbon fabrics on the meso-scale. The results showed a quantifiable effect of dual-scale porous media in composite processing, with generally higher permeability on the meso-scale.

Next, a three-dimensional meso-scale analysis of a plain weave composite fabric was performed using the homogenized micro-scale permeability. Comparisons were made between the numerical modeling approaches developed in this dissertation with the available permeability measurement techniques for validation. The meso-scale permeability calculations compared well with experimental permeability measurements. The effect of fabric variability is seen in all scales of interest. Finally, this work included a meso-scale, two-phase, transient simulation to investigate tow saturation and the formation of meso-scale voids. The results qualitatively show the nature of the advancing fluid front and the lagging tow saturation, which is seen though experimental analysis.

Dedicated to Dr. Kayla Luchini, Dr. John and Tamara Luchini, Dr. Kenneth Wyckoff

ACKNOWLEDGEMENTS

There have been many invaluable sources of guidance for me as I have worked to complete my doctoral dissertation. I would like to thank my advisor Dr. Alfred Loos for his mentorship as I learned composite manufacturing techniques and where my contributions could be made. My committee, Dr. Charles Petty, Dr. Dahsin Liu, and Dr. Ronald Averill have each been extremely helpful in having supportive discussions about my findings. Additionally, Stephen Sommerlot, Nariman Mansouri, Nick Kamar, Andy Vanderklok, and Martin Ducote have made significant time contributions to my success and have been important colleagues. Stephen Sommerlot provided hours of discussion as well as teaching about experimental measurement for permeability validation.

My family has been critical to my success and I would like to thank Dr. Kayla Boespflug-Luchini, Dr. Kenneth Wyckoff, Dr. John Luchini, Dr. Katy Colbry, Dr. Dirk Colbry, Tamara Luchini, Mark Luchini, Dolly Luchini, Nan Luchini, and Frank Luchini for their guidance in all things scientific. Dr. Kayla Boespflug-Luchini has been extremely supportive of me and made efforts to keep me motivated and on track with my personal goals.

TABLE OF CONTENTS

LIST OF TABLES

LIST OF FIGURES

LIST OF SYMBOLS

A	area
$C_{\parallel}$	parallel fiber packing arrangement constant
$C_{\perp}$	perpendicular fiber packing arrangement constant
D	coefficient of hydraulic dispersion due to spatial variations in porous media
d_f	fiber diameter
d_p	particle diameter
g	gravitational constant, momentum / (mass – time), length / time^2
k	permeability of a specific phase
K	permeability of the porous media
L	preform length in direction of flow
m	slope parameter in saturated and unsaturated permeability formulation
n	number of fabric layers
P	static fluid pressure
P_{atm}	atmospheric pressure
p	relative pressure
r	mass rate of phase lost
S	phase saturation in the porous medium
t	time

u	superficial velocity averaged over a small region of space, length / time
Q	Darcy volumetric discharge
q	Darcy flux
S	permeability
S_{xx}	permeability in fabric warp direction
S_{yy}	permeability in fabric weft direction
S_{zz}	through thickness or transverse permeability
S_{11}	first principal permeability
S_{22}	second principal permeability
S_{33}	third principal permeability
t	time or thickness
$V_a{}'$	empirically defined maximum available fiber volume fraction
V_f	fiber volume fraction
V_{fmax}	maximum fiber volume fraction
α	fluid volume fraction
β	orientation of first principal permeability in reference to the fabric warp direction
μ	fluid viscosity or micrometer
v	superficial fluid velocity
ρ	density
ρ_f	fiber density
ρ_{fluid}	fluid density

τ_{ij}	stress tensor
φ	porosity
Φ	porosity function
$\sum$	summation
^{o}	degrees
ε	porosity, ratio of pore volume to total volume, fractional void space
τ	shear stress
Δ	difference
$\cdot$	dot product

1. INTRODUCTION

1.1 Background

Material characterization is an important step in the processing of high-performance composite parts with liquid composite molding and computational tools are increasingly able to help with the characterization process. Through a better understanding of composite manufacturing and increasing computer power, high-quality finished composites can be produced. Without material characterization for fibrous reinforcements in composite processing, accurate process models cannot be created, resulting in poor part quality or on-the-fly corrections in a manufacturing environment. In this section, a reason for research in composites will be discussed focusing on two aerospace applications. The basic application of Darcy's law will be discussed and methods for permeability measurement will be introduced. The first references to micro-scale and meso-scale permeability will be presented and discussed. This section will conclude with a statement of need.

1.1.1 Reasons for Research in Composites

Composites are designed materials that combine two or more material ingredients to achieve desirable properties for various industrial applications. For example, the GEnx (General Electric Next Generation) engine incorporates materials that are a composite of carbon fiber and thermosetting epoxy resin, giving high structural efficiency at low weight [1]. This makes the composite valuable for applications in aerospace that have traditionally relied on lightweight metal materials like aluminum and titanium [2]. In addition to designing composites to meet specific weight and strength requirements, composite materials can be designed to resist the fatigue and corrosion issues sometimes seen with specific metals [3]. Furthermore, composites allow for lighter vehicles and higher performance in an economic environment that is consistently shifting towards better fuel economy, lower cost, and higher efficiency.

Boeing's 787 "Dreamliner" is a great example of the importance of composites research. Composed of 50% by weight composite content, the "Dreamliner" was designed to be 17% more fuel efficient than the aluminum 767 [4]. This weight reduction was achieved in part by redesigning the fuselage, wings, empennage, fin, and nacelles using carbon and epoxy composites. Creating a composite fuselage on the scale of the 787 "Dreamliner" required extensive research and development. Many of the composite material problems Boeing tackled and solved in this design were industry firsts. Constructing the "Dreamliner" required understanding and addressing challenges such as using composite materials to develop a pressurized airline cabin and understanding the behavior of these composites after lightning strikes, impact damage, delamination and fatigue. This includes having a somewhat electrically conductive airframe and the ability to control thermal conductivity. In addition to designing a new airplane, Boeing had to create new manufacturing processes as well as the service and repair procedures for defect detection.

The results of this research are impressive: for instance, the composite fuselage saved 50,000 fasteners versus traditional designs. The overall "Dreamliner" design consumed one-fifth less fuel per passenger mile than the older 767, equating to more savings for passengers and more profits for the airliners [2], and the company boasted that the composite cabin could be pressurized to a more comfortable level during flight. The final design leverages composites within a highly advanced material structure to safely and efficiently transport people and goods to their final destinations.

The Boeing “Dreamliner” also offers two engine variants: the traditional Rolls-Royce Trent 1000, and the highly advanced GEnx [1]. The GEnx is the next step in the GE90 engine technological innovations, designed with carbon fiber fan blades on the compressor and a composite fan case [4]. The GEnx composite blades are made using fiber preforms composed of up to 1000 plies of unidirectional pre-preg tape; these plies are cut ultrasonically and the preform is placed into an resin transfer mold (RTM) where resin is injected [1]. For composite manufacturing this approach to preforming is not uncommon and the consistent layup process is extremely important to the final composite properties.

The composite fan blades on the GEnx give significant weight reductions, reduced fuel consumption and enhanced durability; the dynamics of the fan rotation can multiply this weight savings. More specifically, the composite blades and case combine to save 350 lbs. per GEnx engine [1]. This weight savings has a domino effect: a lighter engine means less robust fixturing is needed and weight is reduced in other parts of the aircraft, which allows for increased payload on the aircraft and reduced fuel consumption [5].

Creating the “Dreamliner” required a diverse, international team of suppliers and technical experts: of the more than 50 suppliers, 28 are international companies. Japan provided $6 billion worth of carbon; Italy contributed the horizontal stabilizer; the tail fin was made in the USA; Australia developed the ailerons and flaps; Canada provided the fairings; the aircraft doors came from France; and the floor beams came from India [6]. The next leap for composite vehicle components is in the automotive sector to meet new government mandated fuel economy standards. As the popularity of composite materials continues to grow, international collaborations will be critical to achieving further advances in the areas of manufacturing, modeling, new material development, and ultimately lead to ongoing changes in the composite vehicle market.

1.1.2 Background Equation Formulations

The work described in this dissertation focuses primarily on the manufacture of fiber reinforced epoxy resin composite materials. This generally encompasses a number of liquid composite molding techniques where a liquid resin is infused into a fiber preform and then processed through a cure cycle. This section and Appendix B outlines the basic fluids equations that are useful in modeling these flow scenarios. The background equations described here are also important for understanding flow through porous media, which is applicable because the geometrical nature of the fiber preform allows them to be treated as a porous media. On the micro-scale the Navier-Stokes equations are solved directly for the flow around fibers and particles. The meso-scale couples the Navier-Stokes equations in the fluid region with a modified form of the Navier-Stokes equations in the tows. The boundaries of the tows have a conservation of mass and momentum assumption applied. The component level uses the modified Navier-

Stokes equations for porous zones and can couple the traditional Navier-Stokes models to account for resin runners, flow channels, and other non-porous zones.

Darcy’s Law governs the flow of fluid through porous media on a quantitative basis, and is used to describe a variety of similar processes in disciplines such as hydrology, hydrogeology, soil science, civil engineering, petroleum engineering, chemical engineering, and composite manufacturing [7]. In composite manufacturing, Darcy’s Law is used to predict the flow through a fiber network, where the critical empirical parameter is geometrical permeability [8].

Darcy’s Law was first described by Henry Philibert Gaspard Darcy, an engineer in Dijon, France [9]. Darcy originally developed this law to describe behaviors within sand columns, and included the law in an appendix of his book, “The Public Fountains of the City of Dijon” [10]–[12]. The structure of Darcy’s Law is very similar to that of Fourier’s law of heat conduction [13] or Fick’s law of mass diffusion [14], all of which describe diffusion of some parameter (heat, mass, pressure).

Darcy’s Law can be extended to simplify complex flow scenarios of a resin flow through a fiber preform. Flow through fiber preforms and porous media is often modeled using Darcy’s Law in the following form:

$$\bar{q} = -\frac{\bar{\bar{S}}}{\mu}\nabla P \qquad (1)$$

In this formulation, S is the permeability tensor encompassing the internal directional fiber properties, the superficial pressure is represented by P, and q is the Darcy flux. Additionally, μ represents the absolute or dynamic viscosity of the resin or fluid considered. Permeability is described as a tensor in three-dimensional space based on another extension from Darcy's original law: for a random fiber composite mat, the permeability is often taken as isotropic; for a directional fiber preform, the permeability tensor is orthotropic and there is a principal coordinate system that can be found, similar to the concept of principal stresses. Physically, the equation states that the discharged volume of fluid running through a porous media is proportional to the pressure loss.

An alternative expression is shown in Eq. 2, which gives Darcy's Law for the total fluid discharge. Here, Q is the total volumetric fluid discharge, A is the area, and L is the characteristic length in the flow direction. This model assumes that the fluid is Newtonian and that inertial and capillary effects can be neglected.

$$Q = \frac{\bar{\bar{S}}A}{\mu}\frac{\Delta P}{L} \tag{2}$$

Darcy's Law relates the velocity vector to the pressure gradient, and uses the permeability tensor as a proportionality tool. Darcy's Law is a one-phase flow model, where the single-phase in liquid composite molding is resin [15]. Two-phase models have also been formulated to describe the motion of resin and air in an enclosed region, and some of these Darcy two-phase models can be generalized into multi-phase flow models [16]. The velocity in Darcy's Law is the apparent fluid velocity [17], [18], which is the actual fluid velocity accounting for the porosity of the reinforcement and the fact that part of the mold cavity is occupied by fibers. Another important factor on permeability is the volume fraction, which is equal to one minus the porosity [8].

1.1.3 Permeability Calculation and Measurement

In order to simulate flow in component-level composite manufacturing, it is important to obtain accurate permeability data for any fabric preforms. These fiber preforms can vary significantly in geometry including fabric architecture, fiber tow size, and fiber orientation. Permeability is the measure of the resistance to flow through a porous media and is generally considered as a geometrical parameter that relies heavily on Darcy's Law in order to predict a flow scenario. Without accurate experimental data for permeability, attempts to numerically calculate resulting flow scenarios are often problematic. The ability to accurately predict permeability would also enable more accurate models of this flow, which could significantly reduce experimental effort.

Boundary conditions are important in this type of flow scenario, and models that attempt to predict permeability while neglecting the permeable nature of tows have been shown to underestimate the permeability of macroscopic and microscopic porous media [19]. Considering boundary effects at the interfaces of the porous tows and macro-voids in the stitching has been the topic of a few important areas of research [15], [20]–[22]. For instance, one system for modeling the flow in a fiber tow uses Darcy's Law coupled with the Navier-Stokes flow equations to describe the open regions between tows of stitched fabrics [23]. Other attempts to model the flow at an interface have used a slip condition at the boundary of the porous media to mate the Darcy flow with the Navier-Stokes flow [24].

There are is a large body of literature on various approaches to permeability measurement and no standard approach. The principles are the same but various texting fixtures and methods have been implemented. There have been attempts to standardize methods for measurement studies where consistency and reduction in variation was focused on [25]–[28]. In another attempt, a group attempted to make a database of permeability [29]. Still further, there was a proposal for a three-dimensional woven fabric to be used for referencing the results from various fixtures [30]. An epoxy-based reference specimen of non-fibrous architecture was proposed for test validation as well [31]. Li *et al*. [32] described a fixture that could be used in transverse permeability measurements of fibrous reinforcements. The fixture allowed a fiber bed to be compressed in a cavity under constant compaction pressure while micrometers with dial indicators measured the fiber volume fraction based on the thickness and fiber areal weight.

Measurement of reinforcement permeability is known to be notoriously variable in results where variation has been found to be up to an order of magnitude between test methods for the same material [27]. From a fundamental perspective, the various permeability measurement techniques generally fall in either a one-dimensional channel flow or two-dimensional radial measurement method. One-dimensional methods involve linearly injecting a test fluid into a preform placed in a rectangular cavity where measurements can be made along warp and weft directions as well as off axis directions based on the ply layup. Two-dimensional measurements are often conducted radially by centrally injecting a test fluid in a preform and observing the resulting propagation of the flow front ellipse in the in-plane directions. There have been reported differences between the two-dimensional unsaturated and one dimensional saturated experiments [33]. As a less common approach, there are also methods to measure the three-dimensional permeability tensor of a preform [34]–[38]. There is also a small body of literature on a capillary rise technique to find tow or fiber bundle permeability [39]–[41].

1.1.4 Micro-scale vs. Macro-scale Modeling

Producing repeatable, experimental permeability values is difficult even for simple flat geometries and flows through sand. This difficulty arises because of variations in experimental setup and user interactions that reflect directly on the processes taking place. For composites, in a manufacturing environment, the variation is a known factor that must be understood as completely as possible [42]. In some cases fibers or porous media can move or compact, requiring a compaction parameter to be implemented. Evidence also shows that the randomness in fibers at the same volume fraction accounts for some of the difference in measured permeability but this has not often been completely investigated or quantified [43], [44]. The inherently variable nature of textiles requires a relatively large number of measurements to eliminate those influences, as well as effects like race tracking on the data results. Modeling of woven fabrics is also different than directly modeling porous media because weaves have both open regions between the tows and porous regions inside the tows. Another way to consider this is as a dual-scale porous media where micro-scale porosity is coupled with meso-scale porosity. There are a number of common approaches to model woven fabrics and fiber composite preforms [45].

Looking at traditional materials in composite fabrication, the dual-scale porosity can be seen. Figure 1 shows a traditional four harness satin carbon fiber material on the left and a plain weave glass fiber reinforcement on the right. The individual carbon or glass fibers are arranged into tows or yarns. These yarns are then braided or woven into a fabric. The fabric combines regions of meso-scale porosity with regions of micro-scale porosity inside of the tows. This creates a fabric with a dual-scale porous nature. The scale bars in Figure 1 are in millimeters and emphasizes the size of the yarns and the gaps between them. The carbon fabric on the left appears to be more loosely woven than the glass fiber material on the right. Additionally, the uniformity of the fabric can be seen where the glass fiber appears to be more dimensionally consistent than the more variable tow spacing and dimensions seen in the carbon fiber material.

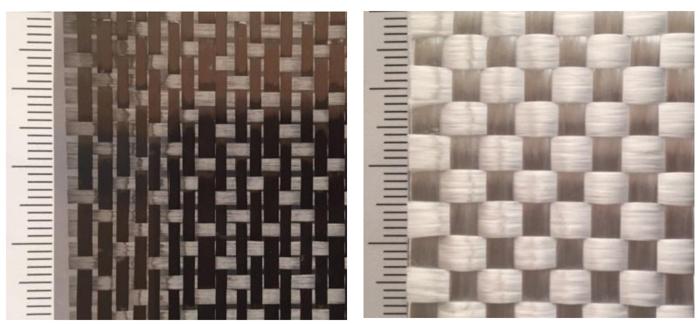

Figure 1: Two traditional forms of fibrous reinforcement for composite manufacturing. Left is a four harness satin carbon fiber material. Right is a plain weave glass fiber reinforcement.

1.1.5 Kinetic Theory

Kinetic theory is a microscopic model of the fluid flow where the fundamental laws of nature are applied directly to the atoms and molecules [46]. This modeling approach is accurate, but far too computationally intensive to be practical at the scales of interest for composite manufacturing. Using molecular simulation tools to examine resin flow in fiber preforms would only account for small-scale properties, which would still need to be extended dramatically to reach the dimensions of interest for manufacturing processes. The Lattice Boltzmann method is one approach to do this.

1.1.6 Application of Darcy's Law in Two-Phase Transport

This section will discuss two-phase flow through porous media. This is motivated by resin transfer molding (RTM) and two-phase flow through composite fiber preforms. Darcy's flow through porous media can be described as being governed by the equations of motion and continuity. These equations are the smoothed continuity equation and the Darcy equation of momentum described by Bird *et al.* [47] in transport phenomena. Darcy's equation was initially proposed empirically to describe seepage of fluids through granular media at low Reynolds numbers. Simplified Darcy's Law expresses flow through porous media proportionally to the difference between pressures over a prescribed length applied to the outside surfaces. The surfaces are described as the entry and exit of the bulk porous medium [48].

Kuan and El-Gizaway [49] applied Darcy's flow to a two-phase flow through porous media to model the resin flow process through fiber mats in composite manufacturing for a two-dimensional simulation. They utilized a fraction volume of fluid approach to describe the free boundary at the interface between resin and air during the resin transfer molding infiltration process. They located the interface between the phases of resin and air by the solution of a continuity equation for the volume fraction of the resin phase.

This section starts with a model of the equation of motion for porous media using an approach with Darcy's Law. Next, an equation for two-phase momentum is developed for the resin transfer molding process to describe what takes place detailing the equations used for solutions. Finally, an application is developed for two-phase transport to resin/air permeation.

The general equation of continuity is shown in Eq. 66 and the equation of motion is shown in Eq. 75. Darcy's equation is also important and can be seen in Eq. 1. The derivation of two-phase momentum transport for resin transfer molding is not necessarily a trivial process, and it is important to understand. Next, the mass balance of phase α is shown for the macroscopic equation of continuity.

$$\frac{\partial}{\partial t}(\varepsilon_\alpha \rho_\alpha) + \nabla(\rho_\alpha v_\alpha) - \nabla \cdot (\varepsilon_\alpha D_\alpha \cdot \nabla \rho_\alpha) + \boldsymbol{r}_\alpha = \boldsymbol{0}\ ;\ \varepsilon_\alpha = \boldsymbol{\phi}(\boldsymbol{s}_\alpha - \boldsymbol{s}_{ij}) \qquad (3)$$

In this equation, α is the phase of fluid, ε_α is the porosity as the ratio of pore volume to total volume, $\boldsymbol{\phi}$ is porosity as a function, and ρ_α is the density of the phase in units of mass per volume. Also, v_α is the volumetric flux of a given phase, D_α is the coefficient of the hydraulic dispersion due to spatial variations in the porous media, $\boldsymbol{r}_\alpha$ is the mass rate of phase lost, and $\boldsymbol{s}_\alpha$ is the resin saturation in the porous media. When Eq. 3 is summed over all α phases, the total mass balance equations can be written (Eq. 4).

$$\frac{\partial}{\partial t}(\boldsymbol{\phi\rho}) + \nabla \cdot (\boldsymbol{\rho v}) - \nabla \cdot (\boldsymbol{\phi D} \cdot \nabla \rho) + \boldsymbol{r} = \boldsymbol{0} \qquad (4)$$

Where the following average quantities are used

$$\rho = \sum_j S_j \rho_j \; ; \; \rho v = \sum_j \rho_j v_j ; \; \boldsymbol{D} \cdot \nabla \rho = \sum_j S_j D_j \cdot \nabla \rho_j \; ; r = \sum_j r_j \qquad (5)$$

For incompressible fluids, a volumetric balance equation is

$$\frac{\partial}{\partial t}(\boldsymbol{\phi}) + \nabla \cdot (\boldsymbol{v}) + \boldsymbol{q} = \boldsymbol{0} \; ; \qquad \boldsymbol{where\, q} = r_j/\rho_j q = \sum_j q_j \qquad (6)$$

The two-phase transport concept can then be easily extended to a resin and air flow case. First, the mass balance of phase α or the macroscopic equation of continuity is shown.

$$\frac{\partial}{\partial t}(\phi(S_{resin})\rho_{resin}) + \nabla \cdot (\rho_{resin} v_{resin}) - \nabla \cdot (\varepsilon_{resin} D_{resin} \cdot \nabla \rho_{resin}) + \boldsymbol{r_{resin}} = \boldsymbol{0}$$
$$\frac{\partial}{\partial t}(\phi(S_{air})\rho_{air}) + \nabla \cdot (\rho_{air} v_{air}) - \nabla \cdot (\varepsilon_{air} D_{air} \cdot \nabla \rho_{air}) + \boldsymbol{r_{air}} = \boldsymbol{0} \qquad (7)$$

The volumetric fluxes through the porous media can be given by

$$v_{resin} = \frac{-k_{resin}}{\mu_{resin}} K \cdot (\nabla p_{resin}) = \mathbf{0}$$

$$v_{air} = \frac{-k_{air}}{\mu_{air}} K \cdot (\nabla p_{air}) = \mathbf{0} \tag{8}$$

If it is important, a capillary pressure can be input. Where a capillary pressure can be defined by $p_c = p_{resin} - p_{air}$ and utilized and the total volumetric flux can be written as $v = v_{resin} + v_{air}$. When the volumetric fluxes, Eq. 8, are combined they yield

$$v = \left(\frac{-k_{resin}}{\mu_{resin}} + \frac{-k_{air}}{\mu_{air}}\right) K \cdot (\nabla p_{resin}) - \frac{k_{air}}{\mu_{air}} \frac{d\rho_c}{dS_{resin}} K \cdot (\nabla S_{resin}) \tag{9}$$

Following a rearrangement of terms, ∇p_{resin} can be removed and produce

$$v_{resin} = \left(1 + \frac{k_{air} * \mu_{resin}}{k_{resin} * \mu_{air}}\right)^{-1} \left(v + \frac{k_{air}}{\mu_{air}} \frac{d\rho_c}{dS_{resin}}\right) K \cdot (\nabla S_{resin}) \tag{10}$$

The boundary value problem above is developed with consistent use of simplifying assumptions. Some of those assumptions include: constant viscosity and permeability, incompressible liquid, gravity is negligible, rigid mold cavity with no deformation, no curing of resin takes place during the isothermal filing process, low Reynolds number flow, and negligible surface tension [49]. These assumptions are reasonable given the time scale and flow dimensions of interest. The pressure drop in a one-dimensional flow problem can be done to quickly calculate an exact solution to a simple problem involving any type of porous media flow with the above assumptions held valid. The pressure drop and velocity profile are common points of interest in engineering design and analysis. The equations of motion and continuity are shown to be valid with Darcy's Law to formulate solutions to boundary value problems.

Derivation of two-phase momentum transport equations for the resin transfer molding process is a much more specific application to a manufacturing process. The system of equations here would be of interest in visualizing flow patterns of resin as it permeates a mold and calculating the velocity profiles. These flow patterns could be used to identify areas of high void probability and resin dense areas. Park and Woo [50] stated that mechanical air entrapment is the main reason for void creation in the resin transfer molding process. Further, they stated that the flow front is not uniform and air can be entrapped to form air bubbles. Therefore, the interface between resin and air during the resin transfer molding infiltration process is a significant cause of air pockets or voids in the final manufactured part.

The method of integrating simplified equations of motion and continuity for analytical solutions is appropriate for many simple problems in transport phenomena. As the problems increase in complexity and geometries are less consistent, analytical solutions developed for specific experimental cases become less useful. Specific real world cases may diverge from the well-known solutions to simplified boundary value equations. Here, a numerical solution technique can be applied to account for complex geometries. However, this does not take the place of the boundary value problem, and only acts to extend it based on the complexity of the problem. These fundamentals must be understood in order to produce useful results.

1.2 Conclusion and Statement of Need

Composite manufacturing is a complicated subset of composite engineering with a number of unique problems that are left unsolved. In seeking to implement theory into applied manufacturing of composite materials, some of the art in manufacturing can be understood by increasing the boundaries of applied science. By knowing the processes used in composite manufacturing, engineering research can give insight into the physical process taking place and refine the tools used to set up production. The advances in high fiber content, high strength and high stiffness composite materials are a product of engineering research. This research is ultimately driven by the economic value anticipated by the application of scientific tools to composite manufacturing.

In applying these tools to the study of composite processing methods, there are a number of useful areas to study. In this research document, numerical tools will be used to study composite fiber reinforcement permeability and the effect it has on the processing parameters inside of a closed mold process. The ability to predict permeability could help to reduce the need for numerous measurement techniques and experimentation in the lab through an automated numerical process. The micro- and meso-scale numerical approaches outlined in this document will help to meet an industry inspired need to understand the fiber reinforcements used when creating high performance structural parts. The governing fluids equations during a resin infusion into a fiber preform are based on natural phenomena, but they can be applied to reduce cost, increase repeatability, emphasize safety, and optimize composite part production.

Translating the problems that are traditionally solved by trial and error to a solvable set of empirical, intuitive, and numerical tools is an instructive advancement.

2. LITERATURE REVIEW

2.1 Composite Manufacturing Processes

Liquid Composite Molding (LCM) is a robust class of manufacturing processes that can be used to create composite parts with good reliability and desirable performance properties. Finished composite parts can be made in many sizes and geometries through closed molding processes. The LCM class can be divided into a number of similar but distinct manufacturing techniques such as resin transfer molding (RTM) and vacuum assisted resin transfer molding (VARTM) [51]–[53]. Similar processes, such as Resin Film Infusion (RFI) [54]–[56] and Structural injection Molding (SRIM) [57]–[59], have been developed for specific manufacturing applications. Additionally, many of the commercial processes have been patented or made into trade secret variations [55], [60], [61]. The underlying goal of these variations is to create reliability and repeatability in the manufacturing process.

Controlling design variables is a difficult but necessary component in producing a quality finished part. There are many manufacturing inconsistencies that are challenging to control, creating a relatively large statistical variation in material properties [62], and even identically-designed processes do not always result in identical finished products. Ongoing research is exploring many processing variables, including draping, compaction, impregnation, location of injection ports, resin kinetics, gel time, viscosity change with temperature or cure, and textile weave – all of which are known to affect manufacturing results and permeability [63]. Given the complexity of the individual variables and their interaction effects, it can be particularly difficult to develop accurate simulations and models for component manufacturing processes.

Thermosetting resins and thermoplastics are the two main forms of matrix material used in LCM. The resin is chosen based on the viscosity, gel time, glass transition temperature, cure time, mechanical properties, physical characteristics, and the component to be produced [64]. The most common thermosetting resins are polyester and epoxy based. Composite materials are designed for specific applications and therefore they can be customized for various uses. This involves a designed matrix material which is produced to optimize performance and manufacturability.

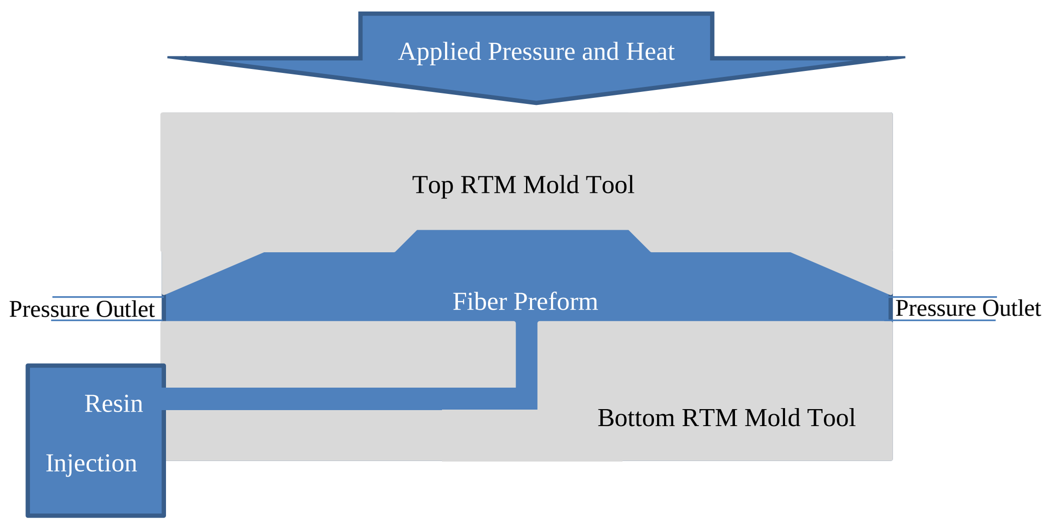

Figure 2: Illustration of the general Resin Transfer Molding Process with a Constant Injection

Resin transfer molding is a manufacturing process that uses a rigid, two-sided, closed mold containing a fiber preform, which is then injected with resin as shown in Figure 2. The matrix material in this process is most commonly thermosetting, with pressure pots or flow rate pumps used for injection [65]. Both injection methods are used to inject resin under pressure in an effort to completely impregnate the preform. Following an infusion, the composite can be cured in the mold to create a finished product. The process produces complex geometries with good tolerances and surface finish. A strong understanding of the process is necessary in order to create the desired finished part [66], and such understanding is even more critical in the modeling phases of design. Generally, there is a constant pressure outlet condition but a negative vacuum pressure can also be applied.

Competition for composites on a performance basis is as important as competition on a cost basis. Composites are high performance materials and Resin Transfer Molding is popular for many low-volume applications where the cost basis gives it some advantages over metal stamped parts [67]. The process is also popular where a number of components need to be integrated into one part with reduced assembly manpower. There is a need to further the understanding of the manufacturing processes discussed above and to be able to control the material variations that result in scrap, waste, and added expenses. Scientific modeling tools will help in this understanding and ultimately lead to increased reliability and lower production costs.

2.1.1 Fiber or Inter-tow Permeability Modeling

For a given fiber volume fraction, the differences in experimentally-measured permeabilities from test to test are generally large. Permeability Benchmark II [68] showed about 20% variability in permeability when different groups used the same methods to measure. Variability on the order of 10-50% is common, and variability of over 100% is not unheard of [69]. This variability makes it extremely difficult to identify the correct permeability value without numerous tests being run in order to identify a reasonable average value and statistical variation. The variability also makes the prediction of permeability using analytical and numerical methods more attractive, but just as difficult to accomplish robustly. There are a number of efforts to develop numerical solutions that correlate well with experimental measurements that show promise [70], [71]. Furthermore, there is an even larger basis of empirical equations that have been created to fit specific data sets [72], [73].

Permeability is ideally a geometric property that should be attainable based on analytical considerations if a strong understanding of that geometry is known [74]. Flow scenarios based on Darcy's Law can be used to obtain average permeability for a sample preform on the macroscopic scale, while the tow-scale permeability has a number of models that are accepted [63], [75]–[77]. These models attempt to quantify the effects of geometry on the resulting flow in an analytical manner. Numerical approaches have been applied to consistent geometries but less time and effort has been spent to create realistic microstructures.

The Kozeny-Carman equation is a common starting place for many other permeability models where a known volume fraction is used with empirical parameters to represent porous media [78]. Various channel cross sections with specific lengths can be combined and solved based on the fluids equations. The equation uses a relation of the permeability to the porosity through the Kozeny constants, fiber volume fraction, and surface area [79]. The specific surface of the porous medium is used to express the permeability that was deduced from the hydraulic radius of the channels. The original equation is derived from the lubrication approach for granular beds and treats the fluid resin flow like capillary flow.

The adapted Kozeny-Carman equation for the permeability of unidirectional reinforcement is as follows:

$$K = \frac{R^2}{4C}\frac{(1 - v_f)^3}{{v_f}^2} \tag{11}$$

Where R is the fiber radius, v_f is the fiber volume fraction, and C is an empirical constant. Some authors have used 0.5 for flow parallel to fibers and 10 perpendicular to the fibers [80]. Another case used 1.78 and 1.66 for quadratic and hexagonal packing assumptions, respectively [76]. Many papers have been written using this model to describe isotropic media, and there have been extensions of the model made to anisotropic preforms [77], [81]–[83]. The Kozeny-Carman equation has been shown to fit a number of cases that benefit from the use of this model. In most cases a fit is derived.

Limitations of this model include that it is a strictly one dimensional capillary model that works best in isotropic porous media and has difficulty extending to directional fabrics [84]. The Kozeny-Carman equation does not have a direct application to parallel or transverse flow through fiber preforms because it does not account for the inter-laminar porosity, dual-scale porosity, or fibrous geometries [79]. When used to calculate transverse permeability, the values produced are not always realistic but have been shown to effectively model a complete block of the transverse flow in unidirectional reinforcements [76], [80]. Additionally, the Kozeny constant is an experimentally-obtained factor and is of heuristic origin. The results of applying this equation consistently show that flow is less resisted along the fibers than transverse to them. This result is intuitive but can also be non-physical and fiber volume fractions beyond complete blockages of flow or where a region is porous but that porosity is not interconnected.

It was indicated from one application of the Kozeny-Carman equation that around 50% volume fraction, a 1% increase in fiber volume fraction causes a 10% decrease in permeability [85]. This can help to explain another confounding factor in the experimental results, because measurements will be affected by mold deflections and preform compression including local nesting. If small changes in local volume fraction cause large changes in permeability that effect could drastically influence measurements. Understanding this variation at a constant fiber volume fraction is difficult with the Kozeny-Carman equation because the information about the fiber dispersion and how that affects permeability at a single volume fraction is lost.

There are a number of other models including one by Gutowski *et al.* [77], which is an empirical model that agreed with the Kozeny-Carman equation at a maximum theoretical fiber volume fraction. One specific drawback of this method is that the resulting permeability value diverges to a lower value than experimentally shown when the volume fraction drops. Additionally, models built on empirical basis need empirical parameters that can be more difficult to obtain than simply measuring the fibers or fabric for permeability directly.

Bruschke *et al.* [86] invented a hybrid model, for flow transverse to the fiber direction, that approaches the values given by other models at low porosities and approaches an analytical cell model solution at high porosities. Strong correlations were shown between the model and numerical results of flow in arrays of aligned fibers for a number of test cases. The porous media was represented by a geometry of perfectly aligned cylinders. This model used the drag resistance across the cylinders, but it is not useful in predicting permeability for flow parallel to an aligned group of fibers. Additionally, this equation is quite large but is largely parameterized to only require fiber radius and total fiber volume fraction as inputs.

Another strategy is the unit cell model. This makes the assumption that the fibers are spaced widely enough and that the flow scale is small enough to neglect the interaction of drag on each fiber from another fiber [87]. A number of unit cells can be geometrically created to predict permeability based on what relates to the real world geometry. The permeability is then predicted based on the resulting flow field solutions. This solution is suitable for widely spaced fibers with high porosity [63].

Gebart *et al.* [76], [85] was interested in modeling quadratic, hexagonal, and periodic arrays of fibers. This approach used lubrication theory and extended the Kozeny-Carman equations, where the flow of fluids in one dimension is much smaller than the flow in another direction. This was done to solve for the flow rate and pressure drop relationship analytically and obtain an expression for the permeability both parallel to and perpendicular to aligned fiber tows. Stokes flow was used to derive different expressions to fit the permeability of flow along and perpendicular to the fibers arranged in a geometric array. In the model, the fibers are arranged in perfectly packed, aligned, bundles with channels between them.

A number of constants were defined for various packing arrangements including C_1 depending on the packing arrangement, c depending on cross section shape, and the theoretical maximum volume fraction V_f max. These values were determined analytically based on the packing arrangement geometry for square (Eq. 12) and hexagonal packing (Eq. 13). Of additional importance, this equation set allows for the transverse flow to stop when a maximum fiber volume fraction is met, which is not always accounted for in other models. The equation for flow parallel to the fibers is theoretically the same as the Kozeny-Carman equation with a different scaling factor and approach to the derivation. Reports have been made fitting analytical models based on the Gebart equations and experiments for unidirectional reinforcement and unidirectional fiber tows [76], [85]. This is also generally done by scaling a parameter like effective fiber radius to fit the data set.

$$K_{square} = \frac{16}{9\pi\sqrt{2}}\left(\sqrt{\frac{\pi}{4v_f}} - 1\right)^{2.5} R^2 \tag{12}$$

$$K_{hexagonal} = \frac{16}{9\pi\sqrt{6}}\left(\sqrt{\frac{\pi}{2\sqrt{3}v_f}} - 1\right)^{2.5} R^2 \tag{13}$$

2.1.2 Woven Textile Permeability Modeling

Textiles are made up of random mat, woven, braided, or aligned fibers that are often bundled together into fiber tows. These fiber materials can vary in composition, such as fiberglass, carbon fiber, or aramid fibers to name a few. There can be 6,000-12,000 fibers per tow and modeling each fiber on this scale is prohibitive. Specific textiles are designed for their desired structural properties in the finished product. Generally, processing the composite and manufacturing considerations come second to the structural design. Currently, the most effective way to generate accurate permeability values is to conduct numerous measurements. This is reasonable for a small set of sample materials over a small range of fiber volume fraction, but becomes costly and labor intensive if a large array of different fabrics needs to be characterized. These measurements are further confounded when a large geometry change or fabric shear is expected in the composite mold because this is often not accounted for in the in-plane experimental measurement. Additionally, because of the variability in fiber preforms and experiment layups, a large range of permeability values are seen for a single textile [88]. This permeability variation can also be seen because of testing procedures [68], [69]. Permeability Benchmark II cut variability to 20% by comparing similar testing procedures. When comparing various testing procedures on the same fabric, an order of magnitude difference in permeability is not uncommon. When comparing measured results of the same material between research groups and various fixture designs, even more variation can be seen. There is no ASTM standard for measuring composite fiber reinforcement permeability so researchers are often using very different approaches developed by their lab.

In textile modeling, there are generally three agreed-upon length scales. This starts at the micro-scale with individual fibers; followed by the mesoscopic length scale, which is the length between tows; and the macroscopic or component scale that describes the whole fabric preform [89]. Models can be run at a length scale of interest, where the resulting data can be used to create model data at the next larger length scale in a sequential modeling approach. Figure 3 shows an infographic where the length scales of interest are illustrated. The micro-scale is composed of individual fibers aligned into yarns in the order of micrometers. The meso-scale is composed of yarns braided or woven into a fabric on the order of millimeters. The macro-scale is composed of a near net shape component or sub-component on the order of meters.

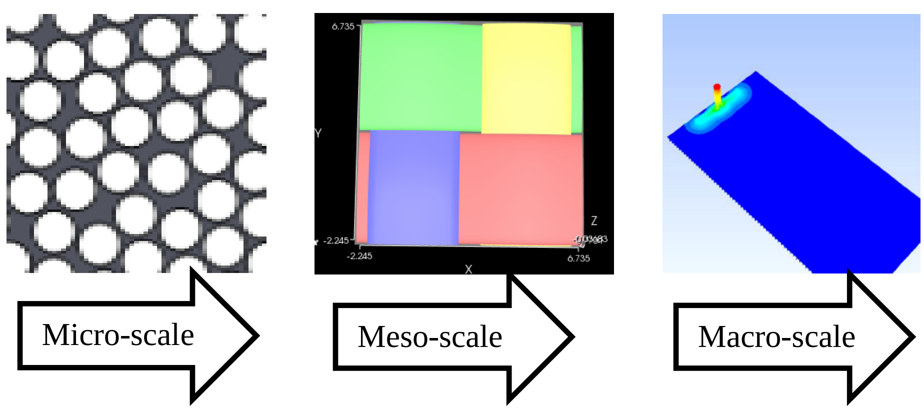

Figure 3: Length Scales of Interest in Composite Manufacturing. The micro-scale is composed of individual fibers aligned into yarns in the order of micrometers. The meso-scale is composed of yarns braided or woven into a fabric on the order of millimeters. The macro-scale is composed of a near net shape component or sub-component on the order of meters.

A numerical prediction of permeability should be possible because, on its most basic level, permeability is a geometrical consideration. On a macroscopic and component level, flow through porous media describes the process of resin injection composite molding. The fiber preform has a number of scales, starting at the micro-fiber level, continuing to a meso-scale of fiber bundles, and up to the full-scale woven textile [90]. The creation of a robust predictive model would allow for the rapid characterization of a large number of fabrics, while creating variables for easy modification of fiber volume fraction, compaction including nesting, lay up, and in-plane shear.

Relatively strong analytical solutions exist for simplified cases of fiber orientation and packing, but these approaches tend to break down for complicated woven or braided structures. Additionally, it is difficult to account for the effect of random fiber orientation and spacing when a rectangular or hexagonal packing arrangement cannot be identified or justified. A numerical approach can combine a more complicated geometry with analytical or numerical descriptions of tow properties. This can allow for complex modeling of fiber preforms while accounting for factors such as porosity, nesting, tow profile, and these geometrical models can be solved for the resulting flow scenarios. Further, macroscopic permeabilities can be calculated based on Darcy's Law. This approach requires good material property data and an understanding of effects volume fraction plays. Direct applications of the Navier-Stokes and Darcy's equations to numerically model flow in the inter-tow and intra-tow regions should apply and be valid [19], [91]–[94]. Ngo *et al.* [95], [96] used the finite element method to solve for flow through a three-dimensional unit cell of a plain weave fabric and obtained good correlations between the predicted permeability values and published data.

Studies have been conducted into the effect of intra-tow and inter-tow porosities on the effective transverse permeability of a square array of permeable tows [97]. The boundary element method in this example used the Navier-Stokes equations for flow through all regions to avoid representing the flow at the fluid / tow interface. An empirical power law function was used to describe the dependence of the effective permeability on the intra-tow and inter-tow porosities.

Further research efforts [98] use a homogenization method to formulate the governing equations for a dual porosity media based on the Navier-Stokes equations. This approach solved flow in a single ply, as well as a three ply three-dimensional model of a woven fabric; however, no quantitative agreement with experimental values was demonstrated for the calculated permeability.

Amico *et al.* [99] used a model to predict the permeability of an assembly of unidirectional tows. This flow scenario modeled the spaces between the tows as channels with rectangular cross sections and used Darcy's flow through the elliptical porous tows. Experimental results were able to validate the modeled transient flow front. In these experiments, a unidirectional fabric at low injection pressures was used. Often cited, they found that at high injection pressures the difference between the flow fronts in the porous tows and free channels is negligible. This is used as a justification for not considering capillary effects separately from the total pressure. Specifically, this assumption applies at high pressure injections over one atmosphere.

A number of optical methods have been used to investigate the geometry of the fiber preform accurately. When creating models of a unit cell fiber preform, the predicted permeability values will be highly dependent on the quality of the measurements and the acquisition of tow shape and fiber packing arrangements. Dunkers *et al.* [92] used a non-destructive technique called optical coherence tomography to image the microstructure of a composite. This approach was able to slice the domain and obtain data for geometrical modeling.

Furthermore, digital measurement methods have been used to find the dimensions of the fiber tows, channels between tows and thickness [99], [100]. This appears to be a powerful method to accurately and quickly obtain large amounts of data for unit cell construction. This unit cell can then be used in mechanics or fluids based problems. Woven fiber preforms have been imaged using X-ray analysis [101] to create a representative model of the preform layers and calculate the permeability of the reinforcement. The predicted permeability value can be in the same order of magnitude as experimental values.

Endruweit and Long [102], [103] created an open source project and a set of python scripts and identified that that variation in the tow properties caused changes in the modeled results. The Gebart equations were used to predict local permeability values, and then injection simulations were simulated for a fabric over a range of variations in permeability. These models have also been adapted to look at physical properties and effects that take place in forming through coupling them with Abaqus [104]. The results have occasionally been presented without experimental results.

A number of papers have been written using TexGen for mechanics and fluids [105]–[109], which is an open source general purpose textile generator written in the Python coding language. TexGen works by defining vectors that describe the path taken by a tow within a textile unit.

Bezier curves are then used to create mathematically-smoothed path lines integrating the user-defined cross sections. These user-defined geometric properties are input parameters that have been taken from a characterized fabric. The dimensional parameters are then iterated in order to follow each vector path line to form the tow or yarn volumes. Next, an assumed geometry domain is generated for the fluid flow case. This fluid volume makes up the matrix material not composed of fibers and tows. Furthermore, the geometries can be defined manually for special flow scenarios. A number of cross sections can be implemented in TexGen including circles, ellipses, and lenticular shapes using the generalized ellipse equation.

The originators of WISETEX, Lomov *et al.* [110], [111], also developed a general textile geometry software that can be used to construct models for various woven and knitted fabrics. Currently a commercially available package, WISETEX has many of the same geometry generation tools but couples proprietary flow and mechanics solver packages as add-ons. These geometry models can be fed into permeability models and mechanical models to predict flow and mechanical behavior. The software is widely used in literature [110]–[112]. Occasionally these results have been compared to experimental data. Generally, the results have been mixed and largely dependent on the material characterized. Furthermore, this tool also uses analytical approximations for the micro-scale flow variables based on the Gebart equations.

In one case of permeability prediction from a group at the University of Auckland, the researchers do not account for the microstructural porosity of the tows [113]–[115]. Some modeling approaches have fit specific data sets while assuming that the tows are solid bodies that are impermeable to fluid flow. In these simulations the boundary conditions are set as pressure inlet and pressure outlet conditions with solid tow bodies. The geometries are unit cells and the data they are generated from is made using image analysis techniques. The geometries are made into voxel based meshes and flow simulations are conducted on these meshed geometries. In this series of papers data is compared with previous results from literature and shown to fit well.

The unit cell approach to preform permeability using the geometrical makeup of a fabric or reinforcement has been successful in some cases [116]–[121]. Using the unit cell approach allows for the dual-scale porosity of intra-tow and inter-tow domains to be modeled. Generally, this involves modeling the inter-tow regions with the Navier-Stokes equations and the intra-tow regions with Darcy based flow [120]. Permeability prediction with a unit cell aims to reduce or eliminate the time consuming experimental characterization step of this numerical modeling process. Tan *et al*. [118] created permeability models of small and large representative unit cells for biaxial stitched mat. Gebart's [76] analytical permeability for tow permeability and applied an finite element method (FEM) approach to solve the fluid equations. It was found that the large unit cells over predicted permeability, while the small unit cells under predicted the permeability compared to the experimental results. Chen *et al*. [120] also used a similar unit cell method and found acceptable agreement between numerical and published experimental permeability results for several plain weave fabrics.

Robust methods for numerically predicting permeability would be useful to quickly characterize a large array of fabric types. The basic procedure includes modeling the fiber preform structure, which is closely related to the real fabric from measurements taken of the real architecture at compaction. The smallest repeating unit cell of geometry is modelled and computational fluid dynamics is used to compute the resin flow through the structure. The permeability is back-calculated from Darcy's Law and the flow through this structure by the pressure profile, length, viscosity, and velocity.

2.1.2.1 Permeability Measurements

Permeability measurements can be taken in a rectangular cavity that forces unidirectional flow by injecting resin through a constant flow rate line in and releasing resin through a constant discharge line out. This is a measurement using saturated flow where two pressure sensors are placed a known length apart. Since the pressure difference can be calculated, viscosity is known, and because the flow rate is a prescribed condition, the permeability can be calculated directly. The fiber preform is thin so that the flow can be assumed one dimensional, with little to no through thickness change, and Darcy's Law can be used to calculate the permeability in a given direction. Radial flow experiments can also be done to predict permeability [70], [90], [122]–[127]. The results gained from in-plane permeability experiments and radial experiments usually agree well with each other but there is no guarantee because the results are heavily preform dependent. Additionally, a modified form of Darcy's Law should be applied if pressure boundary conditions are used.

Permeability will vary with orientation angle and layup. The apparent permeability is usually different than the principal value unless it coincides with one of the principle directions in the reinforcement or model. This is where transformation tensors become important. In order to find the principle permeabilities and create a tensor, three tests must be run. Starting with an x, y, z coordinate system (which often aligns with the warp, weft, and transverse directions for convenience), samples must be tested at the directions corresponding to 0^0, 45^0, and 90^0. From this information, the principle permeabilities can be found; Weitzenbock *et al.* [128] provide a good reference on the transformation.

2.2 Component Process Modeling

Once permeability is characterized, it is important to know how to apply that information about the flow to a model of manufacturing interest. The component scale cannot account for all of the geometry changes from the micro- and meso-scale and so a homogenized permeability is used to represent the resistance to resin infiltration. Computational fluid dynamics (CFD) is a useful tool in a number of manufacturing processes where direct visualization of time-dependent processes is not possible due to considerations such as a closed mold, heat, and pressure. One example is during the heated composites manufacturing cure cycle in resin transfer molding. This is a time-dependent process often conducted at high temperatures where the finished component is also of interest. Without simulation tools, the processes taking place within a complex mold could not be fully understood or predicted. Since the governing equations are known and researchers have developed an understanding of the physical properties, it is possible to create a complex simulation that discretizes the domain of interest and lets the computer run an experiment to show what takes place inside of the filling mold. This process allows researchers to move inlet and outlet injection port locations to discover how various streams of fluid may impinge or enhance the final component.

The functionality of computational fluid dynamics can be further extended to the realm of invisible physics. It is likely that without computer simulations the effect of nanoparticles and macro-scale material interactions would remain a mystery. With the use of simulations, the physics provide a way to visualize how a small particle flows through a porous substrate. As a research tool, computational fluid dynamics can provide information for direct application in manufacturing.

To understand the complicated flows taking place in composite component processing, the manufacturing procedure must be clear. Resin Transfer Molding (RTM) takes place with two matching machined tools, where the fiber preform is placed in the cavity and the mold is closed [129], [130]. Following the closure of the mold, resin is injected and the part is run through a heated cure cycle. The final step is to remove the part from the mold and do any necessary trimming and finishing. This whole process takes place above atmospheric pressure. The mold shape in RTM can be relatively complex and the fiber preform is expected to fit the complex shape of the mold. This can often require significant changes to the fiber orientations and tow shearing, which will affect the flow of resin later in the injection stage. Thus, realistic models are needed to select and locate injection ports and vents. The injection pressures and flow rates reduce the expected voids in the composite part. The ultimate goal is to fill the entire mold cavity before the resin gels and to create parts that reduce waste. When modeling the filling of a RTM mold, the fill time is often short in relation to the gel time of the resin.

A variant of resin transfer molding is Vacuum Assisted Resin Transfer Molding (VARTM) where the key difference is that this process takes place under a vacuum [5]. This means that the maximum pressure seen is the value of the local atmospheric pressure. This is also a one-sided mold with a vacuum bag where a vacuum pump draws the resin into the mold. There are variants of this process that use two solid tools or a solid tool plate and a vacuum bag with distribution media. Other variations of this process are called Resin Infusion under Flexible Tooling (RIFT) and the patented Seamann Composites Resin Infusion Molding Process (SCRIMP) [131], both of which use a hard tool on one side and a vacuum bag on the other. Pultrusion and Structural Reaction Injection Molding (SRIM) are further processes where resin flows through a fiber preform [132].

A slightly different Liquid Composite Molding (LCM) process is called Compression Resin Transfer Molding (CRTM), which has a few stages [133]. First, during the injection stage a quantity of resin is injected into a mold that is not completely compacted. This allows the fiber preform to begin to wet out and removes some voids. Second, the mold is closed completely, allowing the resin to be forced into the fiber preform and ideally replace all of the remaining air left in the mold. Third, this process can then pump more resin into the mold or begin the cure cycle immediately.

The cure cycle used in component processing will have a significant effect on the mechanical properties of the finished part and therefore it is necessary to consider separately when it is not considered in the injection step. The curing reaction depends on temperature but the polymerization of the thermosetting class of matrix material is also a heat-generating process in itself, which directly affects the temperature [134]. In a perfect situation, the preform is fully saturated with resin and then the RTM mold is heated in a resin specific cure cycle. Resin curing is usually designed to be minimal during infusion stage in order to maintain a low resin viscosity. This allows for a fast fiber reinforcement saturation before the resin gels [135]. With and isothermal fluid flow assumption the mold fill time is shorter than the time required for the cure to affect viscosity of the resin [136]. This is often the case and will be a basis assumption for the work in this dissertation. Although resin cure and kinetics are an important aspects of the RTM process, this is outside the scope of this study. If the resin is significantly curing and changing during the infusion, a coupled solution and a cure kinetic model can be introduced. This is implemented as an additional term in the heat and mass balance equations, as well as relating to the flow model by through the variable resin viscosity [137]. A specific example of this method and implementation has been done in literature [137].

The traditional method for modeling composite infusion is to model flow through a fabric reinforcement that obeys a macroscopic model such as Darcy's Law [63]. This approach does not consider the details of the reinforcement on the nano-, micro-, or meso-scales. The reinforcement is treated as having a permeability tensor that applies to its principle coordinate directions. The tensor will account for the fact that the resistance to flow is not the same in all directions.

The intricate fiber microstructure cannot currently be modeled for the entire preform geometry because of limitations in computational resources, so it is necessary to create efficient methods of computation with the most important effects accounted for in the model. As computational power continues to increase, computer modeling is an increasingly important component in design and waste reduction through digital prototyping. There are a number of commercial software packages available specifically for the composites marketplace as well as general physics solvers that can be applied. Flow models can be used to simulate manufacturing processes if there are accurate data and a strong understanding of the governing mathematical tools that characterize the flow during resin impregnation [63].

Many two-dimensional flow scenarios in composite modeling are valid because most composite parts have much smaller thicknesses than other part dimensions. In this case, the transverse, through thickness flow can be neglected and a two-dimensional problem can be solved [49]. As more complex geometries are modelled with significant through thickness components, a three-dimensional case is necessary in order to produce accurate results [138]. Also, non-isothermal simulations are necessary when temperature and degree of cure vary through the part.

In many practical situations fiber volume fraction will vary across different parts of a preform, thus the resulting permeability will also vary in the preform. Using Darcy's Law calculation for the fluid flow, a pressure drop is created across length, the appropriate flow equations are solved, and the permeability is calculated using the resulting pressure and velocity fields. Lekakou *et al.* [139] described the flow through the intra-tow and inter-tow regions in a textile reinforcement using a model that incorporated the effects of viscous and capillary forces on the flow. Their computational studies on a woven fabric model showed that it is only important to separately incorporate capillary flows at very low injection pressures (below half of an atmosphere). The pressure that is important is also a function of tow diameter and volume fraction. At pressures below 50kPa, this capillary flow is more significant within the tows and would influence the predicted global permeability. Since in practice most resin infusion processes use high injection pressures, it is reasonable to not specially treat the capillary forces for modeling purposes. Additionally, in very low injection pressures, vacuum pumps are often attached to the outlet which again would reduce the need for capillary effect considerations.

2.2.1 PAM-RTM Modeling

PAM-RTM is a software code owned by the ESI group and originally was based on a non-conforming finite element method developed by Gauvin and Trochu [140]. In this paper, the code is called RTM-FLOT and it is used to solve the RTM mold filling problem based on Darcy's Law. The code defines a fill factor for each element and no further control volume is constructed for each node. The method used by Gauvin and Trochu ensures the flow rate across inter-element boundaries is conserved. The first applications of PAM-RTM looked at flow through multi-layer preforms and edge effects where the resin racetracks along the mold. They were able to deduce flows based on poor preform fit and obtained good agreement with experimental observations. Along the physics, only a simplified form of Darcy's transient equation is being solved; this reduces the computation time but also reduces the level of complexity that can be solved without special considerations.

2.2.2 FLUENT Modeling

Isoldi *et al.* [138] used Fluent to model the RTM manufacturing process. The method they implemented used a volume of fluid method for the transient filling solution to produce a total fill time. In this solution, they neglected any heat effects or time sensitive resins but they were able to implement edge effects seen by resin runners inducing race tracking. Preliminary examples were presented to compare analytical, experimental, and numerical solutions. A final problem was solved without experimental validation as an extension of previous validated solutions. This solution looked at light resin transfer molding and verified the ability to combine porous media regions with open regions. For these simulations the Navier-Stokes equations are directly applied with a sink term for momentum, which accounts for the Darcy permeability.

3. MODELING TO PREDICT MICRO-SCALE PERMEABILITY FOR FIBER REINFORCEMENT IN LIQUID COMPOSITE MOLDING

3.1 ABSTRACT

In liquid composite manufacturing, permeability is the driving process parameter for mold fills and is critical for understanding the infusion flow and pressure distribution that results. Permeability has been identified as a complex variable which can vary significantly in magnitude for similar test cases. Permeability has also been isolated at different levels because of the multi-scale nature of composite fiber reinforcement. In the micro-scale, fibers are formed into randomly aligned tows composed of thousands of fibers. A second scale, the meso-scale, considers the tow dimensions and weave parameters, but inputs a Darcy based permeability to make up for physical geometry variations. On the micro-scale, fibers are generally considered as ordered in some kind of idealized packing arrangement, for example hexagonal or square packing. This is not always realistic and defining permeability as a function of porosity alone may not be enough to achieve an accurate permeability prediction on the micro-scale. Here, we isolate the micro-scale structures of unidirectional fiber reinforcements and investigate flows across aligned fiber geometries and infusion characteristics during manufacturing. Reduced geometries are utilized to represent the fiber and matrix interactions during a liquid infusion. The overarching goal of this research is to use numerical tools to create better understanding of composite manufacturing processes. A systematic computational approach is utilized to understand how material packing changes the fluid flow regime during composite manufacturing, helping to select appropriate infusion parameters to produce a part. This

approach incorporates a numerical modelling procedure to predict unidirectional permeability on the micro-scale. The results set up a baseline that compares well with analytical models as a function of fiber diameter and volume fraction. Results show that variations due to fiber packing can be identified independently of fiber volume fraction.

3.2 Introduction

Liquid composite molding (LCM) is a class of composite manufacturing procedures composed of many commercial composite manufacturing techniques. Specific LCM processes that are commonly used include resin transfer molding (RTM) and vacuum assisted resin transfer molding (VARTM). These manufacturing techniques are able to produce high performance composite parts with good finished properties [4]. These processes have been critical to the aerospace industry for a number of years, are often used in nautical and marine applications, and are of growing importance in the automotive industry to meet new fuel economy standards [141]. LCM processes are extremely important to creating lightweight parts that have high performance density.

The general LCM process injects a thermosetting or thermoplastic resin into a fiber preform. This fiber preform is composed of individual fibers that can be woven, braided, knitted, stitched, or randomly placed in mats to create the fibrous reinforcement. When a composite component is designed, modeling techniques are necessary to predict what will take place in this closed mold process. These models for the injection processing rely heavily on the properties of reinforcement permeability that act as a proportionality constant in Darcy's Law. Neglecting accurate values for permeability, the design and placement of injection ports, flow rates, resin runners, and resin outlets cannot be confidently conducted on the component scale. Without this modeling step, the designed mold could unintentionally promote the formation of voids or dry spotting in the finished composite part.

Unidirectional permeability has been shown in the past to agree well with Darcy's Law for porous media but it is important to note that this permeability value is heavily dependent on the total fiber volume fraction of the part. As fiber volume fraction increases, permeability rapidly drops. Darcy's Law is dependent on the flow rate through a volume, the characteristic length, the pressure drop over that length, the fluid viscosity, and the permeability of the medium [68]. Darcy's one dimensional formulation is

$$Q = \frac{\bar{\bar{S}}A}{\mu}\frac{(P_{IN} - P_{OUT})}{L} \tag{14}$$

Where, Q is the total fluid discharge in units of volume per time. Permeability S, with units of length squared, is multiplied by the cross sectional area A, and the total pressure drop $(P_{IN} - P_{OUT})$ over the length perpendicular to flow. The viscosity is accounted for and the fluid flows from high pressure to low pressure. The equation can be expanded to three-dimensional by removing the cross sectional area and perpendicular length giving,

$$\bar{q} = -\frac{\bar{\bar{S}}}{\mu}\nabla P \tag{15}$$

Where q is not the velocity but is the Darcy Flux, known as the discharge per unit area and is related to the velocity times porosity. Also, the pressure gradients are used to replace the pressure drop across length. The in-plane directions are often denoted as S_{xx} or S_{yy} in the x- and y-directions and S_{zz} in the transverse z-direction [98].

$$\begin{bmatrix} q_x \\ q_y \\ q_z \end{bmatrix} = -\frac{1}{\mu}\begin{bmatrix} S_{xx} & S_{xy} & S_{xz} \\ S_{yx} & S_{yy} & S_{yz} \\ S_{zx} & S_{zy} & S_{zz} \end{bmatrix}\begin{bmatrix} \frac{\partial p}{\partial x} \\ \frac{\partial p}{\partial y} \\ \frac{\partial p}{\partial z} \end{bmatrix} \tag{16}$$

The principal permeabilities are often denoted as S_{11}, S_{22}, and S_{33}. In anisotropic media, a second order tensor is generated noting the pressure drop in three dimensions across an element of porous media. The tensor is symmetric and diagonalizable where the eigenvectors denote the principal directions of flow and the eigenvalues are the principal permeabilities. The most common way to obtain these values is experimentally through tests that prescribe the boundary conditions of Darcy's Law to calculate permeability. These tests require the preform to be measured in principle directions as well as at all fiber volume fractions of interest. Furthermore, the accuracy of permeability values is critical to infusion process simulations, but the permeability measurement techniques are known to be subject to large variations that may be due to structural variations, non-uniformity, and deformation of the preform during measurement [76], [80], [82], [86], [142].

A number of analytical models have been posed for permeability. For example, the Kozeny-Carman equations were originally developed for granular beds and have been adapted for permeability of aligned fiber beds. The equation was proposed as an option for predicting permeability in terms of geometrical properties in fiber beds [77]. The equation is

$$S = \frac{(1 - V_f)^3}{4kV_f^{\ 2}} r^2 \tag{17}$$

Where, V_f is the fiber volume fraction, r is the fiber radius, and k is the empirically derived Kozeny-Carman constant, typically in the 0.35-1.78 range. Unfortunately, in the original equations, the permeability is larger than zero at volume fractions that go above the theoretical maximum packing arrangement. Also, the Kozeny-Carman equation does not specifically account for the interconnected nature of the porous tow. At the theoretical maximum packing, transverse flow should be completely restricted because the fibers are blocking all possible flow channels. Furthermore, discrepancies can arise in the Kozeny-Carman constants when moving from idealized and ordered fiber arrays to the much more random and less structured arrangements seen in composite cross sections [82], [86], [143], [144].

Another attempt by Gebart [76], specific to unidirectional composite preforms, set up analytical models for the flow parallel to and transverse to the fiber orientations. Good results were shown for fitting these equations to experimental results for a medium range of volume fractions, and a parameterized set of equations were created based on the fiber radius. An effective fiber radius about four times larger than the real fiber radius was used. Additionally, the equations are developed for ideal hexagonal and quadratic packing arrangements that are much more organized than what is traditionally seen in micrographs of composite samples. The Gebart analytical models for permeability of unidirectional reinforcements may not represent very high and very low volume fractions and are unable to account for outside effects such as stochastic fiber packing, fiber diameter variation, and particulate effects. Also, studies on unidirectional fibers and unidirectional fabrics are not interchangeable [95], [145], [146]. Unidirectional fabrics are composed of tows often bound together with another material and still have a dual-scale nature with larger, meso-scale, spacing combined with micrometer spacing on the fiber intra-tow level. This is important to note because if you want to extend the Gebart formulas to simulations of woven structures, the equations may or may not be appropriate for meso-scale inputs [147].

The Gebart equations for unidirectional fibers are derived analytically and can be expressed for flow perpendicular or parallel to the fiber direction. Tow permeabilities are computed using the hexagonal and quadratic packing arrangement. The theoretical maximum volume fraction for a hexagonal packing assumption is $\pi/(2\sqrt{3})$ or 90.69% and is necessary for the analytical equations. Eq. 18 describes the hexagonal packing for the Gebart analytical permeability in flow perpendicular to the fibers and shows the result for the input parameters used. The term $16/(9\pi\sqrt{6})$ or 0.2310 comes from the fiber arrangement and varies for hexagonal and square packing.

$$S_{perpendicular} = \frac{16}{9\Pi\sqrt{2}}\left(\sqrt{\frac{V_{fmax}}{V_f}} - 1\right)^{5/2} R^2 \qquad (18)$$

Eq. 19 describes the hexagonal packing for Gebart's analytical permeability in flow along the fibers. Of further note, c is equal to the Kozeny constant of 53 for a hexagonal packing case. Looking back at Eq. 17 and comparing to Eq. 19, the relationship on formulation can be seen between the Gebart's and Kozeny-Carman equations. The two equations come from the same source and the empirical formulations are slightly different with equation Eq. 19 considering the square of the fiber volume fraction in the denominator and 8 in the numerator.

$$S_{parallel} = \frac{8R^2}{c} \frac{\left(1 - V_f\right)^3}{{V_f}^2} \tag{19}$$

Using a numerical method, Happel [87] solved for the longitudinal permeability of fiber alignments using the unit cell approach. The unit cell was reduced to a circle and an approximate solution to the Stokes equation was found. A zero shear stress boundary condition was applied on the surface of the circle. From there, additional attempts were made, fixing the boundary conditions at the unit cell [148]–[151]. Further, increasingly complex flow simulations can be considered based on the unit cell approach, because of increasing computer power. In these simulations, Darcy's Law can be used to back-calculate a permeability from the unit cell simulation. Of current interest is the effect of fiber variations on the realized permeability.

It has been stated that uniform arrangements yield lower permeability than non-uniform arrays of fibers [148]–[151]. However, the opposite result has also been reported. Bechtold and Ye [152] studied the numerical transverse permeability of random fiber arrangements and applied the Morishita number to quantify the randomness. The Morishita number measured the variation of fiber spatial distribution. With a larger Morishita number the regularity of the fiber arrangement decreases and so does the permeability.

Chen and Papathanasiou [43], [44], [153] produced a set of papers looking at the transverse and parallel permeability of aligned fiber beds, respectively. They adopted a Monte Carlo procedure to generate random fiber arrays up to 571 fibers noting the mean inter-fiber distance and a variation of permeability at the same fiber volume fraction. The range of volume fractions investigated in [44] was from 10-55%. They concluded that the inter-fiber spacing can have a large effect on the permeability at the same porosity.

The review of literature shows that unidirectional fiber permeability is of interest and an accurate description of resin flow in composite manufacturing relies on it. The correlation of fiber volume fraction and fiber randomness affects permeability but how remains unclear. In this study, a numerical method of permeability prediction is developed that allows for the effects of various fiber diameters and volume fractions to be accounted for in parallel and transverse flow scenarios. The geometries are generated based on an algorithm described by [154] and then used as an input for a macro program that reads the file and extrudes a geometry. Then this geometry is solved using computational fluid dynamics and the Navier-Stokes equations. The results are compared with literature for flows through unidirectional fiber preforms as well as compared to the Gebart's and Kozeny-Carman analytical equations. The numerical results have the potential to be used in component level simulations where permeability is needed as a definition for a preform layup. Furthermore, these results can be used on the meso-scale for simulations of a woven fabric and its repeating unit cell

3.3 Fiber Modeling

An algorithm by Desmond and Weeks [154] was adapted for this numerical study. The original algorithm was used to study random close packing of spheres and disks in confined geometries to advance the understanding of how random packing orientations affect the maximum packing volume fraction. Here, this algorithm is adapted to create random cylindrical geometries for numerical permeability experiments.

In two dimensions, a mixture of disks is inserted into a 1x1 square dimensionless domain. Each configuration is implemented by building on the method by Xu *et al*. [155], Clarke and Wiley [156], and Desmond and Weeks [154]. At the beginning, a set of infinitesimal particles are placed in the system using the Pseudorandom Mersenne Twister Algorithm to randomize the starting points. These points are gradually given volume and location by being expanded and moved. They are translated in two dimensions to prevent the overlapping of fiber ends. At time zero, infinitesimal particles are injected into the system and gradually expanded and moved at each step. When a final state is found where the disks can no longer be expanded without overlapping, this step of the packing process ends.

The algorithm alternates between treating the disks as hard particles, where overlapping is not allowed, and as soft particles where overlapping is allowed. This is done by using a soft potential described by

$$V(r_{ij}) = \frac{\epsilon}{2}\left(1 - \frac{r_{ij}}{d_{ij}}\right)^2 \Theta\left(1 - \frac{r_{ij}}{d_{ij}}\right) \tag{20}$$

Where r_{ij} is the center to center distance between two disks i and j, ϵ is a characteristic energy scale, d_{ij} =(d_i+d_j)/2 and the Heaviside step function is used $\Theta\left(1 - \frac{r_{ij}}{d_{ij}}\right)$ making V nonzero for r_{ij}<d_{ij}. Particles are prevented from overlapping based on a user defined threshold. After each expansion step, the disks are checked for any overlapping by checking the condition 1-

$r_{ij}/d_{ij} > \epsilon r = 10^{-5}$ for every particle. This limit is set by choosing a point where overlap is negligible. If disks are found to be overlapping, the nonlinear conjugate gradient method [157] is used to move the centers in order to make them no longer overlap. Physically, the average force per particle is minimized in order to ensure fiber ends are not overlapping.

The algorithm handles up to a binary mixture of disks of a desired ratio. For each configuration, disks are packed into a box of prescribed unit less dimensions. The boundaries of the box are prescribed as fixed and a final configuration is generated from the algorithm [155], [156]. A 1x1 unit square is generated where the number of fibers desired is input. A starting volume fraction is selected and a starting volume fraction step size is prescribed. The algorithm packs a volume fraction of fiber ends into the square. The wall boundaries are treated as mirrors where, as a plate moves closer to a boundary, it is reflected back by its own projection. Up to this point, all calculations are dimensionless.

Dimensions are added by selecting a fiber radius and goal volume fraction. The dimensions of all other parameters are driven by the dimensions of the nominal fiber radius. This fiber radius defines the fiber end area, which can be used to calculate the total area of fibers within a square. The total area of fibers is divided by the target volume fraction and this gives a new area of the square unit cell. The new area is used to define the lengths of the bounding box sides that make up the fluid region that is solved for permeability. This square fluid length is also used to create the cubic volume in three dimensions. Before this step, the previous x-, y-, and z-coordinates were values from 0 to 1. After this step, the new x-, y-, and z-coordinates are generated by taking the cube length in any dimension and multiplying the dimensionless coordinates by that length.

The new coordinates are saved as a text file and read automatically to generate a STEP geometry file. This section of the code creates an outer cube, the fluid volume, with a set of fibers approximated as randomly placed, perfect cylinders. Particle size ratios of 1 are investigated in this paper. The model adopted also limited the maximum achievable packing arrangement because of wall induced structure, small fiber counts, and the maximum theoretical packing arrangements are not possible here.

3.4 Flow Modeling

Here, models are created for the longitudinal and transverse flow through fiber beds. The solution for the permeability of flow perpendicular and parallel to the fibers has been conducted in three-dimensions with the finite volume code FLUENT. The computations are done at low flow rates so that the creeping flow assumption is valid. This implies that inertial forces are neglected and the results for permeability should result in linear pressure gradients.

The simulations have been repeated for volume fractions of 10-60% in increments of 10% volume fraction. The simulations have been run at fiber counts of 10 and 100 as well as a several random packing arrangements at each fiber count. A characteristic geometry for 10 and 100 fibers can be seen in Figure 4. In the volume cell, the fiber surfaces are assumed to have a standard no slip, wall boundary condition. The boundaries of the volume are assumed to be translationally periodic and are matched to opposing faces. The inlet condition is a velocity inlet and an atmospheric pressure outlet is assumed. The results output the inlet and outlet pressures, as well as the interstitial velocity. Periodic boundary conditions are used on boundaries not prescribed as pressure inlets or outlets. The steady state laminar flow conditions are assumed to accurately represent the flow that takes place under experimental permeability measurements. A tetrahedral mesh is generated for the unit cell. Currently, a new and unique mesh is required for each volume of fibers and is a limiting factor in the number of random packing arrangements that can be realistically investigated.

The fluid used in the numerical simulation was motor oil, often used in experimental investigations of permeability (Viscosity 0.24Pa*s, Density 709 kg/m^3). The bulk, macroscopic, component level permeability is a function of the micro- and meso-scale permeabilities. The component level permeability is of manufacturing interest because it is used in modeling the impregnating resin during infusion in the most computationally efficient manner.

3.5 Results

Two generated geometries generated with the process described above are shown in Figure 4, with 10 and 100 fibers. They are characteristic geometries generated using the adapted algorithm, and the corresponding boundary conditions are reasonably representative of the results of the geometry generation tool. The velocity inlet and pressure outlet are prescribed along with the periodic boundary conditions. The fibers are treated as walls with no slip boundary conditions along their surfaces. The fluid region is shown as green in Figure 4a and the fibers are approximated as perfect cylinders which can more clearly be seen in Figure 4b where the fiber walls are in green and the fluid is transparent.

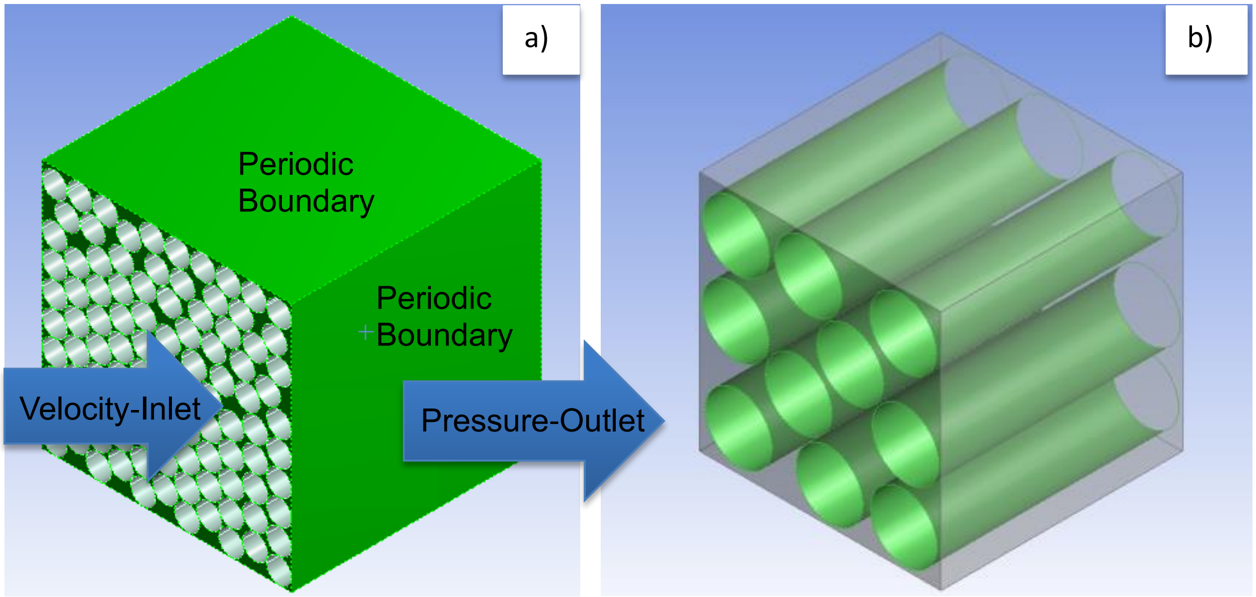

Figure 4: Characteristic Geometries Generated for Flow Simulations a) 100 Fibers at 70% Fiber Vf b) 10 Fibers at 60% Fiber Vf

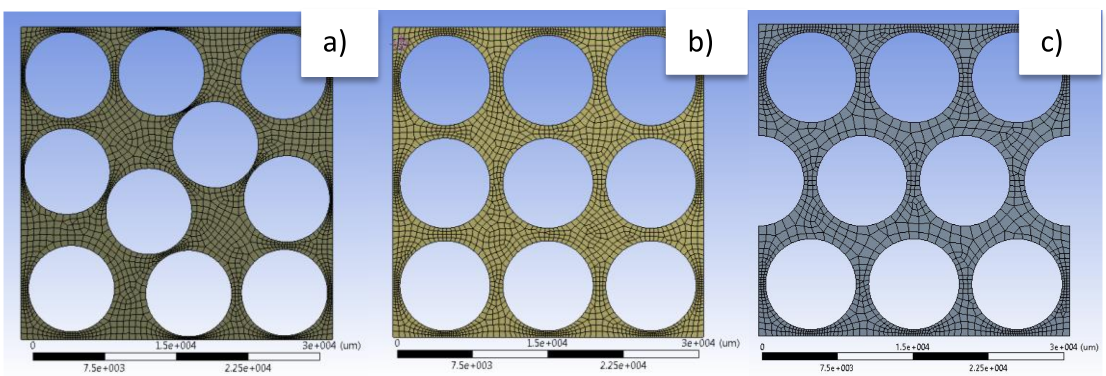

Figure 5: Meshed Geometries at 60% Fiber Vf Comparing a) Random Packing, b) Square Packing, and c) Hexagonal Packing

Figure 5 shows a characteristic example of a "random" geometry at 60% fiber volume fraction, as well as, a perfect square packing and hexagonal packing case at 60% fiber volume fraction. The effects of the flow channels that form in the packing arrangements can be seen and directly affect the computed pressure distribution in the transverse and parallel flow and the correspondingly computed permeability.

Figure 6 shows the numerical results of parallel permeability for square, hexagonal, 10 fiber, and 100 fiber with corresponding results from literature. The literature results are Gebart (GebHex, GebQuad) and Kozeny-Carman [76] for flows along the fibers. Occasionally, in literature the results have been non-dimensionalized with the square of the fiber radius in order to remove fiber diameters. The results show that with the geometry of 10 fibers or 100 fibers, considered at high volume fractions, the permeability prediction tends to converge towards the rest of the analytically computed results. The numerical results for a hexagonal and square case compare well. With a 100 fiber geometry considered, the numerical model diverges at the two extremes of volume fraction plotted. There is a clear effect of fiber count and packing seen on the permeability results. Comparing the numerical results of ten fibers versus 100 random fibers packed shows a percent difference of 71% in permeability at 60% fiber volume fraction. This drops to a difference of 39% at 10% fiber volume fraction.

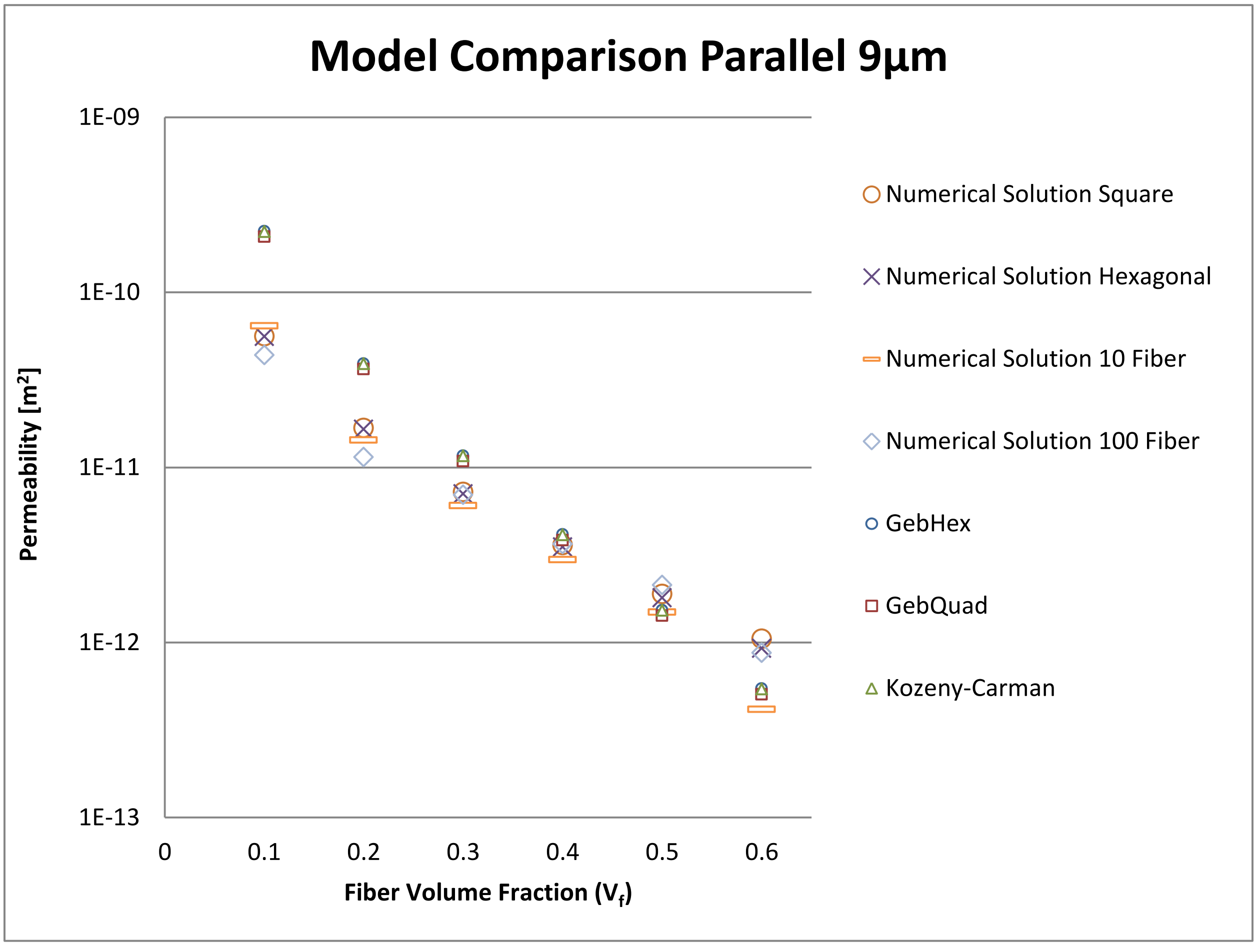

Figure 6: Inter-fiber Parallel Numerical Permeability Results

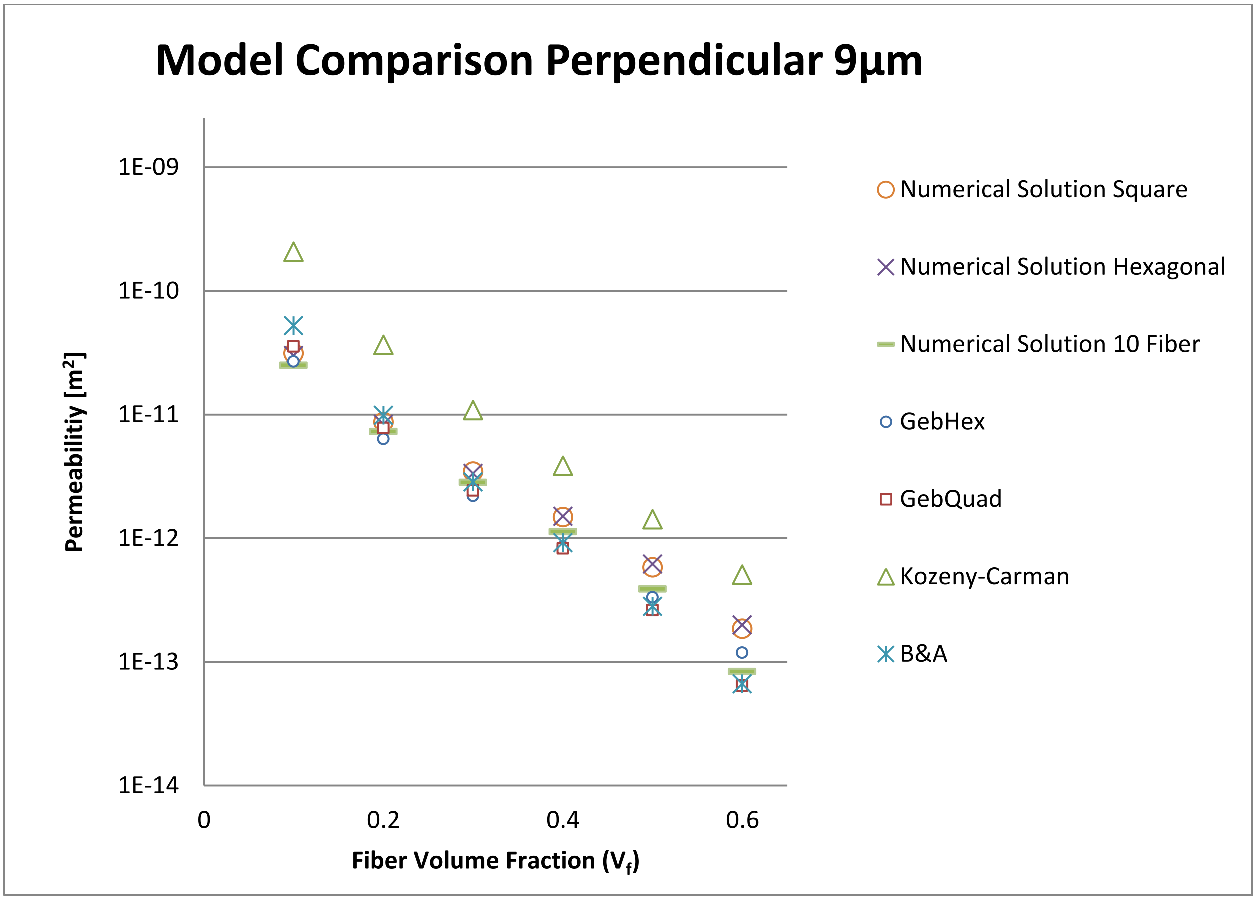

Figure 7: Inter-fiber Perpendicular Numerical Permeability Results

Figure 7 shows the plots of perpendicular permeability numerical results for square, hexagonal, and ten fibers with comparisons to literature. The plots of the Gebart (GebHex, GebQuad) [76] and *Bruschke et al.(B&A)* [86] equations are extremely close to the numerical square packing and 10 fiber results. The ten fiber solution seems to converge towards the GebHex formulation for higher fiber volume fractions. The data tend to scatter more at high and low volume fractions. Comparing the numerical results of square packing versus random packing shows a difference of 62% in permeability at 60% fiber volume fraction. This drops to a difference of 4% at 10% fiber volume fraction. The numerical results conducted here for a square packing and hexagonal packing case tend to compare well with each other.

Figure 8 and Figure 9 shows a linear relationship between pressure and flow rate. This shows that in the simulated results that there is not a significant variation in permeability based on flow rate accounted for. Experimental results tend to validate this assumption. This was investigated for the Newtonian creeping flow assumptions and the neglecting of inertial effects as a significant source of pressure build up in a closed mold process.

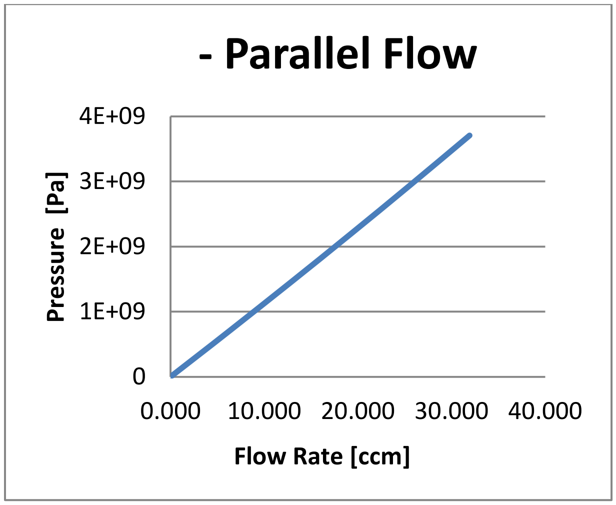

Figure 8: Investigation on Dependence of Pressure on Flow Rate – Parallel Flow.

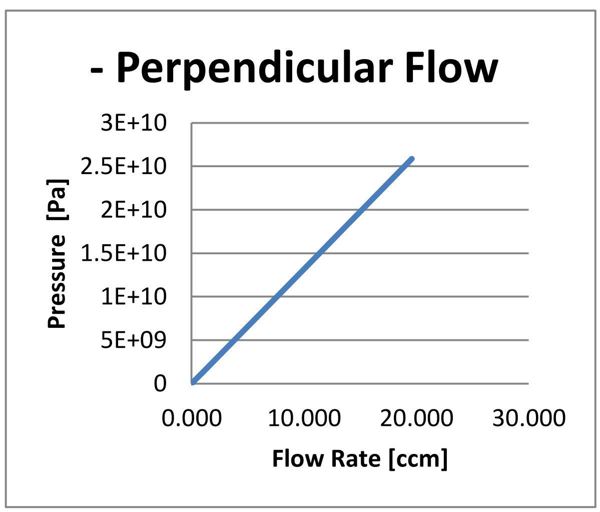

Figure 9: Investigation on Dependence of Pressure on Flow Rate – Perpendicular Flow.

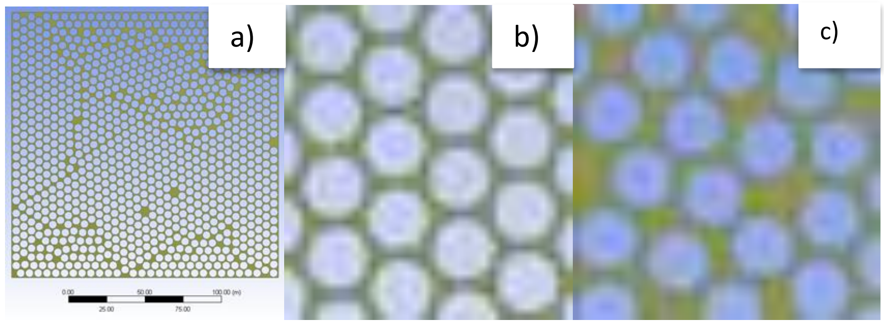

Figure 10: Unit Cell and Local Volume Fraction a) Global Volume Fraction is 70%, b) High Local V_f, c) Lower Local V_f

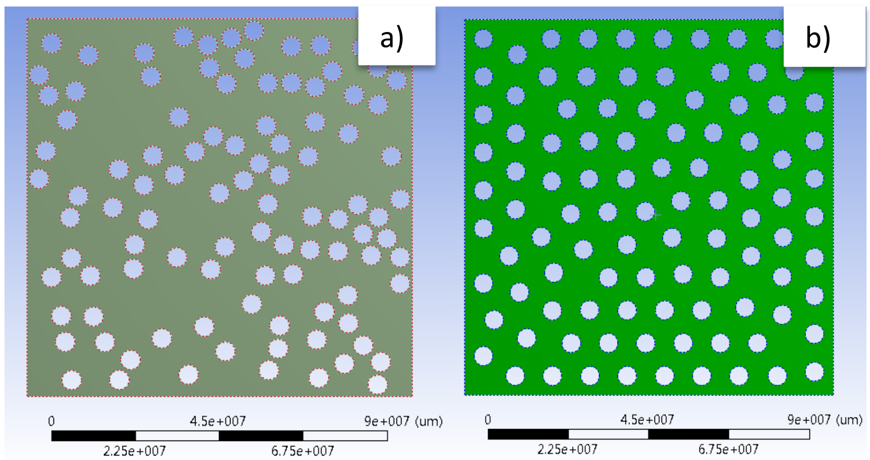

Figure 11: Two geometries generated at 20% fiber volume fraction and Investigated for the effects of interstitial fiber spacing on composite fiber reinforcement permeability. The permeability result for these two packing arrangements varies by 11% in the transverse direction.

Figure 10 shows a large unit cell with 1000 fibers and local fiber variations. Using the algorithm developed, Figure 11 shows how averages and standard deviations could be found within the same global fiber volume fraction. This indicates that additional parameters such as the mean nearest fiber spacing could be used to help quantify the microstructure and the level of local heterogeneity. The effects of interstitial fiber spacing are apparent on permeability and the results in this figure vary by 11% from each other. For 7 random geometries at 20% fiber volume fraction with 100 fibers, the average non-dimensionalized permeability was 1.47E-01 with a standard deviation of 8.03E-3.

3.6 Discussion

In modeling micro-scale permeability, the random packing does have an effect on permeability. It is hypothesized that this is due to local permeability variations that differ from the global unit cell average. For example, in Figure 11, a global unit cell of 100 fibers, there will be pockets of higher volume fraction and lower volume fraction in the unit cell. This is emphasized in Figure 6. These pockets will have higher and lower permeabilities respective to their local volume fractions. The local variations will affect the global average and this will effectively raise or lower the computed global average. The higher volume fraction regions within the domain will allow flow blockage near the pressure inlet and corresponding pressure build ups.

Additionally, in these results, confining the boundaries of the unit cells to square walls will have the effect of artificially inducing order into the arrangements because periodic boundaries are not used in the generation of the geometries and partial fibers are not allowed to cross the walls of the representative volume element. This will also reduce the total fiber volume fraction that can be achieved because perfect hexagonal packing is necessary for a maximum packing. This would require a hexagonal shaped unit cell or periodic boundary conditions in the geometry generation step. While permeability is a function of a large number of fibers, the real systems with fixed size may have boundaries that influence the flow characteristics.

The fiber distribution is able to generate variability in the computed permeability at the same fiber volume fraction. The average permeability as well as the standard deviation is of particular interest. The reported permeability is an ensemble average of the entire domain. This should take into account the well dispersed and agglomerated fibers in the domain and average them out over a large enough ensemble. At high volume fractions, flow channels can become blocked and the permeability will be low in these areas as the porosity becomes less interconnected. This is because the pressure will be allowed to build up in areas restrictive to flow and that will have an upstream effect on the rest of the computational domain.

In practice, variation exists between the experimental, numerical, and analytical results coming from a number of places. First, the experimental setup occasionally sees high pressures that cause the mold sides to displace from one another and the assumed volume fraction could lose some validity. Second, temperature variation in the experimental setup could cause unseen variations of viscosity and therefore an error in the computation of permeability could propagate. Along this same line, small amounts of sizing or fiber content could change the effective viscosity of the fluid and cause a change in the permeability calculated. Third, an ideal fiber preform for this comparison would consist of only parallel fibers -- but this is impractical. Some binder stitching is necessary to keep the fibers oriented together in the correct direction and this can clearly affect the results of permeability. Furthermore, injection pressures could cause fiber distortions and shift the fibers so that they displace and violate the perfectly aligned assumption. All of these effects can compound to create some variability in measured permeability. In computations, we have the unique ability to control for these factors and incrementally modify them. For these reasons, if intra-tow permeability is of interest, numerical tools may be the only way to investigate fully them and the various effects of parameters like the level of randomness.

3.7 Conclusions

Liquid composite molding is a process with low investment costs with a wide range of possible resins and reinforcements. When trying to create a part with good finished properties, a strong understanding of the flow properties is required across a number of scales of interest. Using a numerical approach, like the one outlined above, allows for a strong understanding of the micro-scale flows and a solution that can be coupled into the other scales of interest. Taking advantage of this approach will simplify the modeling of components with complex geometries and allow for the design of better molds.

In modeling micro-scale or pore scale permeability, the random packing does have an effect on permeability. It is hypothesized that this is due to local permeability variations that differ from the global unit cell average. For example, in a global unit cell of 100 fibers, there will be pockets of lower volume fraction and higher volume fraction in the unit cell. These pockets will have higher and lower permeabilities respective to their local volume fractions. The local variations will affect the global average and this will effectively raise or lower the computed global average.

In future work, the ability to characterize multiple fiber diameters at various volume fractions would be interesting. A quick tool for numerical permeability simulations on the micro-scale could be coupled into the meso-scale to predict bulk permeability values as the randomness of the micro-scale is allowed to vary. This should create a statistical variation in permeability predictions on the meso-scale. Moving away from packing assumptions allows us to progress towards more realistic geometries and correspondingly more realistic permeability values. The ability to investigate the importance of flow rate and pressure drop is also interesting.

3.8 Acknowledgements

This work is sponsored by General Electric Aviation, Cincinnati, OH

Computational work in support of this research was performed at Michigan State University's High Performance Computing Center.

4. ANALYTICAL MODEL COMPARISIONS WITH EXPERIMENTAL MEASUREMENTS AND DIRECT NUMERICAL SIMULATIONS FOR UNIDIRECTIONAL FIBERS AND FABRICS

4.1 ABSTRACT

In liquid composite manufacturing, permeability of the fiber preform generally drives the results of an infusion. A strong characterization of permeability is used for process modeling, which can save time and money before resources are spent in fabrication. Governing the resin flow, fiber reinforcement permeability has been modeled analytically and numerically in the past. These models have attempted to account for architecture and preform geometry. Modeling accurate permeability has proven to be difficult because of variable porosity coupled with dual-scale micro- and meso-flow channels, nesting, and complex textile architectures. Accurately obtaining permeability is important on all scales of interest, whether that value is from measurement or modeling. In this study, a unidirectional carbon fabric is measured for permeability. Experimental measurements are obtained in a custom test fixture and are compared with analytical and numerical results. Second, a direct numerical simulation of fiber geometries is run to isolate the micro-scale. Steady state, single phase permeability simulations are conducted on all models to obtain unidirectional permeability. Direct numerical simulations provide a set of statistical results given a fiber volume fraction over multiple random fiber packing arrangements. Third, available permeability models from literature are benchmarked for their ability to fit a direct numerical simulation and a measured unidirectional fabric. The unidirectional fabric chosen possesses a dual-scale porosity that proved to be important. The formation of inter-tow

channels allows for preferential flow paths to form in the measured unidirectional fabric results. The intra-tow permeabilities are significantly lower than the meso-scale permeability. Bulk permeability of a unidirectional fabric cannot be treated directly as a micro-scale or meso-scale material because it incorporates elements of both. Further, analytical models can be modified to fit experimental results but this leads to semi-analytical or empirical models. The results justify continued effort in measuring permeability and attempting to generate a comprehensive, multi-scale, modeling approach for liquid composite molding.

4.2 Introduction

Composite manufacturing with liquid resins can be a complicated process, with the complexity determined in part by fiber reinforcement permeability. It is important to have a strong understanding of permeability and its stochastic variation in order to develop process models, as these parameters govern the resulting mold velocities and pressure gradients. Liquid composite molding (LCM) processes present a number of manufacturing challenges, some of which can be addressed through simulations of the mold filling process. These types of simulation require accurate permeability inputs to get realistic mold fill outputs, and the permeability inputs are often produced through numerous in-plane and transverse experiments at various volume fractions expected in the mold.

In measuring and modeling the flow of resin through fiber reinforcement, the general approach is to consider the resin as a Newtonian fluid propagating through a porous medium [158]. The micro-scale (also called the pore scale in porous media) considers the physical fiber geometry of a unit cell, which allows users to model the physical effects of fibers in the domain and produce a unidirectional permeability. The meso-scale considers bundles of fibers, often 6-12k in a tow, with a tensor permeability that can be input in two transverse directions and a parallel direction. This meso-scale is also referred to as the Darcy scale in porous media literature, where the individual pores or fibers are no longer modeled. Instead, they are replaced by a permeability value representing the resistance to flow. The component-scale represents the desired composite part and can be represented by a bulk permeability value. Component-scales no longer consider physical fibers or tow geometries due to numerical modeling limitations; instead, the component-scale has an effective permeability that can be different from the micro- and meso-scales through its domain.

Characterization of fiber reinforcement permeability has been done by a number of authors for complex fabrics [110], [147], in plane unidirectional materials [76], [85], and on a micro-scale basis [43], [63]. Along these lines, many attempts have been made to extrapolate measured permeability into strong analytical models [76], [77], [86], [159]. These models have been shown to strongly fit the measured data, but these models have not been extended to general materials and they have not been benchmarked against each other because they often give different predictions. Some of the difficulty in making accurate predictions stems from the level of variability of the fabrics.

The Kozeny-Carman equation used the capillary model from soil mechanics to define a simple expression for the permeability as a function of volume fraction and an empirically derived constant based on the fiber or porous network [159]. This approach does not capture all of the physics because permeability is greater than zero at fiber volume fractions that should be greater than the theoretical maximum packing. The Kozeny-Carman equation is shown in Eq. 21, where R is the fiber radius, k is the Kozeny constant, and V_f is the fiber volume fraction. Here, permeability will be denoted as S with units of m^2.

$$S = \frac{R^2}{4k}\frac{(1-V_f)^3}{{V_f}^2} \tag{21}$$

One of the most common analytical models for permeability is the Gebart [76] unidirectional permeability. It is a useful model to understand the necessary parameters in unidirectional fabrics, and is popular for modeling the permeability of fibers parallel and transversely oriented in the flow field as a function of fiber volume fraction. Gebart's equations for unidirectional fibers are derived analytically based on the fiber direction in reference to the flow direction. Eq. 22 describes the hexagonal packing for Gebart's analytical permeability in flow perpendicular to the fibers and shows the result for the input parameters used. The term 16/(9 Π$\sqrt{\mathbf{6}}$) or 0.2310 comes from the fiber arrangement.

$$S_{perpendicular} = \frac{16}{9\Pi\sqrt{2}}\left(\sqrt{\frac{V_{fmax}}{V_f}} - 1\right)^{5/2} R^2 \tag{22}$$

Eq. 23 describes the hexagonal packing for Gebart's analytical permeability in flow along the fibers for the input parameters used in a hexagonal case. Of further note, *c* is equal to the Kozeny constant of 53 for a hexagonal and 57 for a square packing case. The values for radius, fiber volume fraction, and theoretical maximum fiber volume fraction are added to calculate the fiber permeabilities.

$$S_{parallel} = \frac{8R^2}{c}\frac{\left(1 - V_f\right)^3}{{V_f}^2} \tag{23}$$

Bruschke and Advani [86] used lubrication theory and a cell model to describe permeability across an array of fibers as a function of fiber volume fraction. The equation they implement is shown in Eq. 24. The value of R is the radius, S is the permeability, and L^2 is equal to $4V_f/\pi$.

$$\frac{S}{R^2} = \frac{1}{3}\frac{(1-L^2)^2}{L^3}\left(\frac{3L\,tan^{-1}\sqrt{\frac{1+L}{1-L}}}{\sqrt{1-L^2}} + \frac{L^2}{2} + 1\right)^{-1} \tag{24}$$

Gutowski [77] modified the Kozeny-Carman equations for unidirectional reinforcements by using different values of the Kozeny constant in different directions. Empirical parameters were implemented for k' and V_a', as shown in Eq. 25.

$$S = \frac{R^2}{4k'}\frac{\left(\sqrt{\frac{V_a'}{V_f}} - 1\right)^3}{\left(\frac{V_a'}{V_f} + 1\right)} \tag{25}$$

In general, analytical models show that the permeability of a preform decreases as fiber volume fraction increases because of reduced flow channels between fibers. It is difficult to identify a single formula relating the permeability and fiber volume fraction because fiber packing can greatly affect local permeability [43]. It has also been shown that permeability at the same volume fraction is affected by fabric type because of the nominal fiber radius and fiber diameter variation at a single volume fraction. Figure 12 shows the meso-scale tows and the micro-scale fibers for a unidirectional fabric. Some of the difficulty in finding an analytical model stems from the fact that, in micrographs of fibers, the fibers are packed in a random manner. For an analytical model, the assumption is often made to assume a quadratic or hexagonal packing is reasonable. This may account for some difficulty in fitting unidirectional fiber and unidirectional fabric data when looking at very disordered micrographs.

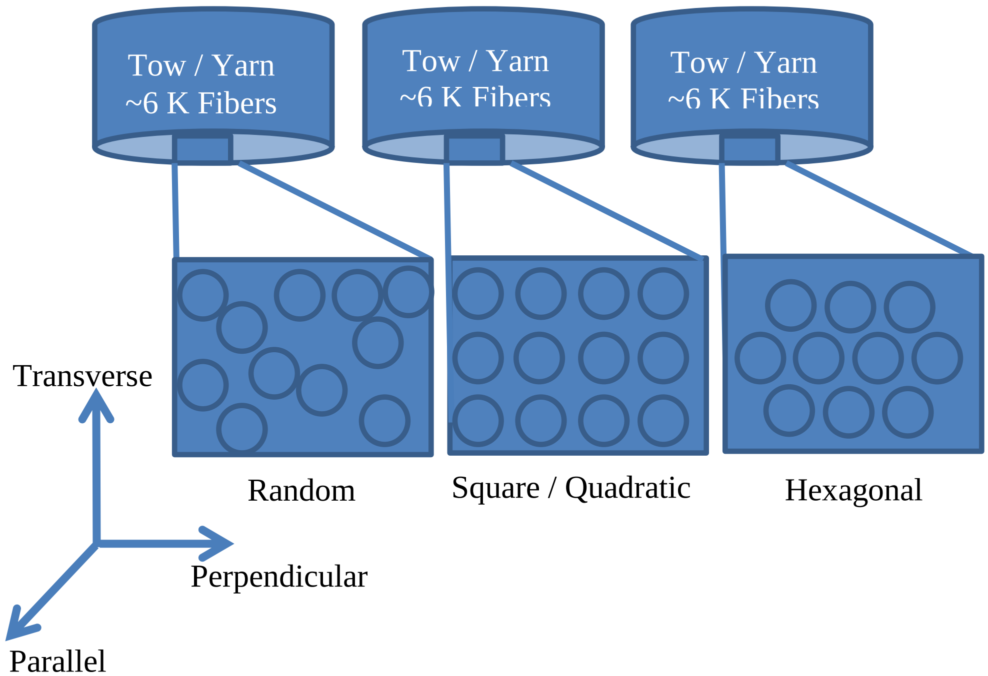

Figure 12: Unidirectional Fabric Tows Shown with Representative Volume Elements of Random, Square, and Hexagonal Fibers. Fabrics and tows are represented by the empirical value for permeability because the number of tows time's approximately 6,000 fibers per tow is too numerically intensive to account for.

The measurement of permeability often involves a setup consisting of a mold loaded with a fiber preform or chopped fiber filler. The resistance to flow is characterized by the permeability tensor and there are a number of devised experimental techniques available to obtain this parameter. They generally fall into saturated or unsaturated measurements [69], [79], [128], [160]. There is disagreement on a standard testing procedure and this has been shown to cause variation when comparing the same fabric characterized by different methods [68], [69]. Experimental procedures vary widely and the testing method can be important. Additional human factors, such as layup, may affect the result of experimental permeability values [161], and experimentalists have found permeability scatter of up to one order of magnitude for the same material [69].

Modeling permeability could aid in refining the variations between experimental results, help identify acceptable experimental methods, or ultimately eliminate experimental characterization entirely. Further, numerical and analytical meso-scale models cannot model an entire volume of fibers currently and measurements are still often required.

Geometric variability directly affects the variability seen in permeability. Previous researchers found that at around 50% fiber volume fraction, a 1% increase in fiber volume fraction would cause a 10% decrease in permeability [85]. Other researchers [43], [44], [162], [163] have shown that permeability variation can be seen by changing the reinforcement dimensions at the same volume fraction. These results are critical to understanding how to create a quality finished part with LCM. Additionally, the local variation of complex reinforcements from the continuous fiber reinforcement manufacturing approach will have large effects on the resulting models of composite materials. Some fabrics are very uniform and others have non-uniform tow dimensions and spacing.

Prediction of permeability requires fluid models on the micro-scale and the consideration of a number of factors relying heavily on geometry. In relating measured permeabilities to predicted permeabilities, factors such as edge effects, preform deformation, micro-flow, temperature, and steady state vs. advancing front permeability all combine to cause variability in the data. Frequently, the creation of geometrical models for fiber preforms involves the use of statistically averaged dimensions within the unit cell [103]. This is done to give an average representation of the preform geometry. Later, the statistical variation can be accounted for by implementing the standard deviations of the preform variability.

In this study, a permeability benchmark of various analytical models is compared to DNS of the microstructure and measurements of a unidirectional carbon fiber fabric. First, unidirectional carbon fabrics are measured. Experimental measurements are obtained in saturated, steady state, single phase experiments. Scaled analytical model results are compared with measured results yielding moderate fits. Second, a direct numerical simulation of fiber geometries is run to isolate the micro-scale. Third, available permeability models from literature are benchmarked for their ability to fit a direct numerical simulation and a measured unidirectional fabric. The dual-scale nature of the unidirectional fabric chosen proves to be important and is discussed. The intra-tow permeabilities are significantly lower than the meso-scale permeability. Further, analytical models are modified to fit experimental results but this leads to semi-analytical or empirical models. The results justify continued effort in measuring permeability and attempting to generate a comprehensive modeling approach for composite fiber reinforcement.

4.3 In-Plane Permeability Measurement

The composite fiber reinforcement chosen for this analysis was a unidirectional IM7 carbon fabric made by Sigmatex. It has 6,000 IM7 carbon fiber tows and a loose e-glass stitching. Saturated permeability values were obtained for the unidirectional carbon fabric through in-plane measurements along and perpendicular to the tows. The fixture implemented a line-source to line-sink channel flow measurement. This fixture is shown in Figure 13, where a constant flow rate pump is used to advance the flow. The fixture consists of a cavity to hold fabrics of 15.24 cm in width by 15.32 cm in length. The compaction and volume fraction are controlled by the testing frame. A compaction plunger is guided to close the cavity and the thickness is controlled. The preform thickness is set by the operator and allowed to reach steady state before pressure measurements are taken. Two linear voltage differential transducers (LVDTs) are used to track the thickness. Using a saturated permeability value removes the effects of tow saturation, surface tension, and capillary effects that may be seen in two-phase flow scenarios.

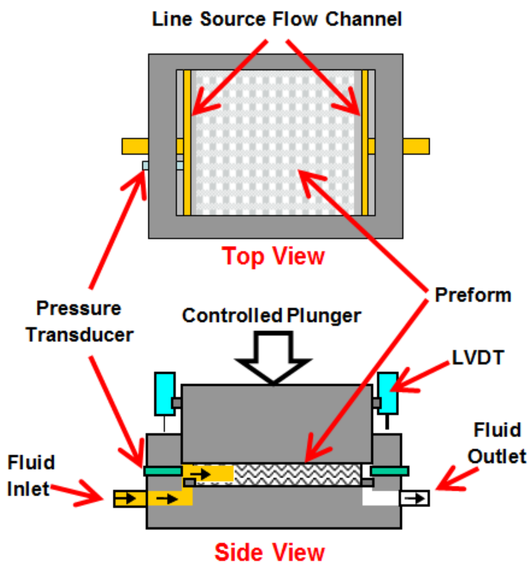

Figure 13: Experimental In-plane Saturated Permeability Fixture Schematic

The carbon fiber volume fraction is calculated from the LVDT location using the definition of fiber volume fraction in Eq. 26, where V_f is the fiber volume fraction, n is the number of plies, A_w is the fiber areal weight, ρ_f is the fiber density, and t is the preform thickness.

$$V_f = \frac{nA_w}{\rho_f \ t} \tag{26}$$

Since the measurements of permeability are saturated instead of unsaturated, the fixture allows for in-plane permeability measurements to be obtained at multiple fiber volume fractions from a single preform. This is not possible with unsaturated tests. A Parker Zenith® Precision Gear Metering Pump injects fluid at a constant flow rate into the cavity, while pressure transducers at the fixture inlet and outlet monitor the pressure drop across the perform. The steady-state, saturated permeability is governed by Darcy's Law [10] shown in Eq. 27, where Q is volumetric flow rate, *S* is preform permeability, μ is fluid viscosity, ΔP is the recorded pressure drop across the preform, A is the area normal to flow, and L is the preform length in the flow direction.

$$Q = \bar{\bar{S}} \frac{A}{\mu} \frac{\Delta P}{L} \tag{27}$$

The test fluid used was NAPA SAE 40 oil at room temperature (viscosity of 0.24 Pa*s, density 709kg/m^3). For carbon fiber layup preparation, six plies of the unidirectional carbon fabric were cut to 15.24 cm in width by 15.32 cm in length and stacked with the yarn direction of each ply aligned. The in plane permeability was measured in each of two directions. The permeability values were found by preparing preforms so that the fluid flow progressed along the yarn direction, while flow across the yarn direction produced the second set of values. Three tests were run in both the in plane and transverse fabric directions. Volume fractions of manufacturing interest were selected at 50%, 55%, 60% and 65%.

4.4 Transverse Permeability Measurement

In a separate testing procedure, the transverse or through thickness permeability was also measured. The fiber volume fraction was varied from 30-50% fiber volume fraction in increments of 5% fiber volume fraction. The 50% fiber volume fraction limit was required due to the extremely low permeabilities and the limitations of the pressure transducers.

Desired fabric volume fraction for tests was then obtained by the relation seen in Eq. 26. For the tests conducted in this study, 6 plies of unidirectional carbon fiber fabric were cut to exact mold cavity dimensions and stacked with the warp direction of each ply aligned. Again, NAPA SAE 40 oil was used as the test fluid.

4.5 Direct Numerical Simulation of Unidirectional Permeability

Analytical models are useful because they are quick and have varying degrees of validation but they lack the ability to investigate natural variability of tows and fabrics. The analytical results sometimes are found to lead to errors because many of these results were derived from unidirectional fabrics which are not the same as unidirectional fibers regarding their effects on fluid flow. They are often derived with empirical parameters to fit specific data sets.

The approach used a micro-scale simulation of an array of 1000 fibers to predict the intra-tow permeability in the same way meso-scale permeability is obtained. Five random packing simulations of unidirectional fibers were generated at each fiber volume fraction and the corresponding fluid permeability was calculated.

An algorithm by Desmond and Weeks [154] was adapted for the unidirectional fibers in this numerical study. Here, this algorithm is adapted to create random cylindrical geometries for numerical permeability experiments. In two dimensions, a mixture of disks is inserted into a 1x1 square dimensionless domain. Each configuration is implemented by building on the method by Xu *et al*. [155], Clarke and Wiley [156], and Desmond and Weeks [154]. At the beginning, a set of infinitesimal points are placed in the system using the Pseudorandom Mersenne Twister Algorithm to randomize the starting locations. These points are gradually given volume and location by being expanded and moved. They are translated in two dimensions to prevent the overlapping of fiber ends. At time zero, infinitesimal particles are injected into the system and gradually expanded and moved at each step. When a final state is found where the disks can no longer be expanded without overlapping, this step of the packing process ends.

Dimensions are added by selecting a fiber radius and target volume fraction. The dimensions of all other parameters are driven by the dimensions of the nominal fiber radius. This fiber radius defines the fiber end area, which can be used to calculate the total area of fibers within a square. The total area of fibers is divided by the target volume fraction and this gives a new area of the square unit cell. The new area is used to drive square lengths which make up the fluid region that is solved for permeability. This square fluid length is also used to create the cubic volume in three dimensions. Before this step, the previous x-, y-, and z-coordinates were values from 0 to 1. After this step, the new x-, y-, and z-coordinates are generated by taking the cube length in any dimension and multiplying the dimensionless coordinates by that length. The new coordinates are saved as a text file and read automatically to generate a STEP geometry file. This section of the code creates an outer cube, the fluid volume, with a set of fibers approximated as randomly placed, perfect cylinders. The geometry is then solved for the fluid flow and permeability results [163].

The fluid used in the numerical simulation was modeled after the fluid used in the experimental permeability measurement. Microscopic permeabilities were calculated in the parallel and perpendicular directions depending on the flow directions based on Darcy's Law in Equation 2 and the flow rate, pressure drop, and length in the simulation. The total flux of fluid is represented by Q, the permeability S, the area is A, the viscosity is μ, the change in pressure is ΔP, and L is the length parallel to the flow direction.

4.6 Results and Discussion

Figure 14 shows a characteristic representation of what was found when comparting measured fabrics to simulated fibers. The top trend is the meso-scale contributions to the bulk permeability and the bottom trend is the contributions to the flow from the micro-scale or intra-tow flows. In this figure the measured meso-scale permeability is higher than the direct numerical simulations of permeability at the same fiber volume fraction. The difference is the contributions of dual-scale scale flow. The meso-scale unidirectional fabrics generally measured higher permeability than the direct numerical simulations of unidirectional fibers. This figure emphasizes the dual-scale nature of the fabric versus the unidirectional fibers. The difference between the permeabilities is attributed to the large meso-scale flow channels that can form and the scale of this difference shows how susceptible a fabric is to dual-scale flows.

This effect is coupled flow between the micro- and meso-scale and can be quantified based on the contributions of the dual-scale flow effect. Additionally, the dual-scale nature of this material is quantified for the material across fiber volume fraction as shown in Figure 14. The generally higher meso-scale permeability is attributed to the large meso-scale flow channels allowing for a smaller pressure build up inside of the measurement fixture.

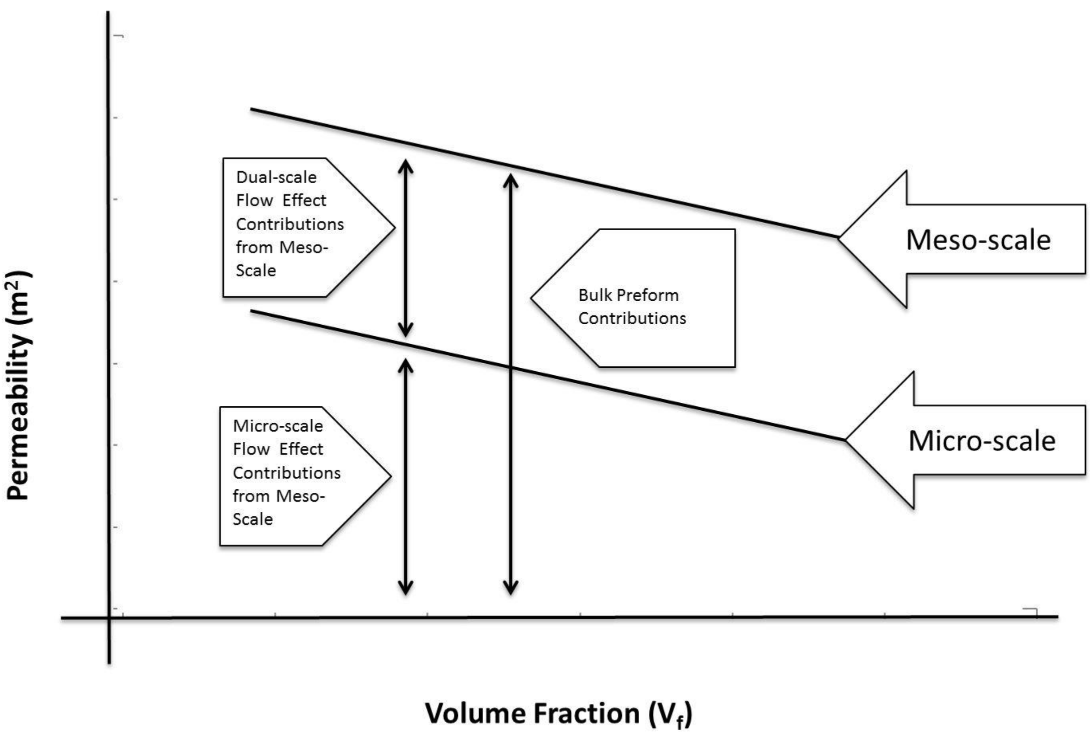

Figure 14: Infographic of the Dual-Scale Porous Media and the Permeability Variation

The results of comparing various analytical models to direct numerical simulations and experimental measurement are shown in Figure 15 to Figure 23. The effect of dual-scale flow between measurement of unidirectional fabrics and simulations of unidirectional fibers is plotted over a range of volume fractions from 50-65% for parallel and perpendicular flows. This range was selected because it is a fiber volume fraction set of practical interest in composite manufacturing for aerospace composites in a resin transfer molding scenario. The percent difference is used to quantify the dual-scale effect. This appears relatively large but is partially justified by the variation expected in permeability measurements and the large flow channels that can form in a fabric.

The transverse case in Figure 17 is plotted on a range from 30-50% fiber volume fraction because of limitations on the pressure transducers used in the transverse flow fixture. Permeability was seen to more rapidly decrease in the transverse direction than the perpendicular direction as a function of fiber volume fraction. This may be attributed to a lack of flow channels as layers of the fabric nest inside of the closed mold. For the discussion, the models from Gebart [76] are used for hexagonal and quadratic cases and denoted by GebHex and GebQuad respectively. The Kozeny-Carman [159] models used are denoted by KCHex and KCQuad for hexagonal and quadratic parameters. The model by Bruschke *et al*. [8] only applies for flow across cylinders and is denoted by Bruschke. The model from Gutowski *et al*. [77] is denoted based on empirical parameters used by Gutowski 0.82 and Gutowski 0.76. The direct numerical simulations are denoted as DNS in the figures.

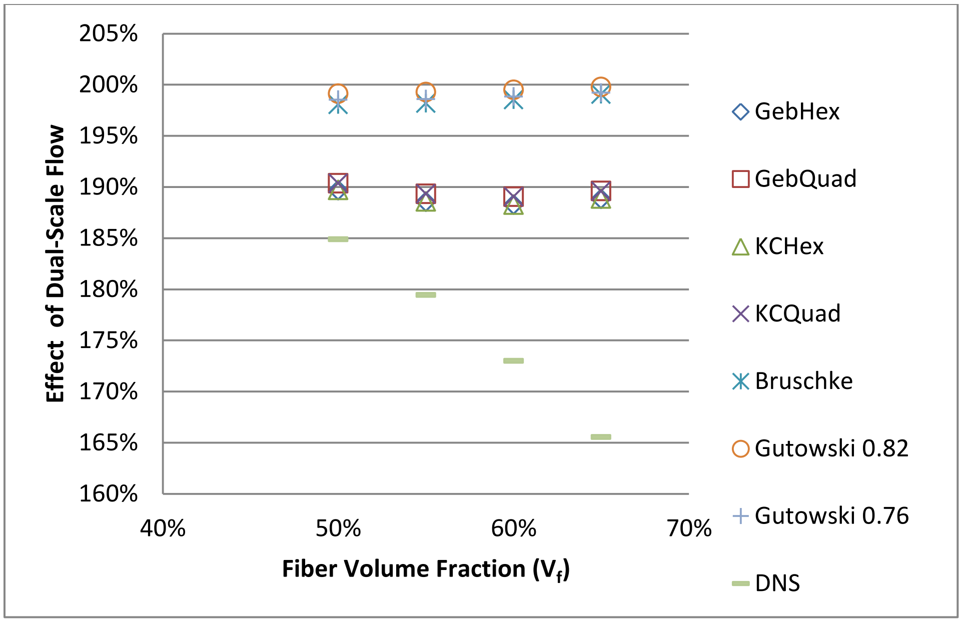

Figure 15: Parallel Permeability Models Plotting Fiber Volume Fraction vs. Effect of Dual-Scale Flow Compared to Measurement

Figure 15 shows the parallel permeability models plotted against fiber volume fraction and effect of dual-scale flow from measurement. Analytical parallel permeability models are expected to vary widely when comparing to direct numerical simulations and measurement because the fundamental basis for the Kozeny-Carman equations is for flow around granular beds and not along aligned fibers. The Gebart and Gutowski relationships come as extensions directly from the Kozeny-Carman formulations. The direct numerical simulations are shown converging towards the measured result as volume fraction is increased but there is still a large difference present at 65% fiber volume fraction. This indicates that as the fiber volume fraction increases there is a decreasing effect of dual-scale flow. Ideally, the DNS would directly fit an analytical model. This has proven to be difficult though because there is no direct analytical solution for flow along fiber reinforcements in composites that has been shown to fit a large range of material cases. The model by Bruschke *et al*. [86] and Gutowski *et al*. [77] are the least accurate at 50%

fiber volume fraction and slightly diverge as volume fraction increases. This is interesting because the analytical model by Bruschke *et al*. [86] [86] and Gutowski *et al*. [77] are only designed for transverse flows. The results from Gebart [76] for quadratic packing and the Kozeny-Carman [159] hexagonal case fit nearly identically to each other, which is reasonable since one is a derivative of the other. It should be pointed out that only the models from Gebart [76] and the DNS results are designed to be used in a parallel flow scenario. The model by Gutowski *et al*. [77] and Kozeny-Carman [76] can be extended to parallel cases through the use of empirical constants.

It is hypothesized that the DNS results appear to converge because as the unidirectional fiber volume fraction increases, the inter-tow spacing is forced to diminish, as the tows nest closer and closer together. This begins to reduce the dual-scale nature of the material and simplifies it as a closer approximation of unidirectional fibers. In the unidirectional DNS simulations it is seen that the more evenly dispersed the fibers are at a given volume fraction, the lower the permeability, in comparison to a less uniform packing arrangement. Agglomerates of fibers lead to higher permeabilities at a given volume fraction because larger channels form and allow for preferential, uninterrupted, flow channels. This reduces the magnitude of the total pressure drop, correspondingly creating a higher permeability. Since the DNS does not directly fit, the “effect of dual-scale flow” is a quantification of how significant the unidirectional fabric is affected by dual-scale flow. When comparing measurement to simulation, 185% dual-scale nature is seen at 50% fiber volume fraction and this drops slightly to 165% dual-scale nature at 65% fiber volume fraction. This shows that as fiber volume fraction increases, the larger gaps between the tows are diminishing. This is emphasizing the compaction as the dual-scale material is compressed.

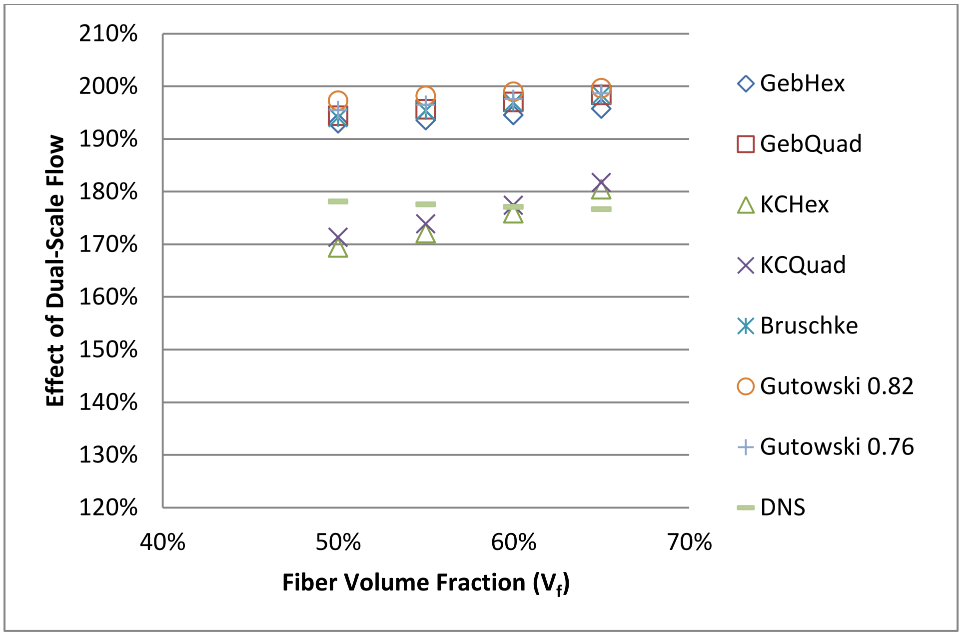

Figure 16: Perpendicular Permeability Models Plotting Fiber Volume Fraction vs. Effect of Dual-Scale Flow Compared to Measurement

Figure 16 shows perpendicular permeability models plotted against fiber volume fraction and effect of dual-scale flow compared to measurement. Analytical perpendicular results give a larger scatter in the comparison to unidirectional measurement results than was expected. Additionally, the analytical models investigated generally lower permeabilities than the DNS results. The results from Gutowski *et al*. [77] and Gebart [76] are showing large amounts of dual-scale nature. This is because the two formulations under predict permeability by a fair amount. Further, the models all trend in very similar directions seeming to diverge from the measured result. This is interesting because the DNS results appear to slightly converge towards the measured results as the effect of dual-scale porosity decreases with increasing fiber volume fraction.

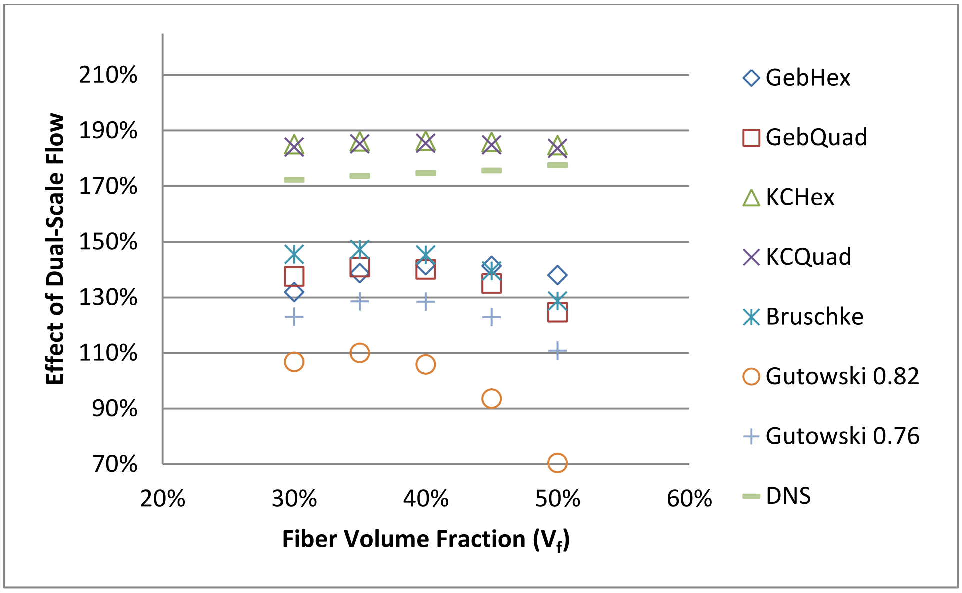

Figure 17: Transverse Permeability Models Plotting Fiber Volume Fraction vs. Effect of Dual-Scale Flow Compared to Measurement

Figure 17 shows the transverse permeability results plotting fiber volume fraction and effect of dual-scale flow from measurement. On a unidirectional fiber basis, the transverse analytical and DNS results are the same as the perpendicular results. Additionally, the available analytical models do not have special treatments for transverse versus perpendicular permeabilities. In practice, the unidirectional fabrics measured are not the same in the transverse and perpendicular directions. This is because the fabrics are very thin in the transverse directions and the fabrics tend to compact rapidly in the through thickness direction. Since analytical unidirectional models over predict permeability in the transverse direction and under predict it in the parallel direction. It was thought that the transverse measurements may be closer to the analytical models, however this was not the finding for all analytical models. The dual-scale flow for the analytical models is fairly consistent for the DNS and Kozeny-Carman results and creates a 20% error band from 170-190%. The transverse measurements are much lower than the perpendicular measurements and the Gutowski models appear to be converging towards measured results at higher fiber volume fractions.

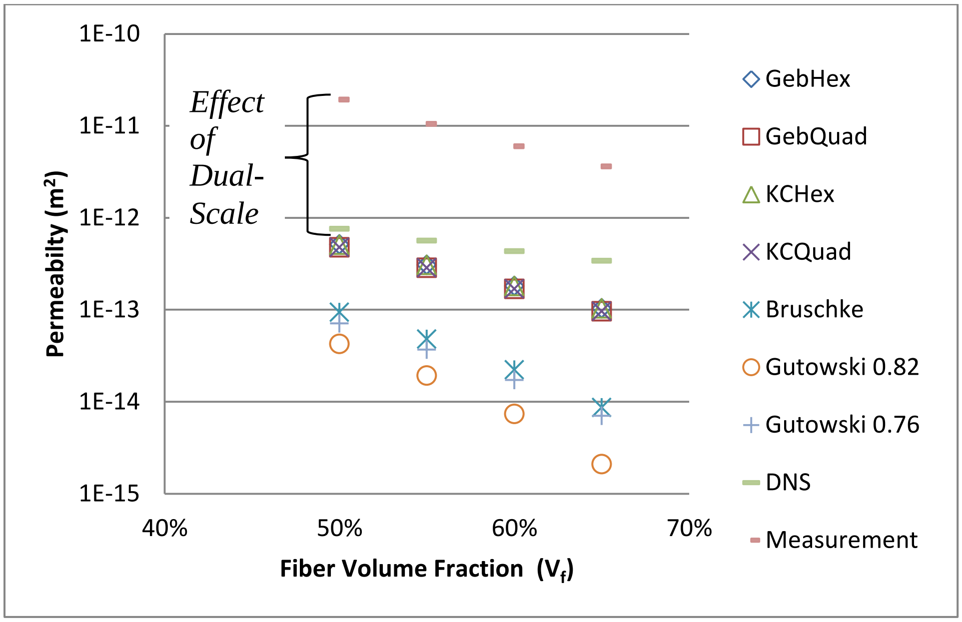

Figure 18: Parallel Permeability Models Plotting Fiber Volume Fraction vs. Permeability

Figure 18 gives the permeability value for parallel models, measurement, and DNS plotted against fiber volume fraction. The results for measured permeability and fiber volume fraction are plotted in corresponding permeability units of m^2 in Figure 18. Here, the trends for measured, DNS, and analytical models can all be clearly seen. This meso-scale measurement data can also be directly taken for other component level simulations. The various models have various levels of agreement with each other but generally show some variation from DNS and measurement. The models by Gebart [76] and Kozeny-Carman [159] are reasonably close to DNS but permeabilities are low for comparisons to measurement. It is somewhat surprising how well these models can fit parallel flow DNS trends because they all are fundamentally designed from flow around spheres or across circular fiber ends. However, the scatter is still large and the analytical models appear to diverge from DNS simulations as fiber volume fraction increases. This is seen as the DNS results tend to converge towards the measured result. The models by Bruschke *et al*. [86] and Gutowski *et al*. [77] do not compare particularly well but they are not expected to since they are designed to model perpendicular flows.

For the measured results in Figure 18, the coefficients of variation (COV) are 28.25 at 50% fiber volume fraction, 19.90 at 55% fiber volume fraction, 12.15 at 60% fiber volume fraction, and 4.96 at 65% fiber volume fraction. The coefficients of variation correspond to an observation that the measured permeabilities of the materials are less variable as fiber volume fraction increases. This is assumed to be because the materials are again being forced to minimize the effect of dual-scale porosity. The measured data is consistently found to have a higher permeability at a given volume fraction because the material has meso-scale inter-tow flow channels that allow for local preferential flow channels and lower pressure build ups in the mold.

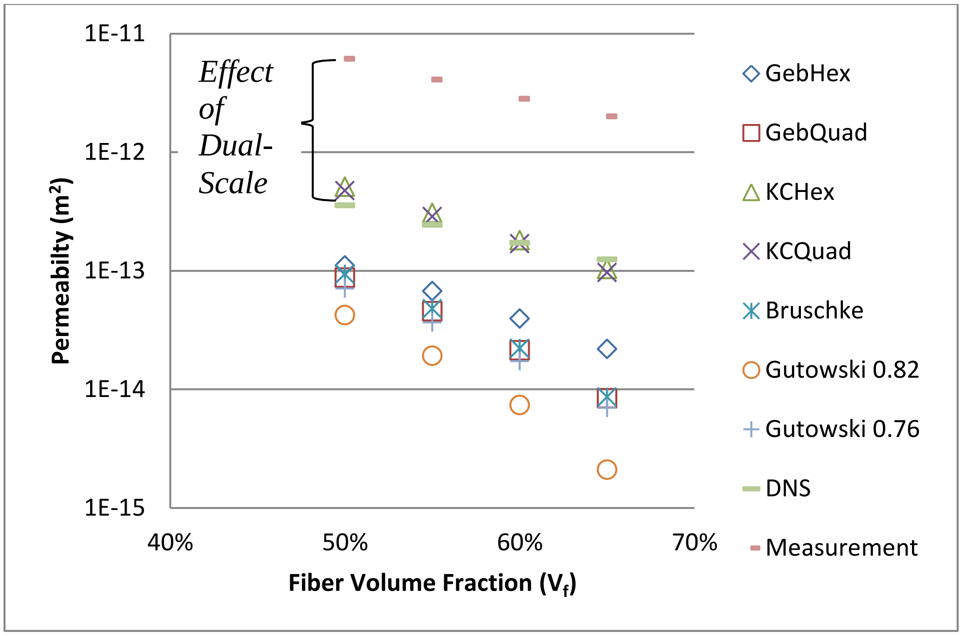

Figure 19: Perpendicular Permeability Models Plotting Fiber Volume Fraction vs. Permeability

Figure 19 shows a plot of the perpendicular permeability analytical models, measurement, and DNS, for fiber volume fraction versus permeability. Perpendicular permeability models predict results that are less than unidirectional fabric measurement. The results for the DNS and Kozeny-Carman [159] formulations are fairly good matches to each other. This is important because they may be useful inputs into meso-scale simulations that couple the micro- and meso-scale effects. The models by Bruschke *et al*. [86] and Gebart [76] look to be in good agreement each other for this case.

For the perpendicular measurement results the coefficients of variation (COV) are 7.58 at 50% fiber volume fraction, 2.49 at 55% fiber volume fraction, 2.16 at 60% fiber volume fraction, and 6.43 at 65% fiber volume fraction. The coefficients of variation for the perpendicular permeabilities appear to show that the fabric measurements in this case are less variable than for the parallel case. This may be because there are less preferential flow channels that can form if the tows are nesting in the perpendicular direction. Again, it might be reasonable to say the measured permeabilities of the material are less variable as fiber volume fraction increases.

The analytical models are consistently under-predicting permeability in these cases because attempts are being made to model meso-scale features in a fabric with models that only account for micro-scale spacing effects. The micro-scale analytical models do not account for the physics of geometry features that have such large differences between micro- and meso-scales. The physical geometrical features of the unidirectional fabric cause clear discrepancies in the analytical model predictions.

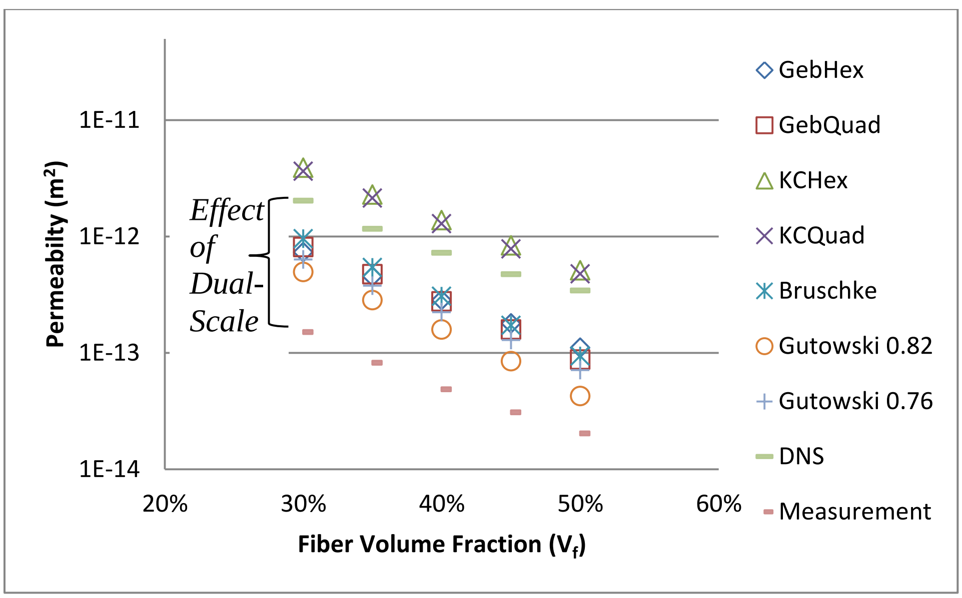

Figure 20: Transverse Permeability Models Plotting Fiber Volume Fraction vs. Permeability

Figure 20 shows the transverse, through thickness, analytical permeability models, DNS, and measurement, plotting fiber volume fraction against permeability. These results are done for a smaller fiber volume fraction range of 30-50%. Transverse permeability says that permeability is higher than measured but the models fit reasonably well with DNS results for, Kozeny-Carman [159] cases. The permeabilities of these models at 50% fiber volume fraction are particularly comparable. The models by Gutowski *et al*. [77] seem to fit the measurement data closer than the rest of the analytical models for this case. This is interesting because the transverse permeabilities are so much lower than the perpendicular permeabilities and this model has been less effective at predicting the parallel and perpendicular flow.

The measured results are significantly lower than the modeled results here. This is a reversal of the trend that was seen for parallel and perpendicular flows. The coefficients of variation (COV) are 7.56 at 30% fiber volume fraction, 3.30 at 35% fiber volume fraction, 4.40 at 40% fiber volume fraction, 3.66 at 45% fiber volume fraction, and 6.58 at 50% fiber volume fraction.

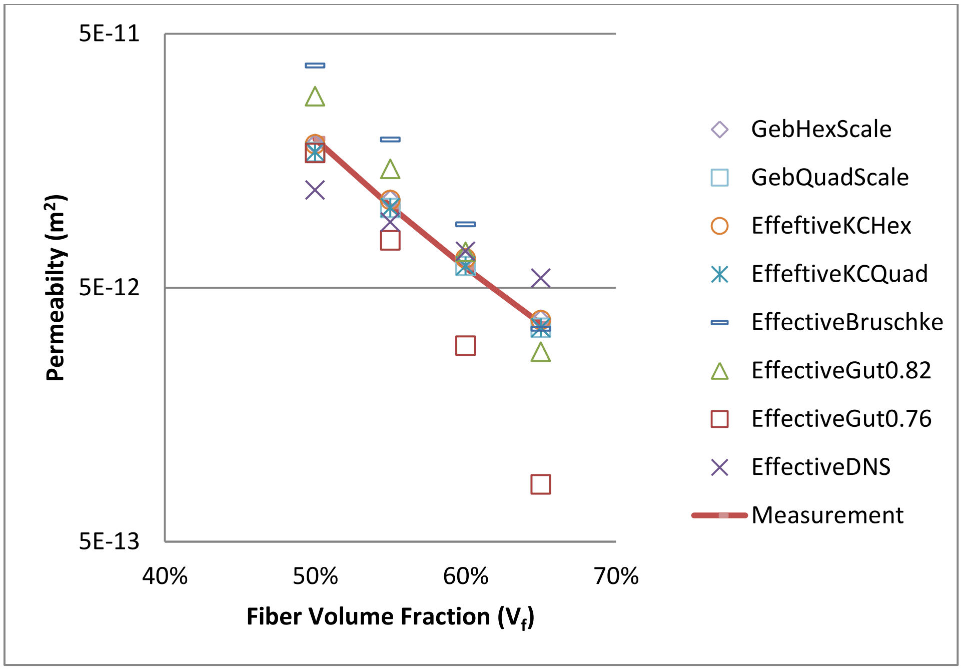

Figure 21: Parallel Permeability Results Modified by Effective Radius Multiplier

Figure 21 shows the parallel permeability results using an effective radius multiplier. The measured results have been shown in a solid red line to clarify them from the various scaled models. In the work by Gebart [76], an effective fiber radius was used in order to fit measured data. This was generated as approximately eight times larger for perpendicular flows. For the results in Figure 21-Figure 23, the actual fiber radius was modified by a multiplier for parallel, perpendicular, and transverse flows. In order to identify if this approach was repeatable it was implemented here for all of the models used in this work. The values for the parallel flow cases with an effective fiber radius multiplier were 6 for Kozeny-Carman [159], 4 for DNS, 20 for Gutowski *et al*. [77], 20 for Bruschke *et al*. [86], and 8 for Gebart [76]. The average effective radius here is 11.5 and 6.4 neglecting Bruschke *et al*. [86] and Gutowski *et al*. [77]. Gebart used and effective radius that was about 8 times and this appears to be somewhat repeatable since this value works here for the parallel flow case.

In Gebart's work, increasing the effective fiber radius was essentially shifting the analytical model from a micro-scale basis to a meso-scale basis. In this sense, the effects of inter-tow gaps on the macro-scale measured permeability could be captured. This makes the analytical model into a semi-analytical meso-scale model. This is what is happening here as the analytical models are modified to reduce the amount that permeability is under predicted by.

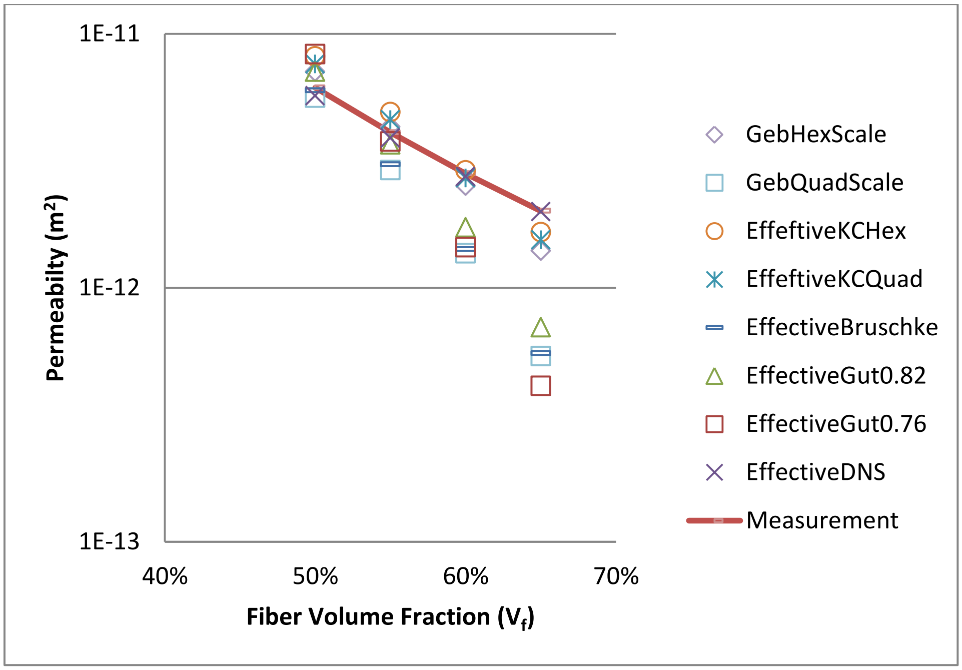

Figure 22: Perpendicular Permeability Results Modified by Effective Radius Multiplier

Figure 22 shows the perpendicular permeability results with an effective radius multiplier. The values for the perpendicular flow cases with an effective fiber radius multiplier were 4 for Kozeny-Carman [159], 4 for DNS, 10 for Gutowski *et al*. [77], 8 for Bruschke *et al*. [86], 8 for Gebart's hexagonal equations and 8 for Gebart's quadratic equations [76]. The average effective radius here is 7.5 and 6 neglecting Gutowski *et al.* [77]. Large scatter in the data is seen, while reasonable matches to measurement are possible.

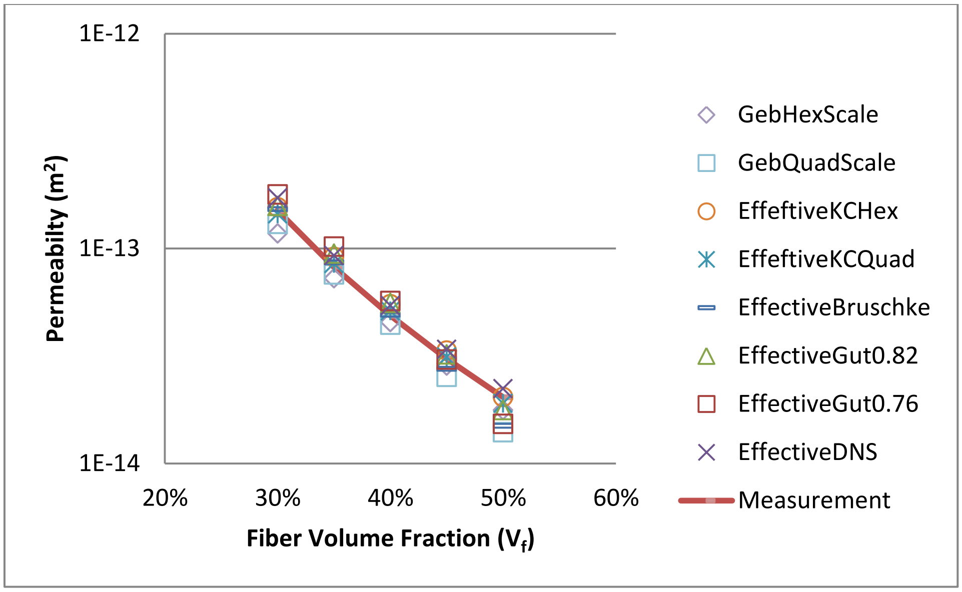

Figure 23: Transverse Permeability Results Modified by Effective Radius Multiplier

Figure 23 gives the results for the transverse permeability with an effective fiber radius multiplier. The ability to match this data set would be useful when translating this data into a processing simulation. The values for the transverse flow cases with an effective fiber radius multiplier were 1/5 for Kozeny-Carman [159], 1/4 for DNS, 1/2 and 3/5 for Gutowksi *et al*. [77], 2/5 for Bruschke *et al*.[86], and 2/5 and 2/5 for Gebart's hexagonal and quadratic respectively [76]. The average effective radius here is 0.37 and 0.31 neglecting Gutowski *et al.* The fits are relatively good and obtainable for the trend seen in the measurements. However, this is a semi-analytical approach and the repeatability is not known. This may be largely fabric dependent. The fabric measured here is similar to those measured by Gebart [76] and the effective radius is also similar, indicating that there may be a fabric or material specific multiplier to use. For reference, an image and scale bar of the fabric used in this study is shown in Figure 24. The scale bar is in millimeters.

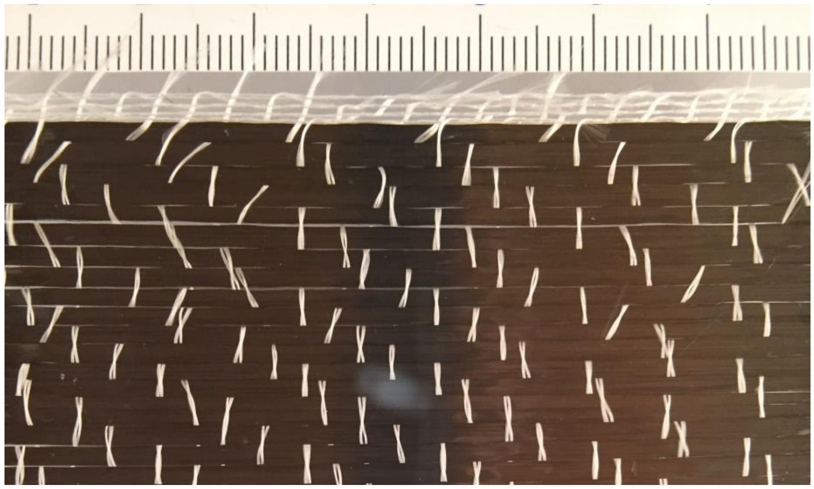

Figure 24: Unidirectional Carbon Fabric Measured in This Study

There have been a number of efforts to create analytical permeability models to simplify composite fiber reinforcement. Lundström *et al*. [25] commented that the theoretical expressions that have been derived for permeability are based on some specific and simplified fiber arrangement and do not apply to a general case. This comment helps show the need for continuing permeability work in both terms of measurement and modeling efforts. The identification of a general, robust, and adaptive permeability modeling tool has not been definitively described. Of the general models investigated here the empirical, analytical, and numerical nature of them does not completely satisfy the need for repeated and time consuming measurements.

4.7 Conclusions

The multi-scale nature of unidirectional fabrics is created by fibers and tows and is apparently important to consider, even on a unidirectional basis. The micro- and meso-scales are coupled and the effects of the micro-scale propagate to the meso-scale. These coupled scales combine with the millimeter flow channels that are present to locally increase the permeability and reduce resistance to flow. In fabrics, the transverse and perpendicular flows are significantly different because the materials are extremely thin and appear to effectively block flow channels in the transverse direction. DNS results are useful for making comparisons to analytical results and investigating their fit on the varying microstructure.

Ideally, there would be a simple analytical model that could be used to predict permeability of a fabric because analytical models are efficient. However, this study shows that there is continued justification for ongoing research in permeability as well for as continuing to use measurement as a fundamental basis for obtaining permeability for component level flow simulations. Here, an effect of dual-scale flow was quantified as the difference between a measured fabric and a simulated collection of fibers. The idealized analytical models may be useful for rapid calculations, but it is likely that a DNS result, accounting for randomness in the material, may be more realistic inside of the tow since in practice perfect hexagonal and quadratic packing arrangement are rarely seen. However, these models may be useful as a way to match experimental data without defaulting to a power law or Kozeny-Carman fit for measured results. By finding a reasonable fit for scaling the effective fiber radius, it could be concluded that a meso-scale model can be extrapolated from micro-scale effects.

4.8 Acknowledgements

This work is sponsored by General Electric Aviation, Cincinnati, OH.

Computational work in support of this research was performed at Michigan State University's High Performance Computing Center.

5. MODELING UP TO A BINARY MIXTURE OF FIBERS TO PREDICT MICRO-SCALE PERMEABLITY FOR FIBER REINFORCEMENT IN LIQUID COMPOSITE MOLDING

5.1 ABSTRACT

Permeability is the driving process parameter for mold fills in liquid composite manufacturing. It is critical for understanding the infusion flow and pressure distribution that results from closed mold infusions. A complex variable, permeability can vary significantly in magnitude for similar test cases and a number of reasons have been given for this variability. Permeability has also been isolated at different scales because of the multi-scale nature of composite fiber reinforcements. In the micro-scale, fibers are formed into randomly aligned tows composed of thousands of fibers. A second scale, the meso-scale, considers the tow dimensions and weave parameters, but often inputs a Darcy based permeability to make up for physical geometry variations. On the micro-scale, analytical models generally consider fibers as ordered in some kind of idealized packing arrangement, for example, hexagonal or square packing. This is not always realistic and defining permeability as a function of porosity alone may not be enough to achieve an accurate permeability prediction on the micro-scale. The overarching goal of this research is to use numerical tools to create a better understanding of composite manufacturing processes, developing a numerical modeling approach for the permeability of fiber reinforcement. Representative volume elements are utilized to recreate the fiber and matrix interactions during a liquid infusion. Here, we isolate the micro-scale structures of unidirectional fiber reinforcements and investigate flows across aligned fiber geometries and infusion

characteristics with applied periodic boundary conditions. A novel numerical approach is utilized to model three-dimensional randomly aligned fiber placements of up to 1000 fibers. This includes numerical modelling to predict unidirectional permeability on the micro-scale up to a binary mixture of fibers. The full Navier-Stokes equations are solved for the pressure drop and volumetric flow rate. Simulations are run for parallel and transverse cases. Material packing changes on the fluid flow regime during composite manufacturing are investigated. The results set up a baseline that compares well with analytical models as a function of fiber diameter and volume fraction. The ability of this numerical procedure goes above current analytical models because it can predict permeability variation based on the level of randomness in the domain. It can also handle various fiber diameters, fiber count, random packing arrangements, and flow rates. Specific areas that analytical models lack, like the effects of a fabric that incorporates a binary mixture of both carbon fiber and polymer or glass elements, is investigated. Results show that variations due to fiber packing can be identified independently of fiber volume fraction. Furthermore, the results show that permeability is higher as a function of volume fraction for an identical packing case with 9µm fibers as compared with 5.2µm fibers.

5.2 Introduction

The manufacturing of composite materials with liquid composite molding (LCM) methods is a popular approach for creating high fiber volume fraction and high performance composites. Specific LCM processes that are commonly used include resin transfer molding (RTM) and vacuum assisted resin transfer molding (VARTM). These manufacturing techniques are able to produce high performance composite parts with complex net shape geometries and attractive mechanical properties [4]. The advantage of part consolidation over metal assembly is that multiple components can be consolidated into one composite part. LCM composite manufacturing processes have a long history in the aerospace field and are often used in nautical and marine applications. Furthermore, LCM processes that were once used to produce low volume or high cost parts are growing in importance for the automotive industry to meet new fuel economy standards [141]. LCM processes are extremely important for creating complex, lightweight, and high fiber volume fraction parts.

The general LCM process injects a thermosetting resin into a fiber preform. The thermosetting resin is often treated as a Newtonian fluid because it is relatively insensitive to shear rates and has a viscosity of 50 to 500 times that of water [63]. Fiber preforms are composed of individual fibers that can be woven, braided, knitted, stitched, or randomly placed in mats to create the fibrous reinforcement. When a composite component is designed to be manufactured by LCM processes, modeling techniques are often used to understand resin infiltration and cure. Because of all of these conditions, models for the injection processing rely heavily on the properties of reinforcement, which are often simplified and treated as porous media. Without accurate properties for the simplified porous region, the design and optimization of injection ports, flow rates, resin runners, and resin outlets cannot be confidently conducted on the component scale. Detailed design simulations can help avoid the formation of voids or dry spotting in the finished part. Understanding the flow phenomena taking place in the fiber reinforcement is important on all scales of this multi-scale problem. The design of the fiber bundles on the micro-length scale is important and coupled to the design of the tow, weave, and macro-scale properties.

In order to approximate the resistance of the porous media to resin infusion, permeability and Darcy's law can be used. Permeability acts as proportionality constant in Darcy's Law to relate flow rate to pressure drop as shown in Equation 30. Darcy's Law relates the flow rate through a volume *(Q)* in units of volume per time, the characteristic length (L), the pressure drop over that length $(P_{IN} - P_{OUT})$, the fluid viscosity μ, and the permeability of the medium ($\bar{\bar{S}}$) [68]. Dividing the volumetric flow rate (Q) by the cross sectional area (A) gives ($\bar{q}$) and a replacement of the pressure drop over length can be made by the negative pressure gradient.

$$\bar{q} = \frac{-\bar{\bar{S}}}{\mu} \nabla P \tag{28}$$

Furthermore, $\bar{q}$ is called the Darcy Flux, known as the discharge per unit area and is related to the interstitial velocity times porosity. Also, the pressure gradients are generally linear across length.

When measuring permeability it is common to measure the in-plane directions of the fabric, often denoted as S_{xx} or S_{yy} in the x- and y-directions and S_{zz} in the transverse z-direction [98].

These directions are arbitrary but are often selected with the warp and weft directions of the reinforcement. Permeability can then be measured based on the flow rate and pressure drop in a fixture and a tensor of permeability values can be found. The most common way to obtain these values is experimentally through tests that prescribe the boundary conditions of Darcy's Law to calculate permeability. The tensor of permeability values is symmetric and diagonalizable where the eigenvectors denote the principle directions of flow and the eigenvalues are the principal permeabilities. These tests require permeability of the preform to be measured in each direction as well as at all fiber volume fractions of interest. Furthermore, the accuracy of permeability values is critical to infusion process simulations, but the measurement techniques result in large variations in permeability that may be due to structural variations, non-uniformity, and deformation of the preform during measurement [76], [80], [82], [86], [142].

Permeability measurements are standard for macro-scale flows but can be prohibitively difficult on the micro-scale. For example, unidirectional fibers and unidirectional fabrics differ because fabrics are composed of dual-scale porous zones. The composite continuous fiber reinforcements are aligned into tows with both micro- and macro- flow channels. A number of permeability measurement approaches have been developed for fibrous media and composites research [68], [69], [164]. The permeability of unidirectional fibers has been shown in the past to agree well with Darcy's Law for porous media but it is important to note that this permeability value is heavily dependent on the total fiber volume fraction of the part and stochastic packing. As fiber volume fraction increases, permeability rapidly drops.

A number of analytical models have been posed for calculating permeability in an effort to reduce the measurements needed. For example, the Kozeny-Carman equations were originally developed for calculating the permeabilities of granular beds and have been adapted for permeability of fibrous reinforcement. The equation was proposed as an option for predicting permeability in terms of geometrical properties in fiber beds for flows transverse and parallel to the fiber axis [77]. The equation is

$$S = \frac{(1 - V_f)^3}{4kV_f^{\,2}} r^2 \tag{29}$$

where, V_f is the fiber volume fraction, r is the fiber radius, and k is the empirically derived Kozeny-Carman constant, typically in the 0.35-1.78 range. Unfortunately, in the original equations the permeability is larger than zero at volume fractions that are above the theoretical maximum packing arrangement. This means that at the theoretical maximum packing permeability is higher than zero. In this case, transverse flow should be completely restricted because the fibers are blocking all possible flow channels and the porosity is no longer interconnected. Furthermore, discrepancies can arise in the Kozeny-Carman constants when moving from idealized and ordered fiber arrays to the much more random and less structured arrangements seen in composite cross sections [82], [86], [143], [144]. The quality of prediction from this equation is material dependent and heavily relies on the value of the Kozeny-Carman constant.

Another attempt by Gebart [76], specific to unidirectional composite preforms, set up analytical models for the flow parallel to and transverse to the fiber orientations. Gebart's equations for unidirectional fibers are derived analytically and can used to predict permeability based on the parallel or perpendicular fiber direction in reference to the flow direction. Tow permeabilities are computed using assumptions about the hexagonal and quadratic fiber packing arrangement. The theoretical maximum volume fraction for a hexagonal packing assumption is $\pi/(2\sqrt{3})$ or 90.69% and is used in the analytical equations. Equation 30 describes Gebart's hexagonal packing analytical permeability in flow perpendicular to the fibers. The term $16/(9\pi\sqrt{6})$ comes from the fiber arrangement and is distinct for hexagonal and square packing.

$$S_{perpendicular} = \frac{16}{9\pi\sqrt{2}}\left(\sqrt{\frac{V_{fmax}}{V_f}} - 1\right)^{5/2} R^2 \tag{30}$$

Equation 31 describes Gebart's analytical permeability in flow along the hexagonally packed fibers. The relationship between this equation and the Kozeny-Carman equation can be clearly seen and *c* in Equation 31 is equal to the Kozeny constant of 53 for a hexagonal packing case.

$$S_{parallel} = \frac{8R^2}{c}\frac{\left(1 - V_f\right)^3}{{V_f}^2} \tag{31}$$

Good results were shown for fitting these equations to experimental results for a medium range of volume fractions, and parameterized equations were created based on the fiber radius and fiber volume fraction. An effective fiber radius was used to fit experimental data for a dual-scale unidirectional fabric. Additionally, the equations were developed for ideal hexagonal and quadratic packing arrangements that are much more organized than what is traditionally seen in micrographs of composite samples. The Gebart analytical models for permeability of unidirectional reinforcements do not account for outside effects such as stochastic fiber packing, fiber diameter variation, and particulate effects. Also, studies on unidirectional fibers and unidirectional fabrics denote that dual-scale flows can become important [95], [145], [146]. Unidirectional fabrics are composed of tows often bound together with another material and still have a dual-scale nature with larger, meso-scale tow spacing combined with micrometer spacing on the fiber or intra-tow level. This is important to note if the Gebart's formulas are going to be extended to fluids simulations of woven structures [147]. Most researchers simply apply an analytical model for the yarns or tows of woven structure without worrying about the stochastic packing of fibers which may influence the results. There may be a more robust method of accomplishing this goal.

Happel [87] predicted the longitudinal permeability of aligned fibers using the unit cell approach. The unit cell was reduced to a circle and the Stokes equation was used to find an approximate solution for the pressure gradient and interstitial velocity. A zero shear stress boundary condition was applied on the surface of the circle. Other researchers have made various models where the boundary conditions at the unit cell were varied [148]–[151]. It is clear from the numerical approached implemented that increasingly complex flow simulations can be considered based on the unit cell approach. This is partially because of increasing computational power. In many of these simulations, Darcy's Law can be used to calculate a numerically calculated permeability from the unit cell or representative volume element used in the simulation.

Past investigations have shown that uniform fiber arrangements yield lower permeability than non-uniform arrays of fibers at the same fiber volume fraction [148]–[151]. However, the opposite result has also been reported. Bechtold and Ye [152] numerically predicted the transverse permeability of various fiber arrangements and applied the Morishita number to quantify the distribution. The Morishita number measured the variation of fiber spatial distribution. With a larger Morishita number, the regularity of the fiber arrangement decreases and so did the permeability.

Chen and Papathanasiou [43], [44], [153] produced a set of papers looking at the transverse and parallel permeability of aligned fiber beds. They adopted a Monte Carlo procedure to generate fiber arrays up to 571 fibers. They noted that a variation in permeability could be detected at the same fiber volume fraction. They also noted that 571 fibers were enough to minimize the effect of fiber count variations on the flow field. The range of fiber volume fractions investigated in [44] was from 10-55%. They concluded that the inter-fiber spacing can have a large effect on the permeability at the same porosity.

Multiple fiber diameters in a domain with large variations in diameter have not been investigated for fully three-dimensional domains and could directly affect permeability. A binary mixture of fibers could be composed of different materials with different nominal fiber diameters. For example, in some cases a carbon fiber has been commingled with polymer fibers occupying space between reinforcing fibers [63], [165]. In another case, a carbon could be comingled with glass fibers because carbon is light but still relatively expensive. Glass is inexpensive and has properties that could be advantageous in certain applications. Additionally, glass is often used as stitching in carbon fabrics.

The review of literature shows that the permeabilities of unidirectional fibers are an important parameter for an accurate description of resin flow in composite manufacturing. Fiber volume fraction and fiber randomness have both been shown to affect permeability but how remains unclear. Further, how the statistical variation in fiber diameters around the average value changes permeability is unknown. In this study, a numerical method of permeability prediction is developed that allows for the effects of various fiber diameters, volume fractions, and realistic random fiber placement to be accounted for in parallel and transverse flow scenarios. The unidirectional fibers are generated based on an algorithm described by Desmond and Weeks [154] and then input into a code that reads the file and extrudes a set of fibers. Then, permeability is calculated for this set of fibers using computational fluid dynamics and the direct application of the Navier-Stokes equations. Simulations are run with 5 cases of random packing at each fiber volume fraction for parallel flows and 10 cases are investigated for transverse flows. Fiber volume fractions are varied from 0.20 to 0.80 in increments of 0.10. A binary mixture of fibers is also investigated with a fiber diameter ratio of 1.73 and it is found that as the fraction of small fibers increases the corresponding permeability drops on a corresponding volume fraction. The mean nearest inter-fiber spacing is utilized to help quantify the heterogeneity of the fiber distribution. Results are compared with literature for a number of analytical equations for unidirectional permeability. Furthermore, these computed permeabilities could be used for the meso-scale simulations of a woven fabric and its repeating unit cell as yarn or town inputs. The ability to quantify microstructure variations and investigate it in a controlled model is useful. This study is a step in meeting that quantification.

5.3 Fiber Modeling

For geometry generation, fiber arrays are treated as cylinders with their axes aligned transverse or parallel to flow. The permeability can be directly solved for with the Navier-Stokes equations as discussed in the introduction. An algorithm by Desmond and Weeks [154] was adapted for this numerical study. The original algorithm was used to study random close packing of three-dimensional spheres and two-dimensional disks in confined geometries to advance the understanding of how packing properties can change with random packing orientations in realistic scenarios that deviate from perfect packing. Here, this algorithm is adapted to create three-dimensional random cylindrical geometries for numerical permeability predictions.

In two dimensions, a mixture of fiber ends is inserted into a 1x1 square dimensionless domain. Each configuration is implemented by building on the method by Xu *et al*. [155], Clarke and Wiley [156], and Desmond and Weeks [154]. At time zero, infinitesimal points are randomly dispersed in the system and are gradually expanded and moved at each step. The infinitesimal points are initialized in the system using the Mersenne Twister Algorithm to randomize the starting points. These points are gradually given area and position by being expanded and moved. They are translated in two dimensions to prevent the overlapping of fiber ends. When a final state is found where the fiber ends can no longer be expanded without overlapping, this step of the packing process ends.

The algorithm alternates between treating the fiber ends as hard surfaces, where overlapping is not allowed, and as soft surfaces where overlapping is allowed. This is done by using a soft potential described by

$$V(r_{ij}) = \frac{\epsilon}{2}\left(1 - \frac{r_{ij}}{d_{ij}}\right)^2 \Theta\left(1 - \frac{r_{ij}}{d_{ij}}\right) \tag{32}$$

where r_{ij} is the center to center distance between two fibers *i* and *j*. Further, ϵ is a characteristic energy scale, d_{ij} =(d_i+d_j)/2 and the Heaviside step function is used $\Theta\left(1 - \frac{r_{ij}}{d_{ij}}\right)$ making *V* nonzero for r_{ij}<d_{ij}. Fiber ends are prevented from overlapping based on a user defined threshold. After each expansion step, the fiber ends are checked for any overlapping thorough the condition 1-r_{ij}/d_{ij}> ϵ =10^{-5} for every fiber end. This limit is set by choosing a point where overlap is negligible. If fiber ends are found to be overlapping, the nonlinear conjugate gradient method is used to move the centers in order to make them no longer overlap [157]. Physically, the average force per fiber end is minimized in order to ensure fibers are not overlapping.

The algorithm handles up to a binary mixture of fibers of a desired ratio. For each configuration, fiber ends are packed into a box of prescribed unitless dimension. The boundaries of the box are prescribed as fixed and a final configuration is generated from the algorithm [155], [156]. A 1x1 unit square is generated where the number of fibers desired is input. A starting volume fraction is selected and a starting volume fraction step size is prescribed. The algorithm packs the maximum volume fraction of fiber ends into the square. The wall boundaries are treated as mirrors where, as a fiber moves closer to a boundary, it is reflected back by its own projection. Up to this point, all calculations are dimensionless.

Dimensions are added by selecting a fiber radius and goal fiber volume fraction. The dimensions of all other parameters are driven by the dimensions of the nominal fiber radius. This fiber radius defines the fiber end area, which can be used to calculate the total area of fibers within a square. The total area of fibers is divided by the target area fraction and this gives a new area of the square unit cell. The square root of this area is the length of the square which is used to control the dimensions and make up the fluid region that is solved for permeability. This square fluid length is also used to create the cubic volume in three dimensions. Before this step, the previous x-,y-, and z-coordinates were values from 0 to 1. After this step, the new x-, y-, and z-coordinates are generated by taking the square length in any dimension and multiplying the dimensionless coordinates by that length. The new coordinates are saved as a text file and read automatically to generate an international standard STEP geometry file. This section of the code creates an outer cube, the fluid volume, with a set of fibers approximated as randomly placed, aligned, perfect cylinders. Fiber size ratios of 1 and 1.73 were investigated in this paper. The model adopted also limited the maximum achievable packing arrangement because of wall induced structure and the maximum theoretical packing is not possible here. In each parallel case, 5 random geometries were created for each investigated fiber volume fraction. The random geometry was held constant when changing fiber volume fractions through scaling to see the effects of volume fraction with a consistent random packing. In the transverse cases, 10 random geometries were created in the same way. The ensemble average permeability for the entire 1000 fiber domain was calculated but an average for a smaller intra-tow region could also be sampled and computed for sub-regions consisting of smaller amounts of fibers. For example 20 fibers could be computed for permeability instead of 1000.

Chen et al [44] chose the minimum inter-fiber spacing to be one tenth of a fiber radius. This has been chosen by other authors as well, due to numerical meshing considerations, but was not selected as a consideration here. The required discretization time does dramatically increase however when the distance between two fiber boundaries diminishes.

5.4 Flow Modeling

Here, models are created for the longitudinal and transverse saturated flow through fiber beds. Flow is driven by a flow rate in a three-dimensional representative volume element. The fibers are treated as impermeable solids possessing no slip boundaries. The size of the representative volume element was selected in order to reduce the fiber count effects. In other words, to get a sufficiently random domain, a certain threshold of fibers is needed. This threshold is discussed by Chen *et al*. [43]. The solution for the permeability of flow perpendicular and parallel to the fibers has been conducted in three dimensions for the complete Navier-Stokes equations with the finite volume code Fluent. The computations are done at low flow rates so that the single phase creeping flow assumption is valid. This implies that inertial forces are neglected and the results for permeability should result in linear pressure gradients. The permeability results from Fluent simulations were validated by comparing with previous published analytical and numerical models.

The simulations were performed for fiber volume fractions of 20-80% in increments of 10%. The simulations have been run at fiber counts of 1000 as well as five random packing arrangements at volume fraction. A characteristic geometry for 1000 fibers can be seen in Figure 25. The boundaries of the volume are assumed to be translationally periodic and are matched to opposing faces. A specified velocity inlet condition is applied and an atmospheric pressure outlet is assumed. The results output the area weighted average inlet and outlet pressures, as well as, the interstitial in plane average velocity. The stead- state laminar flow conditions are assumed to accurately represent the flow that takes place under experimental saturated permeability measurements. A tetrahedral mesh is generated for the unit cell. Currently, a new and unique mesh is required for each fiber volume fraction and is a limiting factor in the number of random packing arrangements that can be realistically investigated.

The viscosity of the fluid used in the numerical simulations was the same as the viscosity of the fluid used in experimental investigations of permeability measurements (Oil, Viscosity 0.24Pa*s, Density 709 kg/m^3). The local fiber reinforcement permeability is of manufacturing interest because the impregnating resin can be modeled without accounting for all of the fibers in a mold individually. This is useful for simulating the LCM infusion in the most computationally efficient manner.

5.5 Results

To obtain the results in this section, the velocity inlet and pressure outlet are prescribed along with the periodic boundary conditions. For parallel cases, the velocity is applied along the fiber direction. For transverse or perpendicular cases, the velocity is applied across the fiber surfaces. The fibers are treated as walls with no slip boundary conditions along their surfaces and compaction due to the force of the fluid is assumed to be negligible. The fluid region is the area not made up of fibers and is solved for the interstitial in plane velocity.

A representative volume element generated with the process described in the modeling section is shown in Figure 25 with 1000 fibers at a high fiber volume fraction of 70%. Within this region, the geometry shows selected sub-areas of high and low local fiber volume fraction in a) and b). It is interesting to note that the areas of high and low volume fraction will affect the permeability locally. It is also worth noting that as the fiber volume fraction increases there is less space for the random fiber packing to occupy and the reinforcing fibers will trend towards an idealized fiber packing arrangement.

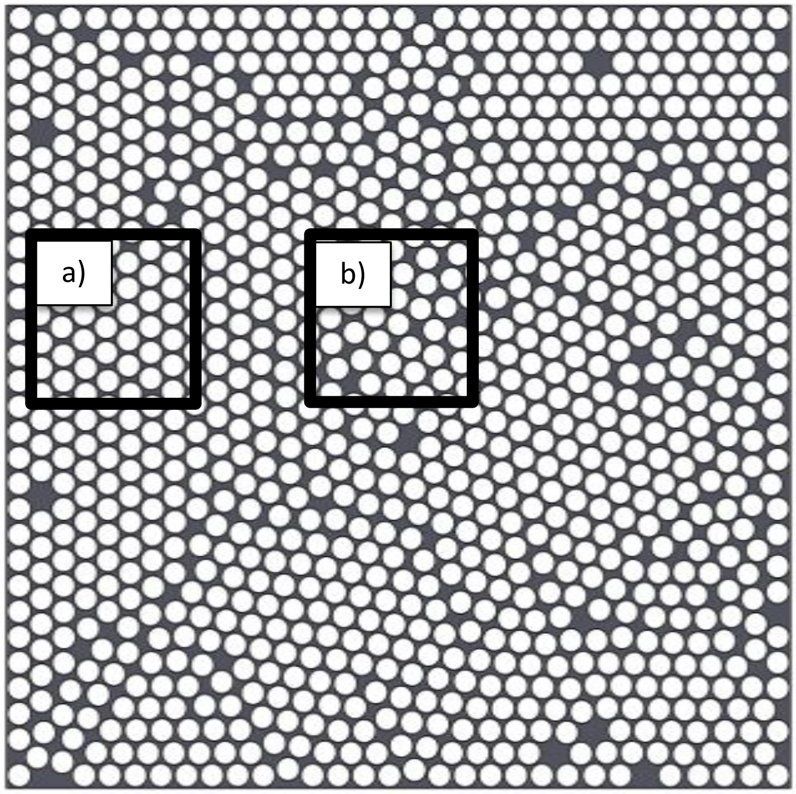

Figure 25: Unit cell and corresponding volume fraction, global volume fraction is 70%, a) sub region with high local V_f, b) sub region with lower local V_f

Figure 26 gives two characteristic geometries generated using the adapted algorithm for 100 fibers emphasizing fiber packing variability. All the simulations in the presented results were run with 1000 fibers but these geometries were selected because they clearly emphasize the differences in the random packing possible. The transverse permeability varies by 11% for the two cases shown at 20% fiber volume fraction and the permeability is higher in a) than in b) due to uninterrupted flow channels.

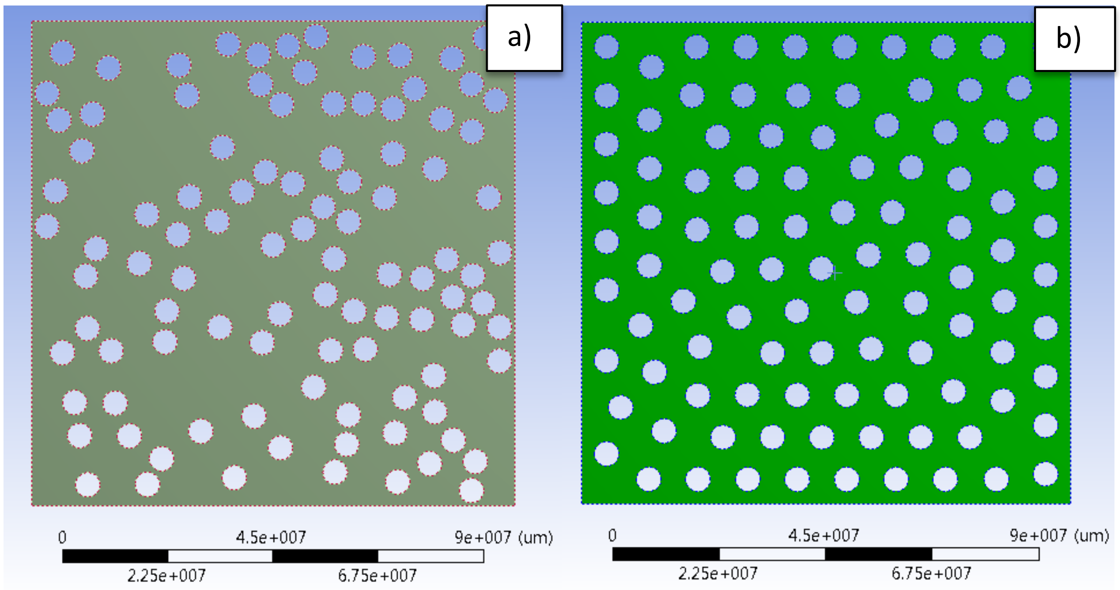

Figure 26: Two geometries generated at 0.20 fiber volume fraction and investigated for the effects of interstitial fiber spacing on composite fiber reinforcement permeability a) less uniform geometry generation with increasing randomness, and b) more uniform geometry generation with decreasing randomness. The permeability result for these two packing arrangements varies by 11%.

Figure 27 shows a geometrical representation of a binary mixture of fibers at 60% fiber volume fraction. In each simulation, the fiber count was held fixed at 1000. The total volume of each representative volume element varies. Figure 27 a) 70% 9µm fibers with 30% 5.2µm, b) 50% 9µm fibers with 50% 5.2µm, and c) 30% 9µm fibers with 70% 5.2µm. Inside these regions, locally high and low fiber volume fractions can be seen differing from the global average. Additionally, the smaller fibers can be seen nesing between the larger fibers which allows for small fibers to fill gaps between large fibers.

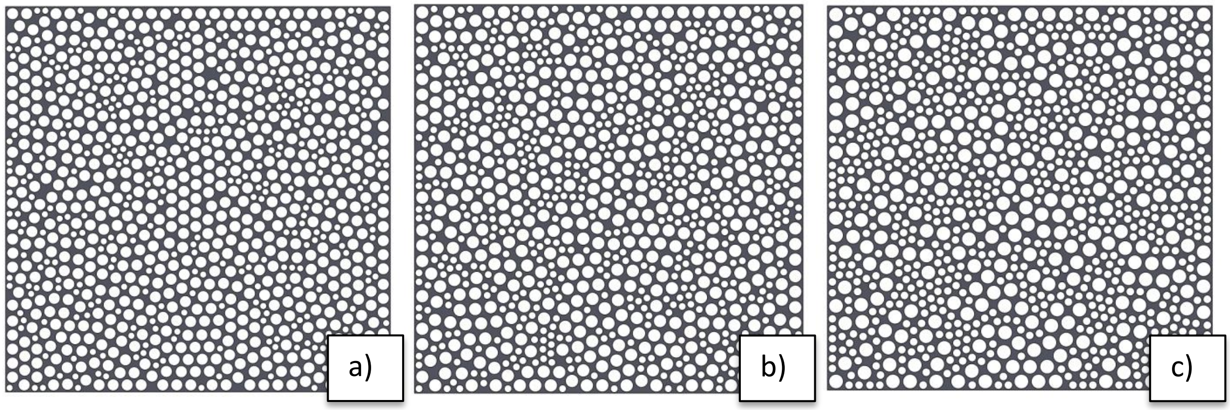

Figure 27: Three representative binary mixtures at 60% fiber volume fraction. Fiber count it 1000 in each case so the total volume of each representative volume element varies. a) 70% 9µm fibers with 30% 5.2µm b) 50% 9µm fibers with 50% 5.2µm c) 30% 9µm fibers with 70% 5.2µm

Figure 28 and Figure 29 show the numerical results for the average inter-fiber parallel and perpendicular permeabilities versus fiber volume fraction computed with 1000 fibers. Simulations were run with two different fiber diameters set at 5.2µm and 9µm. These fiber diameters would closely represent a carbon fiber material and a glass fiber material, respectively. The simulations shown here were an average of 5 simulations in the parallel direction and 10 simulations in the perpendicular direction for each fiber volume fraction. Twice as many transverse simulations can be run without requiring twice as many meshes because there are two transverse directions for each meshed representative volume element. The computed permeabilities are not necessarily the same in each transverse direction for the same representative volume element. The trend shows a rapid drop in permeability as fiber volume fraction increases. Also, the smaller fiber diameter has an apparent effect on the computed permeability because it is effectively creating a finer filter in the volume element.

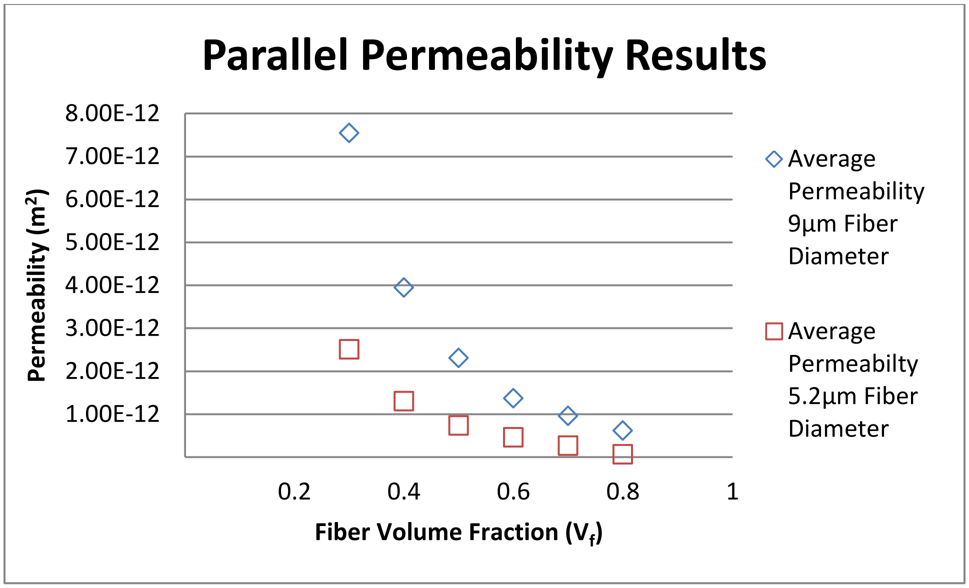

Figure 28: Average parallel numerical permeability results vs. fiber volume fraction for 1000 fiber count simulations

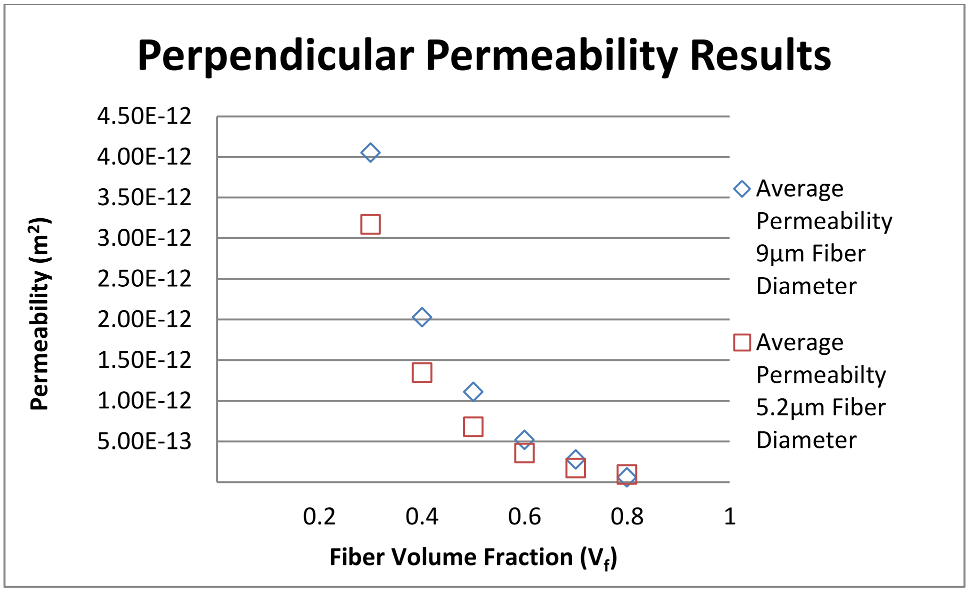

Figure 29: Average perpendicular numerical permeability results vs. fiber volume fraction for 1000 fiber count simulations

Figure 30 and Figure 31 show the numerical results of parallel and perpendicular permeability plotted against the fiber volume fraction and mean nearest inter-fiber spacing, respectively. In order to quantify the microstructure with a parameter of the microstructure other than the fiber volume fraction, the mean inter-fiber spacing was adopted. The mean nearest neighbor is a common metric used to determine the degree of local heterogeneity [166]. A search algorithm was written to calculate the center to center distances of all fibers from one another. This gave an array of values with zero along the axis where the search algorithm calculated the distance of the search fiber from itself. Infinity was then added along the axis of the matrix and the minimum distance of each fiber to its neighbor was then found. This nearest neighbor was then averaged to find the mean nearest neighbor in the generated volume. From this, the fiber diameter (or mean fiber diameter for binary mixtures) was subtracted in order to calculate the mean inter-fiber distance. Furthermore, the permeability results have been non-dimensionalized with the square of the fiber radius. The results show that as the mean spacing between fibers increases the permeability also rapidly increases. This corresponds with an increase in fiber volume fraction.

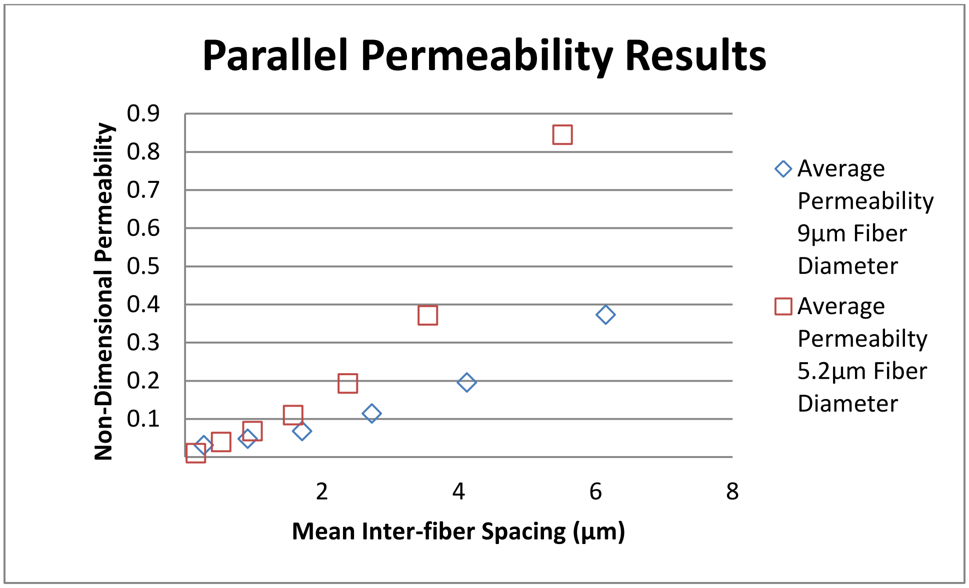

Figure 30: Average parallel numerical permeability results vs. mean inter-fiber spacing for 1000 fiber count simulations

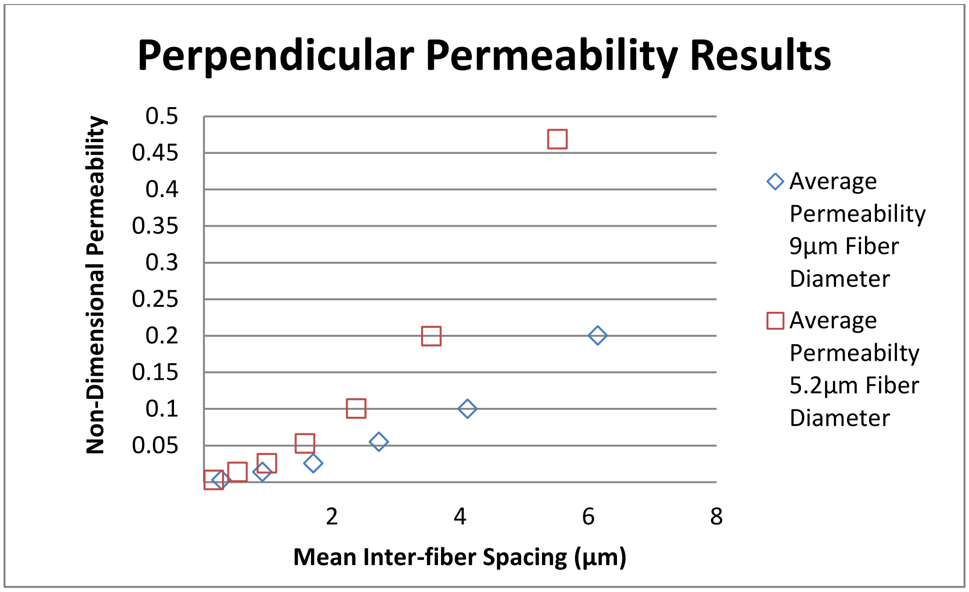

Figure 31: Average perpendicular numerical permeability results vs. mean inter-fiber spacing for 1000 fiber count simulations

Figure 32 shows a sample of the variation seen for 1000 fibers, 9um in diameter, at 60% fiber volume fraction in a transverse flow scenario. Figure 33 shows a sample of the variation seen at 50% fiber volume fraction for the same set of cases. These figures are plotted against the mean inter-fiber spacing to show the variability more clearly than plotting it across a range of volume fractions. Generally, as the mean inter-fiber spacing grows, the permeability increases. However, this is not always the case if the flow inlet has a large collection of conglomerated fibers, allowing the pressure at the inlet to rise and the computed permeability to drop. The results here show a 10-13% difference between values.

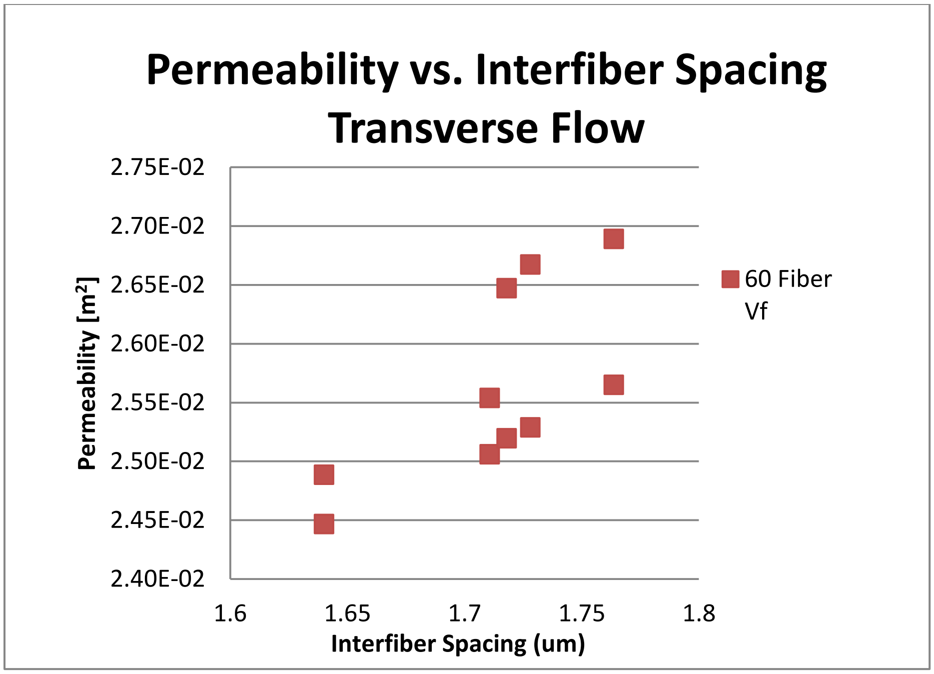

Figure 32: Transverse Flow Sample of Variation at 60% Fiber Volume Fraction, 9µm Fibers

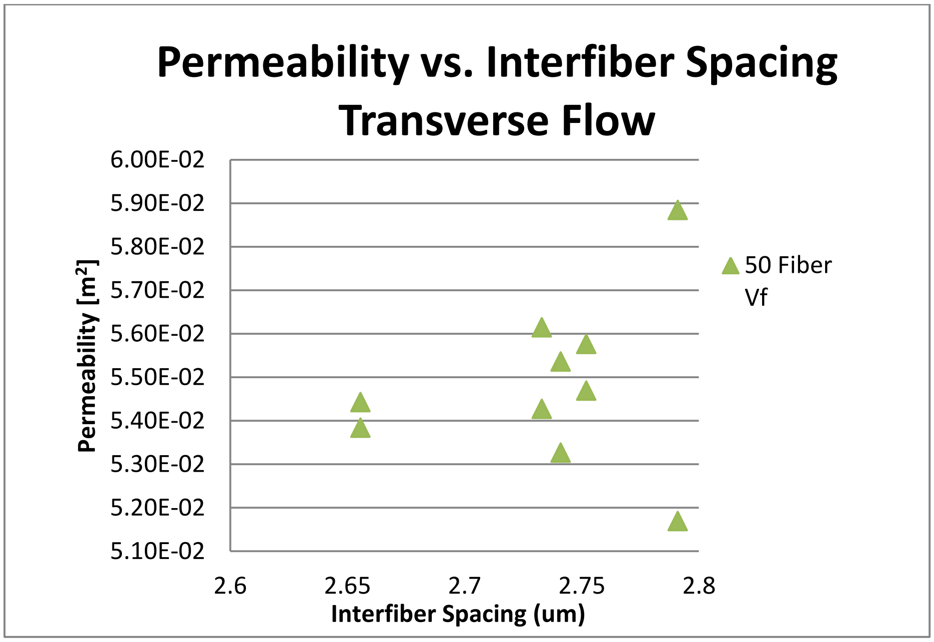

Figure 33: Transverse Flow Sample of Variation at 50% Fiber Volume Fraction, 9µm Fibers

Figure 34 shows a sample of the variation seen for 1000 fibers, 9um in diameter, at 60% fiber volume fraction in a parallel flow scenario. Figure 35 shows a sample of the variation seen at 50% fiber volume fraction for the same set of cases. These figures are plotted against the mean inter-fiber spacing to show the variability more clearly than plotting it across a range of volume fractions. In the parallel flow scenario there is less variation (4-9% difference) in permeability as the inter-fiber spacing changes. This appears to indicate that parallel flows are less susceptible to aligned fiber packing variation. However, this is not always the case there is a large collection of agglomerated fibers creating other areas of preferential flow.

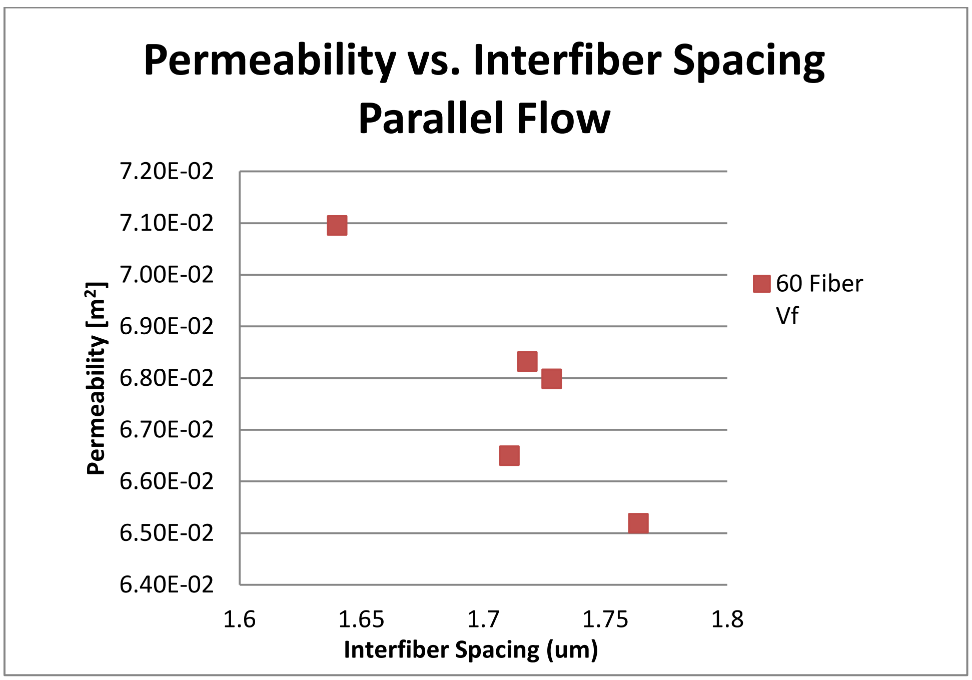

Figure 34: Parallel Flow Sample of Variation at 60% Fiber Volume Fraction, 9µm Fibers

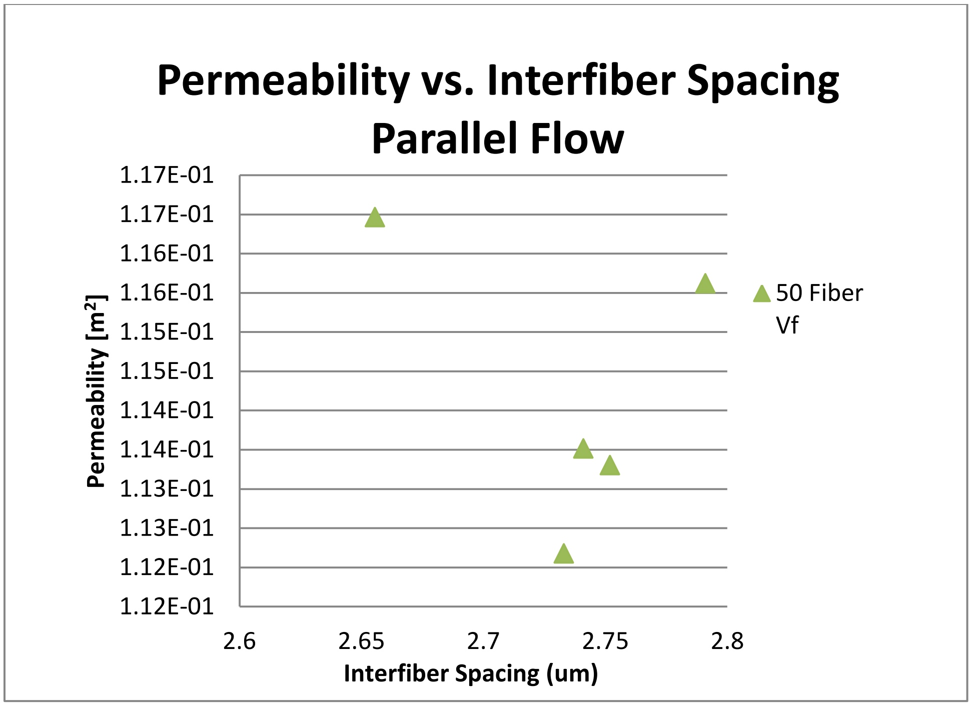

Figure 35: Parallel Flow Sample of Variation at 50% Fiber Volume Fraction, 9µm Fibers

Figure 36 and Figure 37 show all the simulated cases of permeability with 1000 fibers. Figure 36 shows the plots of parallel permeability for non-dimensionalized permeability and mean inter-fiber spacing. Figure 37 shows the plots of parallel permeability for non-dimensionalized permeability fiber volume fraction. Each point on the graph is a separate numerical simulation and the random data is colored by the same data point icon on the graph. The data tends to scatter more at low fiber volume fractions where there is more space between fibers. The variability is also not necessarily negligible as can be seen when investigating the plot of inter-fiber spacing.

Figure 38 and Figure 39 give the perpendicular simulations and again the variability is emphasized at lower volume fractions. Figure 38 is the perpendicular permeability cases with non-dimensionalized permeability and mean inter-fiber spacing simulated with 1000 fibers.

Figure 39 is the perpendicular permeability cases with non-dimensionalized permeability and fiber volume fraction simulated with 1000 fibers. Variation is seen in the plots of permeability with fiber volume fraction meaning that there are fiber packing dependences. This is where mean-inter-fiber spacing is applied in an attempt to rectify this. However, if permeability is plotted with the non-dimensionalized average permeability vs inter-fiber spacing the data is still scattered. It is also worth pointing out that a significant variation in permeability was not seen based on flow rate. This was investigated for validation of the Newtonian creeping flow assumptions and the neglecting of inertial effects as a significant source of pressure build up in the simulations.

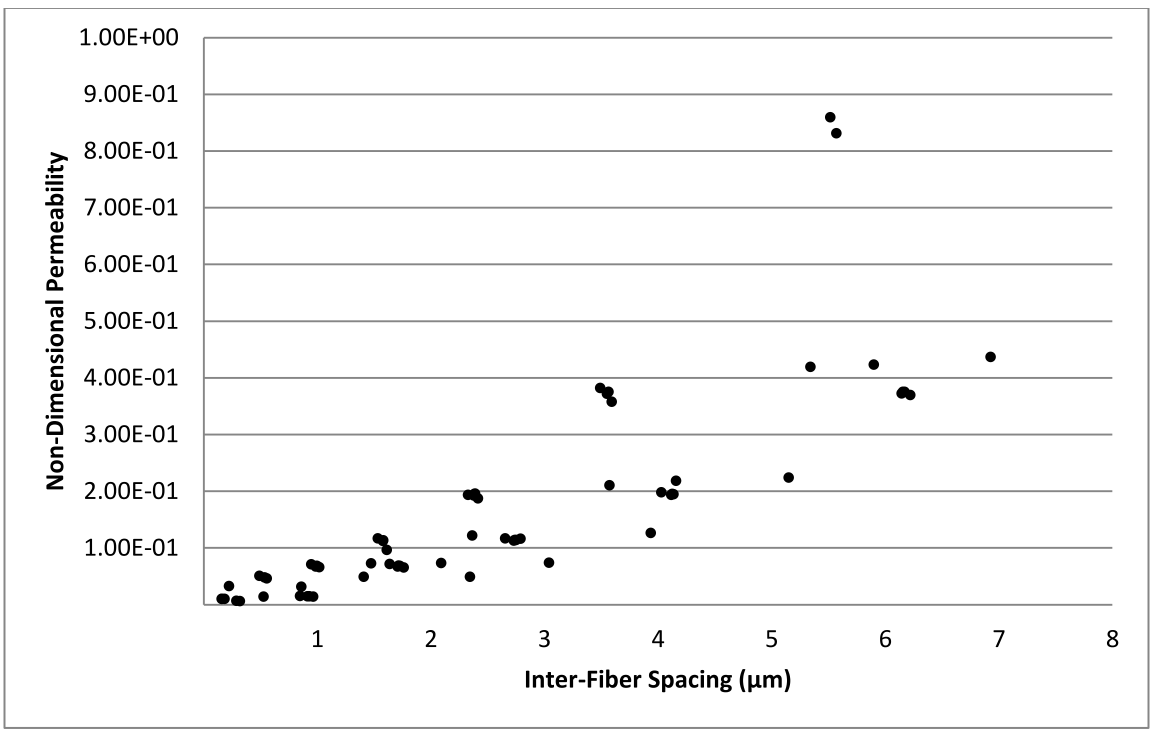

Figure 36: Parallel permeability cases with non-dimensionalized permeability and mean inter-fiber spacing simulated with 1000 fibers

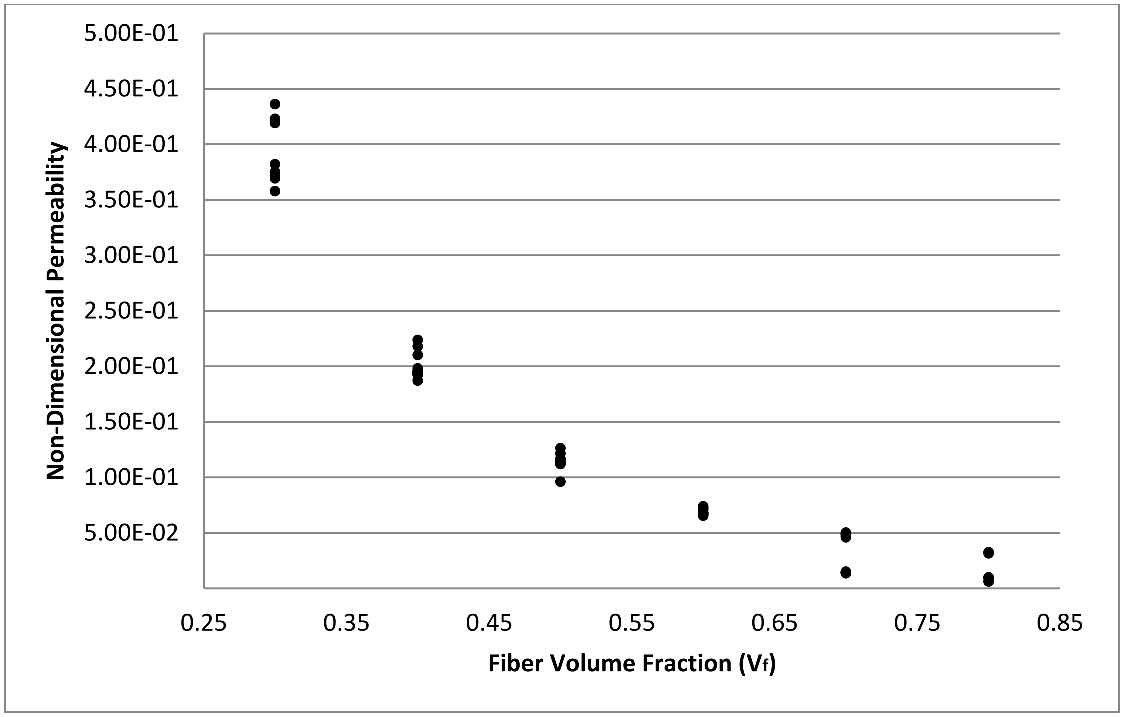

Figure 37: Parallel permeability cases with non-dimensionalized permeability and volume fraction simulated with 1000 fibers

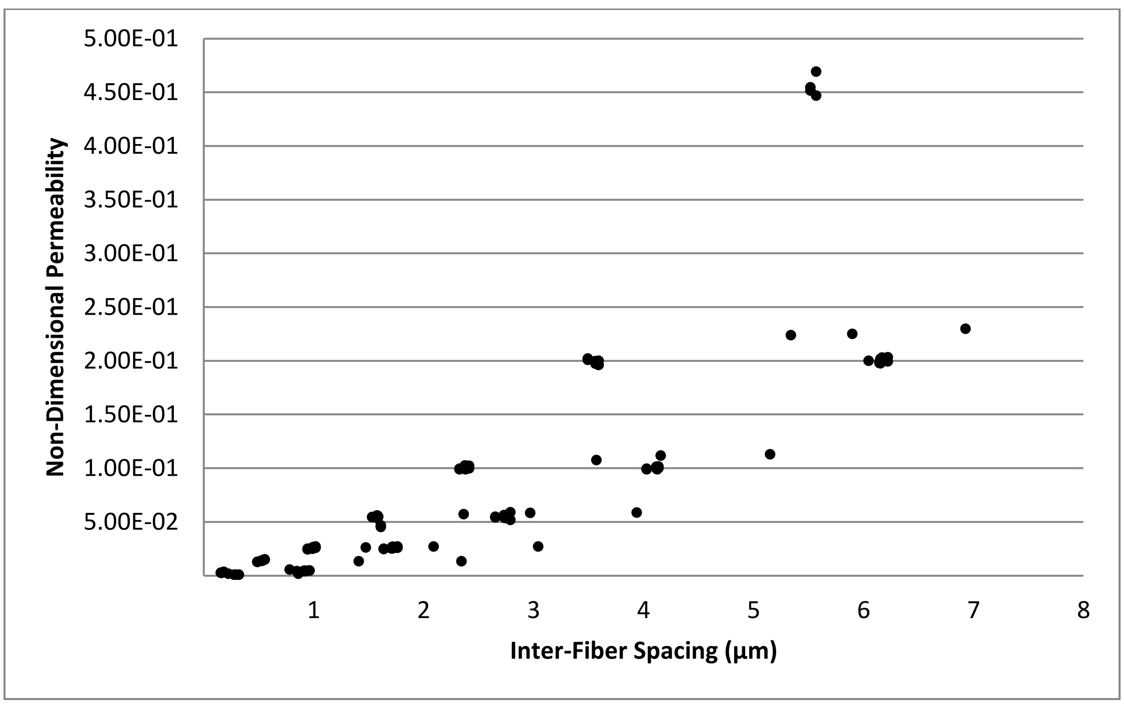

Figure 38: Perpendicular permeability cases with non-dimensionalized permeability and mean inter-fiber spacing simulated with 1000 fibers

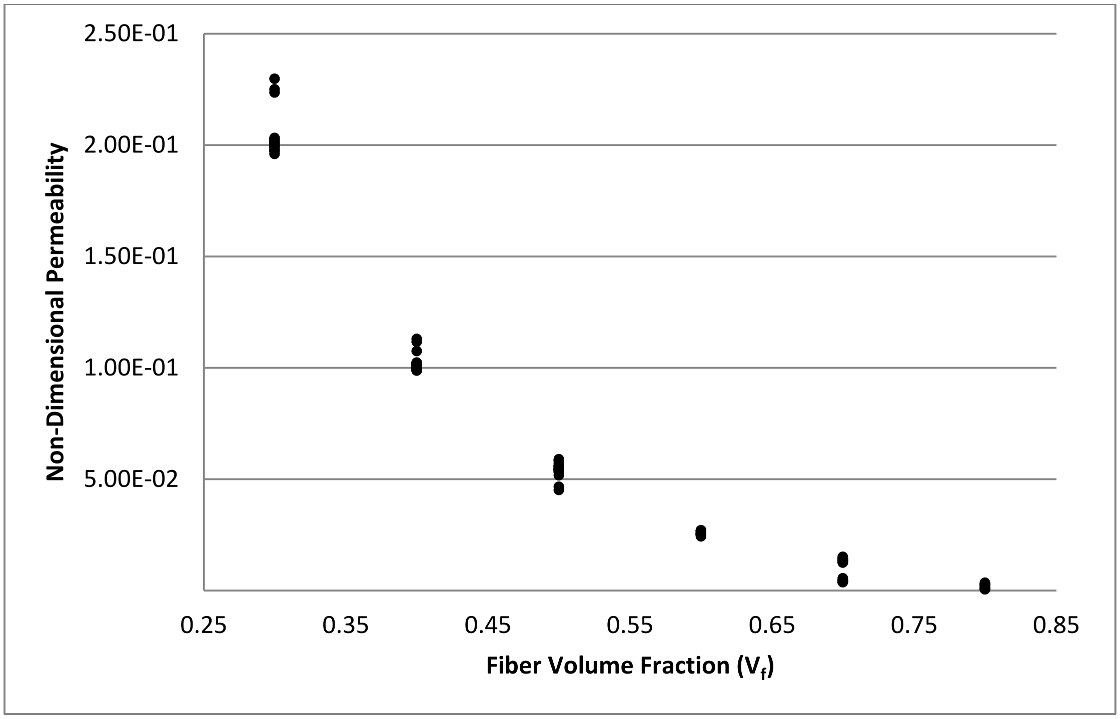

Figure 39: Perpendicular Permeability cases with non-dimensionalized permeability and fiber volume fraction simulated with 1000 fibers

Figure 40 shows a characteristic pressure contour plot of a transverse flow case with a relatively uniformly packed case. This case is a 0.60 fiber volume fraction and has a fairly smooth pressure gradient transition. For a Darcy's law assumption to be applicable there should be a relatively linear pressure gradient present and there should not be flow rate dependence. If there is flow rate dependence then a formulation based on the Forchheimer equation would need to be applied.

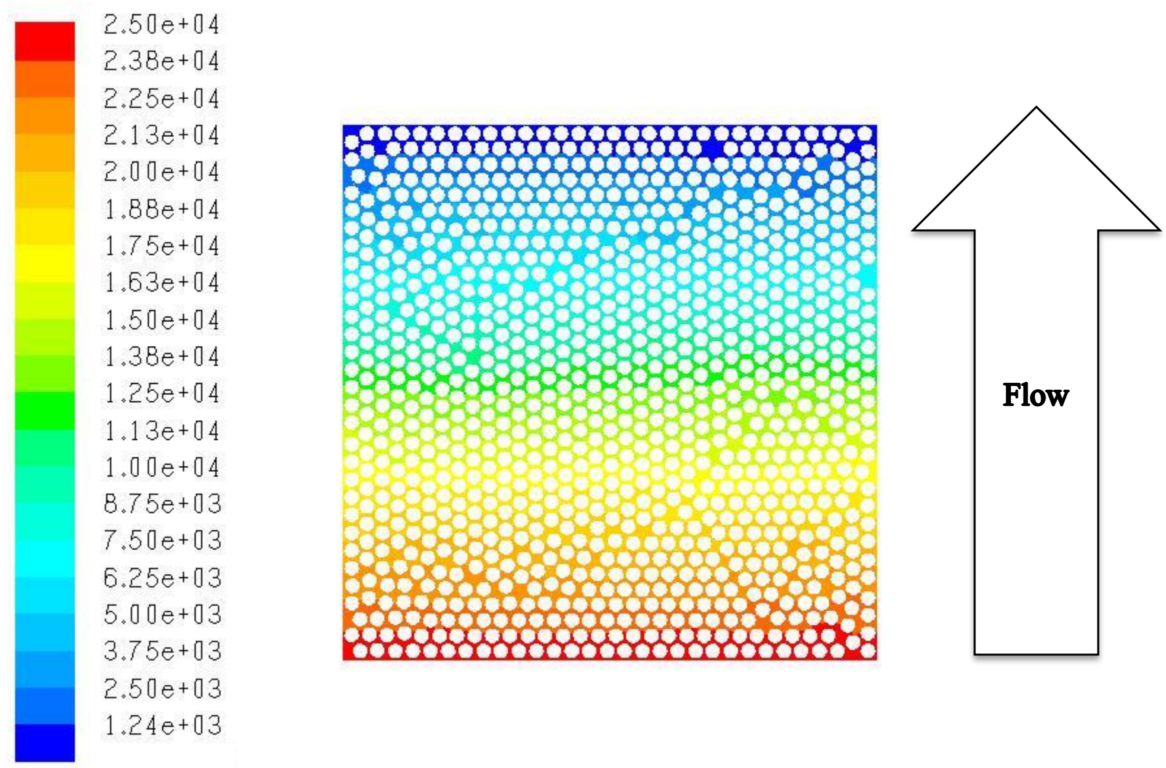

Figure 40: Pressure contours of a transverse flow through 60% fiber volume fraction in Pascal's (Pa)

Figure 41 and Figure 42 show the numerical results for the average inter-fiber parallel and perpendicular permeabilities of 1000 fibers. Figure 41 shows the average parallel numerical permeability results versus fiber volume fraction for 1000 fiber count simulations across fiber diameters ranging from 9µm to 5.2µm. Figure 42 shows the average perpendicular numerical permeability results versus fiber volume fraction for 1000 fiber count simulations across fiber diameters ranging from 9µm to 5.2µm. These fiber diameters would closely represent a carbon fiber material and a glass fiber material, respectively. The simulations shown here were an average of 5 simulations in the parallel direction and 10 simulations in the perpendicular direction for each fiber volume fraction. Twice as many transverse simulations can be run without requiring twice as many meshes because there are two transverse directions for each meshed representative volume element. The computed permeabilities are not necessarily the same in each transverse direction for the same representative volume element. The trend shows a rapid drop in permeability as fiber volume fraction increases. Also, the smaller fiber diameter has an apparent effect on the computed permeability because it is effectively creating a finer filter in the volume element. It is interesting to note how a binary mixture of fibers will affect the computed permeability if multiple fiber types will be used in a composite or if there is a large range in the nominal fiber diameter of the composite. The effect of binary mixtures on the flow can be seen by increasing concentration of smaller fiber diameters with constant fiber counts of 1000. The total volume of each representative volume element varies shown in Figure 27 a) 70% 9µm fibers with 30% 5.2µm, b) 50% 9µm fibers with 50% 5.2µm, and c) 30% 9µm fibers with 70% 5.2µm. Figure 41 and Figure 42 show a clear trend where, with decreasing fiber volume fraction, permeability decreases as expected for parallel and transverse flows. However, it also shows that as the fiber diameter decreases, the permeability decreases at a constant fiber volume fraction. This correlates with experimental measurements of glass and carbon fiber fabrics where smaller carbon fibers often lead to lower permeabilities at the same fiber volume fraction. The trend clearly shows that if a larger percentage of smaller fibers are incorporated then the permeability drops.

The results tend to show ~100% difference between fiber diameters at the same fiber volume fractions and ~4-15% difference between cases of random packing at the same volume fraction. These results compare reasonably well to the variation seen from various literature results. As results trend towards 90.93% fiber volume fraction, permeability should trend towards zero as the fiber randomness is forced to become increasingly hexagonally structured, and eventually the porous media is no longer interconnected. At lower fiber volume fractions, more variability in permeability is expected because there is more space for random packing to occupy. At higher fiber volume fractions, there is expected to be less variation because there is less space for fibers to occupy. Also, there is less space for stochastic randomness.

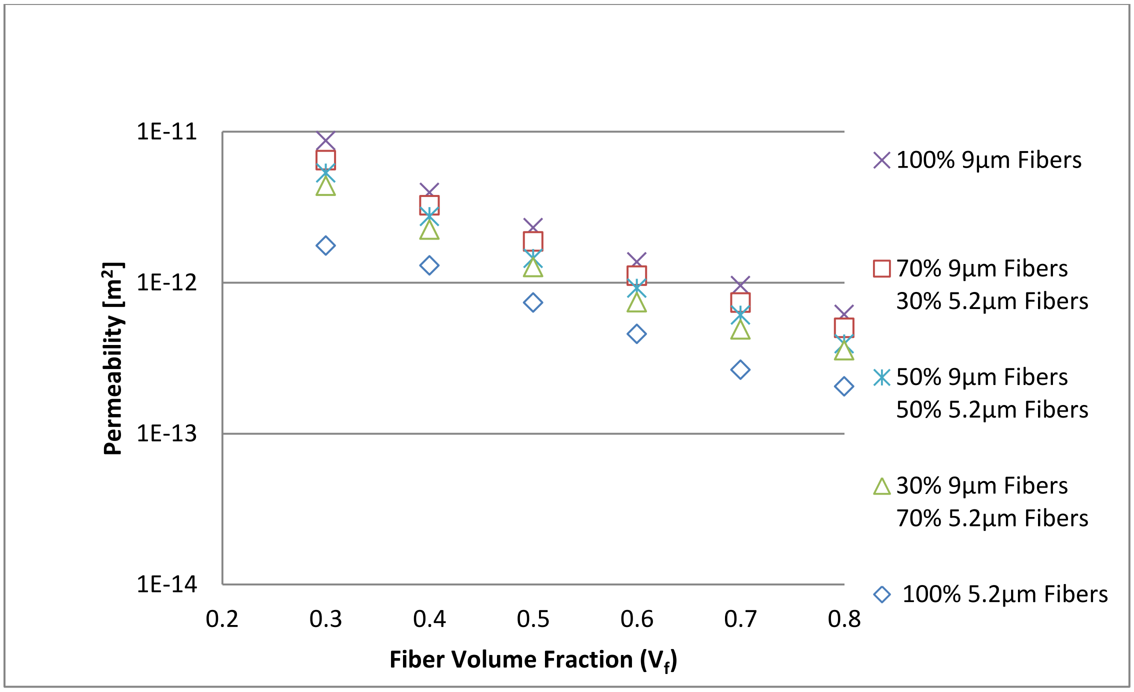

Figure 41: Average parallel numerical permeability results vs. fiber volume fraction for 1000 fiber count simulations

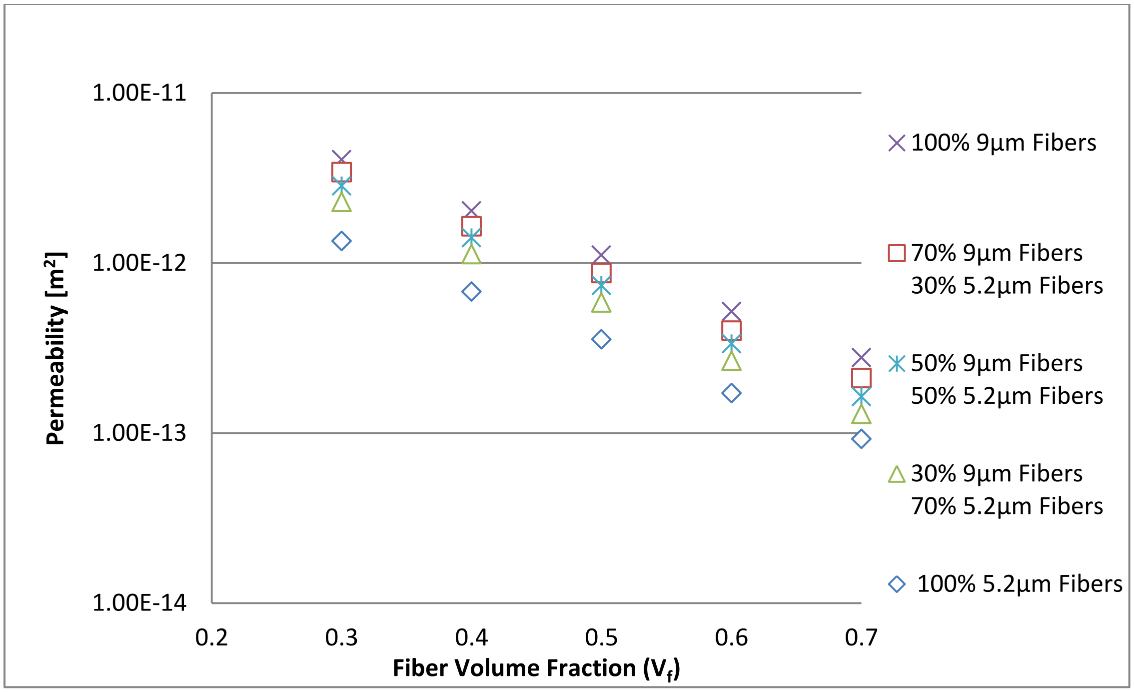

Figure 42: Average perpendicular numerical permeability results vs. fiber volume fraction for 1000 fiber count simulations

Figure 43 and Figure 44 plot previous results from literature are compared with current simulations. The abbreviations denote: Gebart *et al* [76] (Gebart Hexagonal, Gebart Quadratic), Kozeny-Carman [76] (Kozeny-Carman Hexagonal, Kozeny-Carman Quadratic), Bruschke *et al*. [63] (Bruschke), Gutowksi *et al*. [77] (Gutowski 0.82, Gutowksi 0.76), Chen *et al*. [44] (Chen Hexagonal, Chen Quadratic, Chen Random) Drummond *et al*. [72] (Drummond Hexagonal, Drummond Quadratic). The difference has been plotted versus current averaged numerical results to the corresponding numerical or analytical results for 5.2 µm diameter fibers.

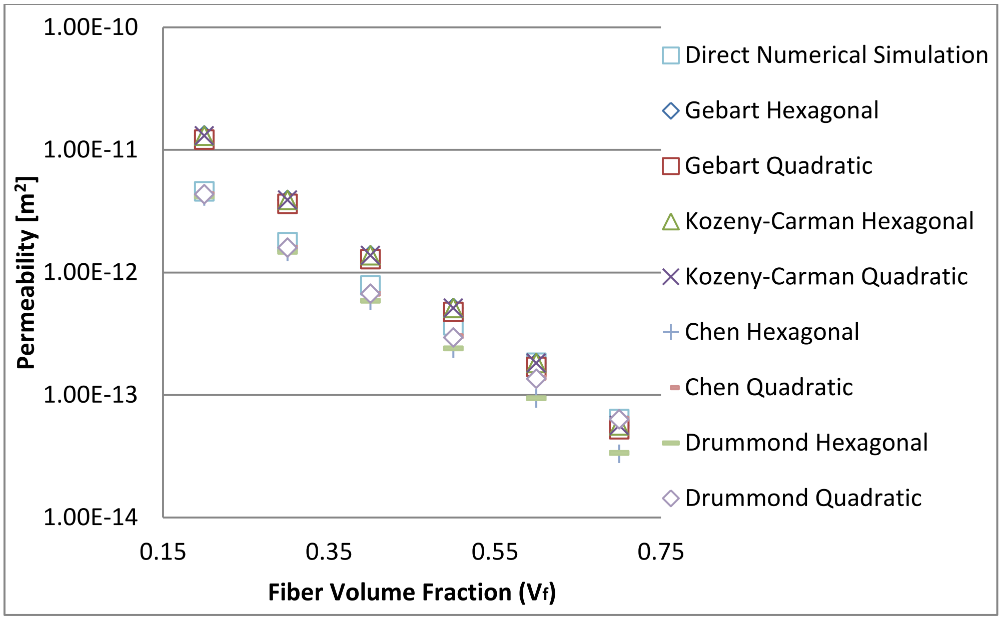

Figure 43: Comparisons for parallel permeability with results from literature at 5.2 µm fibers

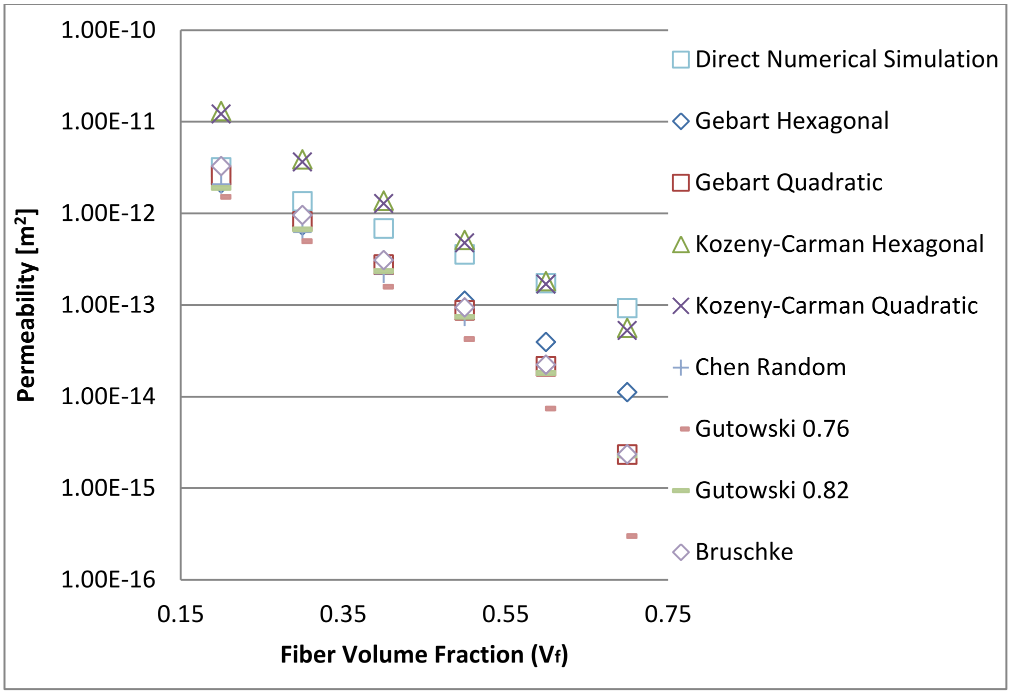

Figure 44: Comparisons for perpendicular permeability with results from literature at 5.2 µm fibers

In Figure 43 and Figure 44 it is clear that various analytical models differ from each other in their predictions of permeability. Perpendicular analytical models for permeability have a strong basis in first principles but many still require empirical parameters. Furthermore, the parallel analytical models often are weak because it is more difficult to derive an analytical solution from first principles for flow along the fiber surface. Depending on the materials and fiber volume fractions of interest, various analytical models can be justified. Since the approach reported in this paper is a direct numerical simulation of a set of realistic geometries, it is assumed that the numerical result is a more correct value compared to analytical models because it has better geometry representation. It is assumed that the analytical models from literature would converge towards numerical results across volume fraction but these analytical results are generally derived to fit experimental data with empirical parameters, which may make certain models semi-analytical.

5.6 Discussion

The results show that when isolating micro-scale permeability, the random packing and fiber size does have an effect on permeability. It is hypothesized that this is due to local permeability variations that differ from the global unit cell average. For example, there will be pockets of higher fiber volume fraction and lower fiber volume fraction in the unit cell. These pockets will have higher and lower permeabilities respective to their local volume fractions. The local variations will affect the global average and this will effectively raise or lower the computed global average. The higher volume fraction regions within the domain will create flow blockage near the pressure inlet and corresponding pressure build ups. The fiber distribution is able to generate variability in the computed permeability. The average permeability, as well as, the standard deviation is of particular interest. The reported permeability is an ensemble average of the entire domain. This should take into account the well dispersed and agglomerated fibers in the domain and average them out over a large enough ensemble. At high volume fractions, flow channels can become blocked and the permeability will be low in these areas. This is because the pressure will be allowed to build up in areas restrictive to flow and that will have an upstream effect on the rest of the computational domain.

In these results, confining the boundaries of the unit cells to square walls during geometry generation will artificially induce order into the arrangements. This is because periodic boundaries are not used in the generation of the geometries and partial fibers are not allowed to cross the walls. During the fluid simulations however, translationally periodic boundary conditions are applied. Wall induced structure will also reduce the total fiber volume fraction that can be achieved if the goal was to reach a perfect hexagonal packing arrangement. To achieve maximum packing would require a hexagonal shaped unit cell or periodic boundary conditions in the geometry generation. While permeability is a function of a large number of fibers, boundary conditions will influence the flow characteristics.

Furthermore, injection pressures could cause fiber distortions and shift the fibers so that they displace and violate the perfectly aligned assumption. This displacement would also affect the local porosity. Simulations assume perfectly fixed fibers that can sometimes be seen to washout in high pressure RTM molds. All of these effects can compound to create variability in the measured permeability. In computations, we have the unique ability to control for these factors and incrementally modify them. For these reasons, if microstructural permeability is of interest, numerical tools may be the only way to investigate parameters like the level of randomness. Even at high fiber volume fractions, a 4-15% variation in permeability is seen with constant fiber diameters. More variability is seen when fiber diameters are varied in size. Additionally, fiber packing disorder and fiber size variation is normal in fiber reinforcement and a method has been shown to model the resulting permeability with those effects.

5.7 Conclusions

In this paper a novel modeling approach has been applied to investigate the permeability of fiber reinforcement for liquid composite molding. Simulating the process on the micro-scale can help reduce investment costs and investigate a possible range of resins and reinforcements. When manufacturing a composite, a strong understanding of the flow properties across a number of scales of interest is required. Using a numerical approach, like the one outlined above, allows for a strong understanding of the micro-scale flows and a solution that can be coupled into the other scales of interest. In modeling micro-scale or pore scale permeability, the random packing does have an effect on permeability even at a constant fiber volume fraction. It is hypothesized that this is due to local permeability variations that differ from the global unit cell average. For example, in a global unit cell of 1000 fibers, there will be pockets of lower volume fraction and higher volume fraction in the unit cell. These pockets will have higher and lower permeabilities respective to their local volume fractions. The local variations will affect the global average and this will effectively raise or lower the computed global average. Furthermore, fiber diameter affects permeability when only considering permeability as a function of volume fraction. Larger fibers have a larger permeability and a binary mixture of fibers has permeability between the maximum and minimum permeabilities. This is a function of the percentage of fibers at each fiber diameter. It is hypothesized that the variability in the permeability at a single volume fraction could be used to induce variability into meso-scale permeability models without requiring dimensional variability in the tows. The numerical results have the potential to be used in component level simulations where permeability is needed as a tool to simplify the porous structure.

5.8 Acknowledgements

This work is sponsored by General Electric Aviation, Cincinnati, OH

Computational work in support of this research was performed at Michigan State University's High Performance Computing Center.

6. EFFECTS OF DISORDERED TOUGHENING PARTICLES ON UNIDIRECTIONAL FIBER REINFORCEMENT PERMEABILITY

6.1 ABSTRACT

Compared to traditional metal materials, composites are generally brittle and have a low resistance to crack initiation and propagation. Researchers have addressed this issue by incorporating particulate based fillers to increase material properties like fracture toughness. However, additives can be detrimental to processing variables like permeability and the consistency of parts. This limits more widespread applications because liquid composite molding processes can become prohibitively difficult. During the manufacture of particle and fiber composites, the infiltrating fluid can experience particle filtration causing pressure build-ups. Hence, a robust body of research investigating particle effects on resin infiltration is needed. Generally, it is difficult to distinguish the effects of particles from other processing variables; for instance measured permeability can vary by an order of magnitude. Here, an effort is made to numerically predict the effects of incorporating particles and toughening agents on the steady state, single phase permeability, of randomly aligned composite reinforcement fibers. Specifically, variations in filler particle size and concentration were studied. Over 500 simulations were conducted on three-dimensional geometries, with particle volume fractions between 0-10.5%, and fiber volume fractions of 60-64%. The particles were randomly inserted into the domain, fixed in space, and solved for as part of the mesh. These particles have mass and occupy physical volume in the computational domain. Baseline permeability results of fiber geometries without particles compared well with analytical and numerical results. The findings

of this study include permeability as a function of particle volume fraction, independence over a small range of particle sizes, and independence from various drag laws numerically implemented on fixed particles. The results also indicate that this is an area of interest for future work.

6.2 Introduction

Processing of composites is complicated and varies significantly from processing traditional metal based materials. Liquid composite molding (LCM) is a class of composite manufacturing techniques that is commonly used to manufacture finished composite parts. This class of methods includes resin transfer molding (RTM) and vacuum assisted resin transfer molding (VARTM). Variations to these methods have been created for trade secret and specific commercial applications. Particulates can be composed of a number of toughening and strengthening particles and have been used to advance composite mechanical properties [167]–[170], but these inclusions can add a layer of difficulty to the manufacturing process.
The critical processing parameter in LCM simulations is permeability, which drives the mold filling time and pressure distribution. Permeability is a function of the fiber reinforcement geometry, fiber volume fraction, and fiber type. If the fiber preform and boundary conditions are not well designed, then the mold will be filled slowly or incompletely. Additionally, effects like fiber washout can occur where the fiber arrays are deformed and the designed mechanical properties will not be achieved in the manufactured composite. Fiber reinforcement can have a filtration effect when particles are flowing along with a fluid [171]. The particles can cause complete flow blockages if the particulate sizes are inappropriate or tend to agglomerate reducing the interconnected nature of the porous material.

The flow resistance with fiber reinforcement increases rapidly with increasing fiber volume fraction, while the particulate incorporation can have a large effect on infusions creating added resistance to flow. If the production of parts by liquid composite molding processes is desired, it is important to understand the effects that particles will have on the infusion parameters. In mold design, it can be difficult to identify what the final flow properties will be like before a tool is built because there are so many coupled parameters. Poor mold design will lead to poorly finished parts with large quantities of air entrapment.

Composite manufacturers started to incorporate particulate additives in production for special purposes such as electrical conductivity [167], thermal conduction [168], flame resistance [169], and cost reduction[170]. To achieve these ends, it is important to distinguish between micro- and nano-particles. Nano-particles (1E-9m) generally require a lower filler percentage than micro-particles (1E-6m) to achieve a designed effect like mechanical property improvement [172]. Some particles incorporated into a composite may bridge the gap between the standard particle sizes, encompassing features of both scales. For example, exfoliated graphene is generally 3-5nm thick but can easily have an effective diameter of 5-15µm.

Two main methods exist for incorporating particles into laminated composites. One uses liquid composite molding where the particles are dispersed into a resin system and then the resin is infused into the fiber reinforcement. In some cases, the high surface area of particles and the large aspect ratio of some particles leads to significant increases in resin viscosity [173]. Additionally, this approach can cause filtration of the particles by the fiber reinforcement and result in gradient dispersion of the particles. A second approach coats the particles directly onto the fiber surfaces in a sizing approach [174]. This approach can reduce the issue of gradient material properties but permeability reductions still exist. However, in one case the investigation of transient permeability of a plain weave S-glass fabric with graphene nano-platelets found that permeability increased due to an inter-ply spacing effect [175].

Particle filled resins and particle coated or filled preforms are different. Particle filled resins with particles in suspension can have viscosity increases as well as thixotropic properties. The issue of filtration leads to gradient mechanical properties and is also a design parameter that must be understood. All this combines to change the resin flow and can lead to dry spots, poor saturation, and changed cure times [170]. Well dispersed particles in the preform may have smaller effects on filtration but may still have important effects on permeability. The effect on permeability would also be a function of particle size.

This investigation is a first attempt at discovering the effects of spherical particles on a flow field in composite manufacturing and their effect on permeability. Numerical tools are utilized to predict the effects of incorporating particles and toughening agents on the steady state, single phase, permeability of unidirectional, randomly aligned composite reinforcement fibers. Specifically, variations in filler particle size and concentration at a single fiber volume fraction are simulated. The study was designed to simulate and model fixed particles with a future work to include transient particles and agglomeration. Over 500 simulations were conducted on three-dimensional geometries, with particle volume fractions between 0-10.5% and fixed fiber volume fractions of 60-64%. The particles were randomly inserted into the domain, fixed in space, and solved for as part of the mesh. These particles have mass as well as occupying physical volume in the computational domain. Permeability of just the fiber geometries were taken as a baseline for permeability. Those results were then compared with results from including particles and showed reasonable decreases in permeability. The findings of this study include permeability driven by particle volume fraction and independence from various drag laws numerically implemented. Results show an independence from particle size over a small range of particle diameters and no effects due to the randomness of the well distributed particle dispersion. The results also indicate that this is an area of interest for continued work.

6.3 Fiber Reinforcement Modeling

The fiber reinforcement modeling approach has been described in another paper [163]. For this study, the micro-scale is isolated for direct numerical simulations. One characteristic fiber geometry and packing at volume fractions of 60-64% are studied. This fiber volume fraction range was selected based on what is commonly seen in unidirectional tows. The fiber packing arrangement is forced to be identical at each volume fraction in order to remove the effects of packing arrangements on the results. Packing arrangement has been shown to affect the resulting permeability because of the blockage of preferential flow channels.

6.4 Flow Modeling

Here, models for the longitudinal and transverse flow through fiber beds with incorporated particles are created. The solution for the permeability of flow perpendicular and parallel to the fibers has been conducted in three dimensions with the finite volume code FLUENT. The computations are done at low flow rates so that the creeping flow assumption is valid. This implies that inertial forces are neglected and the results for permeability should result in linear pressure gradients. The single phase, saturated flow, is simulated to simplify the case. The solid phases are solved for but only one fluid phase is considered. Two-phase fluid flow disturbances like capillary effects and saturation are often present in manufacturing mold fills but will not be considered here.

The simulations were performed for fiber volume fractions of 60-64% in increments of 1% volume fraction. In each simulation there were 10 fibers in the computational domain using a geometry generation code from previous research [163]. A characteristic geometry for 10 fibers can be seen in Figure 45. In the volume cell, the fiber surfaces are assumed to have a standard no slip, wall boundary condition. The boundaries of the volume are assumed to be translationally periodic and are matched to opposing faces. The inlet condition is a velocity inlet and an atmospheric pressure outlet is assumed. The steady state laminar flow conditions are assumed to accurately represent the flow that takes place under experimental permeability measurements. The model results output are the inlet and outlet pressures as well as the interstitial average velocity. A tetrahedral mesh is generated for the unit cell. Currently, this approach allows for a consistent mesh between particle volume and packing. However, a new mesh is required for each fiber volume fraction and the particles must occupy a minimum number of mesh elements in the domain. This requires that the mesh be fine enough to incorporate the particle size of interest. As the particles become smaller, an increasingly fine mesh is required, and corresponding computation times increase.

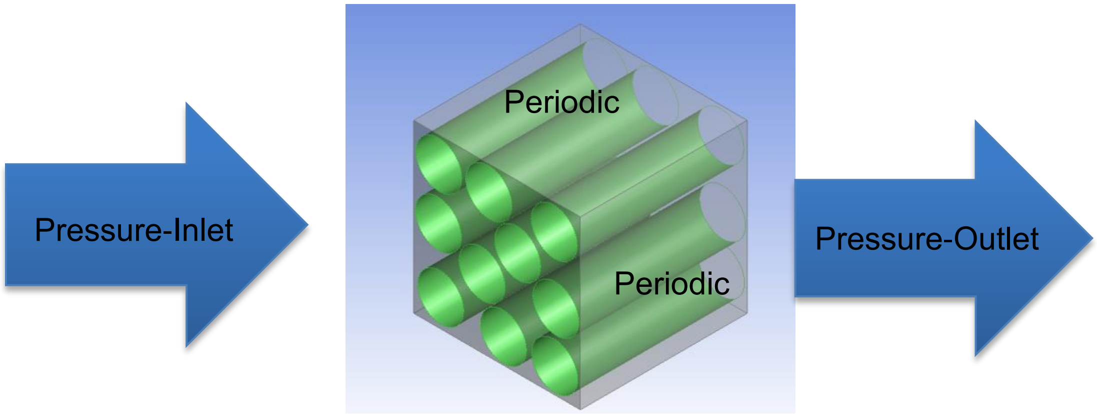

Figure 45: The fiber geometry for the majority of simulations with a set of parallel flow boundary conditions. The fluid region is gray and the fibers are green. The fiber volume fraction here is 60%.

The properties of the fluid used in the numerical simulation were motor oil, often used in experimental investigations of permeability (Motor Oil, Viscosity 0.24Pa*s, Density 709 kg/m^3) [164]. It is envisioned that, the micro-scale permeability with particulate incorporation could be used to aid in the prediction of the macroscopic, component level permeability. This would be done using the results of these simulations as averaged permeability inputs for tow geometries on meso-scale permeability simulations. The component level permeability is of manufacturing interest because it models the impregnating resin in liquid composite molding without having to account for every individual fiber and tow leading to a more computationally efficient solution.

6.5 Macroscopic Particle Model

Typical particle tracking methods assume that particles are point masses that do not interact [176]. When trying to consider relatively large particles in a flow field, large meaning larger than multiple discretized cells, special considerations have to be made. Factors such as a blockage of fluid volume, which directly affect permeability because of its effect on porosity, have to be taken into account. Further, the proper evolution of the drag force, particle-particle collisions, particle-wall collisions, torque, and friction dynamics can be significant for large moving particles [177]. In the macroscopic phase model, particles are treated in the Lagrangian frame of reference and each particle spans several computational grid points.

In modeling fibrous preforms for composite manufacturing, a porous media assumption is often valid. If the domain of interest is the micro-scale, the interactions between a well dispersed micro-particle phase and the computational domain has to be considered. Two critical problems that evolve during composite manufacturing with toughening particles include gradients in material properties caused by a filtering effect from the fiber preform and uneven particle dispersion caused by the flow and inter-particle forces. Here, it is assumed that we have a well dispersed particle inclusion in our domain as in Figure 46. In order to simplify this first investigation and reduce computation time, particles are fixed in the domain to investigate their effect on the pressure distribution.

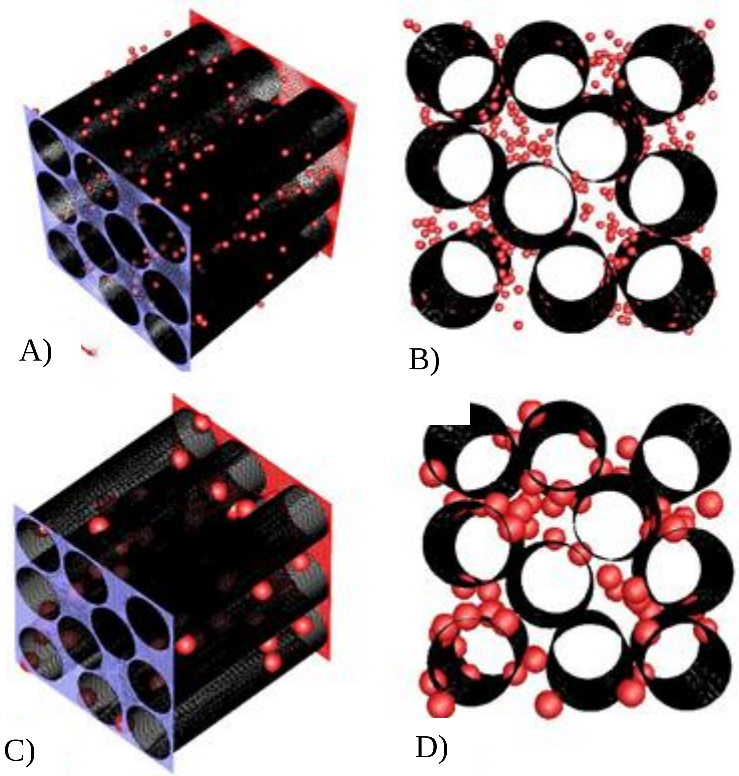

Figure 46: An isometric (A) and parallel flow (B) view are shown as a characteristic example of random particle incorporation at 1µm particle size and 1% particle volume fraction An isometric (C) and parallel flow (D) view are shown as a characteristic example of random particle incorporation at 3µm particle size and 5% volume fraction. These particles are assumed to be fixed in space and not allowed to flow with the resin or affect the resin viscosity. The flow is treated as a single phase fluid and particles are allowed to partially exit the computational domain.

The Discrete Phase Model (DPM) works for some domains, but this treats a particle as a point mass and these point masses have the properties of the fluid as the particles move [176]. In this investigation of particulate incorporation, 1, 3, and 5µm particles are inserted with 9µm fibers. In the general use of the DPM model, the particles of interest are considered to be much smaller than the computational grid cell in the discretization. The modeling of particles that have mass and volume requires a different and unique approach. If properties such as permeability are of interest, this approach must also account for effects such as a change in geometry and a blockage of fluid volume.

The Macroscopic Phase Model (MPM) developed by Agrawal *et al*. [177] meets many of the needs stated for composite interactions with a dispersed particle phase. The model accounts for effects such as drag forces, particle torque, friction dynamics, particle-particle and particle-wall interactions. The model is designed for finite volume computational fluid dynamics solvers where direct numerical simulations (DNS) are avoided because of a large number of particles of interest. Furthermore, this model assumes that the particles of interest fill multiple computational mesh cells.

This model in the transient case, has the ability to track any particle through a volume, the most common way to do this is to use a Lagrangian frame of reference. Each particle is assumed to span several computational cells. Cells that contain at least one node within the region occupied by the particle are affected by the particle. Six degrees of freedom are assigned to each particle to account for the translational and rotational motions. However, in this first investigation the particles are forced to be fixed because of the time consuming transient simulations required for moving and interacting particles. At every computational time-step, the particle motion is described by a solid body velocity and patched to the computational domain. This adds the momentum of the particle to the momentum of the fluid. In the future the effects of moving particles should be investigated more fully.

Body forces are included in the model natively. Drag forces and torque in a particle are expressed as the integral of linear and angular momentum respectively. When these forces are solved for they are then applied to iterate the new velocities and particle locations at the next time step. The drag and torque calculations for the particle can be seen in Agrawal *et al*. [177], [178].

$$Drag = \left(\sum_{touched\ cells} m_f \left(\bar{V}_f - \bar{V}_P \right) \alpha_P \right) \frac{1}{\Delta t} \tag{33}$$

$$Torque = \left(\sum_{touched\ cells} m_f \left(\bar{V}_f - \bar{V}_P \right) \cdot \bar{r}\ \alpha_P \right) \frac{1}{\Delta t} \tag{34}$$

Here, m_f denotes the mass of the fluid, V_f is the fluid velocity, V_p is the particle velocity, r is the radius vector from the fluid center to the particle center, α_P is the particle volume fraction in the domain. A particle volume fraction of one is assigned to fluid cells that are completely within the particle volume.

Partially filled computational cells are treated differently. The volume fraction for the particle in those cells is calculated by accounting for the effective cell nodes inside of the particle volume. The model has the ability to account for a continuous particle injection inlet as well and maintain an overall mass balance. When particles are continuously injected, a mass source term based on the displaced fluid per unit time is included in the model.

Particle collisions between walls and other particles are also accounted for in a model by purely kinematic and geometric considerations. The surface of walls and particles are identified and if a second particle comes in contact with the first wall or particle in a previous time step, a collision is registered. When this collision takes place, the particle velocity is projected onto the normal and tangential components of the reflected particle velocity. Within a time step, the minimum separation distance becomes less than or equal to the sum of their radii and is detected. The coefficient of restitution and friction factor are applied when appropriate. When particles come in contact with other particles, then the principle of conservation of momentum is applied to obtain the final velocity of both particles.

The model accounts for field forces and body forces like electrostatic or magnetic forces by a potential force model [177]. Inter-particle forces are described with:

$$F_i = \sum_i \frac{G_P M_i^{n1} M_j^{n2}}{R_{i-j}^{n3}} \tag{35}$$

Where, F_i is the force on particle i, M_i is the particle mass, R_{i-j} is the interparticle-distance. Model constants are defined for each particle describing the system as G_p, n1, n2 and n3. Many of these constants come from empirical or analytical models for the reaction of a single particle. The sign of the model constants decides whether the field force is attractive or repulsive.

Written in the SCHEME programing language, a set of user defined functions (UDF) are used to implement the MPM model. Initial properties for a particle or set of particles are implemented by prescribing the initial position, velocity, density, and radius. Particles can be inserted into a domain as a point, line, or surface injection. Those particles can also be a continuous particle injection in both cylindrical and rectilinear coordinates. Further, particles can be injected into a domain randomly. To date, results on steady-state particles are all that will be presented and transient results will be presented in the future.

6.6 Results

The results given below are computationally intensive and a large set of data was generated in order to obtain the figures.

Figure *45* shows the characteristic geometry at 60% fiber volume fraction. This was meshed in order to run the fluids simulation and the mesh had to be correspondingly refined to reduce the nominal mesh size to have at least five fluid volumes inside of each particle. The periodic boundary conditions are used to help make up for the reduced domain. Pressure inlets and outlets were applied here and the volume average velocity was calculated.

Figure 46 shows isometric (A, C) and parallel flow (B, D) views as a characteristic example of random particle incorporation. Additionally, A and B show 1μm particle size and 1% particle volume fraction inside of 60% fiber volume fraction geometry. Here, the small particles each incorporate multiple mesh volume elements and the particle velocity is fixed at zero.

Figure 46 C and D shows a characteristic example of random particle incorporation at 3μm particle size and 5% volume fraction. The particles only partially fill the computational domain due to their size in reference to the inter-fiber flow channels. Particles are assumed to be well dispersed, fixed in space, and not allowed to flow with the resin. Comparisons were made between allowing partial particles and only complete spheres in a computational domain. Little difference was seen between partial and complete particles in the domain.

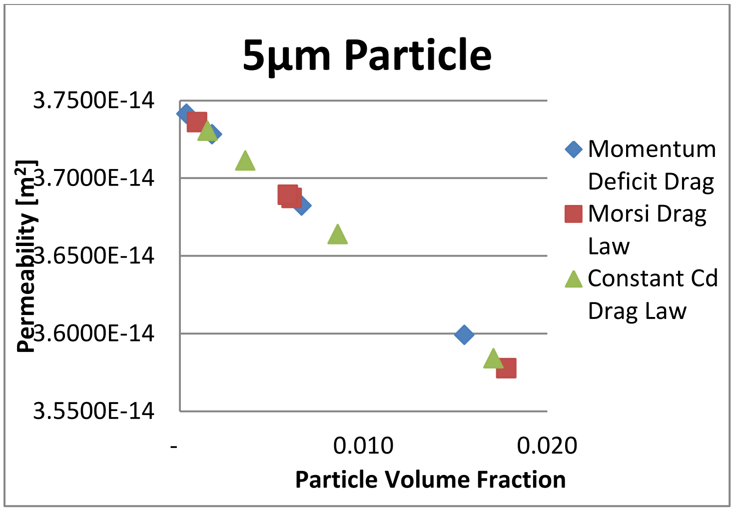

Figure 47: The Effects of Drag Law Selection on Fixed Particles for Perpendicular Permeability. The particle volume fraction adds to the fiber volume fraction (60%) to become the global volume fraction.

Figure 47 shows drag law effects on perpendicular permeability for 5µm particles. It can be seen that fixed particles in the domain are not largely different in their effect on the pressure drop through the domains from various drag laws. This was expected given that the particles have no momentum, for that reason the momentum deficit drag law has little effect. All permeabilities calculated for the same particle volume fraction, at the same boundary conditions, are nearly identical. Figure 48 reinforces the same results as in Figure 47 for a set of parallel flow cases. These results are the same trend seen with particles ranging in size from 0.5, 1, 3, and 5 µm.

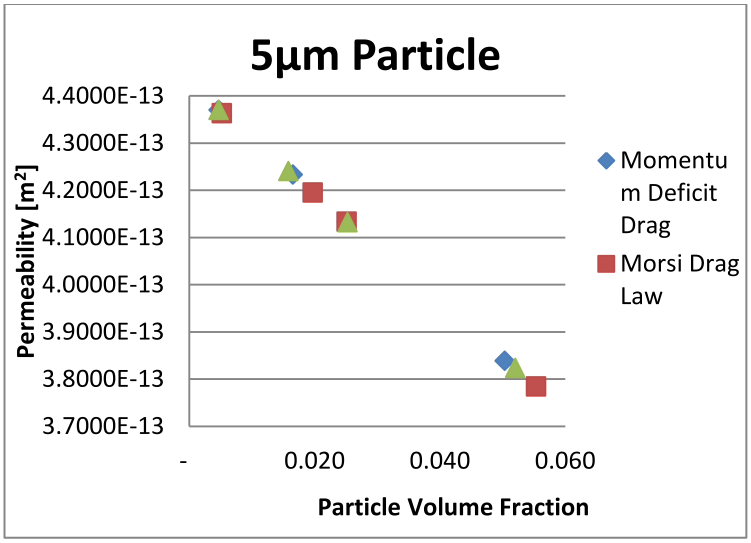

Figure 48: The effects of Drag Law Selection on Fixed Particles for Parallel Permeability. The particle volume fraction adds to the fiber volume fraction (60%) to become the global volume fraction.

Figure 49 shows the non-dimensional perpendicular permeability vs. global volume fraction with particles sizes varied from 500 nm to 5 µm. The global volume fraction is the combination of the fiber volume fraction and particle volume fraction. The results are non-dimensionalized by the square of the fiber radius. The particle size was selected in order to investigate a small range of size variations, while the corresponding mesh was refined to meet the requirements for investigating the smallest particle and maintaining the minimum number of elements in that particle. Additionally, decreasing the particle size requires a further refined mesh and an increasing computation time. Figure 50 shows the fiber volume fraction fixed at 60% and the particles added in increasing global volume fractions up to 70%. The volume fractions studied were increased to see if any non-linearity could be identified. Results show an independence from particle size over a small range of particle diameters and no effects due to the randomness of the particle dispersion.

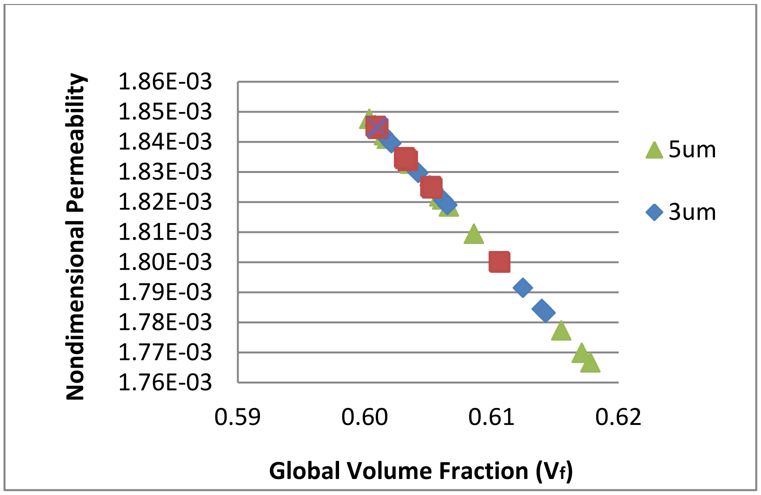

Figure 49: Perpendicular Permeability vs Global Volume Fraction. This case starts at 60% Fiber Volume Fraction and Increases in Volume Fraction by Increasing the Number of Particles Incorporated. The results of 150 perpendicular permeability simulations are plotted against volume fraction and colored by particle size.

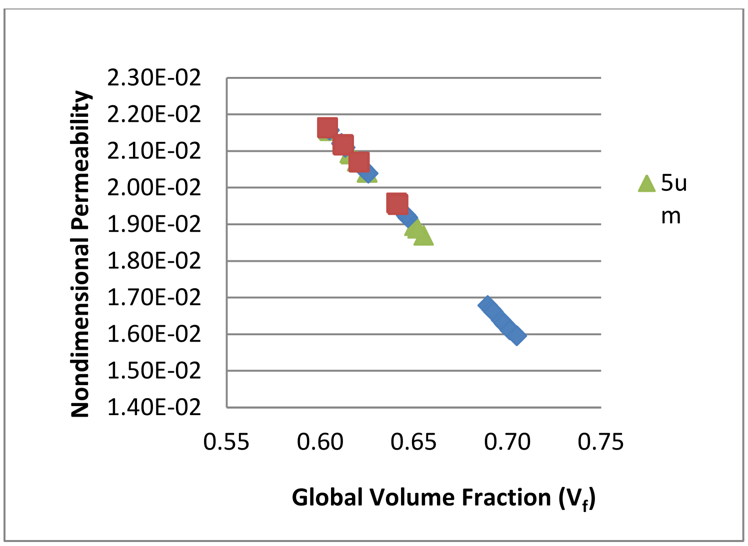

Figure 50: Parallel Permeability vs Global Volume Fraction. This case starts at 60% Fiber Volume Fraction and Increases in Volume Fraction by Increasing the Number of Particles Incorporated. The results of 150 parallel permeability simulations are plotted against volume fraction and colored by particle size.

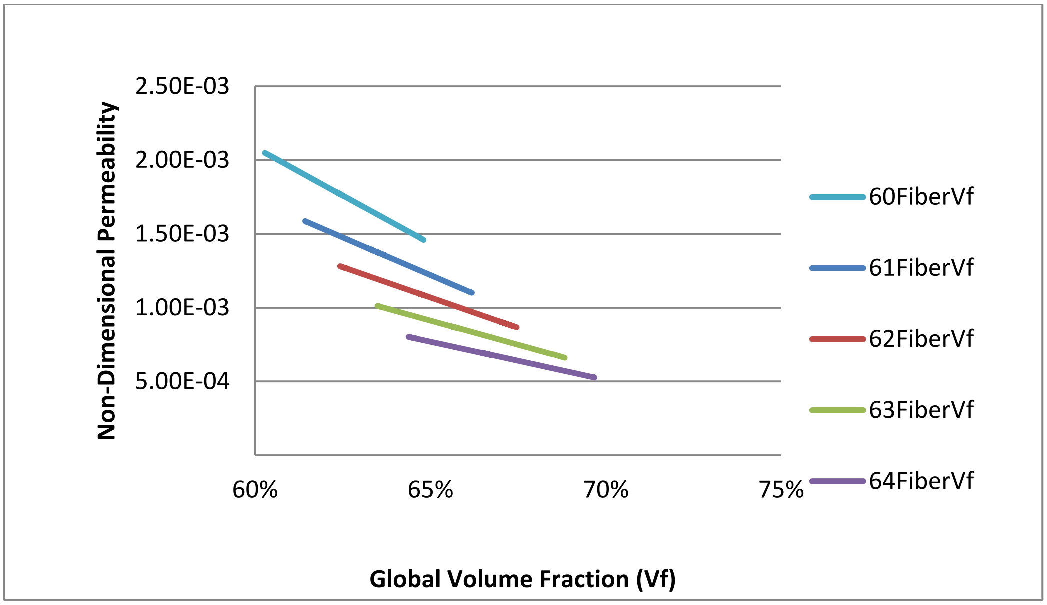

Figure 51: Perpendicular Permeability vs Global Volume Fraction. This case starts at 60, 61, 62, 63, and 64% Fiber Volume Fraction and Increases in Volume Fraction by Increasing the Number of Particles Incorporated. Particle size is a constant 3µm here.

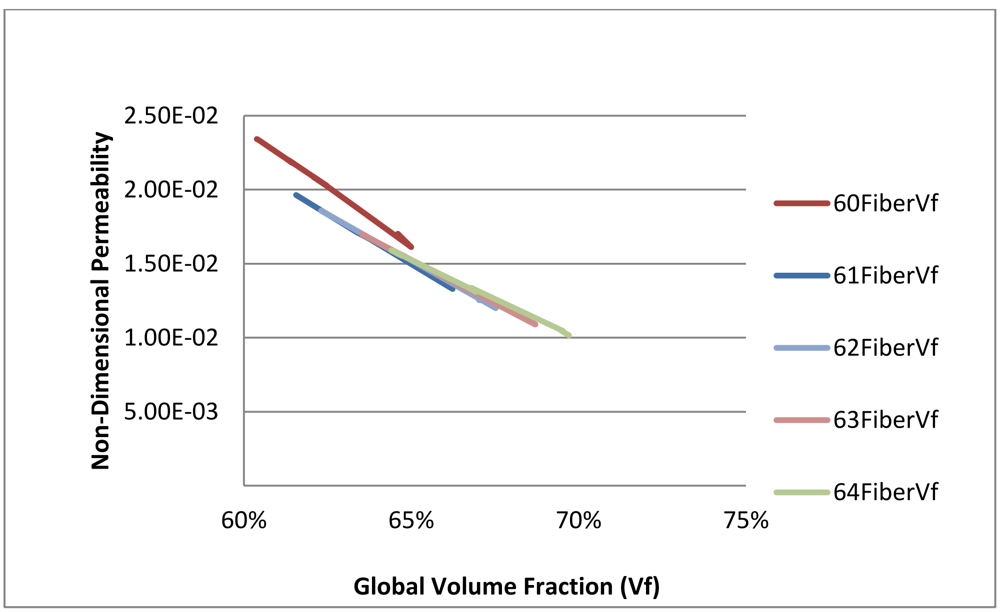

Figure 52: Parallel Permeability vs Global Volume Fraction. This case starts at 60, 61, 62, 63, and 64% Fiber Volume Fraction and Increases in Volume Fraction by Increasing the Number of Particles Incorporated. Particle size is a constant 3µm here.

Figure 51 gives the perpendicular permeability versus fiber volume fraction by particle volume fraction. Figure 52 shows the parallel permeability versus the fiber volume fraction. The results here are also non-dimensionalized by the square of the fiber radius. The initial fiber volume fraction is varied from 60-64% and then increasing particle volume fractions are added. These results are interesting because it seems that the fiber volume fraction has a larger effect on decreasing permeability than well dispersed particles. This may be partially because the permeability will not monotonically approach zero at higher volume fractions as long as the pore network is interconnected.

6.7 Discussion and Conclusions

The effect of particle drag on fixed particles has been shown to have little effect on the results of permeability simulations because particles are fixed in steady-state simulations. Steady-state simulations are much faster to conduct and therefore a large number of steady-state results can be computed where the same number of transient results would require exponentially more resources. These steady state results could be useful for inputs into meso-scale permeability models for tow inputs already containing particles.

It is assumed that fiber volume fraction increases cause a more drastic decrease in permeability than increasing the volume fraction of particles because increased fiber volume fraction reduces flow channels, while well dispersed particles allow for more flow around them at the same volume fraction. Furthermore, the current simulations look at the effect of particles on the flow but is neglecting their ability to flow and change resin viscosity. This assumption has not been validated for a wide variety of cases and the applicability of this approach will only apply to a very select case of processing conditions. There will be a particle size threshold where the particles are too small to be treated as a part of the mesh and this approach will break down when the corresponding mesh is not sufficiently fine. This threshold is a function of the mesh element size and the particle size and maintains a minimum relative ratio of about 5 computational volumes contained in each particle.

The results are limited to predicting permeability on scales comparable to mesh element size because of the semi-direct numerical approach and the computational resources required. Important processing variables can be obtained in this manner including the velocity and pressure distribution. The permeability of unidirectional fibers, woven fabrics, and fiber preforms has been well studied, but permeability becomes more complicated when considering the effects of particulate incorporation into the fiber preform or resin system. For this reason, modeling research on the subject has been limited. During the manufacture of particle and fiber composites, the infiltrating fluid can experience high pressures, and permeability can be difficult to find. This is one attempt to distinguish the particle effects from the many other processing variables. This is one explanation for how preform permeability could vary due to local particle concentrations or by a lack of saturation.

Inclusions are another processing parameter that could be modeled in the approach given here. These inclusions could be made up of micro-scale voids, entrapped air bubbles, or other defects. As a tow or yarn is initially beginning to saturate, the advancing resin flow front tends to only partially saturate the volume as a function of time and pressure [15]. At any instant in time, this modeling approach could be used to approximate the volume fraction of resin saturation with the particles being treated as air bubbles. This would approximate the effect of partial saturation on permeability and could be used as a function of increasing permeability with increasing saturation as the fluid zone modeled trends towards complete saturation. Hence, incorporating partial saturation on the steady state, single phase, permeability of unidirectional, randomly aligned, composite reinforcement fibers could be achieved.

The variations in filler particle size and concentration at a fiber volume fraction trended down as was expected but did not directly follow the trend of the fiber volume fraction increases. The cause of this is assumed to be because the interconnected flow network is larger with spherical particles at a certain fiber volume fraction than the network is with cylindrical fibers at the same fiber volume fraction.

The results increase our understanding of particulate effects on manufacturing properties that are critical during liquid composite molding. Over 500 simulations were conducted on three-dimensional geometries. Particle volume fractions were varied between 0-10.5% in order to investigate how increasing particle concentrations affect permeability. This was applied to 60, 61, 62, 63, and 64% fiber volume fractions in a 10-fiber, micro-scale domain.

Randomness of particles insertions seemed to have little effect because they were well dispersed in the domain. The fact that the simulations incorporated the particle mass as well as physical volume is unique in computational approaches. The findings of this study include permeability effects from particle volume fraction. Results show an independence from particle size over a small range of particle diameters.

6.8 Future Work

The results of these simulations show a consistent drop in permeability with the incorporation of increasing numbers and volume fraction of particles. This is an appropriate first step in attempting to predict the permeability. The future work with this approach will investigate the effects of transient particles that are allowed to interact with each other as well as fiber reinforcement. Further, the corresponding drag laws investigated are expected to play a more important role once particles are moving. The transient clogging of flow channels by particle agglomeration will have an effect on permeability and quantifying that effect is a goal of future work. A more fully characterized set of materials with the effects of toughening particles on composite permeability would be useful. These models could be used a precursors to micromechanical models where the final properties and manufacturing effects of particulate incorporation could be more fully investigated. For instance, when particles are mechanically designed to be well dispersed but the liquid molding process does not accomplish this. Additionally, an in-house direct numerical simulation approach is being developed to repeat these results.

6.9 Acknowledgements

This work is sponsored by General Electric Aviation, Cincinnati, OH

ANSYS Fluent provided the Macroscopic Particle Model

Computational work in support of this research was performed at Michigan State University's High Performance Computing Facility

7. MODELING MESO-SCALE PERMEABILITY AND ADVANCING FLOW FRONTS IN LIQUID COMPOSITE MOLDING

7.1 ABSTRACT

In liquid composite manufacturing, reinforcement permeability drives the resin infusion. Permeability can be modeled using a unit cell and flow front propagation is subject to the dual-scale architecture. Here, a plain weave fabric is modeled and a permeability prediction is presented. The dual-scale porosity of the preform is considered, solving the fluid flow in the inter-tow and the Darcy flow in the intra-tow. The micro-scale permeabilities are generated from a stochastic set of numerical models. Steady state simulations are conducted to predict in-plane permeability. A multiphase simulation is then conducted to investigate the unsaturated infusion. Two cases of transient infiltrations are made: one with the fiber tows as solid boundaries, and one with the tows as porous. The in-plane permeability and advancing front simulations are validated with measurements from two test fixtures. Multiphase simulations are then shown to account for the air to resin phase transition seen in mold fills.

7.2 Introduction

Liquid composite molding (LCM) processes present a number of manufacturing challenges, some of which can be addressed through a strong characterization of fiber preform permeability and simulations of the mold filling process. Flow front modeling and prediction of the mold filling phase can help anticipate manufacturing problems such as the formation of voids or dry spots, where no fluid impregnates the preform. Once the flow front profile is known, it is possible to optimize parameters such as pressure, flow rates, placement of gates, and preform layup [158]. In order to model LCM processes effectively, it is important to start with the characterization of the fiber reinforcement including the permeability. These permeability results are often produced through numerous and time consuming in-plane and transverse experiments at various volume fractions.

Previous research has characterized the permeability of aligned fibers, unidirectional fabrics, and intra-tow regions composed of fibers with microscale dimensions within unidirectional tows [43], [44], [75], [76], [86]. Many of these characterizations focus on an analytical basis for permeability. However, there is a gap in research exploring the extension of analytical permeability results (predicted using geometric parameters and analytical results like Gebart's [76] unidirectional permeability) to understand the necessary parameters in complex, three-dimensional, woven fabrics. The level of variability in permeability and the geometric causes are difficult to account for in simulations. This may partially be caused in the level of inconsistency in woven fabrics on this scale and difficulties dealing with a homogenized domain where fluid acceleration is no longer modeled.

In modeling the flow of resin through a fiber reinforcement, the general approach is to consider the resin as a fluid propagating through a porous medium [158]. The way the porous media is treated depends on the scale of interest in the simulation. Figure 53 shows three commonly discussed scales when considering composite fiber reinforcement. The micro-scale is also often called the pore scale in porous media and considers the physical fiber geometry of a unit cell under consideration. This scale can model the physical effects of fibers in the domain and produce a unidirectional permeability. The meso-scale considers bundles of fibers, often 6-12k in a tow, with a tensor permeability that can be input in two transverse directions and a parallel direction. This scale is also referred to as the Darcy scale in porous media literature where the individual pores or fibers are no longer modeled. Instead, they are replaced by a permeability value representing the resistance to flow. The component-scale represents the desired composite part and can be represented by a bulk permeability value. Component scales no longer consider physical fibers or tow geometries and instead have an effective permeability through its domain.

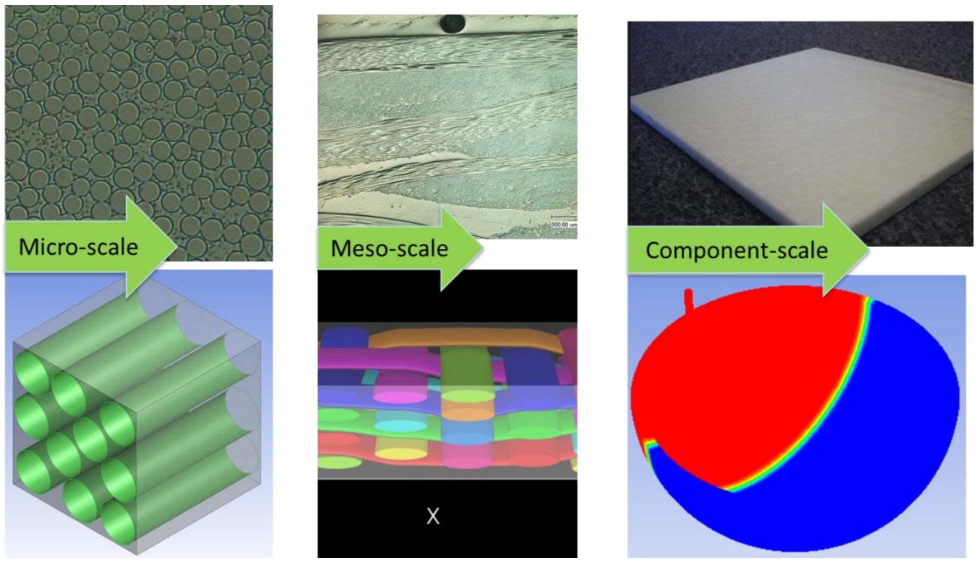

Figure 53: Representative Geometries for the Micro-scale, Meso-scale, and Component or Macro-scale

Defining accurate resin flow fronts for complex fabrics is challenging, as the permeating fluid often progresses unevenly due to variable porosity and flow channels created by statistical variation in the textile geometry. The dual-scale nature of woven fiber reinforcement often leads to a global resin front passing ahead of a lagging tow saturation in pressure based injections [16]. Constant flow rate injections often have a more even flow front. Accurately modeling the advancing flow fronts in LCM is an important tool for designing to avoid air entrapment and void formation due to resin and air phase interaction. Modeling of void formation at the fiber or tow level requires consideration of real geometry, while the global resin flow can be treated as an averaged flow front through an anisotropic or orthotropic porous media. These are important considerations for mold design, prediction of voids, and finished part evaluation, and all of these interests can be modeled in transient flow scenarios.

The LCM manufacturing setup often consists of a mold, die cavity, or vacuum bag with a tool plate, populated with a fiber preform or chopped fiber filler. The resistance to flow is characterized by the permeability tensor and there are a number of devised analytical, numerical, and experimental techniques available to obtain this parameter [69], [79], [128], [160]. Experimental procedures for permeability vary widely, and the testing method itself can account for some of the statistical variation seen in permeability. Additional human factors, such as layup, may affect the result of experimental permeability values [161], and experimentalists have found permeability scatter of up to one order of magnitude for the same material at the same volume fraction [69]. Modeling permeability could aid in refining the variations between experimental results, help identify acceptable experimental methods, or ultimately eliminate experimental characterization entirely.

There has been some question as to whether a difference exists in steady state vs. advancing front permeability results. This is because of the partially saturated zones and variable infiltration, as well as capillary and surface tension effects present in two-phase flow. Furthermore, the reinforcement type can have an effect on how significant the two-phase flow permeability differs from the saturated permeability. Fiber preform characterization experiments and models are often done under both saturated and unsaturated conditions. Shojaei *et al*. [33] saw a variation of around 10% between saturated and unsaturated experiments with a woven glass fabric. The general consensus is that transient and saturated permeability results will be different but depends heavily on the architecture.

In two-phase flow cases, the fluid used to find permeability may be more important. A number of measurements and methods have been used to monitor the progression of the flow front for various fluids. Corn syrup [179]–[181] is commonly used to visualize advancing flow fronts, as are mixtures of corn syrup, water, and dye [51], [182], [183]. Previous research has also justified the use of corn oil [184], hydraulic fluid [125], [127] silicon oil [185], [186], and motor oil [187] in various experimental scenarios. An extensive study by Hammond and Loos [164] concluded that fluid type had very little effect on properties like permeability, which was expected given the steady state cases and well-studied physics associated with geometrical permeability. The fluid type may affect flow however, causing an effect on the apparent permeability. The type of fluid would have larger influence on transient, two-phase flow, because of surface tensions, capillary effects, and wettability of the fibers involved.

In tightly woven fabrics, the tows are much less permeable than the spaces left between the yarns. Thus, resin flowing through fiber reinforcements during composite manufacturing tends to fill these large voids first, before later filling the tows. Some previous researchers have accounted for the delay in tow filling by including a sink term in the continuity equation and having a lagging fill time within the tow [16]. These results showed a good model for the scenario of having two different flow scales in such close proximity to each other.

Often in mold filling situations, full preform saturation is completed before a temperature change or curing takes place. Consequently, simulations of this process may neglect the curing kinetics and temperature change – even though the behavior of the flowing fluid is dependent on its viscosity, which for resins, depends on the temperature and degree of cure. The viscosity and density of the resin is often assumed as constant [49], [138] so that the mold filling process can be solved without considering the cure cycle or non-isothermal conditions. If this assumption can be justified, it significantly reduces the computational needs of the problem at hand. There are cases where the mold and the preform are heated during the injection stage in order to reduce the cycle time and to control curing. In these cases, the resin flow and curing heat transfer problems have to be solved simultaneously.

Most of the difficulties and defects associated with LCM processes occur around the filling stage, when the fiber preform must be completely impregnated with resin while avoiding race tracking and dry spots. This fluid flow scenario is controlled by the underlying fluid dynamics, and computational fluid dynamics (CFD) is an important tool to simulate large sets of similar flows with various boundary conditions [188]. This type of CFD modeling is also a rapid, economical approach to minimizing the risk of producing defective parts.

The inclusions of geometrical variations have corresponding effects on the permeability variations. Previous researchers found that at around 50% fiber volume fraction, a 1% increase in fiber volume fraction would cause a 10% decrease in permeability [85]. Other researchers [43], [44], [162], [163] have shown that permeability variation can be seen by changing the randomness of the reinforcement at the same volume fraction. These results are critical to understanding how to create a quality finished part in LCM, and is valuable information when designing a complex mold. Additionally, the local variation of woven reinforcements from their own manufacturing will have large effects on the resulting models of composite materials.

Prediction of permeability requires fluid models on the micro-scale and the consideration of a number of factors relying heavily on geometry. In relating measured permeabilities to predicted permeabilities, factors such as edge effects, preform deformation, micro-flow, temperature, and steady state vs. advancing front permeability all combine to cause variability in the data. Frequently, the creation of geometrical models for fiber preforms involves the use of statistically averaged dimensions within the unit cell [103]. This is done to give an average representation of the preform geometry. Later, the statistical variation can be accounted for by implementing the standard deviations of the preform variability for the data of interest like mechanical testing.

In this study, optical micrographs are used to compute the geometry of composite fiber reinforcement. An image analysis approach is implemented in Python and MATLAB codes to quantify a large number of images rapidly. Once the images are analyzed for geometry, the intra-tow permeabilities of a plain weave Shield Strand S fabric are predicted numerically using an unique approach to incorporate the stochastic variability in the micro-scale packing arrangements [163]. Permeability for flow parallel and transverse to the fiber orientation is input into the model tows. These are analyzed for their effects on predicted permeability. Additionally, the image results are used to construct fabric unit cells using an open source software package from the University of Nottingham called TexGen [103], [104], [189]. The next step was to run a computational fluid dynamics simulation to solve for the macroscopic or bulk permeability results, with the intra-tow permeability prescribed as a tensor based on the corresponding weave direction. The analysis shows reasonable agreement between experimental and simulated results as well as the ability to produce standard deviations and an average permeability at the macro-scale from variability seen at the intra-tow or micro-scale level. Finally, the paper couples a numerical advancing front simulation procedure with experimental validation. The CFD simulations described here use the control volume technique with a volume of fluid (VOF) solver to model the transient flow front advancement. The VOF method tracks the flow front interface between air and simulated resin [190]. A procedure is outlined demonstrating the match between numerical and experimental results for the flow front advancement at characteristic unit cells representing areas of the manufacturing mold.

7.3 Composite Characterization

The composite fiber reinforcement chosen for this analysis was a plain weave Shield Strand S (9µm 360 TEX 1378 Y Glass Fabric) made by Owens Corning OCV Composite Reinforcements, Toledo, OH. To characterize the reinforcement at the meso- and micro-scale, composite laminates of the fabric were first produced. The matrix used was composed of a toughened commercial SC-15 thermosetting epoxy resin system produced by Applied Poleramic, Inc. (API), Benicia, CA. An 8-ply, plain weave preform was infused with the SC-15 resin in a vacuum assisted resin transfer molding process to a cured, final part, fiber volume fraction of 53%. No large variations were seen in volume fraction through the thickness of the composite part. The manufactured composite panel was cut into one inch square samples and cast into sample holders for optical microscopy. These composite samples were polished for 8 hours in a Struers Abramin Polishing Machine using four increasingly fine sandpaper grits (320, 600, 1200, and 4000 Wet or Dry Silicon Carbide) sold by Leco Corporation, St. Joseph, MI. Then, a final step polished the samples with 0.5 µm alumina for 17 hours in a Vibromet Polisher made by Buehler, Lake Buff, IL.

TABLE I: FIBER PREFORM PARAMETERS

Parameter	
Fabric Weave	0/90 Plain Weave
Fabric Areal Weight	832 g/m^2
Fabric Bulk Density	2.45 g/cm^3
Impregnated Tensile Strength	479-589 ksi
Impregnated Tensile Modulus	92 GPa
Warp Tow (0^0) Weight	394 g/m^2 +/- 5%
Weft Tow (90^0) Weight	437 g/m^2 +/- 5%
Nominal Filament Diameter	9 µm
Fiber Bulk Density	2.45 g/m^3

TABLE II: FIBER PREFORM MEASUREMENTS

Location	Measurements	Tow Width (mm)	Tow Height (mm)	Shape of Region	Yarn Gap (mm)
Warp Tow	321	4.214	0.4749	Ellipse	0.380
Weft Tow	384	4.255	0.4129	Ellipse	0.421

Location	Number of Measurements	Fiber Radius (mm)	Shape of Region
Inter-tow Weft	1675	4.5E-3	Circular
Inter-tow Warp	1675	4.5E-3	Circular

TABLE I shows the Owens Corning data for the plain weave used in this study.

TABLE II shows the measurements resulting from the image processing procedure implemented in Python and MATLAB. It is worth noting that the image processing procedure measured average fiber diameters nearly identical to the manufacturer’s nominal specifications. Furthermore, glass fibers seem to have a fair amount of variability in their diameter.

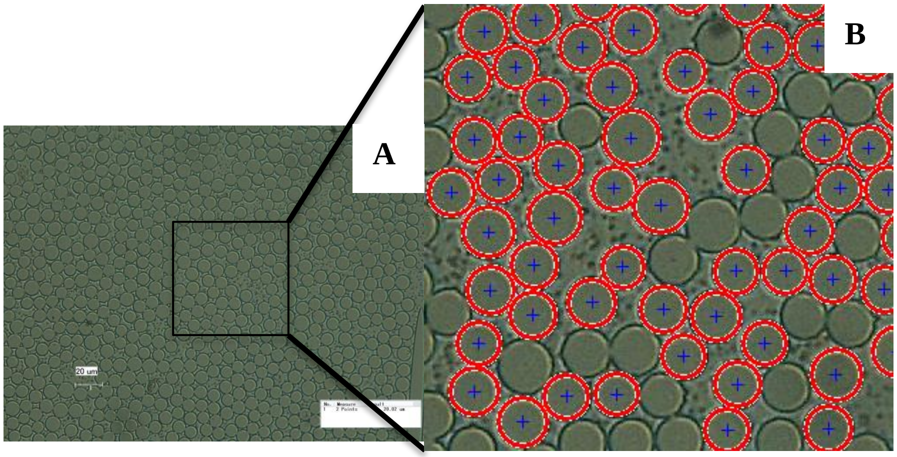

Figure 54: Optical Image Processing Procedure, A) optical micrograph digital output, B) image processing results

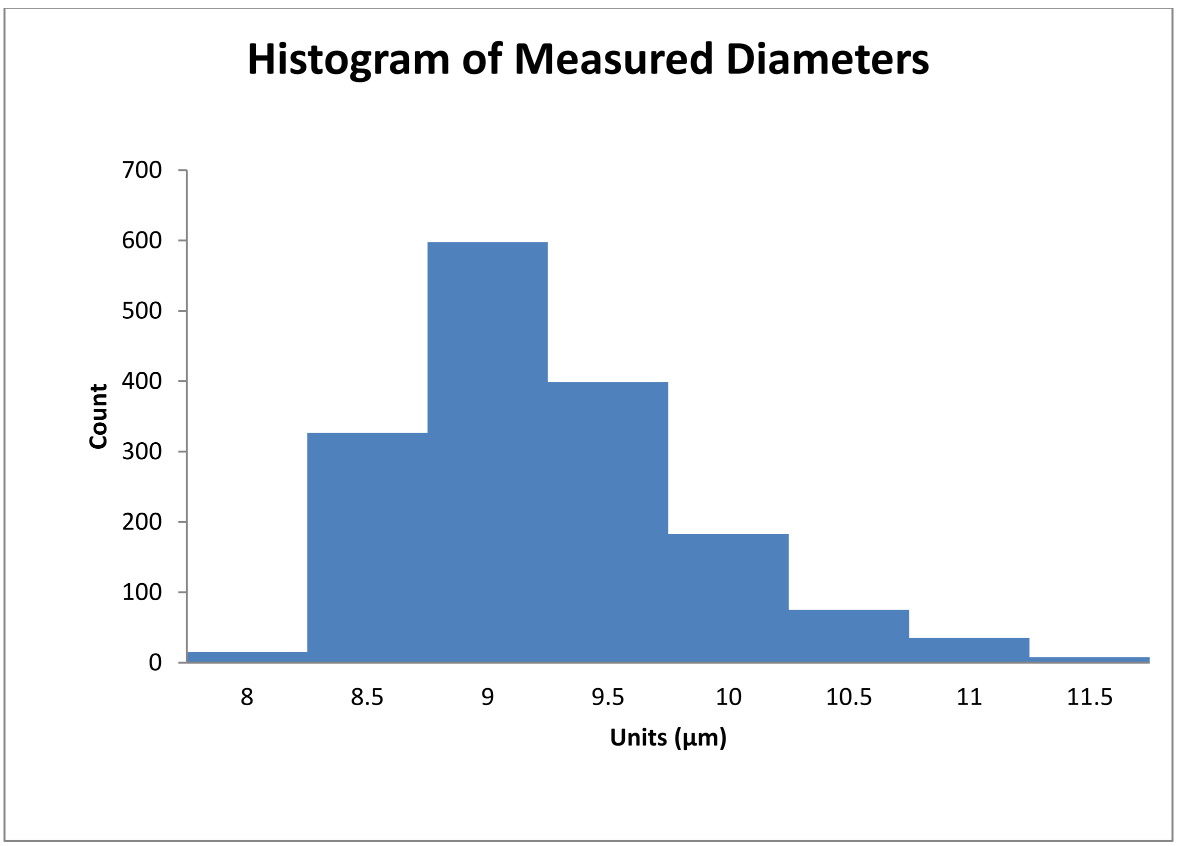

Figure 55: Histogram of Measured Diameters

Figure 54 is composed of two parts: image a) is a typical optical micrograph taken at 1000x and image b) is the results of an image processing code (written in-house using Python) that utilizes circular Hough transforms. Image b) highlights the fibers that are identified by the image processing code and marks their calculated centers to validate the output of the code. The image processing code was able to identify and measure about 78% of the fibers present in the cross-sections. Part of the incomplete detection of fibers was due to poor image contrast between the glass fibers and epoxy resin. The results of the image processing data provide the statistical variation of the fiber diameters. Manual input was needed to calculate the local fiber volume fractions and to attempt to quantify the statistical variation of the inter-tow region because of low image contrast. The average fiber diameter obtained here after 1,675 automatic measurements were 9µm in the warp and weft directions. Figure 55 gives a visual representation of the fiber distribution observed; the calculated standard deviation was 0.618.

7.4 Experimental Permeability Measurement

In-plane saturated permeability values for the Shield Strand S material were measured using a line-source to line-sink channel flow test fixture. A schematic of this fixture can be seen in *Figure 56*, where a constant flow rate injection is used to drive the flow. The fixture consists of a bottom cavity designed to accommodate performs 15.24 cm in width by 15.32 cm in length, and a testing frame–controlled compaction plunger that is guided down to close the cavity. The guided plunger allowed for user control of the perform thickness and was outfitted with two linear voltage differential transducers (LVDTs). A recess was machined on the plunger to accommodate for a rubber O-ring to seal fluid flow in the cavity. A screw-driven mechanical testing frame houses the fixture and controls the location of the plunger. Using a saturated permeability value removes the effects of surface tension and capillary effects seen in two-phase flow scenarios.

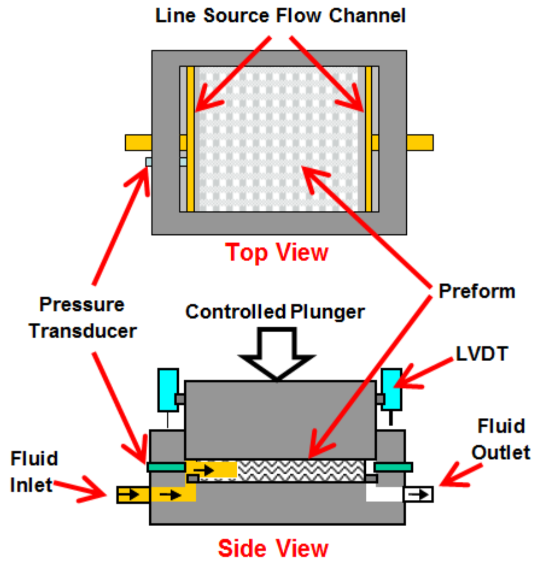

Figure 56: In-plane Saturated Permeability Fixture Schematic

The fiber volume fraction of the material was derived from the LVDT displacements using the definition of fiber volume fraction in Eq. 36, where V_f is the fiber volume fraction, n is the number of plies, A_w is the fiber areal weight, ρ_f is the fiber density, and t is the preform thickness.

$$V_f = \frac{nA_w}{\rho_f \ t} \tag{36}$$

The controlled plunger design of the fixture allows for in-plane permeability measurements to be obtained at multiple fiber volume fractions from a single preform. A Parker Zenith® Precision Gear Metering Pump was used to inject fluid at constant flow rates into the cavity, while transducers at the fixture inlet and outlet monitored the pressure drop across the perform induced from the fluid flow. The pressure drops were recorded at four constant flow rates (5, 7, 10, and 12 cubic centimeters per minute) for each desired fiber volume fraction measurement level. The steady-state, saturated permeability is governed by Darcy's Law [10] shown in Eq. 37, where Q is volumetric flow rate, S is preform permeability, μ is fluid viscosity, ΔP is the recorded pressure drop across the preform, A is the cross-sectional area normal to flow, and L is the preform length in the flow direction.

$$Q = \bar{\bar{S}}\frac{A}{\mu}\frac{\Delta P}{L} \tag{37}$$

The slope of the four constant flow rates vs. recorded pressure drop was found for each volume fraction level and is denoted m, so that in-plane permeability could be expressed by the modified form of Darcy's Law in Eq. 38.

$$\bar{\bar{S}} = \mu\, m\frac{L}{A} \tag{38}$$

The test fluid used was NAPA SAE 40 motor oil, possessing a viscosity of 0.24 Pa*s at room temperature. For preform preparation, four plies of the plain weave Shield Strand S were carefully cut to the width of the fixture cavity and stacked with the warp direction of each ply aligned. The permeability was measured in two directions. The S_{xx} permeability values were found by preparing preforms so that the fluid flow progressed along the warp direction, while flow along the weft direction produced S_{yy} values. Three tests were run in both the warp and weft fabric directions. Each preform was also tested at four different global fiber volume fractions: 45%, 50%, 55%, and 60%. The volume fractions on the global scale are different than the volume fractions on the intra-tow basis because of the dual-scale nature of the weave with large gaps where the fluid can preferentially flow. Average permeability at these fiber volume fractions was fit using a power law model for permeability seen in Eq. 39, which describes the permeability in terms of preform fiber volume fraction and model constants a and b. This approach allowed experimental Shield Strand S permeability to be estimated at any fiber volume fraction between 45% and 60%. Several other researchers [119], [191]–[195] have found an appropriate fit using a power law regression over a range of fiber reinforcements.

$$\bar{\bar{S}} = a\, {V_f}^{b} \tag{39}$$

7.5 Experimental Advancing Front Setup

Experimental advancing flow fronts were produced with an aluminum mold of fixed cavity depth featuring a clear Plexiglas® visualization window. Test fluid was injected at constant pressure by a regulated pressure pot in a line-source to line-sink flow profile. A pressure transducer was instrumented at the mold inlet. The mold cavity was designed to accommodate fabric preforms 15.13 cm in width by 17.11 cm in length, while the fixed cavity depth was 0.635 cm. The mold top was fitted with an O-ring to seal the fluid flow inside the mold, while 0.9525 cm diameter securing bolts firmly fastened the mold top over the cavity. Figure 57 displays a simple, exploded view of the advancing flow front fixture.

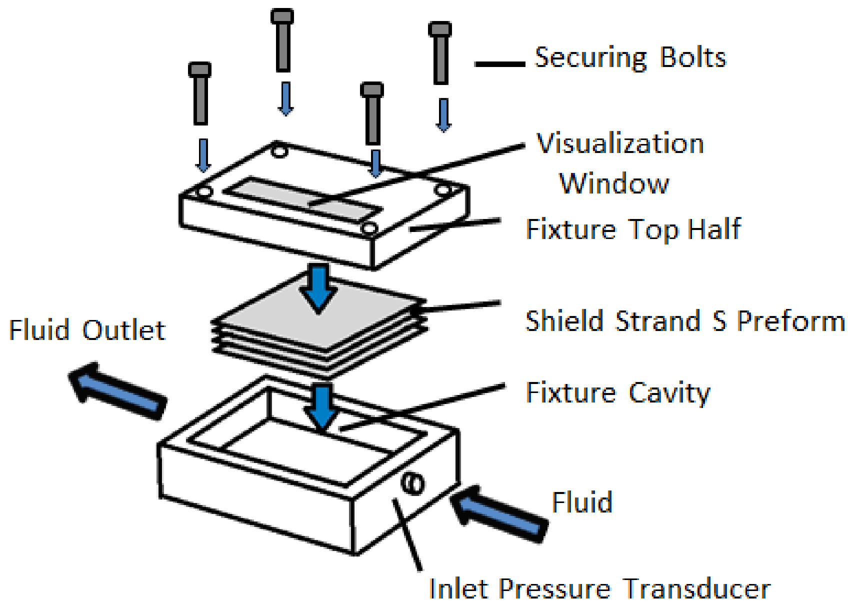

Figure 57: Exploded View Representation of the Linearly Injected Mold used for Experimental Flow Front Visualizations

Desired fabric volume fraction for tests was then obtained by the relation seen in Equation 1. For the tests conducted in this study, 10 plies of Owens Corning Shield Strand S plain weave fabric were cut to exact mold cavity dimensions and stacked with the warp direction of each ply aligned. This produced a Shield Strand S preform at 53.5% fiber volume fraction; NAPA SAE 40 motor oil was also used as the test fluid here. All measured flow front tests were conducted while infusing the preform along the fabric's warp direction. The visualization window allowed for top-view, flow front videos to be recorded while a fabric area 6 tows in width and 15.25 cm in length was captured. A target of 69 kPa (10 psi) was used for the constant inlet pressure injection level.

Infusion images were post-processed by tracing the experimental flow front to retain the uneven flow characteristics produced from the fabric's variable porosity. This was possible as the saturated Shield Strand S material took on a darker color as the oil permeated the tows and gaps between the weave. Also, this approach allowed for observation of areas that had lagging tow saturation, which has been cited as possible locations for void formation [50], [196]. These flow front images could then be used as comparisons to numerical results.

7.6 Fiber Preform Modeling

Nottingham University has created an open source project for an automated three-dimensional geometry textile modeler (TexGen) that takes geometrical parameters as inputs and can handle customized composites for a number of two-dimensional weaves, as well as three-dimensional orthogonal, angle interlock, offset angle interlock, and layer to layer weaves [103], [104], [189]. The software is based on a number of Python scripts and the width, height, spacing, and cross-sectional shape can be specified for each set of yarns or tows. The software generates the weave pattern by generating yarn paths based on nodes.

The desired weave pattern is specified in TexGen using automatically generated scripts. These scripts give a cross section that iterates between the tow height, requested compaction, and total height in order to achieve a realistic final geometry based on the user specified inputs. Zeng *et al*. [189] report that TexGen is capable of realistically modelling volume fractions up to 55%, while at higher levels of compaction, deviations between real geometry and the TexGen model occur.

In some cases, the tow geometries were modeled as solid to visualize the flow effects on the resulting infusion at very small time scales [16].

Finite volume pore scale simulations were obtained with an in-house numerical code for predicting the statistical variability in unidirectional fibers and input into the tow geometries as permeability. This allows for fiber variability to be included in the domain. The approach used a micro-scale simulation of an array of 1000 fibers to predict the intra-tow permeability in the same way meso-scale permeability is obtained. Five random packing simulations of unidirectional fibers were generated and the corresponding fluid permeability was calculated. Once the unidirectional permeability was known, it was used as inputs into the meso-scale unit cell tows for flows perpendicular and parallel to their orientations.

An algorithm by Desmond and Weeks [154] was adapted for the unidirectional fibers in this numerical study. Here, this algorithm is adapted to create random cylindrical geometries for numerical permeability experiments. In two dimensions, a mixture of disks is inserted into a 1x1 square dimensionless domain. Each configuration is implemented by building on the method by Xu *et al*. [155], Clarke and Wiley [156], and Desmond and Weeks [154]. At the beginning, a set of infinitesimal particles are placed in the system using the Mersenne Twister Algorithm to randomize the starting points. These points are gradually given volume and location by being expanded and moved. They are translated in two dimensions to prevent the overlapping of disks. When a final state is found where the disks can no longer be expanded without overlapping, this step of the packing process ends.

Dimensions are added by selecting a fiber radius and target volume fraction. The dimensions of all other parameters are driven by the dimensions of the nominal fiber radius. This fiber radius defines the fiber end area, which can be used to calculate the total area of fibers within a square. The total area of fibers is divided by the target volume fraction and this gives a new area of the square unit cell. The new area is used to drive the length of the fluid region that is solved for permeability. This square fluid length is also used to create the cubic volume in three dimensions. Before this step, the previous x-, y-, and z-coordinates were values from 0 to 1. After this step, the new x-, y-, and z-coordinates are generated by taking the cube length in any dimension and multiplying the dimensionless coordinates by that length. The new coordinates are saved as a text file and read automatically to generate a STEP geometry file. This section of the code creates an outer cube, the fluid volume, with a set of fibers approximated as randomly placed, perfect cylinders. The geometry is then solved for the fluid flow and permeability results [163].

7.7 Flow Modeling

The fluid used in the numerical simulation was modeled after the fluid used in the experimental permeability measurement (NAPA SAE 40 Motor Oil, Viscosity 0.24Pa*s, Density 709 kg/m^3). The macroscopic component level or bulk permeability can be predicted from the micro- and meso-scale permeabilities. The component level permeability is of interest because it models the impregnating resin in the most computationally efficient manner. However, this approach is limited in that it does not capture local deformations in architecture where a simulated part composed of a statistically varying geometry could.

The unit cell can be used as an input in a computational fluid dynamics solver that can handle porous media. In this case, the fluids solver is Fluent and a laminar flow model is used in conjunction with the boundary conditions. The intra-tow permeability is directionally input based on available results for flow parallel and perpendicular to the fibers. The Darcy flux is used in the porous zones to account for the fluid acceleration that take place due to the reduction in area inside the tows. The gaps between tows are modeled with the Navier-Stokes equations. The interface between the tow and matrix is modeled by assuming conservation of mass and momentum.

A velocity input is set and a pressure outlet is assumed to be atmospheric gage pressure. The pressure drop and in plane interstitial velocity based on the Darcy flux are calculated in the flow domain. The steady state laminar flow conditions are assumed to accurately represent the flow that takes place under experimental permeability measurements. Symmetric boundaries are applied on the boundaries of the representative volume element not prescribes as inlets or outlets for the fabric weave. A tetrahedral mesh is generated for the unit cell.

Macroscopic permeabilities were calculated in the warp and weft directions depending on the flow directions based on Darcy's Law in Equation 2 and the flow rate, pressure drop, and length in the simulation. The total flux of fluid is represented by Q, the permeability S, the area is A, the viscosity is μ, the change in pressure is ΔP, and L is the length parallel to the flow direction. For two-phase transient simulations, the volume of fluid (VOF) method simultaneously solves the momentum, continuity, and volume fraction transport equations. A single set of momentum equations is applied to all fluids and the volume fraction of each fluid in every computational cell is tracked throughout the domain [23]. The conservative forms of these equations are solved using a finite volume technique.

The model is composed of the continuity equation given by Eq. 40, where ρ is density, t is the time and V is the local velocity.

$$\frac{D\rho}{Dt} + \rho\nabla \cdot (\boldsymbol{V}) = 0 \tag{40}$$

The resin volume fraction is given by Eq. 41, where f is the volume fraction.

$$\frac{\partial f}{\partial t} + \nabla \cdot (f\boldsymbol{V}) = 0 \tag{41}$$

The momentum equation for each volume is given by Eq. 42, where τ_{ij} is the stress tensor, g is the gravity, and F is an external source vector where Darcy's Law is added as a momentum sink.

$$\frac{\rho D(\boldsymbol{V})}{Dt} = \nabla \cdot (\boldsymbol{\tau}) + \rho g + F \tag{42}$$

The Darcy flux is defines as the porosity times velocity as shown below (Eq. 43) where q is the Darcy flux, $\emptyset$ is the porosity, and $\boldsymbol{V}$ is the velocity

$$q = \emptyset * \boldsymbol{V} \tag{43}$$

In this model, simulated resin is injected into a three-dimensional mold where the geometry consists of a woven fabric. Two cases were studied based on a transient, advancing front infusion: one that looks at the global flow front with tows defined as impermeable solids, and one that attempts to look at the lagging tow saturation with porous tow bodies. Solid tows are modeled for verifying that the global flow front progresses much faster than the tow saturation in the experiment. The porous tows are modeled to investigate how long a tow takes to saturate after the global flow front has passed. The lagging tow saturation effect seen in woven fabrics is still expected to be present in numerical solutions under these conditions.

7.8 Results

Results of the flow modeling and experimental permeability measurements agree well at 53% fiber volume fraction for a woven Shield Strand S reinforcement. A mesh of 3.99 million elements was created and was shown to have good mesh independence in the solution results. Symmetric boundary conditions were applied along the weft and warp tows and along the top and bottom surface. The simulation results are plotted with the experimental measurements in Figure 58 and shows how permeability prediction fits measured data.

Shield Strand S permeability data were fit for the fiber volume fractions between 45% and 60% based on the power law model in Equation 4. The standard deviation of permeability over the fiber volume fraction range fit well with a power law model. Permeability results are displayed graphically in Figure 58, while power law model constants are seen in TABLE III including quality of fit. Figure 59 shows the numerical simulations and the corresponding experimental results. The error bars on the experiments are from three test replicates and the error bars on the numerical results are from three cases of varied meso-scale geometries near the average values for the same fiber volume fraction. The shield strand S material was measured to have permeability of 6.83E-11± 6.315E-12m^2 in the warp (S_{xx}) direction. The measurement in the weft (S_{yy}) was 5.26E-11 ± 1.108E-11 m^2. The model predicted a permeability of 6.31E-11 m^2 in the warp (S_{xx}) direction and 6.14E-11 m^2 in the weft (S_{yy}) direction. The error between the numerical and measured results in the warp direction was 7.97% and the error in the weft direction was 10.27%.

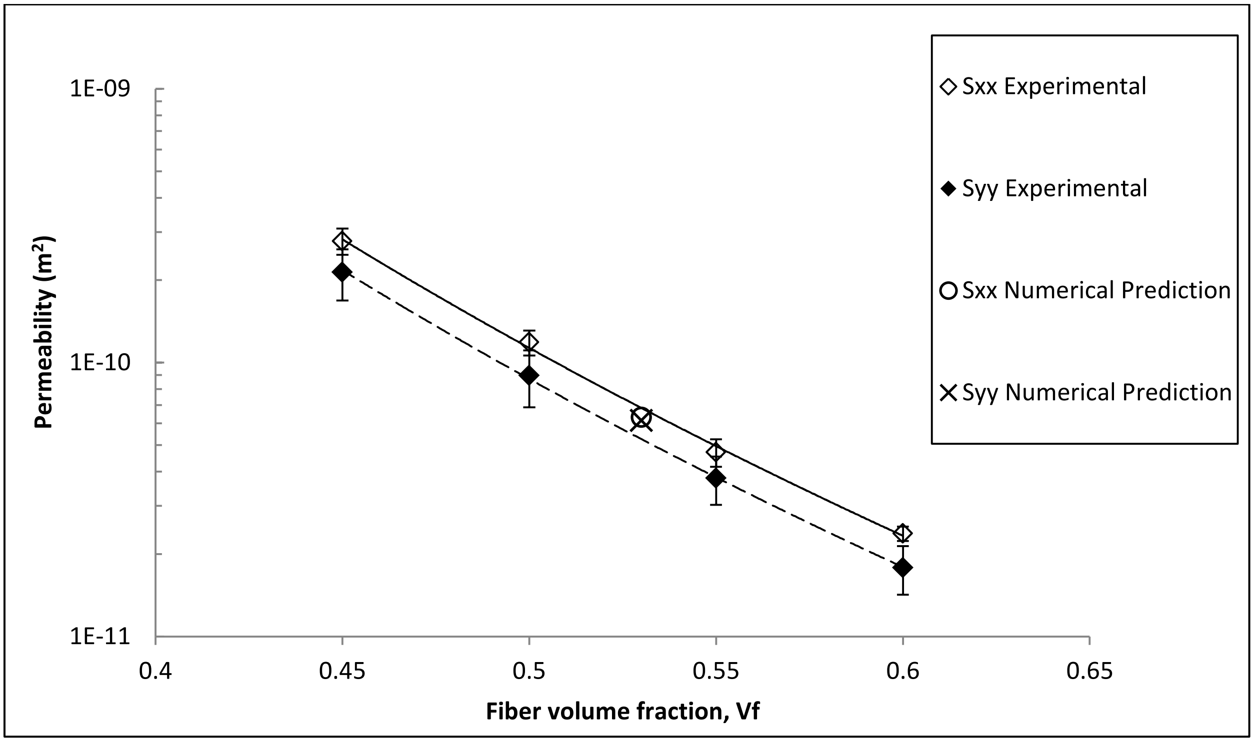

Figure 58: Shield Strand S In-plane Permeability vs. Fiber Volume Fraction, Numerical Results are Shown at 53% Fiber Volume Fraction

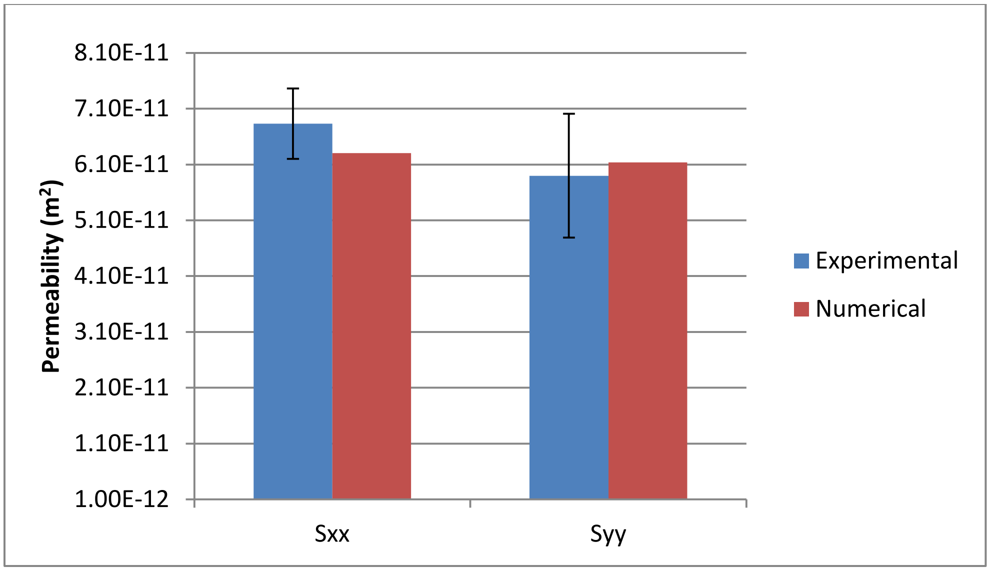

Figure 59: Experimental and Numerical Permeability at 53% Fiber Volume Fraction

TABLE III: POWER LAW MODELS FOR EXPERIMENTAL IN-PLANE PERMEABILITY

Permeability Component	a	b	R^2
S_{xx}	2.793E-13	-8.662	0.9984
S_{yy}	2.127E-13	-8.679	0.9997
Stdev S_{xx}	8.794E-15	-10.359	0.9788
Stdev S_{yy}	3.643E-14	-9.006	0.9949

The transient results investigated two types of cases. Fluent’s native VOF solver is incorporated in order to produce the transient results. First, numerical advancing flow front through a unit cell of Shield Strand S fabric and comparable experimental flow fronts are displayed in Figure 60.

This particular case has solid tows and only a consideration of the global resin flow front in the domain. Figure 60 (A) shows the advancement of fluid along the warp tows before the advancing flow front has made contact with any of the weft tows. Figure 60 (B) shows the advancement of fluid as the fluid preferentially takes the path of least resistance and flows between the tows. Figure 60 (C) captures the entrapment of air rich regions in the resin as the main flow front has past. These flow patterns can also be seen in the experimental infusion for a selected unit cell at progressing time steps.

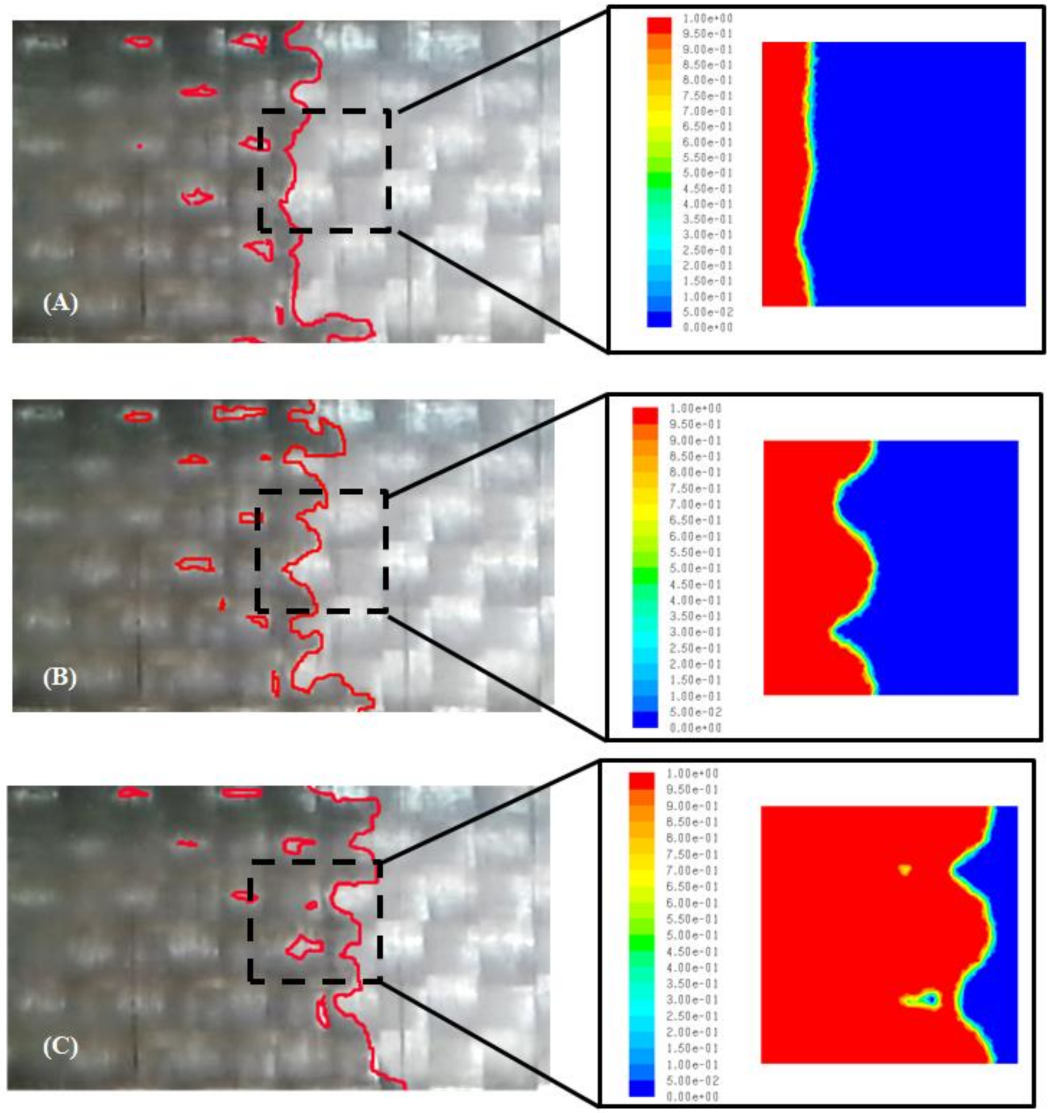

Figure 60: Numerical Advancing Flow Front Results for the Unit Cell of Shield Strand S. From left to right: Contours of Oil (red) Volume Fraction Displacing Air (blue) in the Porous Zones of the Fabric at Increasing Selected Time Steps from (A) Through (C)

An experimental and numerical fluid flow front at a region impregnating the plain weave Shield Strand S fabric clearly shows the fingering flow characteristics that can result in air entrapment. These are short time scales and are investigated with solid tows to see the flow front at a time when the resin is just beginning to flow past the fiber reinforcement. This significantly reduces the computation time and model complexity. Furthermore, three filling cases are often discussed in literature: one where the global flow passes, one where the tows begin to saturate, and one with full saturation [16].

The second case considers the lagging tow saturation and looks for complete saturation of the tows in relation to the saturation of the inter-tow region. Figure 61 and Figure 62 show the results from this set of cases with porous tows and lagging saturation. Computational requirements here are higher than case one and data intensive. Two unit cells are mated together in order to see more downstream effects in the flow domain. A total of two warp tows and four weft tows are modeled. In Figure 61 D), when the fluid domain looks fully saturated, the net average saturation is only about 60%. Additionally, sliced domains can be easily produced to visualize the partially saturating tows.

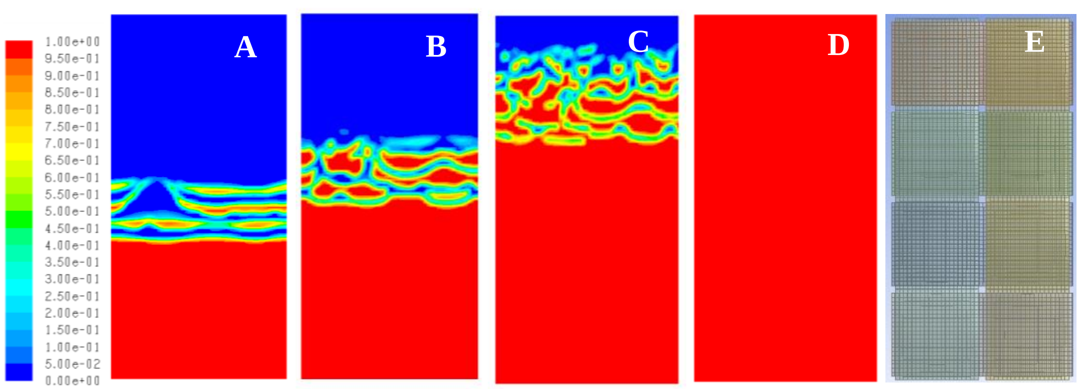

Figure 61: Plot of Global Flow Front with Transient Porous Tow Simulations with Corresponding Time Steps, Resin in Red, Displaced Air in Blue. Pressure Inlet is 275.3 kPa and Pressure Outlet is 246.1 kPa A) 2.78e-3s B) 4.78e-3s C) 9.78e-3s D) 2.33e-2s E) Comparable TexGen Geometry Model

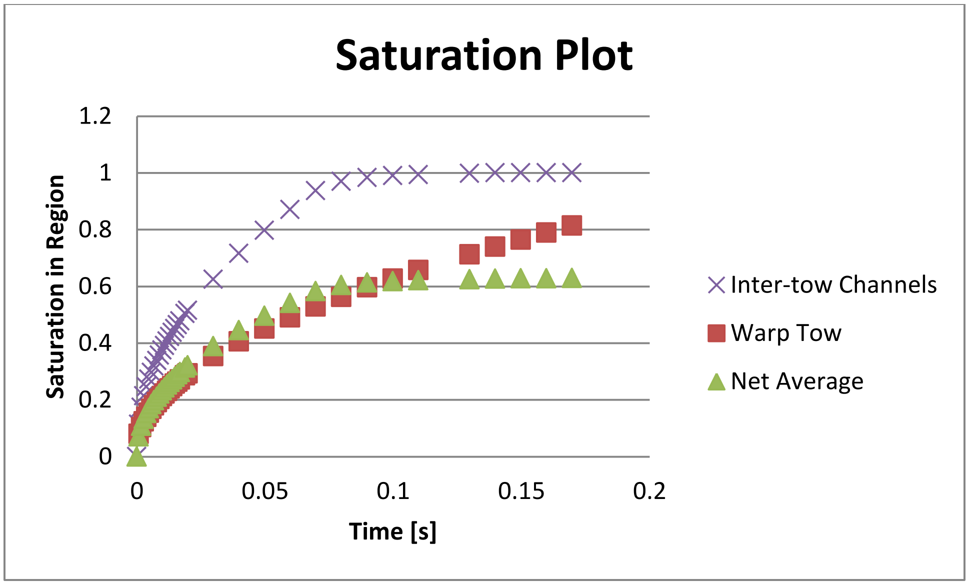

Figure 62: Plot of Saturation by Region and Time

Figure 62 shows how the inter-tow spacing saturates rapidly because there is very little resistance to flow. The warp tows are saturating next because the inlet conditions are such that flow is in the same direction as the warp direction. This allows the flow through the warp tows to be governed by parallel permeability which is much higher than perpendicular permeability. Weft tows are saturating so slowly because the yarns are purely showing transverse permeability in relation to the flow direction and this is lower than the parallel permeability. There are no boundary conditions which are forcing flow into them and this allows the bulk of the fluid volume to flow around them. This saturation case would be different based on the flow scenario. For example, a radial infusion is going to saturate differently than this in-line flow case. Further model development is needed on these transient models in order to increase the computational efficiency and characterize points of interest. The fully coupled Navier-Stokes equations are time consuming to run and produce large case files. For this reason transient simulations are often solved with a simplified form of Darcy's Law accounting for time dependence. This simulation was stopped once the warp saturation reached 80% due to computation time and data storage requirements. Figure 63 shows a reference figure for the Shield Strand S fabric used in this study with the scale bar in millimeters.

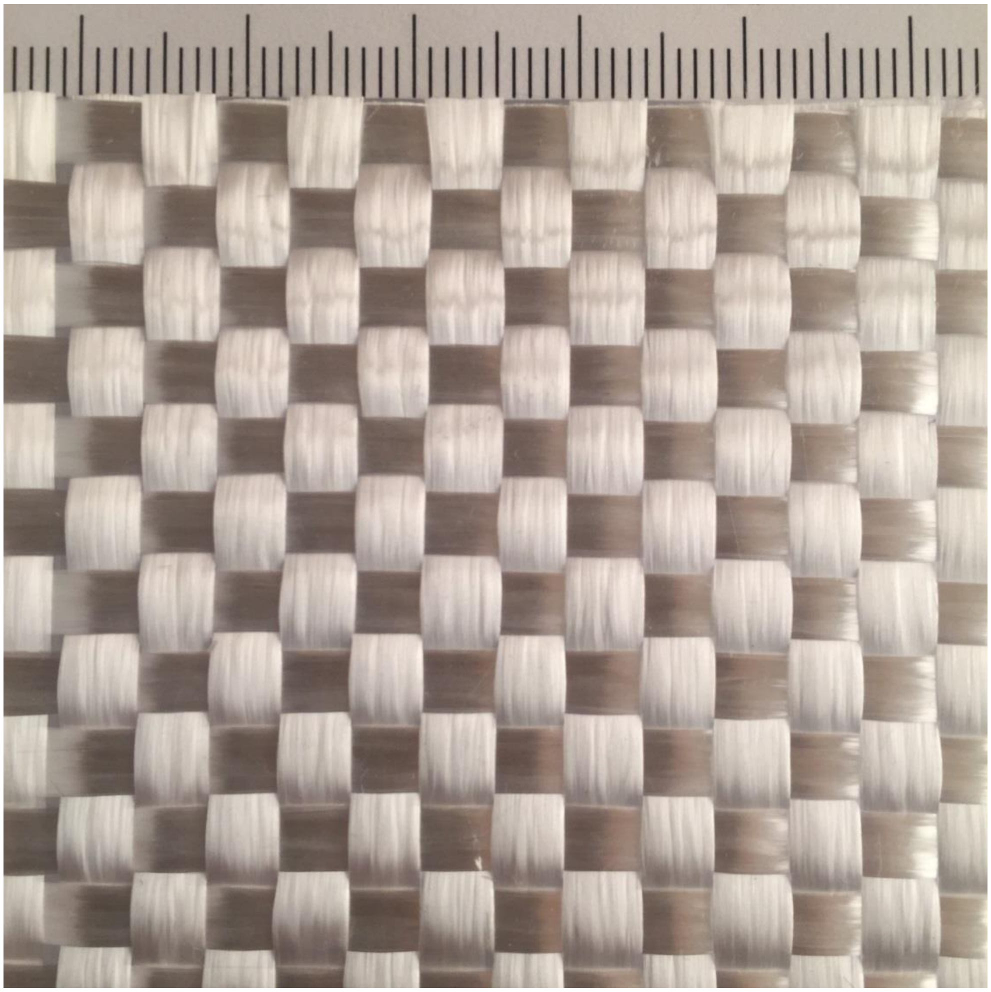

Figure 63: Reference figure of the Shield Strand S Fiberglass Fabric. The Scale Bar at the Top is in Millimeters.

7.9 Discussion

The results presented show a rapid and robust method to quickly quantify and visualize the types of flow expected on the meso-scale during a mold infusion. Figure 54 showed how optical micrographs can be measured digitally using computer software to reduce the time consuming process of hand measurement and create a large, statistically relevant database of measurements for unidirectional tow inputs. The specific mathematical tool implemented was circular Hough transforms after thresholding the images. This process is important for the production of intra-tow permeability values for analytical results. TABLE III and Figure 58 provide a realistic baseline for permeability that can be used to compare numerical predictions. The results in Figure 59 indicate that there is a reasonable agreement between the experimental trend and computational fluid dynamics simulation based on the knowledge of the variability seen in experimental measurements of permeability. The differences in the measured and predicted permeabilities compare well and within the 10-20% experimental variation. This agreement was conducted at a fiber volume fraction of 53%, which is close to reported levels where geometrical deviations from TexGen are expected to occur [189]. In the experimental results, effects such as fiber nesting / inter-layer interactions and edge effects are present, whereas the numerical simulation neglects these effects. It can be a benefit to accurately numerically predict permeability while being able to control for edge effects, nesting, and shear which often populate an experiment unintentionally. The ability to produce accurate geometric data allows us to model permeability using common tools that give reasonable numerical permeability values. These results can be used in conjunction with experimentation, or can be predictive by themselves.

Although, faster characterization tools like computed tomography are necessary if an entire fabric system is to be investigated across volume fraction.

As seen in the experimental flow front, the fiber architecture of the plain weave Shield Strand S produces regions of unsaturated fabric behind the global flow front. Depending on the location of these air rich regions and the total infusion time, these could become initial sites for void formation. Regions with lagging air pockets will need extra time to saturate after the global flow front has passed. Without proper treatment during an infusion, these will become initial locations of micro-void formation within the fiber tows or macro-void formation on the component level [50]. By selecting characteristic points, the approximate infusion time for a unit cell can be found and used to design a mold fill infusion time. As global flow fronts progress, the lagging tow saturation cannot be rapidly visualized or found without simulation tools. Since there is a desire to reduce any void inclusions in a finished composite part, simulation tools are necessary to understand what is happening inside a closed mold.

It should be noted that a race-tracking effect was observed in the experimental results as present in the bottom edges of A B and C in Figure 60. This was due to a loss of edge tows during preform preparation and placement, which created the preferential flow path and faster propagation seen in that area. This was visible because the bottom edge of the visualization window was close to the edge of the preform. These effects were not accommodated for in the numerical model.

Obtaining realistic flow front solutions using a numerical method with tow regions designated as solid bodies (modeling the only the macro-pores) can reduce computation time compared to numerical models using variable porosity parameters, while still displaying lagging tow saturation characteristics on very small time scales. Accurately defining fiber packing arrangements and fiber diameters also increases the time of the preform characterization step of the modeling process, which was bypassed in solid-body tow method.

One potential use of this kind of simulation is employing numerical results to predict if the mold infusion is stopped short of a complete fill. Further, void spaces created by residual air in the preform can migrate through the preform, and air bubble transport should dictate one aspect of final void location. Air entrapment will generally take on a spherical shape in a finished composite when the outside forces are removed as the surface of the bubble will try to minimize its surface energy. This happens once the flow driving forces are removed. If the resin is sufficiently cured when the driving forces are removed, then the flow forces can create shapes that are lenticular or tear dropped as the entrapped air is transported to the flow front [50].

The numerical method implemented here does not include nesting effects or local fabric deformations, which can contribute to flow front differences in more complex molds. In future work, these effects may be accommodated most effectively by statistical averaging techniques. The viewed region was selected at the top because this is an easily visualized area that also displays some edge effects that are often of importance in mold filling scenarios. An added benefit of a numerical solution is that the interior flow propagation can be visualized in a way that is not experimentally approachable. It is also important to note that steady-state tow permeabilities were used for transient simulations. Justifications for this have been made since commonly, steady-state measurements are used for transient mold fill simulations. Measured transient permeabilities are generally lower but trend towards the saturated permeability results as they become saturated. The transient permeability is generally lower because of incomplete saturation at the flow front, which locally changes the apparent porosity.

7.10 Conclusion

The use of geometrical modelling tools, coupled with computational fluid dynamics, can be used to reasonably predict the meso-scale permeability of composite fiber preforms. The motivation for this approach is to be able to quickly characterize composite preforms at various volume fractions without needing to conduct numerous experiments with specialized equipment, which is subject to variations in design and testing procedures. The research presented here demonstrates a clear connection between geometry and permeability that can be taken advantage of for computational simulations. This approach could also minimize the influence of human error, which has been shown to account for some experimental variation in results. The most time consuming portion of this process is the measurement of input parameters, but this can be automated with the use of image processing tools. In the future, local tow geometrical variations could be taken advantage of to create a statistical average of permeability as a function of volume fraction coupled between intra-tow and inter-tow variations, creating a more robust model.

Using CFD modeling, the prediction of a transient simulation could be used to indicate locations where voids and defects may form in a component level infusion. This defect location would be useful in closed mold processes where the flow front is not visible. Numerical tools are also able to define the type of flow front expected through the component level part. This understanding should allow various flow rates, pressures, and boundary conditions to be applied to minimize potential defects, which can result from an unfavorable flow front. More development is needed to investigate this feasibility. In the future, numerical results can be run first to target experimental validation at the pressures and flow rates of interest because of the ability to quickly generate large numbers of numerical results in comparison to the time and equipment needed for one laboratory experiment. Further, this method could be used to predict a numerical advancing flow front permeability to compliment experimentally measured values.

7.11 Acknowledgements

This work is sponsored by General Electric Aviation, Cincinnati, OH.

TexGen is open source software licensed under the General Public License developed at the University of Nottingham for modelling the geometry of textile structures.

Computational work in support of this research was performed at Michigan State University's High Performance Computing Center.

8. CONTRIBUTIONS AND FUTURE WORK

8.1 Contributions

This dissertation work was conducted at the Composite Vehicle Research Center in Lansing, Michigan with industry funding from General Electric Aviation in Cincinnati, Ohio. The goal of the research was to address the fundamental physical understanding of resin flow in composite manufacturing through the processing variable, permeability. Toward this end, the work presented and the conclusions derived have led to several contributions in the field of composites processing and permeability characterization. A multi-dimensional flow analysis isolating the micro-scale, meso-scale, and component level scales has been produced. The characterization of fiber preforms has been conducted to numerically simulate permeability on the micro-scale and meso-scale. Additionally, the meso-scale permeability can be extended to the component level simulations based on Darcy's Law in a direct manner.

First, a new method for analyzing micro-scale composite permeability has been developed and the effects of variation on this scale have been investigated. The simulated microstructure can be controlled and the effects of random fiber packing are now better understood. This micro-scale simulation approach can be a useful component in multi-scale analysis of composite permeability as well as be adopted for micro-mechanics simulations in the future. The direct numerical simulation approach allows for more understanding and control over the processing variables that often propagate through an experimental measurement in an undetected and often uncontrollable way.

Second, a stronger understanding of modeling meso-scale textile preforms and the resulting flows has been built. The ability to obtain accurately predicted permeability data for meso- and macro-scale component processing is a useful technical contribution. Furthermore, discovering validated flow behavior in closed molds allows for the modeling and simulation of closed mold processes.

The effect of dual-scale porous media has been quantified for the difference between micro-scale and meso-scale permeability. A fluids based simulation of the Resin Transfer Molding process for the fabrication of fiber composites has been outlined. Additionally, research on the effect of fixed particles on flow properties has shown a good first step for future work where transient models can be built to track the effects of moving and interacting particles.

Leading up to this, an investigation of commercially available software packages that can simulate liquid molding infusion flow and consolidation processes was conducted. Each software tool was evaluated based on its ability to handle a number of simulation scenarios including: 1) multi-dimensional (two-dimensional and three-dimensional) flow analyses, 2) macroscopic flow simulations based on a Darcy's Law approach, 3) incorporation of preform compaction, either internally within the code or through user-defined subprograms, 4) the ability to handle non-isothermal analysis, and 5) microscopic flow analyses to simulate the impact of toughening agents and nanoparticles on resin infiltration. The main section of this research focused on the fundamental ability to characterize baseline advanced textile architecture preforms to obtain data for use in liquid molding simulations.

8.2 Future Work

Since good research often creates as many or more questions as it answers, the results presented in this dissertation provide several opportunities for future work and further study. The effect of multi-scale coupled or concurrent simulations could be studied. This would ideally iterate local deformation and changes in geometry on the micro-scale and simulate their effects as they propagate though to the meso-scale. Coupled simulations could look at specific points of interest in a mold, for example, resin injection ports, pressure outlets, mold walls, and locations of high fabric shear. This would help to isolate and clearly understand those fundamental effects on processing parameters like permeability. The effects of the micro-, meso-, and macro-scale changes are all coupled together in actual manufacturing cases, so being able to dynamically simulate the influence of one scale on the other would greatly expand understanding of the combined effect on part quality and manufacturing. Even creating generalized processing maps for parts manufactured under a certain set of conditions would be a large step.

In micro- and meso-scale flows, the effect of off-axis, 45 degree, or misaligned fiber angles in a flow field would be a useful extension of this micro-scale and meso-scale modeling approach. This would help to further the modeling tools above and beyond current transverse and parallel permeability models. These features may impact local pressure gradients and produce results that are unique from the simulated effects shown in this dissertation.

Transient micro-particle flows could be simulated and process models could be created to account for particle inclusions. Particle agglomeration and particle interactions on permeability in the mold could be more fully investigated. Finding a design threshold where the particles are small enough, while incorporating surface energies that allow for them to be well distributed in the fiber preform without considering filtration or particle gradient effects would be useful. This would involve the utilization of available tools to simulate the effects of toughening agents on the resin and fiber preform.

Further models looking at the transient saturation models could be applied to look at the variation of micro-scale and meso-scale saturation as boundary conditions are modified. These models are time consuming but as computational resources continue to grow this should be easier to study. Future studies could include model verification studies or the numerical repetition of experimental results from prior literature. Specific studies could include flow visualization studies and instrumented tool studies to obtain pressure and thickness measurements. Flow visualization could also be completed for large scale production parts that are currently designed though practice of the art as opposed to simulation. A prediction of resin flow characteristics and fill time are useful in design.

The modeling of melt processing of comingled fibers would be an interesting investigation that could take the micro-scale geometry generation tool and input a temperature and time dependent viscosity for the fiber reinforcement before a secondary infusion. The tools developed should allow modeling of high temperature melt processing composites. A range of non-isothermal conditions are of interest in a heated mold and these parameters all warrant further study.
In an application away from fluid based process models, micro-mechanical models could build upon the geometry generation tool to investigate the fiber and matrix interface. The addition of a

module that investigates the interface mechanics as well as the processing permeability would be useful in composite design. This would allow for simulations of processing as well as the final part behavior.

APPENDICES

Appendix A: COMMANDS AND PROCEDURE FOR RUNNING A FLUENT MODEL

A.I Fluent Model for Composite Processing Set Up Through GUI

Setting up job through the GUI is appropriate for simple cases and cases that will only be run once but it is recommended that the TUI commands are learned if many jobs will be set up. Below is an example of the GUI commands to set up a model and corresponding comments to define what each line item is. Any unanswered questions can be answered by the FLUENT documentation or on “www.cfd-online.com”.

Prior to setting up a model in FLUENT the geometry has to be created in the geometry or CAD tool of choice. Second, the geometry has to be meshed and the appropriate boundary conditions defined before the model is input into FLUENT.

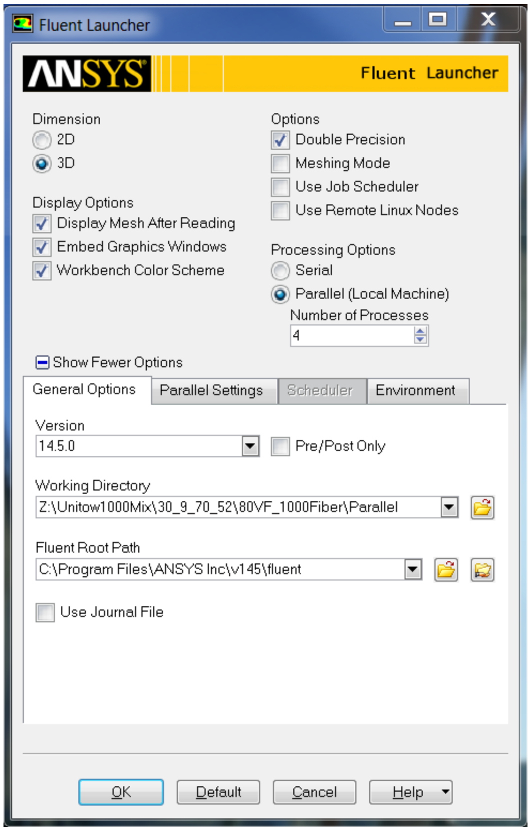

Figure 64: Fluent Launcher

The FLUENT launcher is used to setup the dimensions of the problem, either two-dimensional or three-dimensional. The precision of the problem is set, the number of processors, and the working directory. From this screen a journal file can also be read directly.

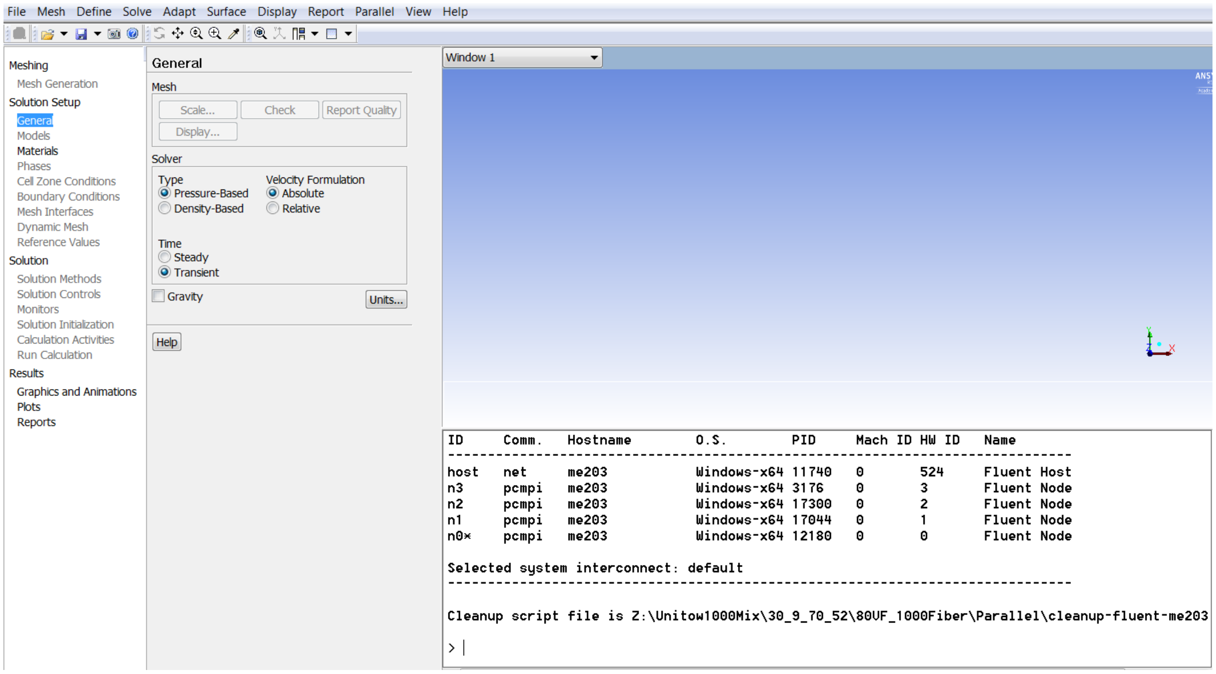

Figure 65: Home Screen

The home screen looks like this where you can immediately input text user interface or TUI commands next to the “>” in the white space at the bottom of the screen.

The first step is to load the mesh by going to file>>read>>mesh>>”_.msh”

A case file can be read in the same manner. It is always to get the mesh statistics and check your mesh for any quality issues. The solver will be set to Transient and a pressure-based solver.

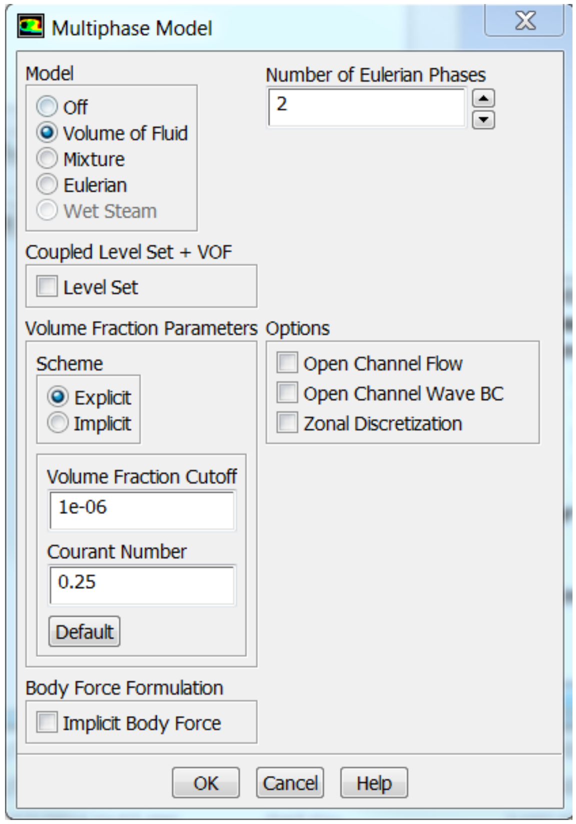

Figure 66: Multiphase Model

The multiphase model used here will be the VOF model. This stands for the volume of fluid model. You will define 2 phases.

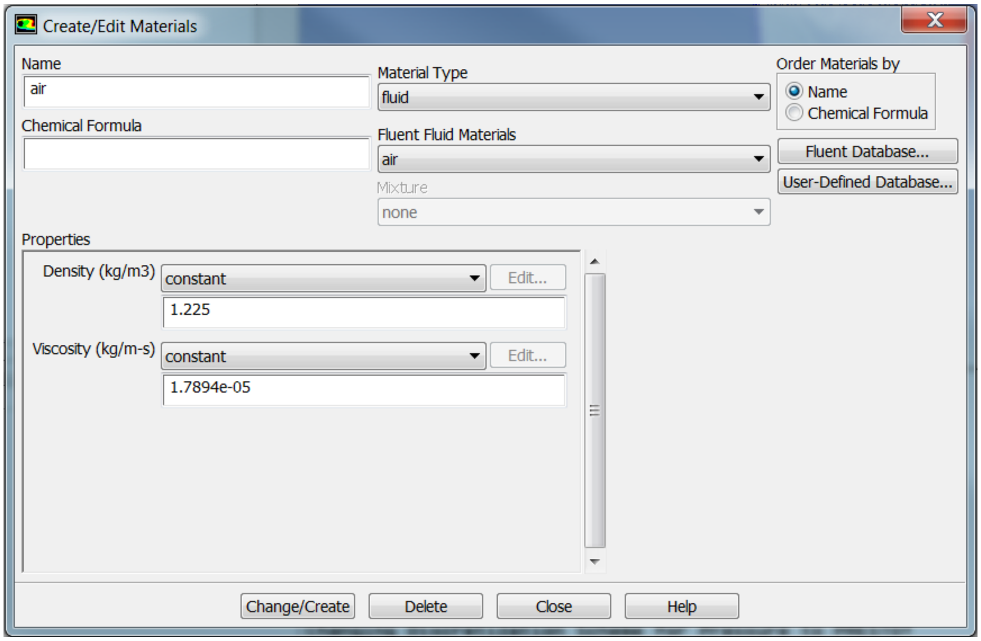

Figure 67: Create/Edit Materials

A second material will be added by modifying air or by importing a material from the fluent database. A good name for the material is "resin" and a reasonable density and viscosity are 709 kg/m3 and 0.24 kg/m-s respectively. If you change or import the material, do not overwrite air.

A second approach is to copy a fluid from the FLUENT database. For example the fluid engine-oil can be copied and modified to the appropriate viscosity and density that you desire. Furthermore, if a heated simulation is being conducted then a power law or polymer can be input as a function of how viscosity changes with temperature for the rheology of the fluid.

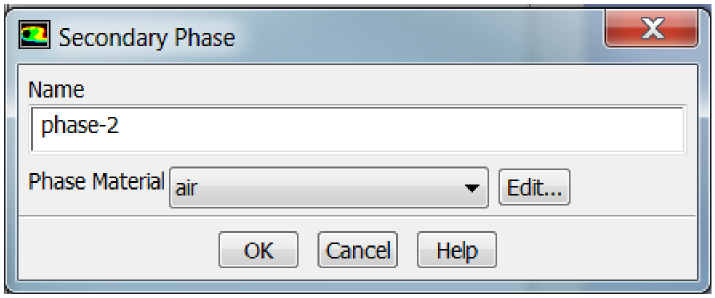

Figure 68: Phase Selection Dialogue

Use the phase selection box by going to phases >> phase-1 >> edit. Define phase-1 as air and rename it air. Define phase-2 as resin and define it resin.

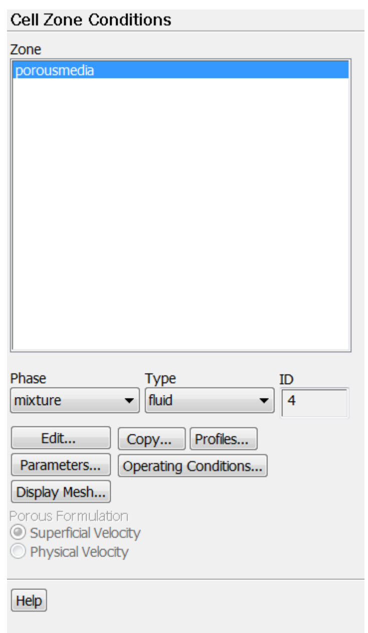

Figure 69: Cell Zone Conditions

The cell zone conditions must be set for the mixture, phase-1, and phase-2. All cell zones should be defined as fluid. Select your porous zone in the zone window and choose phase mixture. Then select edit and check the porous zone box. Next choose the porous zone tab and define the fluid porosity. A good porosity for an example is 0.50. Additionally, for pressure inlets where the velocity of the resin will be decreasing throughout the porous media the physical velocity formulation is recommended.

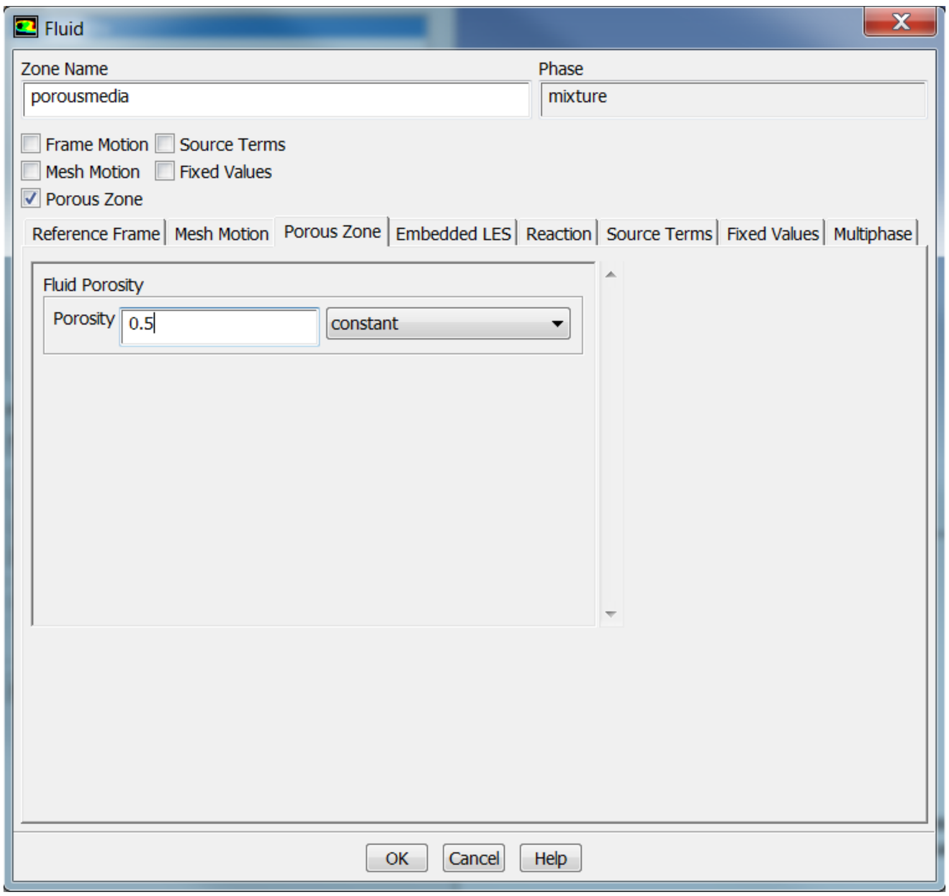

Figure 70: Fluid Porous Cell Zone Conditions

Next, select the phase for air or phase-1 and select edit.

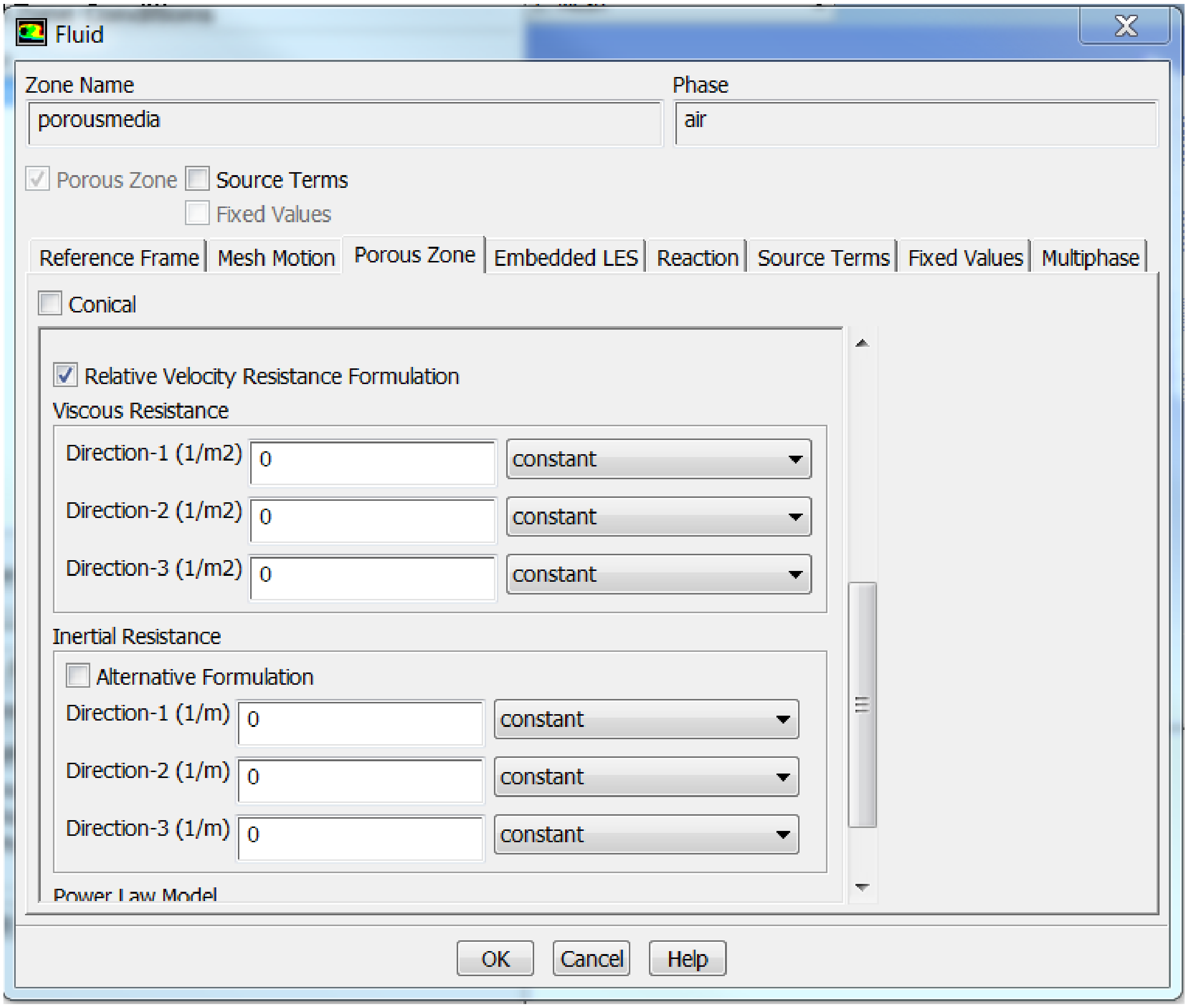

Figure 71: Porous Media for Air

Define the boundary conditions for the fluid in your porous media defined as phase-1 or air. Input the viscous resistance, which is one over the permeability. An example input for direction 1-3 would be 8.44e9, 1.08e10, and 1.46e12 respectively. If the porous media does not have a linear relationship between flow rate and pressure drop than the inertial resistance can also be added. Input the volume fraction here, an example is 0.50.

The same procedure is done for the phase-2 or resin region of your porous media. Define the boundary conditions of your fluid in the porous media as resin. The same viscous resistance coefficients from the previous phase can be used and are unlikely to be different for a different fluid.

In the boundary conditions menu you will have an interior zone, a pressure or velocity inlet, and a pressure or velocity outlet. Additionally, you will have walls that can be treated as no slip boundary conditions. Select the appropriate boundary condition parameters for each zone and each phase.

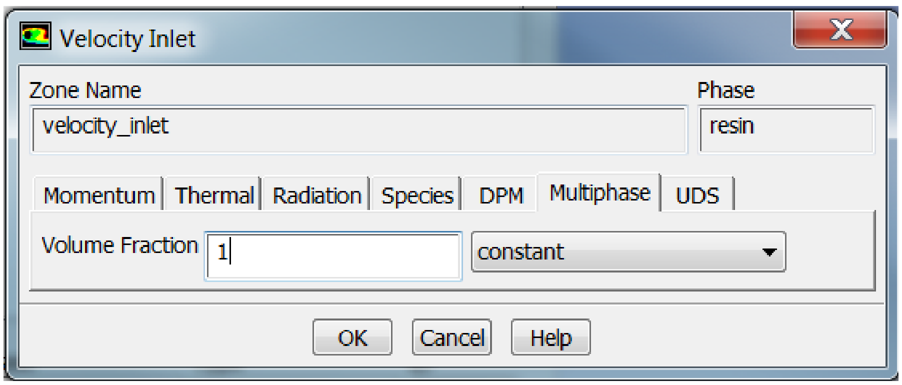

Figure 72: Velocity Inlet Volume Fraction

For your inlet condition, it is important to define the multiphase resin inlet. Here it is set at 1, which means that all of the fluid entering the solution through the velocity inlet boundary condition is resin. This displaces the air that we define in the porous zone later. Some example boundary conditions here are shown next. Define boundary conditions for the pressure outlet as a pressure outlet for the mixture as atmospheric. Define the boundary conditions for the velocity inlet of the mixture as 0.005 m/s. Define the boundary conditions of the walls as no slip. Again remember that it is important to define the velocity inlet of the resin as a volume fraction of one.

It is now time to configure the solver. For most cases, the SIMPLE solver will work well with a pressure based model. This may have to be modified as the model and physics changes.

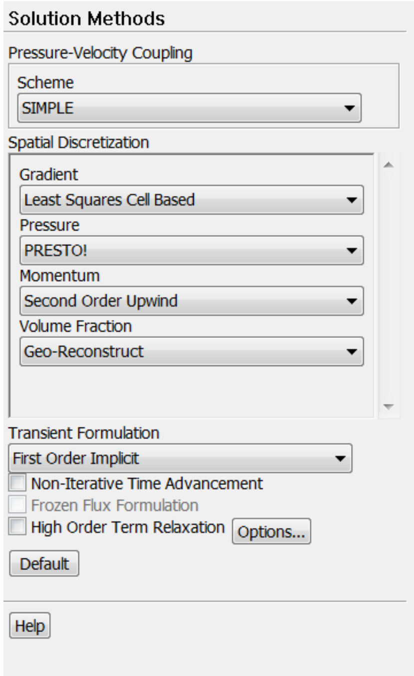

Figure 73: Solution Methods

Standard under relaxation factors are fine to start with and judgement has to be used if they should be modified. Monitoring residuals is recommended and confirming they are converging is important.

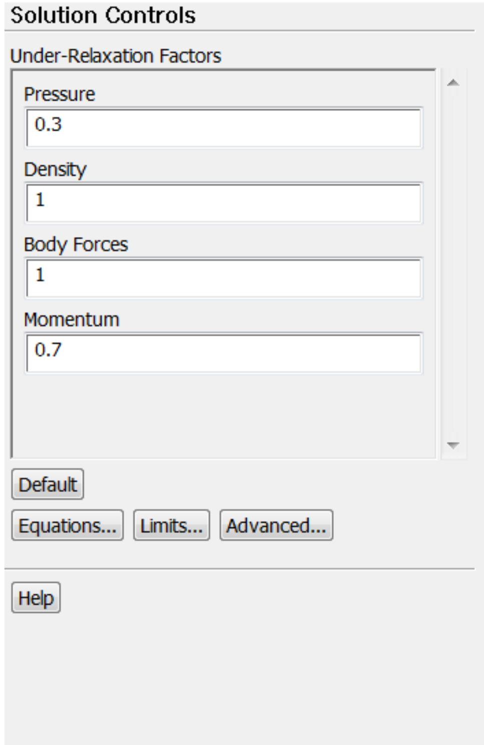

Figure 74: Solution Controls

The under relaxation factors are set from the solution controls window. An example set of parameters is: under-relaxation pressure 0.3, under-relaxation density 1, under-relaxation body-force 1, under-relaxation mom 0.7, and under-relaxation temperature 1.

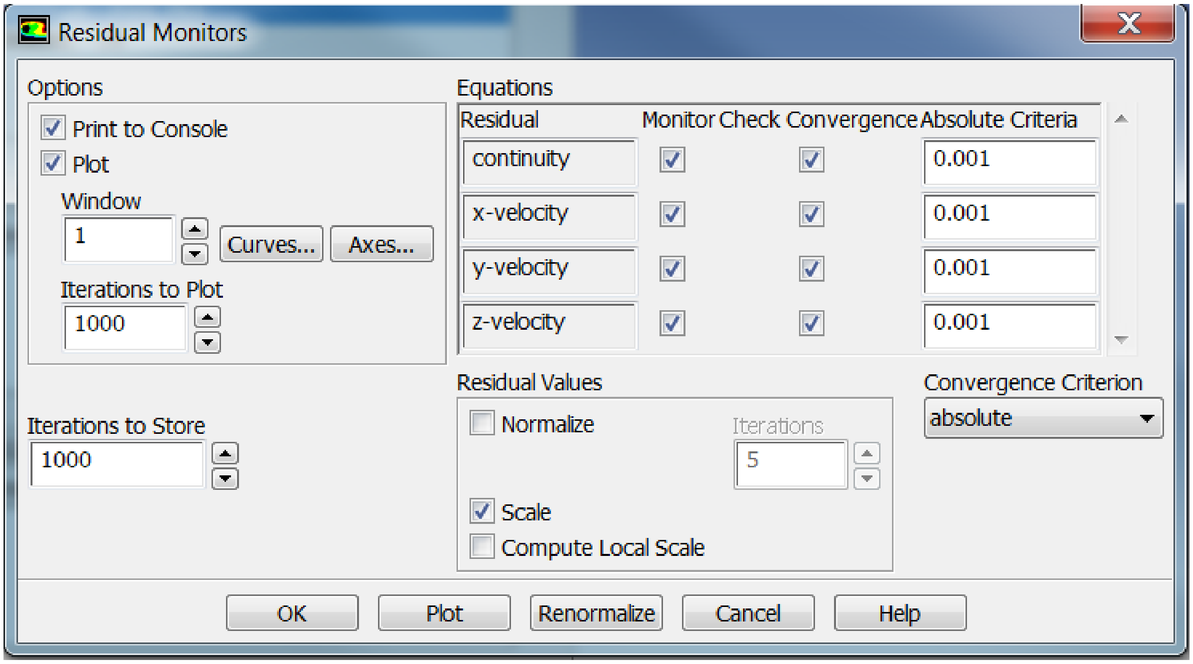

Figure 75: Residual Monitors

The default residual monitors are fine to start with and they can be modified as needed if the solution is not computing correctly. Other monitors can be created, for example, a surface monitor can be created by selecting create >> "Integral" >> resin pressure_outlet. The name and surface can be anything of interest. Additionally, a volume monitor can be created to track the saturation of your porous zones with time.

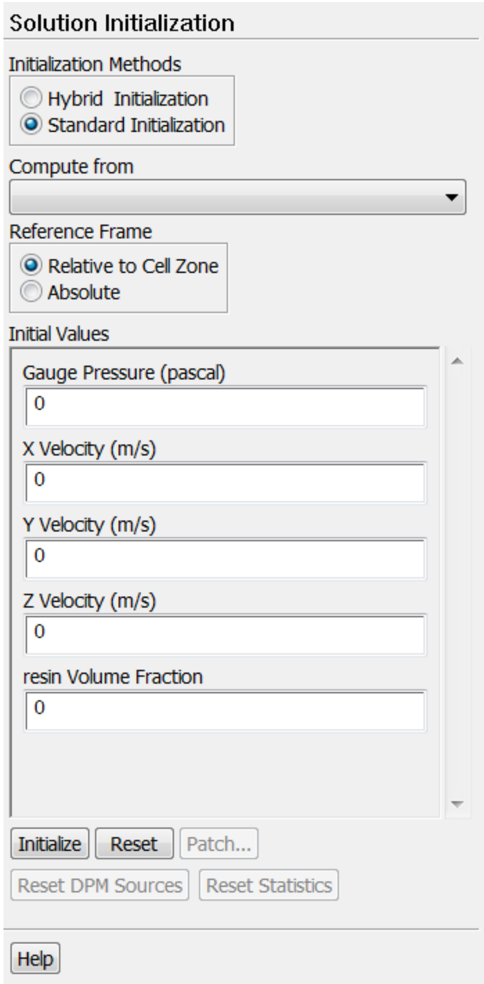

Figure 76: Solution Initialization

The solution can be initialized to specific values or it can be set to the default values. Default values are as follows: pressure 0, x-velocity 0, y-velocity 0, z-velocity 0, temperature 300, and resin volume fraction 0. The next step is to select initialize. Once the solver is initialized you have to patch your porous zones.

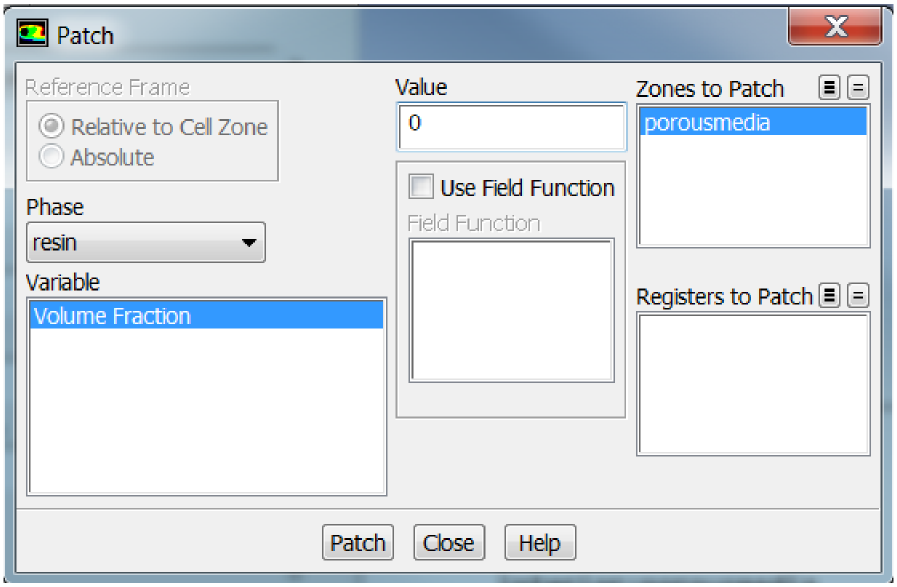

Figure 77: Patch Porous Zones

Porous zones are patched by selecting >> Patch…>> resin >> Volume Fraction >> porous media >> and entering the value for that zone. What you are doing is saying that at time zero, the value of resin in your computational domain is 0. This defaults the entire area to the other phase which is air for this setup. Then as your solution progresses the air is displaced by the resin.

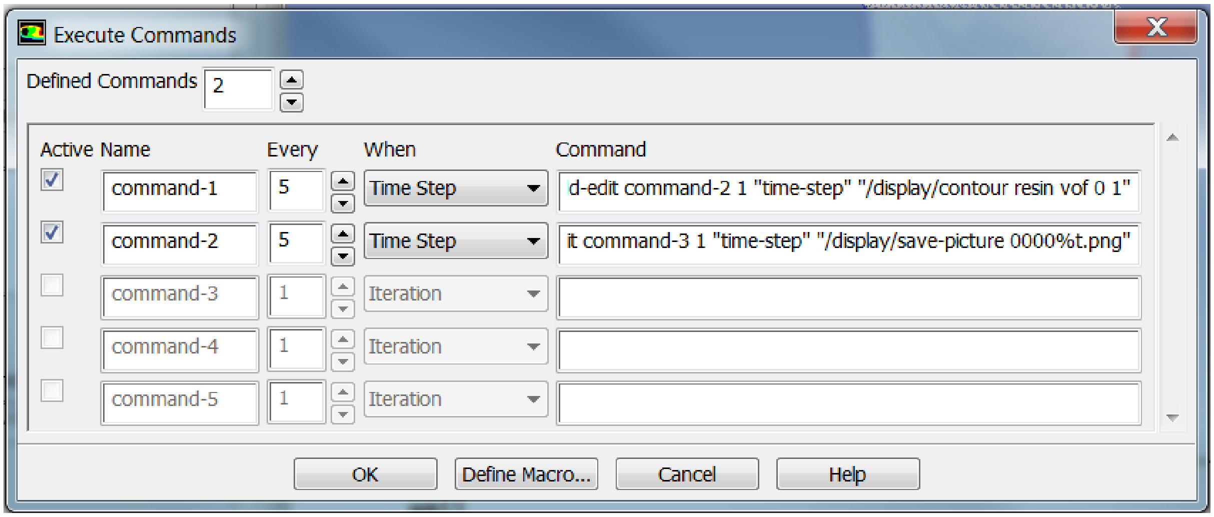

Figure 78: Execute Commands for Image Taking or Other Operations

Two commands are necessary to save images in each time step as your solution progresses without stopping the simulation at points of interest. They are as follows:

solve execute-commands add-edit command-2 1 "time-step" "/display/contour resin vof 0 1"

solve execute-commands add-edit command-3 1 "time-step" "/display/save-picture 0000%t.png"

Additional commands can be defines as needed and the reader is referred to the FLUENT documentation for any specific commands they may want.

Calculation activities can be set up to create saved files at certain time steps. This is useful for investigating saturation at later times. For example, setting up an auto save with and auto save data frequency of 50 if the case is modified is a good idea.

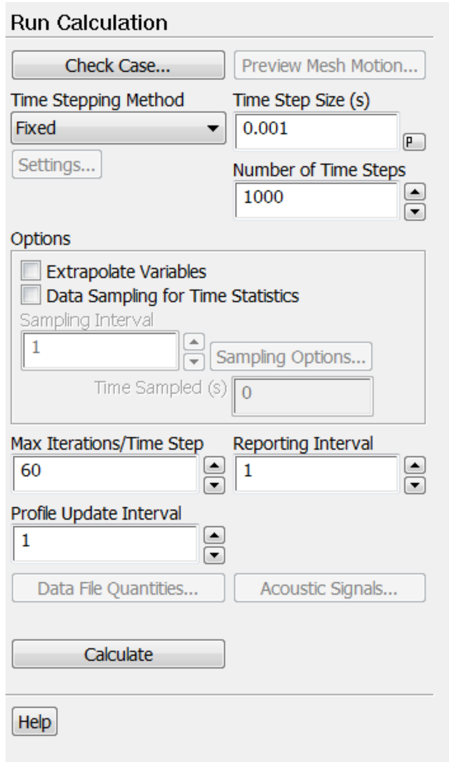

Figure 79: Run Calculations

When the solution has completed, the results can be post processed. Save the case and data files before exiting FLUENT.

A.II Fluent Model Set Up Through Journal File

Submitting jobs through the HPCC or DECS Compute servers can be efficiently and autonomously done by the use of .qsub and .jou files. Below is an example of a .jou file with corresponding comments to define what each line item is. Comments are shown with ";" before them. A file that can be copied into a text file and saved with the ".jou" extension with the comments directly in it is provided. The HPCC uses the Linux operating system and is fully supported. Journal files can also be read through a GUI by selecting, file >> read >> journal. Any unanswered questions can be answered by the FLUENT documentation or on "www.cfd-online.com".

; Load the Mesh generated from whatever meshing tool of choice, ensure that it is saved in the ".msh" format with the correct boundary conditions already defined in the mesh. Case and data files can also be read in this same way and modified through journal file commands.

file read-case H_FloRat_P.msh

;

; Get mesh statistics, always ensure that your mesh is high quality, there are no negative volumes, and no other issues exist.

mesh check

mesh quality

mesh size-info

;

; Configure solver define the model and solver that you are interested in define models solver pressure-based yes

define models unsteady-1st-order yes

define models multiphase model vof

;

; Configure VOF model for a two-phase flow where one-phase is resin and one is defined as air or a displaced fluid.

define models multiphase number-of-phases 2

define models multiphase volume-fraction-parameters explicit 0.25 no 1e-06

define models multiphase options no no no

define models multiphase body-force-formulation no

define models multiphase coupled-level-set no

;

; Create and define materials and give the properties of your resin system to another material. Here we start by importing the properties of motor oil and modifying them.

define materials copy fluid engine-oil

define materials change-create air air no no no no no no no

define materials change-create engine-oil engine-oil yes constant 709 no no yes power-law two-coefficient-method 24.149 -1.465 no no no

;

;Change phases make sure you have identified which phase is air and which phase is resin

define phases phase-domain phase-1 air no

define phases phase-domain phase-2 resin yes engine-oil

;

;Cell zone conditions define the region that will be porous media. The porous media is a region where your Darcy based permeability of Forchheimer inertial resistance can be input. Fluent uses viscous resistance which is equal to 1/permeability.

define boundary-conditions fluid porousmedia mixture no no no no 0 no 0 no 0 no 0 no 0 no 1 no no yes no .505 yes no

define boundary-conditions fluid porousmedia air no no no 0 no 0 no 0 no 0 no 0 no 1 no yes no no 1 no 0 no 0 no 0 no 1 no 0 yes no 8.44e9 no 1.08e10 no 1.46e12 no no 0 no 0 no 0 0 0 no .505 no

define boundary-conditions fluid porousmedia resin no no no 0 no 0 no 0 no 0 no 0 no 1 no yes no no 1 no 0 no 0 no 0 no 1 no 0 yes no 8.44e9 no 1.08e10 no 1.46e12 no no 0 no 0 no 0 0 0 no .505 no

;

;Set Boundary Conditions for pressure or velocity inlets and outlets. Define wall boundaries. Define Volume fractions of fluid at each boundary. The inlet will have 1 for the volume fraction of resin entering at the boundary.

define boundary-conditions pressure-outlet pressure_outlet mixture no 0 no 449.817 no yes no

define boundary-conditions velocity-inlet velocity_inlet mixture no no yes yes no 8.628e-5 no 0 no 297

define boundary-conditions velocity-inlet velocity_inlet resin no 1

define boundary-conditions wall wall mixture 0 no 0 no yes temperature no 449.817 no no no no 1

;

;Set solution methods (20=SIMPLE 21=SIMPLEC 22=PISO 24=Coupled)

```
solve set p-v-coupling 20
;
;Under-Relaxation Factors
solve set under-relaxation pressure 0.3
solve set under-relaxation density 1
solve set under-relaxation body-force 1
solve set under-relaxation mom 0.7
solve set under-relaxation temperature 1
;
;Residual monitors
solve monitors residual criterion-type 1
;
;Surface Monitor
solve monitors surface set-monitor phasefrac "Integral" resin pressure_outlet () no no yes
phasefrac.out 50 yes flow-time
;
;Initialize
solve initialize set-defaults mixture pressure 0
solve initialize set-defaults mixture x-velocity 0
solve initialize set-defaults mixture y-velocity 0
solve initialize set-defaults mixture z-velocity 0
solve initialize set-defaults mixture temperature 300
solve initialize initialize-flow
```

;

;Patch, after initialization you mush patch the whole body to have no resin at time zero when the simulation starts. If you skip this step your solution volume will be randomly initialized and will not give you a good solution

solve patch resin porousmedia () mp 0

;

;Create image file for ffmpeg, this step generates images at defined time steps that can later be stitched together into a video.

display set contours filled-contours yes

display set picture driver png

display set picture landscape yes

display set picture x-resolution 960

display set picture y-resolution 720

display set picture color-mode color

display set contours surfaces interior-porousmedia pressure_outlet velocity_inlet wall ()

display contour resin vof 0 1

display views auto-scale

display views restore-view front

display save-picture 0000%t.png

;

;Create commands to save images every N time steps, you can take them as frequently or infrequently as makes sense for your simulation, you can also track the volume fraction of fluid as it progresses throughout your domain to tell you when your solution volume is solved.

```
solve execute-commands add-edit command-2 1 "time-step" "/display/contour resin vof 0 1"
solve execute-commands add-edit command-3 1 "time-step" "        /display/save-picture
0000%t.png"
;
;Set up auto-save, save the file every so many time steps in case your solution crashes
file auto-save data-frequency 50
file auto-save case-frequency if-case-is-modified
file auto-save append-file-name-with time-step 6
;
;Start simulation, begin solving
solve set time-step 1
solve dual-time-iterate 7200 50
; This line will write your final data and exit the simulation. You can solve for other points of
interest including pressure build up at the inlet, etc. This can be printed to a file before exiting.
file write-data finaldata.dat

exit y
```

A.III Executable Version

The information below this statement can be copied directly and saved with a ".jou" extension for use on the HPCC. Updates will be likely needed for anything after FLUENT ANSYS/14.5.

```
;Load the Mesh
file read-case H_FloRat_P.msh
;
;Get mesh statistics
mesh check
mesh quality
mesh size-info
;
;Configure solver
define models solver pressure-based yes
define models unsteady-1st-order yes
define models multiphase model vof
;
;Configure VOF model
define models multiphase number-of-phases 2
define models multiphase volume-fraction-parameters explicit 0.25 no 1e-06
define models multiphase options no no no
define models multiphase body-force-formulation no
```

define models multiphase coupled-level-set no

;

;Create and define materials

define materials copy fluid engine-oil

define materials change-create air air no no no no no no no

define materials change-create engine-oil engine-oil yes constant 709 no no yes power-law two-coefficient-method 24.149 -1.465 no no no

;

;Change phases

define phases phase-domain phase-1 air no

define phases phase-domain phase-2 resin yes engine-oil

;

;Cell zone conditions

define boundary-conditions fluid porousmedia mixture no no no no 0 no 0 no 0 no 0 no 0 no 1 no no yes no .505 yes no

define boundary-conditions fluid porousmedia air no no no 0 no 0 no 0 no 0 no 0 no 1 no yes no no 1 no 0 no 0 no 0 no 1 no 0 yes no 8.44e9 no 1.08e10 no 1.46e12 no no 0 no 0 no 0 0 0 no .505 no

define boundary-conditions fluid porousmedia resin no no no 0 no 0 no 0 no 0 no 0 no 1 no yes no no 1 no 0 no 0 no 0 no 1 no 0 yes no 8.44e9 no 1.08e10 no 1.46e12 no no 0 no 0 no 0 0 0 no .505 no

;

;Set Boundary Conditions

define boundary-conditions pressure-outlet pressure_outlet mixture no 0 no 449.817 no yes no

define boundary-conditions velocity-inlet velocity_inlet mixture no no yes yes no 8.628e-5 no 0 no 297

define boundary-conditions velocity-inlet velocity_inlet resin no 1

define boundary-conditions wall wall mixture 0 no 0 no yes temperature no 449.817 no no no no 1

;

;Set solution methods (20=SIMPLE 21=SIMPLEC 22=PISO 24=Coupled)

solve set p-v-coupling 20

;

;Under-Relaxation Factors

solve set under-relaxation pressure 0.3

solve set under-relaxation density 1

solve set under-relaxation body-force 1

solve set under-relaxation mom 0.7

solve set under-relaxation temperature 1

;

;Residual monitors

solve monitors residual criterion-type 3

;

;Surface Monitor

solve monitors surface set-monitor phasefrac "Integral" resin pressure_outlet () no no yes phasefrac.out 50 yes flow-time

```
;
;Initialize
solve initialize set-defaults mixture pressure 0
solve initialize set-defaults mixture x-velocity 0
solve initialize set-defaults mixture y-velocity 0
solve initialize set-defaults mixture z-velocity 0
solve initialize set-defaults mixture temperature 300
solve initialize initialize-flow
;
;Patch
solve patch resin porousmedia () mp 0
;
;Create image file for ffmpeg
display set contours filled-contours yes
display set picture driver png
display set picture landscape yes
display set picture x-resolution 960
display set picture y-resolution 720
display set picture color-mode color
display set contours surfaces interior-porousmedia pressure_outlet velocity_inlet wall ()
display contour resin vof 0 1
display views auto-scale
display views restore-view front
```

```
display save-picture 0000%t.png
;
;Create commands to save images every N time steps
solve execute-commands add-edit command-2 1 "time-step" "/display/contour resin vof 0 1"
solve execute-commands add-edit command-3 1 "time-step" "/display/save-picture 0000%t.png"
;
;Set up auto-save
file auto-save data-frequency 50
file auto-save case-frequency if-case-is-modified
file auto-save append-file-name-with time-step 6
;
;Start simulation
solve set time-step 1
solve dual-time-iterate 7200 50
;
file write-data finaldata.dat
exit y
```

A.IV Fluent Model QSUB File for HPCC

Submitting jobs through the HPCC or DECS Compute servers can be efficiently and autonomously done by the use of .qsub and .jou files. Below is an example of a .qsub file with corresponding comments to define what each line item is. Comments are shown with ";" before them. A file that can be copied into a text file and saved with the ".qsub" extension is shown after the comments section. The HPCC uses the linux operating system and is fully supported. Any unanswered questions can be answered on their web site or though the HPCC support team.

#!/bin/sh –login

; This makes output and error files the same file

#PBS -j oe

; This sends an email when the job begins, ends, or is aborted.

#PBS -m abe

; This line requests and email be sent when the job starts with job information

#PBS -M email@msu.edu

; This line requests the number of compute nodes and processes per node. It is necessary to correctly specify the number of shared memory nodes required and the number of processors per node.

#PBS -l nodes=8:ppn=1

; The estimated compute time (walltime) and memory (mem) is specified here, if your job goes over this specification it will be canceled. Time job will take to execute (HH:MM:SS format)

#PBS -l walltime=04:00:00,mem=32gb

; This line requests the appropriate license for Fluent and cfd solvers. The first liscense requested gives you 4 compute nodes and then 4 hpc licenses are needed to generate the 8 nodes requested. Change the processor number by changing the number after “hpc:”

#PBS -W x=gres:aa_r_cfd:1%aa_r_hpc:4

; This line is simply a name for the file, whatever follows the –N will be the job name

#PBS -N HeatedRTM

; Changes the working directory to the original working directory where the job was submitted from

cd ${PBS_O_WORKDIR}

; Outputs the contents of the PBS nodefile

cat ${PBS_NODEFILE}

; Loads the ANSYS module for FLUENT and the corresponding license permissions. The loader defaults to the most recent release of ANSYS but in each version of ANSYS the commands change so you can default to an older version of ANSYS or FLUENT by requesting the ANSYS/”releasenumber”, i.e. ANSYS/14.0

module load ANSYS

Gives the three-dimensional double precision solver, also could use any other solver for example 2d or 3d

#Set variables for script

What version of the solver to use

FLUENTSOLVER=3ddp

;This gives the number of cpus and calculates the licenses

#Automatically calculate the number of cpus required

CPUCOUNT=`cat $PBS_NODEFILE | wc -l`

; You must specify the name of the previously generated journal file here. Previously called "HFloRatP.jou" but the name is not important, only the extension.

#Which input journal file to use to give fluent?

INPUT=HFloRatP.jou

; This directs the output directory to be the same as the working directory.

#Where do we want to put output at?

OUTPUT=${PBS_O_WORKDIR}/${PBS_JOBID}.out

; These are additional commands that can be implemented.

Run Fluent with:

-t$CPUCOUNT use $CPUCOUNT CPUs total

-p use the default ethernet interconnect

-mpi=net use socket protocol

-cnf=$PBS_NODEFILE get the list of machines PBS is running on from the server

-g no graphics, batch mode

-i read the file in $INPUT

> $OUTPUT 2>$1 Redirect program output to a file in your home directory.u

; The variables are passed here

```
fluent $FLUENTSOLVER -t$CPUCOUNT -mpi=pcmpi -cnf=$PBS_NODEFILE -ssh -gu -i
$INPUT > $OUTPUT 2>&1
```

; Prints final statistics about the job and resources used before the job exits.

```
qstat -f ${PBS_JOBID}
```

The information below this statement can be copied directly and saved with a ".qsub" extension for use on the HPCC. Updates will be likely needed for anything after FLUENT ANSYS/15.0.

```
#!/bin/sh --login
#PBS -j oe
#PBS -m abe
#PBS -M luchinit@egr.msu.edu
#PBS -l nodes=8:ppn=1
#PBS -l walltime=04:00:00,mem=32gb
#PBS -W x=gres:aa_r_cfd:1%aa_r_hpc:4
#PBS -N HeatedRTM

cd ${PBS_O_WORKDIR}
cat ${PBS_NODEFILE}

module load ANSYS

#Set variables for script
# What version of the solver to use
FLUENTSOLVER=3ddp

#Automatically calculate the number of cpus required
CPUCOUNT=`cat $PBS_NODEFILE | wc -l`
```

```
#Which input journal file to use to give fluent?

INPUT=HFloRatP.jou


#Where do we want to put output at?

OUTPUT=${PBS_O_WORKDIR}/${PBS_JOBID}.out


# Run Fluent with:

# -t$CPUCOUNT use $CPUCOUNT CPUs total

# -p use the default ethernet interconnect

# -mpi=net use socket protocol

# -cnf=$PBS_NODEFILE get the list of machines PBS is running on from the server

# -g no graphics, batch mode

# -i read the file in $INPUT

# > $OUTPUT 2>$1 Redirect program output to a file in your home directory.u


fluent $FLUENTSOLVER -t$CPUCOUNT -mpi=pcmpi -cnf=$PBS_NODEFILE -ssh -gu -i

$INPUT > $OUTPUT 2>&1


qstat -f ${PBS_JOBID}
```

Appendix B: GOVERNING EQUATIONS AND DERRIVATIONS

B.I Derivation of the Governing Equations

The governing equations for the research described in this dissertation are derived using the substantial derivative form based on lectures on transport phenomena by Petty [197] and the corresponding text by Bird *et al.* [47]. The substantial derivative is that of an infinitesimally small fluid element moving with the fluid flow. This substantial derivative form is then converted into the conservative form used in most computational fluid dynamics codes:

$$\boldsymbol{V} = u\boldsymbol{i} + v\boldsymbol{j} + w\boldsymbol{k} \tag{44}$$

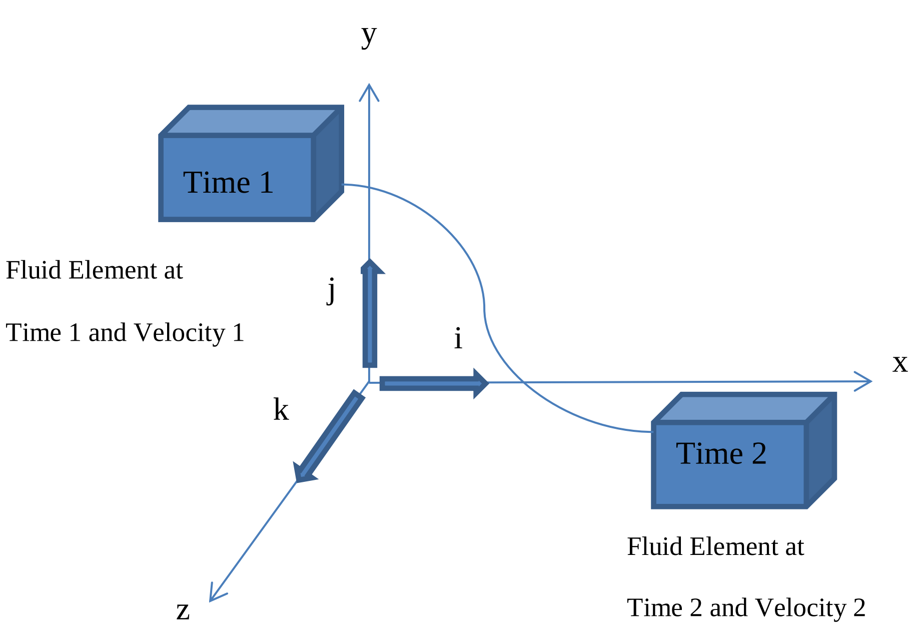

Figure 80: Fluid Element moving in the fluid flow, an illustration of the substantial derivative.

The vector velocity field is described in Cartesian space (Eq. 44). The x, y, and z components of velocity are given by Eq. 45, Eq. 46, and Eq. 47. By default, an unsteady flow is considered where u, v, and w are functions of position and time. Figure 80 is a reference sketch for the following discussion.

$$\boldsymbol{u} = u(x, y, z, t) \tag{45}$$

$$\boldsymbol{v} = \boldsymbol{v}(\boldsymbol{x}, \boldsymbol{y}, \boldsymbol{z}, \boldsymbol{t}) \tag{46}$$

$$\boldsymbol{w} = w(x, y, z, t) \tag{47}$$

Additionally, density is not considered constant here and can vary with position (as a function of space) and time as well.

$$\boldsymbol{\rho} = \rho(x, y, z, t) \tag{48}$$

For example, when the particle body is at point 1 and time 1 in Figure 80, the density could be different than when the particle body is at point 2 and time 2. In order to emphasize that density does not have to remain constant, Eq. 49and Eq. 50define the density at point 1 and 2.

$$\boldsymbol{\rho_1} = \rho(x_1, y_1, z_1, t_1) \tag{49}$$

$$\boldsymbol{\rho_2} = \boldsymbol{\rho}(\boldsymbol{x_2}, \boldsymbol{y_2}, \boldsymbol{z_2}, \boldsymbol{t_2}) \tag{50}$$

Using the known properties of the Taylor series, Eq. 48 can be expanded for density about point one, resulting in Eq. 51.

$$\rho_2 = \rho_1 + \left(\frac{\partial \rho}{\partial x}\right)_1 (x_2 - x_1) + \left(\frac{\partial \rho}{\partial y}\right)_1 (y_2 - y_1) + \left(\frac{\partial \rho}{\partial z}\right)_1 (z_2 - z_1) + \left(\frac{\partial \rho}{\partial t}\right)_1 (t_2 - t_1) + (higher\ order\ terms) \tag{51}$$

Truncating higher order terms and dividing by the change in time $(t_2 - t_1)$ gives the expression:

$$\frac{\rho_2 - \rho_1}{t_2 - t_1} = \left(\frac{\partial \rho}{\partial x}\right)_1 \frac{(x_2 - x_1)}{(t_2 - t_1)} + \left(\frac{\partial \rho}{\partial y}\right)_1 \frac{(y_2 - y_1)}{(t_2 - t_1)} + \left(\frac{\partial \rho}{\partial z}\right)_1 \frac{(z_2 - z_1)}{(t_2 - t_1)} + \left(\frac{\partial \rho}{\partial t}\right)_1 \tag{52}$$

The left side of Eq. 52 is the average time rate of change in the density of the fluid as it moves from point 1 to 2. Taking the limit as t_2 goes to t_1 gives:

$$\lim_{t_2 \to t_1} \frac{\rho_2 - \rho_1}{t_2 - t_1} = \frac{D\rho}{Dt} \tag{53}$$

In this form, Eq. 53 gives the substantial derivative (on the right hand side) for the instantaneous time rate of change of density of the fluid element as it moves through point 1. Thus, the view is fixed on the particle as the particle moves through space and the density changes. The expression $\left(\frac{\partial \rho}{\partial t}\right)_1$ in Eq. 52 is physically different in that it refers to time rate of change of density at the fixed point 1, and with the viewpoint fixed on the stationary point it is possible to watch the density change due to transient fluctuations in the flow field. Partial derivative (local derivative) and substantial derivative forms are physically different, but they can be converted from one form to another through shared relationships.

Following the same procedure and recognizing that the velocities being used are the average velocities, they are written in the limit forms as follows in Eq. 54. After this, the limit as t_2 goes to t_1 can be taken to get the substantial derivative in Cartesian coordinates (Eq. 55).

$$\lim_{t_2 \to t_1} \frac{x_2 - x_1}{t_2 - t_1} = \boldsymbol{u}$$

$$\lim_{t_2 \to t_1} \frac{y_2 - y_1}{t_2 - t_1} = \boldsymbol{v} \tag{54}$$

$$\lim_{t_2 \to t_1} \frac{z_2 - z_1}{t_2 - t_1} = \boldsymbol{w}$$

$$\frac{D}{Dt} \equiv \frac{\partial}{\partial t} + u\,\frac{\partial}{\partial x} + v\frac{\partial}{\partial y} + w\frac{\partial}{\partial z} \qquad (55)$$

The form of the equation on the right can also be expressed as the total differential using calculus in the x, y, z, and t dimensions. In Cartesian coordinates, the equation can be converted to Gibb's notation using the Del Operator, ∇.

$$\nabla \equiv \boldsymbol{i}\,\frac{\partial}{\partial x} + \boldsymbol{j}\frac{\partial}{\partial y} + \boldsymbol{k}\frac{\partial}{\partial z} \qquad (56)$$

Eq. 56 allows the substantial derivative to be rewritten in a more compact way not related to the coordinate system known as vector or Gibb's notation (Eq. 57), which makes it possible to easily extend to cylindrical and spherical coordinate systems.

$$\frac{D}{Dt} \equiv \frac{\partial}{\partial t} + (\boldsymbol{V} \cdot \boldsymbol{\nabla}) \qquad (57)$$

This form of the substantial derivative can apply to any flow variable, such as the static pressure *p* and the temperature *T*. Here, the new term $\boldsymbol{V} \cdot \boldsymbol{\nabla}$ is the convective derivative, which is the time rate of change due to the movement of the fluid element from one location to another in the flow field. Physically, the fluid element is moving to another position in the flow field where the properties are different. With this form, it is assumed that the physical flow properties are not necessarily the same throughout space. Applied to a variable such as pressure, the substantial derivative physically states that the pressure of the fluid is changing as the particle moves past a point in the flow. This is true because, at that point, the pressure may be changing with time and the particle is moving to another point in the flow field where the pressure is different.

B.II Physical Derivation of the Divergence of Velocity

The divergence of velocity ($\nabla \cdot \boldsymbol{V}$) is used frequently in fluid dynamics and is a useful tool, so it will be derived here. Physically, the divergence of velocity is the time rate of change of a volume of a moving fluid element, per unit volume. Considering the same control volume made up of the same fluid particles (constant mass) as it moves with the flow, the volume and surface can change with time as it moves. Therefore, the control volume is increasing or decreasing in volume and changing shape as the flow progresses. Looking at an infinitesimal element of the surface at a point in time, there is a normal that can be described from the surface with a local velocity. The change in volume of the control volume due to the change in the surface over a change in time is Eq. 58, where the total change in volume $\mathcal{V}$ is the summation of all the changes over the control surface:

$$\Delta \mathcal{V} = [(\boldsymbol{V}\Delta t) \cdot \boldsymbol{n}]dS = (\boldsymbol{V}\,\Delta \boldsymbol{t}) \cdot d\boldsymbol{S} \qquad (58)$$

Taking the limit as dS goes to zero, the sum can be expressed as a surface integral.

$$\iint_S (\boldsymbol{V}\Delta t) \cdot d\boldsymbol{S} \tag{59}$$

If this integral is divided by the change in time, the result is the time rate of change of the control volume:

$$\frac{D\mathcal{V}}{Dt} = \frac{1}{\Delta t}\iint_S (\boldsymbol{V} \cdot \Delta t) \cdot d\boldsymbol{S} = \iint_S \boldsymbol{V} \cdot d\boldsymbol{S} \tag{59}$$

Then, using the Gauss-Ostragradsky divergence theorem Eq. 69 from vector calculus, it is possible to obtain Eq. 60.

$$\frac{D\mathcal{V}}{Dt} = \iiint_{\mathcal{V}} (\nabla \cdot \boldsymbol{V}) d\mathcal{V} \tag{60}$$

Following this, the control volume is imagined to be a small infinitesimal differential volume in Eq. 61.

$$\frac{D(\delta \mathscr{V})}{Dt} = \iiint\limits_{\delta \mathscr{V}} (\nabla \cdot \boldsymbol{V}) d\mathscr{V} \tag{61}$$

Next, it is assumed that the differential volume is small enough that the divergence of velocity is the same value throughout the differential volume in the integral. As the limit goes to zero, one of the following two forms can result in Eq. 62.

$$\frac{D(\delta \mathscr{V})}{Dt} = \iiint\limits_{\delta \mathscr{V}} (\nabla \cdot \boldsymbol{V}) d\mathscr{V}$$
$$(\nabla \cdot \boldsymbol{V}) = \frac{1}{\delta \mathscr{V}} \frac{D(\delta \mathscr{V})}{Dt} \tag{62}$$

B.III The Continuity Equation (Constant Position Assumption)

The physical principle of the continuity equation is that mass is conserved. When the conservation of mass principle is applied to a fluid element and derived, the continuity equation results. This means that the net mass flow out of the control volume through a surface is equal to the time rate of decreasing mass inside the control volume. The mass flow of a moving fluid across any surface is equal to the product of density multiplied by area multiplied by the normal component of velocity to the surface. By convention, it is assumed that the normal of the differential surface points out of the volume.

$$\iint_S \rho \boldsymbol{V} \cdot dS = \iiint_{\mathcal{V}} \rho \, d\mathcal{V} \tag{63}$$

The time rate of increase of mass inside the volume can then be written as Eq. 64.

$$\frac{\partial}{\partial t} \iiint_{\mathcal{V}} \rho \, d\mathcal{V} \tag{64}$$

Knowing the time rate of mass increase in Cartesian coordinates, it is possible to write one of the three forms in Eq. 65.

$$\begin{gathered}
\left[\frac{\partial \rho u}{\partial x} + \frac{\partial \rho v}{\partial y} + \frac{\partial \rho z}{\partial z}\right] dx\, dy\, dz = -\frac{\partial \rho}{\partial t}(dx\, dy\, dz) \\
\frac{\partial \rho}{\partial t} + \left[\frac{\partial y}{\partial x} + \frac{\partial y}{\partial x} + \frac{\partial y}{\partial x}\right] = 0 \\
\frac{\partial \rho}{\partial t} + [\nabla \cdot (\rho \boldsymbol{V})] = 0
\end{gathered} \tag{65}$$

In the third form of Eq. 65, the bracketed terms are the divergence of density multiplied by velocity. The equation is obtained in partial derivative form because of the infinitesimally small element assumption. The conservation form is derived for continuity because the model was fixed in space, but it does not have to be. The non-conservative form could be derived in a similar fashion by assuming that the particle is not fixed in space but is instead fixed in mass.

This derivation would give the substantial derivative (non-conservative) form of continuity (Eq. 66).

$$\frac{D\rho}{Dt} + \rho\nabla \cdot \boldsymbol{V} = 0 \tag{66}$$

The partial differential equation form can be obtained from the integral equation (Eq. 67) through the following manipulations, starting with the integral form.

$$\frac{\partial}{\partial t}\iiint_{\mathcal{V}} \rho \, d\mathcal{V} + \iint_{S} \rho\boldsymbol{V} \cdot d\boldsymbol{S} = 0 \tag{67}$$

The control volume is chosen fixed in space, so that the limits of integration are constant and the time derivative can be put inside the integral.

$$\iiint_{\mathcal{V}} \frac{\partial\rho}{\partial t} d\mathcal{V} + \iint_{S} \rho\boldsymbol{V} \cdot d\boldsymbol{S} = 0 \tag{68}$$

Next, the divergence theorem (Gauss-Ostrogradsky) of vector calculus can change the surface integral into a volume integral to simplify the problem.

$$\iint_S (\rho \boldsymbol{V}) \cdot dS = \iiint_{\mathcal{V}} \nabla \cdot (\rho \boldsymbol{V}) \, d\mathcal{V} \tag{69}$$

The Gauss-Ostrogradsky Theorem is then substituted to make the following simplification in Eq. 70.

$$\iiint_{\mathcal{V}} \frac{\partial \rho}{\partial t} d\mathcal{V} + \iiint_{\mathcal{V}} \nabla \cdot (\rho \boldsymbol{V}) \, d\mathcal{V} = 0 \tag{70}$$

Then, the equation is reduced further by taking the volume integral outside of the other collected terms (Eq. 71).

$$\iiint_{\mathcal{V}} \left[\frac{\partial \rho}{\partial t} + \nabla \cdot (\rho \boldsymbol{V}) \right] d\mathcal{V} = 0 \tag{71}$$

Next, because the control volume is of arbitrary origin in space the integrand has to be zero at every point in the control volume.

$$\frac{\partial \rho}{\partial t} + \nabla \cdot (\rho \boldsymbol{V}) = 0 \tag{72}$$

This completes the manipulation from the integral form to the differential form. Next, vector identities can be used to convert from a conservative form to a non-conservative form.

$$\nabla \cdot (\boldsymbol{\rho V}) \equiv (\boldsymbol{\rho \nabla \cdot V}) + (\boldsymbol{V \cdot \nabla \rho}) \tag{73}$$

By taking an identity that uses the divergence of a scalar times a vector and setting it equal the scalar times the divergence of the vector plus the vector dotted into the gradient of the scalar, Eq. 74 is obtained:

$$\frac{\partial \rho}{\partial t} + (\boldsymbol{\rho \nabla \cdot V}) + (\boldsymbol{V \cdot \nabla \rho}) = 0 \tag{74}$$

Here, recognizing that the left most term and the last term are the substantial derivative allows it to be rewritten in the substantial derivative (non-conservative) form.

$$\frac{D\rho}{Dt} + \rho \nabla \cdot \boldsymbol{V} = 0 \tag{66}$$

B.IV The Momentum Equation

Newton's second law of motion can be applied to result in a new equation called the momentum equation. Here, a moving fluid element will be used for simplicity. The momentum of a moving fluid element says that the net force on an element is equal to the mass times the acceleration of the element. There are two sources of forces on an element: body forces and surface forces. The body forces act directly on the volumetric mass of the fluid element, which could consist of gravity, electric forces, or magnetic forces for example. Surface forces act on the surface of the element and are due to the pressure distribution on the surface and the shear and normal stresses.

The momentum equation can be written in conservative form as follows in Eq. 75.

$$\rho \frac{Du}{Dt} = \rho \frac{\partial u}{\partial t} + \rho \boldsymbol{V} \cdot \nabla \mathrm{u} \qquad (75)$$

Expanding the following derivative gives Eq. 76.

$$\rho \frac{\partial u}{\partial t} = \frac{\partial (\rho u)}{\partial t} - u \frac{\partial (\rho)}{\partial t} \qquad (76)$$

Using the vector identity for the divergence of the product of a scalar times a vector gives Eq. 77.

$$\nabla \cdot (\rho u \boldsymbol{V}) = u \nabla \cdot (\rho \boldsymbol{V}) + (\rho \boldsymbol{V}) \cdot \nabla u \qquad (77)$$

Substituting the equations above in Eq. 75 and simplifying gives Eq. 78.

$$\rho \frac{Du}{Dt} = \frac{\partial(\rho u)}{\partial t} - u\frac{\partial(\rho)}{\partial t} - u\nabla \cdot (\rho \boldsymbol{V}) + \nabla \cdot (\rho u \boldsymbol{V}) = \frac{\partial(\rho u)}{\partial t} - u\left[\frac{\partial(\rho)}{\partial t} + \nabla \cdot (\rho \boldsymbol{V})\right] + \nabla \cdot (\rho u \boldsymbol{V}) \quad (78)$$

Recognizing that the term in brackets is the continuity equation and is equal to zero makes that term drop out, and reduces to the following form of the momentum equation (Eq. 79).

$$\rho \frac{Du}{Dt} = \frac{\partial(\rho u)}{\partial t} + \nabla \cdot (\rho u \boldsymbol{V}) \quad (79)$$

B.V The Energy Equation

The energy equation is based on the physical principle that energy is conserved. Additionally, the assumption is made that an infinitesimally small fluid element exists. Physically, the rate of change of energy inside the fluid element is equal to the net flux of heat into the element, plus the rate of work done on the element due to body and surface forces.

The non-conservative form of the energy equation is shown below (Eq. 80) in expanded form for Cartesian coordinates as a sum of both the internal and kinetic energies.

$$\rho \frac{D}{Dt}\left(e+\frac{V^2}{2}\right) = \rho\dot{q} + \frac{\partial}{\partial x}\left(k\frac{\partial T}{\partial x}\right) + \frac{\partial}{\partial y}\left(k\frac{\partial T}{\partial y}\right) + \frac{\partial}{\partial z}\left(k\frac{\partial T}{\partial z}\right) - \frac{\partial(u\rho)}{\partial x} - \frac{\partial(v\rho)}{\partial y} - \frac{\partial(w\rho)}{\partial z} + \frac{\partial(u\tau_{xx})}{\partial x} + \frac{\partial(u\tau_{yx})}{\partial y} + \frac{\partial(u\tau_{zx})}{\partial z} + \frac{\partial(v\tau_{xy})}{\partial x} + \frac{\partial(v\tau_{yy})}{\partial y} + \frac{\partial(v\tau_{zy})}{\partial z} + \frac{\partial(w\tau_{xz})}{\partial x} + \frac{\partial(w\tau_{yz})}{\partial y} + \frac{\partial(w\tau_{zz})}{\partial z} + \rho\boldsymbol{f}\cdot\boldsymbol{V} \tag{80}$$

The linearized Navier-Stokes equation can be used to model porous regions of the preform, as shown in the following equation:

$$\mu\nabla^2\boldsymbol{u} = \nabla\boldsymbol{P} \tag{81}$$

Additionally, the Brinkman equation is useful in the fiber tows to account for the transition between boundaries. In 1949, Brinkman developed a modified form of Darcy's Law that includes a viscous term, which allows the continuity of velocity to be applied as well as stress boundary conditions [198]. In composite manufacturing, the continuity and momentum equations can be used to satisfy the boundary conditions at the interface between the fluid and tow by assuming the conservation of mass and momentum. Furthermore, shear stress boundary conditions can be applied. This can be done based on a generalization of Darcy's Law called the Brinkman's Equation:

$$\mu_e\nabla^2 * \boldsymbol{u} - \mu\,\mathrm{K}^{-1} * \boldsymbol{u} = \nabla\mathrm{P} \tag{82}$$

Where, K is the permeability tensor of the fiber bundles and μ_e is the effective viscosity.

Brinkman's Equation is found repeatedly in literature about heterogeneous porous media [199], [200] with some limitations noted [201].

Appendix C: GLOSSARY

C.I Terms

- Basis weight: nominal weight of mat for a certain area
- Biaxial material: fibers oriented in two directions, the warp (0 degree) and weft (90 degree) direction.
- Binder: glass mat or preforms to bind the fibers prior to laminating or molding
- Bundle: a collection of essentially parallel filaments or fibers
- Capillary Effect: Ability of a liquid to flow without the assistance of or against and external force
- Chop length: length to which fibers have been cut
- Composite: two or more materials combined with reinforcing elements and matrix acting together but being distinct
- Count: number of warp and weft yarns per cm/ inch of fabrics, indicates tightness of weave
- Cure: in a thermosetting resin it is the process of setting by chemical reaction
- Curing of Resin: A chemical cross linking reaction that creates the composite matrix
- Darcy's Law: An relationship useful for relating velocity with pressure drop in porous media
- Directional Preform: A fiber reinforcement with direction dependent properties
- Fabric, woven: interlaced yarns, fibers or filaments
- Fiber: filaments that make up a tow or chopped mat
- Fiber Bundle: A collection of fibers creating a tow or yarn

- Filament: smallest unit of fibrous material in a composite preform
- Fill: also known as weft, fibers running perpendicular to the warp, if on a roll generally the tows aligned with the roll tube
- Flow Channel: an area of no fiber reinforcement that can be either designed or an artifact of an imperfect preform in the mold
- Flow Rate Pump: A constant flow rate injection for resin transfer molding
- Granular Media: Porous media with flow that can be described as grains or soil
- Heterogeneous Porous Media: Material properties vary by direction
- Hexagonal Packing: An ordered packing arrangement that has six fibers surrounding a single center fiber
- Incompressible Liquid: A fluid that follows the assumptions of a Newtonian fluid
- Inertial Effect: Non-linear relationship between pressure drop and flow rate
- Isothermal Filling: Resin injection under constant temperature conditions
- Isotropic: The same value measured in different directions
- Laminate: successive layers of plies or lamina and resin bonded together
- Layup: layers of plies creating the preform
- Liquid Composite Molding: a process of injecting liquid thermosetting resin systems into a preform through a closed mold process
- Macro-scale: the scale of a finished composite part
- Macro-void: A void or defect on the scale of the component or a dry spot in the mold
- Matrix Material: The material the makes up the compressive strength for the composite material
- Meso-scale: the scale of yarns or tows

- Micro-scale: the scale of fibers
- Mold Cavity: A tooling piece that contains a composite to be manufactured
- Orthotropic: Material properties vary based on direction
- Parallel: Flow along an axis
- Perpendicular: At an angle of 90 degrees to an axis or surface
- Permeability: the resistance to flow from the fiber reinforcement acting as a porous media
- Ply: A single layer of reinforcement generally cut to the shape of the mold
- Polymer: an organic compound with a repeated small unit structure, such as polyethylene, rubber, polyester and cellulose
- Porous Media: the fiber or fabric reinforcement through which resin flows
- Porous Tow: A collection of fibers approximated as porous media
- Preform: a material that has undergone a preliminary shaping operation
- Pre-preg: reinforcement fibers that are pre-impregnated with resin and ready for placement in the mold
- Pressure Pot: A pressure based injection source of resin for constant pressure infusions
- Profile: cross-section used in reference to tows for most of the paper
- Quadratic Packing: A square packing arrangement
- Race tracking: A undersigned scenario where resin runs around the fiber reinforcement instead of saturating it
- Random Packing: A disordered packing arrangement

- Resin: thermoplastic or thermosetting organic material flows under stress before being cured and binds the fiber preform, generally the only matrix material
- Resin Runner: a designed area of no fiber reinforcement where resin is allowed to preferentially flow in order to more rapidly infuse a mold and create a composite
- S-glass: A magnesia-alumina-silicate glass, especially designed to provide very high tensile strength glass filaments
- Shear Stress: Layers flowing against each other in opposite directions
- Sizing: a coating consisting of starch, gelatin, oil, wax or other suitable ingredient that is applied to yarn or fibers to aid the process of handling and fabrication
- Square Packing: An ordered packing arrangement that looks square with fibers at four corners and the axis being able to connect and create a square
- Tensor: a mathematical object represented by a matrix of components that are functions of coordinates and direction
- Thermoplastic: a composite matrix which responds to a physical change in temperature rather than a chemical reaction
- Thermoset: cured by application of heat or chemical means and cannot be reversed
- Thermosetting: A chemical crosslinking polymer resin
- Tow: a bundle of fibers also referred to as a yarn
- Transverse: Flow at a perpendicular angle to an axis or surface
- Viscosity: A quantity describing the state of a fluids internal resistance
- Volume Fraction: The volume of a constituent like fiber reinforcement divided by the total volume of all constituents
- Warp: yarns that run lengthwise and parallel generally perpendicular to the weft

- Weave: pattern of intersecting warp and filling yarns
- Weft: fibers running perpendicular to the warp, if on a roll generally the tows aligned with the roll tube
- Woven fabric: fabric that consists of a warp and a weft
- Yarn size: Weight, thickness and coverage of the fabric

REFERENCES

REFERENCES

[1] G. Marsh, “Composites get in deep with new-generation engine,” *Reinf. Plast.*, vol. 50, no. 11, pp. 26–29, Dec. 2006.

[2] M. Wagner and G. Norris, *Boeing 787 Dreamliner*. Zenith Imprint, 2009.

[3] J. Hale, “Boeing 787 from the ground up,” *Aero*, vol. 4, pp. 17–24, 2006.

[4] G. Marsh, “Boeing’s 787: trials, tribulations, and restoring the dream,” *Reinf. Plast.*, vol. 53, no. 8, pp. 16–21, Nov. 2009.

[5] C. Soutis, “Carbon fiber reinforced plastics in aircraft construction,” *Mater. Sci. Eng. A*, vol. 412, no. 1, pp. 171–176, 2005.

[6] S. Kotha and K. Srikanth, “Managing a global partnership model: Lessons from the Boeing 787 ‘Dreamliner’program,” *Glob. Strategy J.*, vol. 3, no. 1, pp. 41–66, 2013.

[7] L. Chery and G. De Marsily, *Aquifer Systems Management: Darcy’s Legacy in a World of Impending Water Shortage: Selected Papers on Hydrogeology 10*. CRC Press, 2007.

[8] M. V. Bruschke and S. G. Advani, “A finite element/control volume approach to mold filling in anisotropic porous media,” *Polym. Compos.*, vol. 11, no. 6, pp. 398–405, 1990.

[9] C. T. Simmons, “Henry Darcy (1803–1858): Immortalised by his scientific legacy,” *Hydrogeol. J.*, vol. 16, no. 6, pp. 1023–1038, Sep. 2008.

[10] H. Darcy, *Les fontaines publiques de la ville de Dijon: exposition et application...* Victor Dalmont, 1856.

[11] H. Darcy and P. Bobeck, *The public fountains of the city of Dijon*. Kendall/Hunt Publishing Company, 2004.

[12] C. T. Simmons, “The Public Fountains of the City of Dijon.”

[13] I. Oppenheim, “A survey of thermodynamics,” *J. Stat. Phys.*, vol. 83, no. 3, pp. 791–792, 1996.

[14] A. Fick, “V. On liquid diffusion,” *Lond. Edinb. Dublin Philos. Mag. J. Sci.*, vol. 10, no. 63, pp. 30–39, 1855.

[15] W. K. Chui, J. Glimm, F. M. Tangerman, A. P. Jardine, J. S. Madsen, T. M. Donnellan, and R. Leek, “Case study from industry: Process modeling in resin transfer molding as a method to enhance product quality,” *SIAM Rev.*, vol. 39, no. 4, pp. 714–727, 1997.

[16] K. M. Pillai, “Modeling the unsaturated flow in liquid composite molding processes: a review and some thoughts,” *J. Compos. Mater.*, vol. 38, no. 23, pp. 2097–2118, 2004.

[17] J. M. Sharp Jr, “Momentum and energy balance equations for compacting sediments,” *J. Int. Assoc. Math. Geol.*, vol. 8, no. 3, pp. 305–322, 1976.

[18] K. O. Temeng, “Effects of high pressure gradients on the flow of real gases through porous media,” Stanford University, 1988.

[19] F. R. Phelan Jr and G. Wise, “Analysis of transverse flow in aligned fibrous porous media,” *Compos. Part Appl. Sci. Manuf.*, vol. 27, no. 1, pp. 25–34, 1996.

[20] C.-Y. Chang, “Tow impregnation of unidirectional fibrous preform during resin transfer molding,” *J. Reinf. Plast. Compos.*, vol. 22, no. 11, pp. 1003–1016, 2003.

[21] N. Patel and L. J. Lee, “Modeling of void formation and removal in liquid composite molding. Part II: Model development and implementation,” *Polym. Compos.*, vol. 17, no. 1, pp. 104–114, 1996.

[22] J. Yang, Y. Jia, S. Sun, D. Ma, T. Shi, and L. An, “Mesoscopic simulation of the impregnating process of unidirectional fibrous preform in resin transfer molding,” *Mater. Sci. Eng. A*, vol. 435, pp. 515–520, 2006.

[23] M. A. Spaid and F. R. Phelan Jr, “Lattice Boltzmann methods for modeling microscale flow in fibrous porous media,” *Phys. Fluids*, vol. 9, p. 2468, 1997.

[24] G. S. Beavers and D. D. Joseph, “Boundary conditions at a naturally permeable wall,” *J. Fluid Mech.*, vol. 30, no. 01, pp. 197–207, 1967.

[25] T. S. Lundström, R. Stenberg, R. Bergström, H. Partanen, and P. A. Birkeland, “In-plane permeability measurements: a nordic round-robin study,” *Compos. Part Appl. Sci. Manuf.*, vol. 31, no. 1, pp. 29–43, Jan. 2000.

[26] J. B. Alms, N. Correia, S. G. Advani, and E. Ruiz, “Experimental Procedures to Run Longitudinal Injections to Measure Unsaturated Permeability of LCM Reinforcements,” 2010.

[27] R. Arbter, J. M. Beraud, C. Binetruy, L. Bizet, J. Bréard, S. Comas-Cardona, C. Demaria, A. Endruweit, P. Ermanni, F. Gommer, S. Hasanovic, P. Henrat, F. Klunker, B. Laine, S. Lavanchy, S. V. Lomov, A. Long, V. Michaud, G. Morren, E. Ruiz, H. Sol, F. Trochu, B. Verleye, M. Wietgrefe, W. Wu, and G. Ziegmann, “Experimental determination of the permeability of textiles: A benchmark exercise,” *Compos. Part Appl. Sci. Manuf.*, vol. 42, no. 9, pp. 1157–1168, Sep. 2011.

[28] N. Vernet, E. Ruiz, S. Advani, J. B. Alms, M. Aubert, M. Barburski, B. Barari, J. M. Beraud, D. C. Berg, N. Correia, M. Danzi, T. Delavière, M. Dickert, C. Di Fratta, A. Endruweit, P. Ermanni, G. Francucci, J. A. Garcia, A. George, C. Hahn, F. Klunker, S. V. Lomov, A. Long, B. Louis, J. Maldonado, R. Meier, V. Michaud, H. Perrin, K. Pillai, E. Rodriguez, F. Trochu, S. Verheyden, M. Wietgrefe, W. Xiong, S. Zaremba, and G. Ziegmann, “Experimental

determination of the permeability of engineering textiles: Benchmark II," *Compos. Part Appl. Sci. Manuf.*, vol. 61, pp. 172–184, Jun. 2014.

[29] R. S. Parnas, K. M. Flynn, and M. E. Dal-Favero, "A permeability database for composites manufacturing," *Polym. Compos.*, vol. 18, no. 5, pp. 623–633, Oct. 1997.

[30] R. S. Parnas, J. G. Howard, T. L. Luce, and S. G. Advani, "Permeability characterization. Part 1: A proposed standard reference fabric for permeability," *Polym. Compos.*, vol. 16, no. 6, pp. 429–445, 1995.

[31] G. Morren, M. Bottiglieri, S. Bossuyt, H. Sol, D. Lecompte, B. Verleye, and S. V. Lomov, "A reference specimen for permeability measurements of fibrous reinforcements for RTM," *Compos. Part Appl. Sci. Manuf.*, vol. 40, no. 3, pp. 244–250, Mar. 2009.

[32] M. Li, Y. Gu, Z. Zhang, and Z. Sun, "A simple method for the measurement of compaction and corresponding transverse permeability of composite prepregs," *Polym. Compos.*, vol. 28, no. 1, pp. 61–70, Feb. 2007.

[33] A. Shojaei, F. Trochu, S. R. Ghaffarian, S. M. H. Karimian, and L. Lessard, "An experimental study of saturated and unsaturated permeabilities in resin transfer molding based on unidirectional flow measurements," *J. Reinf. Plast. Compos.*, vol. 23, no. 14, pp. 1515–1536, 2004.

[34] K. Okonkwo, P. Simacek, S. G. Advani, and R. S. Parnas, "Characterization of 3D fiber preform permeability tensor in radial flow using an inverse algorithm based on sensors and simulation," *Compos. Part Appl. Sci. Manuf.*, vol. 42, no. 10, pp. 1283–1292, Oct. 2011.

[35] D. L. Woerdeman, F. R. Phelan, and R. S. Parnas, "Interpretation of 3-D permeability measurements for RTM modeling," *Polym. Compos.*, vol. 16, no. 6, pp. 470–480, 1995.

[36] J. R. Weitzenböck, R. A. Shenoi, and P. A. Wilson, "Measurement of three-dimensional permeability," *Compos. Part Appl. Sci. Manuf.*, vol. 29, no. 1–2, pp. 159–169, 1998.

[37] S. H. Ahn, W. I. Lee, and G. S. Springer, "Measurement of the Three-Dimensional Permeability of Fiber Preforms Using Embedded Fiber Optic Sensors," *J. Compos. Mater.*, vol. 29, no. 6, pp. 714–733, Apr. 1995.

[38] P. B. Nedanov and S. G. Advani, "A Method to Determine 3D Permeability of Fibrous Reinforcements," *J. Compos. Mater.*, vol. 36, no. 2, pp. 241–254, Jan. 2002.

[39] F. LeBel, "Experimental Characterization by Fluorescence of Capillary Flows in the Fiber Tows of Engineering Fabrics," *Open J. Inorg. Non-Met. Mater.*, vol. 02, no. 03, pp. 25–45, 2012.

[40] G. L. Batch, Y.-T. Chen, and C. W. Macoskot, "Capillary Impregnation of Aligned Fibrous Beds: Experiments and Model," *J. Reinf. Plast. Compos.*, vol. 15, no. 10, pp. 1027–1051, Oct. 1996.

[41] S. C. Amico and C. Lekakou, “Axial impregnation of a fiber bundle. Part 1: Capillary experiments,” *Polym. Compos.*, vol. 23, no. 2, pp. 249–263, 2002.

[42] T. S. Lundström, R. Stenberg, R. Bergström, H. Partanen, and P. A. Birkeland, “In-plane permeability measurements: a nordic round-robin study,” *Compos. Part Appl. Sci. Manuf.*, vol. 31, no. 1, pp. 29–43, 2000.

[43] X. Chen and T. D. Papathanasiou, “The transverse permeability of disordered fiber arrays: a statistical correlation in terms of the mean nearest interfiber spacing,” *Transp. Porous Media*, vol. 71, no. 2, pp. 233–251, Jan. 2008.

[44] X. Chen and T. D. Papathanasiou, “Micro-scale modeling of axial flow through unidirectional disordered fiber arrays,” *Compos. Sci. Technol.*, vol. 67, no. 7, pp. 1286–1293, 2007.

[45] D. A. Nield and A. Bejan, *Convection in porous media*. springer, 2006.

[46] R. S. Dave and A. C. Loos, *Processing of Composites.(2000)*. Hanser Publishers: Munich.

[47] R. B. Bird, W. E. Stewart, and E. N. Lightfoot, *Transport phenomena*. John Wiley & Sons, 2007.

[48] F. Civan, “Comparison of Control Volume Analysis and Porous Media Averaging for Formulation of Porous Media Transport,” in *Modelling and Simulation in Fluid Dynamics in Porous Media*, J. A. Ferreira, S. Barbeiro, G. Pena, and M. F. Wheeler, Eds. Springer New York, 2013, pp. 27–53.

[49] Y. Kuan and A. S. El-Gizawy, “Numerical characterization of mold injection in resin transfer molding process,” *Adv. Polym. Technol.*, vol. 19, no. 3, pp. 173–179, 2000.

[50] C. H. Park and L. Woo, “Modeling void formation and unsaturated flow in liquid composite molding processes: a survey and review,” *J. Reinf. Plast. Compos.*, vol. 30, no. 11, pp. 957–977, 2011.

[51] D. Bender, J. Schuster, and D. Heider, “Flow rate control during vacuum-assisted resin transfer molding (VARTM) processing,” *Compos. Sci. Technol.*, vol. 66, no. 13, pp. 2265–2271, 2006.

[52] R. Peila, J. C. Seferis, T. Karaki, and G. Parker, “Effects of nanoclay on the thermal and rheological properties of a VARTM (vacuum assisted resin transfer molding) epoxy resin,” *J. Therm. Anal. Calorim.*, vol. 96, no. 2, pp. 587–592, 2009.

[53] L.-Y. Lin, J.-H. Lee, C.-E. Hong, G.-H. Yoo, and S. G. Advani, “Preparation and characterization of layered silicate/glass fiber/epoxy hybrid nanocomposites via vacuum-assisted resin transfer molding (VARTM),” *Compos. Sci. Technol.*, vol. 66, no. 13, pp. 2116–2125, 2006.

[54] A. C. Loos and J. D. MacRae, “A process simulation model for the manufacture of a blade-stiffened panel by the resin film infusion process,” *Compos. Sci. Technol.*, vol. 56, no. 3, pp. 273–289, 1996.

[55] L. E. Letterman, *Resin film infusion process and apparatus*. Google Patents, 1986.

[56] V. Antonucci, M. Giordano, L. Nicolais, A. Calabro, A. Cusano, A. Cutolo, and S. Inserra, “Resin flow monitoring in resin film infusion process,” *J. Mater. Process. Technol.*, vol. 143, pp. 687–692, 2003.

[57] A. J. Ryan, J. L. Stanford, and Q. T. XIAO, “The processing, structure and properties of structural composites formed by reaction injection moulding (SRIM),” *Plast. Rubber Compos. Process. Appl.*, vol. 23, no. 3, pp. 151–159, 1995.

[58] T. Eason and O. Ochoa, “Modeling residual stresses and damage initiation in discontinuous random fiber SRIM composites (Structural Reaction Injection Molding),” 1996.

[59] M. Fu and P. K. Mallick, “Fatigue of hybrid (adhesive/bolted) joints in SRIM composites,” *Int. J. Adhes. Adhes.*, vol. 21, no. 2, pp. 145–159, 2001.

[60] W. H. Seemann III, *Plastic transfer molding techniques for the production of fiber reinforced plastic structures*. Google Patents, 1990.

[61] N. G. Chavka and C. F. Johnson, *Resin transfer molding method*. Google Patents, 1991.

[62] R. Pan, Z. Liang, C. Zhang, and B. Wang, “Statistical characterization of fiber permeability for composite manufacturing,” *Polym. Compos.*, vol. 21, no. 6, pp. 996–1006, 2000.

[63] S. G. Advani and E. M. Sozer, *Process modeling in composites manufacturing*, vol. 59. CRC Press, 2002.

[64] C. C. Chamis, M. P. Hanson, and T. T. Serafini, “Criteria for selecting resin matrices for improved composite strength,” 1974.

[65] A. Shojaei, S. R. Ghaffarian, and S. M.-H. Karimian, “Modeling and simulation approaches in the resin transfer molding process: a review,” *Polym. Compos.*, vol. 24, no. 4, pp. 525–544, 2003.

[66] E. Ruiz, V. Achim, S. Soukane, F. Trochu, and J. Bréard, “Optimization of injection flow rate to minimize micro/macro-voids formation in resin transfer molded composites,” *Compos. Sci. Technol.*, vol. 66, no. 3, pp. 475–486, 2006.

[67] R. M. Jones, *Mechanics of composite materials*. CRC Press, 1998.

[68] N. Vernet, E. Ruiz, S. Advani, J. B. Alms, M. Aubert, M. Barburski, B. Barari, J. M. Beraud, D. C. Berg, N. Correia, and others, “Experimental determination of the permeability of engineering textiles: Benchmark II,” *Compos. Part Appl. Sci. Manuf.*, vol. 61, pp. 172–184, 2014.

[69] R. Arbter, J. M. Beraud, C. Binetruy, L. Bizet, J. Bréard, S. Comas-Cardona, C. Demaria, A. Endruweit, P. Ermanni, F. Gommer, S. Hasanovic, P. Henrat, F. Klunker, B. Laine, S. Lavanchy, S. V. Lomov, A. Long, V. Michaud, G. Morren, E. Ruiz, H. Sol, F. Trochu, B. Verleye, M. Wietgrefe, W. Wu, and G. Ziegmann, "Experimental determination of the permeability of textiles: A benchmark exercise," *Compos. Part Appl. Sci. Manuf.*, vol. 42, no. 9, pp. 1157–1168, Sep. 2011.

[70] J. R. Weitzenböck, R. A. Shenoi, and P. A. Wilson, "Radial flow permeability measurement. Part A: Theory," *Compos. Part Appl. Sci. Manuf.*, vol. 30, no. 6, pp. 781–796, 1999.

[71] R. S. Parnas, K. M. Flynn, and M. E. Dal-Favero, "A permeability database for composites manufacturing," *Polym. Compos.*, vol. 18, no. 5, pp. 623–633, 1997.

[72] J. E. Drummond and M. I. Tahir, "Laminar viscous flow through regular arrays of parallel solid cylinders," *Int. J. Multiph. Flow*, vol. 10, no. 5, pp. 515–540, 1984.

[73] A. S. Sangani and C. Yao, "Transport processes in random arrays of cylinders. I. Thermal conduction," *Phys. Fluids 1958-1988*, vol. 31, no. 9, pp. 2426–2434, 1988.

[74] S. V. Lomov, G. Huysmans, Y. Luo, R. S. Parnas, A. Prodromou, I. Verpoest, and F. R. Phelan, "Textile composites: modelling strategies," *Compos. Part Appl. Sci. Manuf.*, vol. 32, no. 10, pp. 1379–1394, 2001.

[75] N. D. Ngo and K. K. Tamma, "Complex three-dimensional microstructural permeability prediction of porous fibrous media with and without compaction," *Int. J. Numer. Methods Eng.*, vol. 60, no. 10, pp. 1741–1757, 2004.

[76] B. R. Gebart, "Permeability of Unidirectional Reinforcements for RTM," *J. Compos. Mater.*, vol. 26, no. 8, pp. 1100–1133, Aug. 1992.

[77] T. G. Gutowski, T. Morigaki, and Z. Cai, "The consolidation of laminate composites," *J. Compos. Mater.*, vol. 21, no. 2, pp. 172–188, 1987.

[78] P. Xu and B. Yu, "Developing a new form of permeability and Kozeny–Carman constant for homogeneous porous media by means of fractal geometry," *Adv. Water Resour.*, vol. 31, no. 1, pp. 74–81, 2008.

[79] K. J. Ahn, J. C. Seferis, and J. C. Berg, "Simultaneous measurements of permeability and capillary pressure of thermosetting matrices in woven fabric reinforcements," *Polym. Compos.*, vol. 12, no. 3, pp. 146–152, 1991.

[80] B. T. Aström, R. B. Pipes, and S. G. Advani, "On flow through aligned fiber beds and its application to composites processing," *J. Compos. Mater.*, vol. 26, no. 9, pp. 1351–1373, 1992.

[81] R. Davé, "A unified approach to modeling resin flow during composite processing," *J. Compos. Mater.*, vol. 24, no. 1, pp. 22–41, 1990.

[82] R. C. Lam and J. L. Kardos, "The permeability and compressibility of aligned and cross-plied carbon fiber beds during processing of composites," *Polym. Eng. Sci.*, vol. 31, no. 14, pp. 1064–1070, 1991.

[83] A. L. Berdichevsky and Z. Cai, "Preform permeability predictions by self-consistent method and finite element simulation," *Polym. Compos.*, vol. 14, no. 2, pp. 132–143, 1993.

[84] A. Costa, "Permeability-porosity relationship: A reexamination of the Kozeny-Carman equation based on a fractal pore-space geometry assumption," *Geophys. Res. Lett.*, vol. 33, no. 2, 2006.

[85] B. R. Gebart and P. Lidström, "Measurement of in-plane permeability of anisotropic fiber reinforcements," *Polym. Compos.*, vol. 17, no. 1, pp. 43–51, 1996.

[86] M. V. Bruschke and S. G. Advani, "Flow of generalized Newtonian fluids across a periodic array of cylinders," *J. Rheol. 1978-Present*, vol. 37, no. 3, pp. 479–498, 1993.

[87] J. Happel, "Viscous flow relative to arrays of cylinders," *AIChE J.*, vol. 5, no. 2, pp. 174–177, 1959.

[88] F. Desplentere, S. V. Lomov, D. L. Woerdeman, I. Verpoest, M. Wevers, and A. Bogdanovich, "Micro-CT characterization of variability in 3D textile architecture," *Compos. Sci. Technol.*, vol. 65, no. 13, pp. 1920–1930, 2005.

[89] P. B. Nedanov and S. G. Advani, "Numerical computation of the fiber preform permeability tensor by the homogenization method," *Polym. Compos.*, vol. 23, no. 5, pp. 758–770, 2002.

[90] R. Gauvin, F. Trochu, Y. Lemenn, and L. Diallo, "Permeability measurement and flow simulation through fiber reinforcement," *Polym. Compos.*, vol. 17, no. 1, pp. 34–42, 1996.

[91] S. Ranganathan, F. R. Phelan, and S. G. Advani, "A generalized model for the transverse fluid permeability in unidirectional fibrous media," *Polym. Compos.*, vol. 17, no. 2, pp. 222–230, 1996.

[92] J. P. Dunkers, F. R. Phelan, D. P. Sanders, M. J. Everett, W. H. Green, D. L. Hunston, and R. S. Parnas, "The application of optical coherence tomography to problems in polymer matrix composites," *Opt. Lasers Eng.*, vol. 35, no. 3, pp. 135–147, 2001.

[93] K. M. Pillai, C. L. Tucker III, and F. R. Phelan Jr, "Numerical simulation of injection/compression liquid composite molding. Part 1. Mesh generation," *Compos. Part Appl. Sci. Manuf.*, vol. 31, no. 1, pp. 87–94, 2000.

[94] K. M. Pillai, C. L. Tucker, and F. R. Phelan, "Numerical simulation of injection/compression liquid composite molding. Part 2: preform compression," *Compos. Part Appl. Sci. Manuf.*, vol. 32, no. 2, pp. 207–220, 2001.

[95] N. D. Ngo and K. K. Tamma, “Microscale permeability predictions of porous fibrous media,” *Int. J. Heat Mass Transf.*, vol. 44, no. 16, pp. 3135–3145, 2001.

[96] N. D. Ngo and K. K. Tamma, “Non-isothermal ‘2-D flow/3-D thermal’developments encompassing process modelling of composites: flow/thermal/cure formulations and validations,” *Int. J. Numer. Methods Eng.*, vol. 50, no. 7, pp. 1559–1585, 2001.

[97] T. D. Papathanasiou, “On the effective permeability of square arrays of permeable fiber tows,” *Int. J. Multiph. Flow*, vol. 23, no. 1, pp. 81–92, 1997.

[98] P. B. Nedanov and S. G. Advani, “A method to determine 3D permeability of fibrous reinforcements,” *J. Compos. Mater.*, vol. 36, no. 2, pp. 241–254, 2002.

[99] S. Amico and C. Lekakou, “Flow Through a Two-Scale Porosity, Oriented Fibre Porous Medium,” *Transp. Porous Media*, vol. 54, no. 1, pp. 35–53, Jan. 2004.

[100] C. Lekakou, S. Edwards, G. Bell, and S. C. Amico, “Computer modelling for the prediction of the in-plane permeability of non-crimp stitch bonded fabrics,” *Compos. Part Appl. Sci. Manuf.*, vol. 37, no. 6, pp. 820–825, 2006.

[101] J.-F. Delerue, S. V. Lomov, R. S. Parnas, I. Verpoest, and M. Wevers, “Pore network modeling of permeability for textile reinforcements,” *Polym. Compos.*, vol. 24, no. 3, pp. 344–357, 2003.

[102] A. Endruweit, A. C. Long, F. Robitaille, and C. D. Rudd, “Influence of stochastic fibre angle variations on the permeability of bi-directional textile fabrics,” *Compos. Part Appl. Sci. Manuf.*, vol. 37, no. 1, pp. 122–132, 2006.

[103] A. Endruweit, P. McGregor, A. C. Long, and M. S. Johnson, “Influence of the fabric architecture on the variations in experimentally determined in-plane permeability values,” *Compos. Sci. Technol.*, vol. 66, no. 11, pp. 1778–1792, 2006.

[104] A. Endruweit and A. C. Long, “Analysis of compressibility and permeability of selected 3D woven reinforcements,” *J. Compos. Mater.*, vol. 44, no. 24, pp. 2833–2862, 2010.

[105] G. A. Bingham, R. J. M. Hague, C. J. Tuck, A. C. Long, J. J. Crookston, and M. N. Sherburn, “Rapid manufactured textiles,” *Int. J. Comput. Integr. Manuf.*, vol. 20, no. 1, pp. 96–105, 2007.

[106] C. C. Wong, A. C. Long, M. Sherburn, F. Robitaille, P. Harrison, and C. D. Rudd, “Comparisons of novel and efficient approaches for permeability prediction based on the fabric architecture,” *Compos. Part Appl. Sci. Manuf.*, vol. 37, no. 6, pp. 847–857, Jun. 2006.

[107] H. Lin, M. J. Clifford, A. C. Long, and M. Sherburn, “Finite element modelling of fabric shear,” *Model. Simul. Mater. Sci. Eng.*, vol. 17, no. 1, p. 015008, 2009.

[108] H. Lin, A. C. Long, M. Sherburn, and M. J. Clifford, “Modelling of mechanical behaviour for woven fabrics under combined loading,” *Int. J. Mater. Form.*, vol. 1, no. 1, pp. 899–902, 2008.

[109] J. J. Crookston, W. Ruijter, A. C. Long, N. A. Warrior, and I. A. Jones, “A comparison of mechanical property prediction techniques using conformal tetrahedra and voxel-based finite element meshes for textile composite unit cells,” *Proc. Finite Elem. Model. Text. Text. Compos.*, pp. 26–28, 2007.

[110] S. V. Lomov and I. Verpoest, “WiseTex–Virtual Textile software,” *Vlakna Text.*, no. 2, pp. 135–140, 2001.

[111] I. Verpoest and S. V. Lomov, “Virtual textile composites software< i> WiseTex</i>: Integration with micro-mechanical, permeability and structural analysis,” *Compos. Sci. Technol.*, vol. 65, no. 15, pp. 2563–2574, 2005.

[112] S. V. Lomov, E. B. Belov, T. Bischoff, S. B. Ghosh, T. Truong Chi, and I. Verpoest, “Carbon composites based on multiaxial multiply stitched preforms. Part 1. Geometry of the preform,” *Compos. Part Appl. Sci. Manuf.*, vol. 33, no. 9, pp. 1171–1183, 2002.

[113] E. E. Swery, P. Kelly, T. Allen, and S. Bickerton, “CAPTURING THE VARIABILITY OF TEXTILE PERMEABILITY FROM SCANNED IMAGES; A TOOL TO AUTOMATICALLY COMPUTE A TEXTILE PERMEABILITY MAP.”

[114] P.-J. Liotier, Q. Govignon, E. Swery, S. Drapier, and S. Bickerton, “Characterisation of woven flax fibres reinforcements: Effect of the shear on the in-plane permeability,” *J. Compos. Mater.*, p. 0021998314565411, 2015.

[115] E. E. Swery, R. Meier, S. V. Lomov, K. Drechsler, and P. Kelly, “Predicting permeability based on flow simulations and textile modelling techniques: Comparison with experimental values and verification of FlowTex solver using Ansys CFX,” *J. Compos. Mater.*, p. 0021998315579927, 2015.

[116] M. Nordlund and T. S. Lundstrom, “Numerical Study of the Local Permeability of Noncrimp Fabrics,” *J. Compos. Mater.*, vol. 39, no. 10, pp. 929–947, May 2005.

[117] C. C. Wong, A. C. Long, M. Sherburn, F. Robitaille, P. Harrison, and C. D. Rudd, “Comparisons of novel and efficient approaches for permeability prediction based on the fabric architecture,” *Compos. Part Appl. Sci. Manuf.*, vol. 37, no. 6, pp. 847–857, Jun. 2006.

[118] H. Tan, E. M. Languri, and K. M. Pillai, “Prediction of Permeability in a dual-scale fiber mat using two different unit cells,” presented at the The 9th International Conference on Flow Processes in Composite Materials, Montréal, Canada, 2008.

[119] T. J. Luchini, S. J. Sommerlot, and A. C. Loos, “Unit Cell Modeling to Predict Permeability for Composite Manufacturing,” in *Proceedings of the American Society for Composites 29th Technical Conference*, San Diego, CA, September 8-10.

[120] Z.-R. Chen, L. Ye, and M. Lu, “Permeability Predictions for Woven Fabric Preforms,” *J. Compos. Mater.*, Dec. 2009.

[121] X. Zeng, A. C. Long, and A. Endruweit, “Numerical prediction of permeability of textiles for the international benchmark exercise,” in *Proceedings of the 11th International Conference on Flow Processing in Composite Materials*, Auckland, New Zealand, 2012.

[122] E. J. Carter, A. W. Fell, P. R. Griffin, and J. Summerscales, “Data validation procedures for the automated determination of the two-dimensional permeability tensor of a fabric reinforcement,” *Compos. Part Appl. Sci. Manuf.*, vol. 27, no. 4, pp. 255–261, 1996.

[123] A. Hammami, F. Trochu, R. Gauvin, and S. Wirth, “Directional permeability measurement of deformed reinforcement,” *J. Reinf. Plast. Compos.*, vol. 15, no. 6, pp. 552–562, 1996.

[124] D. L. Woerdeman, F. R. Phelan, and R. S. Parnas, “Interpretation of 3-D permeability measurements for RTM modeling,” *Polym. Compos.*, vol. 16, no. 6, pp. 470–480, 1995.

[125] C.-L. Lai and W.-B. Young, “Model resin permeation of fiber reinforcements after shear deformation,” *Polym. Compos.*, vol. 18, no. 5, pp. 642–648, 1997.

[126] R. S. Parnas, J. G. Howard, T. L. Luce, and S. G. Advani, “Permeability characterization. Part 1: A proposed standard reference fabric for permeability,” *Polym. Compos.*, vol. 16, no. 6, pp. 429–445, 1995.

[127] W.-B. Young and S. F. Wu, “Permeability measurement of bidirectional woven glass fibers,” *J. Reinf. Plast. Compos.*, vol. 14, no. 10, pp. 1108–1120, 1995.

[128] J. R. Weitzenböck, R. A. Shenoi, and P. A. Wilson, “Measurement of principal permeability with the channel flow experiment,” *Polym. Compos.*, vol. 20, no. 2, pp. 321–335, 1999.

[129] R. S. Parnas, *Liquid composite molding*. Carl Hanser Verlag GmbH Co KG, 2014.

[130] C.-L. Lee and K.-H. Wei, “Effect of material and process variables on the performance of resin-transfer-molded epoxy fabric composites,” *J. Appl. Polym. Sci.*, vol. 77, no. 10, pp. 2149–2155, 2000.

[131] C. Williams, J. Summerscales, and S. Grove, “Resin infusion under flexible tooling (RIFT): a review,” *Compos. Part Appl. Sci. Manuf.*, vol. 27, no. 7, pp. 517–524, 1996.

[132] V. M. González-Romero and C. W. Macosko, “Process parameters estimation for structural reaction injection molding and resin transfer molding,” *Polym. Eng. Sci.*, vol. 30, no. 3, pp. 142–146, 1990.

[133] P. Bhat, J. Merotte, P. Simacek, and S. G. Advani, “Process analysis of compression resin transfer molding,” *Compos. Part Appl. Sci. Manuf.*, vol. 40, no. 4, pp. 431–441, 2009.

[134] M. W. Hyer, *Stress analysis of fiber-reinforced composite materials*. DEStech Publications, Inc, 2009.

[135] K.-T. Hsiao, R. Little, O. Restrepo, and B. Minaie, “A study of direct cure kinetics characterization during liquid composite molding,” *Compos. Part Appl. Sci. Manuf.*, vol. 37, no. 6, pp. 925–933, Jun. 2006.

[136] S. Abrate, “Resin flow in fiber preforms,” *Appl. Mech. Rev.*, vol. 55, no. 6, pp. 579–599, Oct. 2002.

[137] A. Shojaei, S. R. Ghaffarian, and S. M. H. Karimian, “Modeling and simulation approaches in the resin transfer molding process: A review,” *Polym. Compos.*, vol. 24, no. 4, pp. 525–544, 2003.

[138] L. A. Isoldi, C. P. Oliveira, L. A. Rocha, J. A. Souza, and S. C. Amico, “Three-dimensional numerical modeling of RTM and LRTM processes,” *J. Braz. Soc. Mech. Sci. Eng.*, vol. 34, no. 2, pp. 105–111, 2012.

[139] C. Lekakou and M. G. Bader, “Mathematical modelling of macro-and micro-infiltration in resin transfer moulding (RTM),” *Compos. Part Appl. Sci. Manuf.*, vol. 29, no. 1, pp. 29–37, 1998.

[140] R. Gauvin and F. Trochu, “Key issues in numerical simulation for liquid composite molding processes,” *Polym. Compos.*, vol. 19, no. 3, pp. 233–240, 1998.

[141] L. Cheah and J. Heywood, “Meeting US passenger vehicle fuel economy standards in 2016 and beyond,” *Energy Policy*, vol. 39, no. 1, pp. 454–466, 2011.

[142] L. Skartsis, J. L. Kardos, and B. Khomami, “Resin flow through fiber beds during composite manufacturing processes. Part I: Review of Newtonian flow through fiber beds,” *Polym. Eng. Sci.*, vol. 32, no. 4, pp. 221–230, 1992.

[143] M. K. Um and W. I. Lee, “A study on permeability of unidirectional fiber beds,” *J. Reinf. Plast. Compos.*, vol. 16, no. 17, pp. 1575–1590, 1997.

[144] J. S. U. Schell, M. Siegrist, and P. Ermanni, “Experimental determination of the transversal and longitudinal fibre bundle permeability,” *Appl. Compos. Mater.*, vol. 14, no. 2, pp. 117–128, 2007.

[145] D. Shou, J. Fan, and F. Ding, “A difference-fractal model for the permeability of fibrous porous media,” *Phys. Lett. A*, vol. 374, no. 10, pp. 1201–1204, 2010.

[146] Z.-R. Chen, L. Ye, and M. Lu, “Permeability predictions for woven fabric preforms,” *J. Compos. Mater.*, 2009.

[147] H. Lin, L. P. Brown, and A. C. Long, “Modelling and Simulating Textile Structures Using TexGen,” *Adv. Mater. Res.*, vol. 331, pp. 44–47, 2011.

[148] E. M. Sparrow and A. L. Loeffler, “Longitudinal laminar flow between cylinders arranged in regular array,” *AIChE J.*, vol. 5, no. 3, pp. 325–330, 1959.

[149] C. DeValve and R. Pitchumani, “An analytical model for the longitudinal permeability of aligned fibrous media,” *Compos. Sci. Technol.*, vol. 72, no. 13, pp. 1500–1507, 2012.

[150] A. Tamayol and M. Bahrami, “Parallel flow through ordered fibers: an analytical approach,” *J. Fluids Eng.*, vol. 132, no. 11, p. 114502, 2010.

[151] C. Y. Wang, “Stokes flow through a rectangular array of circular cylinders,” *Fluid Dyn. Res.*, vol. 29, no. 2, pp. 65–80, 2001.

[152] G. Bechtold and L. Ye, “Influence of fibre distribution on the transverse flow permeability in fibre bundles,” *Compos. Sci. Technol.*, vol. 63, no. 14, pp. 2069–2079, 2003.

[153] X. Chen and T. D. Papathanasiou, “On the variability of the Kozeny constant for saturated flow across unidirectional disordered fiber arrays,” *Compos. Part Appl. Sci. Manuf.*, vol. 37, no. 6, pp. 836–846, 2006.

[154] K. W. Desmond and E. R. Weeks, “Random close packing of disks and spheres in confined geometries,” *Phys. Rev. E*, vol. 80, no. 5, p. 051305, 2009.

[155] N. Xu, J. Blawzdziewicz, and C. S. O’Hern, “Random close packing revisited: Ways to pack frictionless disks,” *Phys. Rev. E*, vol. 71, no. 6, p. 061306, 2005.

[156] A. S. Clarke and J. D. Wiley, “Numerical simulation of the dense random packing of a binary mixture of hard spheres: Amorphous metals,” *Phys. Rev. B*, vol. 35, no. 14, p. 7350, 1987.

[157] S. J. Wright and J. Nocedal, *Numerical optimization*, vol. 2. Springer New York, 1999.

[158] P. Šimáček and S. G. Advani, “Desirable features in mold filling simulations for Liquid Composite Molding processes,” *Polym. Compos.*, vol. 25, no. 4, pp. 355–367, 2004.

[159] P. C. Carman, “Fluid flow through granular beds,” *Trans.-Inst. Chem. Eng.*, vol. 15, pp. 150–166, 1937.

[160] J. R. Weitzenböck, R. A. Shenoi, and P. A. Wilson, “Measurement of three-dimensional permeability,” *Compos. Part Appl. Sci. Manuf.*, vol. 29, no. 1, pp. 159–169, 1998.

[161] N. K. Naik, M. Sirisha, and A. Inani, “Permeability characterization of polymer matrix composites by RTM/VARTM,” *Prog. Aerosp. Sci.*, 2013.

[162] X. Chen and T. D. Papathanasiou, “Interface stress distributions in transversely loaded continuous fiber composites: parallel computation in multi-fiber RVEs using the boundary element method,” *Compos. Sci. Technol.*, vol. 64, no. 9, pp. 1101–1114, 2004.

[163] Timothy Luchini, Stephen Sommerlot, and Alfred Loos, “Modeling to Predict Microscale Permeability for Fiber Reinforcement in Liquid Composite Molding,” presented at the American Society for Composites 30th Annual Technical Conference, East Lansing, MI, 2015.

[164] V. H. Hammond and A. C. Loos, “The Effects of Fluid Type and Viscosity on the Steady-State and Advancing Front Permeability Behavior of Textile Preforms,” *J. Reinf. Plast. Compos.*, vol. 16, no. 1, pp. 50–72, Jan. 1997.

[165] B. P. Van West, R. B. Pipes, and S. G. Advani, “The consolidation of commingled thermoplastic fabrics,” *Polym. Compos.*, vol. 12, no. 6, pp. 417–427, 1991.

[166] B. D. Ripley, *Statistical inference for spatial processes*. Cambridge university press, 1991.

[167] M. H. Wichmann, J. Sumfleth, F. H. Gojny, M. Quaresimin, B. Fiedler, and K. Schulte, “Glass-fibre-reinforced composites with enhanced mechanical and electrical properties–benefits and limitations of a nanoparticle modified matrix,” *Eng. Fract. Mech.*, vol. 73, no. 16, pp. 2346–2359, 2006.

[168] C.-W. Nan, R. Birringer, D. R. Clarke, and H. Gleiter, “Effective thermal conductivity of particulate composites with interfacial thermal resistance,” *J. Appl. Phys.*, vol. 81, no. 10, pp. 6692–6699, 1997.

[169] A. B. Morgan and C. A. Wilkie, *Flame retardant polymer nanocomposites*. John Wiley & Sons, 2007.

[170] D. Lefevre, S. Comas-Cardona, C. Binétruy, and P. Krawczak, “Modelling the flow of particle-filled resin through a fibrous preform in liquid composite molding technologies,” *Compos. Part Appl. Sci. Manuf.*, vol. 38, no. 10, pp. 2154–2163, 2007.

[171] M. Chohra, S. G. Advani, A. Gokce, and S. Yarlagadda, “Modeling of filtration through multiple layers of dual scale fibrous porous media,” *Polym. Compos.*, vol. 27, no. 5, pp. 570–581, 2006.

[172] J. Cho, M. S. Joshi, and C. T. Sun, “Effect of inclusion size on mechanical properties of polymeric composites with micro and nano particles,” *Compos. Sci. Technol.*, vol. 66, no. 13, pp. 1941–1952, 2006.

[173] Z. Fan, K.-T. Hsiao, and S. G. Advani, “Experimental investigation of dispersion during flow of multi-walled carbon nanotube/polymer suspension in fibrous porous media,” *Carbon*, vol. 42, no. 4, pp. 871–876, 2004.

[174] S. Movva, G. Zhou, D. Guerra, and L. J. Lee, “Effect of carbon nanofibers on mold filling in a vacuum assisted resin transfer molding system,” *J. Compos. Mater.*, vol. 43, no. 6, pp. 611–620, 2009.

[175] R. Umer, E. M. Waggy, and A. C. Loos, “Processing characteristics and mechanical properties of glass fabric reinforcements coated with graphite nanoparticles,” presented at the

2nd Joint US-Canada Conference on Composites - American Society for Composites, 26th Annual Technical Conference: Canadian Association for Composite Structures and Materials, 2011.

[176] R. J. Robinson, P. Snyder, and M. J. Oldham, “Comparison of Particle Tracking Algorithms in Commercial CFD Packages: Sedimentation and Diffusion,” *Inhal. Toxicol.*, vol. 19, no. 6–7, pp. 517–531, Jan. 2007.

[177] M. Agrawal, A. Bakker, and M. T. Prinkey, “Macroscopic particle model—Tracking big particles in CFD,” in *The Proceeding of AIChE 2004 Annual Meeting, Austin, USA. 268b*, 2004.

[178] Madhusuden Agrawal, “Drag Force Formulation in Macroscopic Particle Model and its Validation,” 2009.

[179] T. A. K. Sadiq, S. G. Advani, and R. S. Parnas, “Experimental investigation of transverse flow through aligned cylinders,” *Int. J. Multiph. Flow*, vol. 21, no. 5, pp. 755–774, 1995.

[180] P. Ferland, D. Guittard, and F. Trochu, “Concurrent methods for permeability measurement in resin transfer molding,” *Polym. Compos.*, vol. 17, no. 1, pp. 149–158, 1996.

[181] M. Devillard, K.-T. Hsiao, A. Gokce, and S. G. Advani, “On-line characterization of bulk permeability and race-tracking during the filling stage in resin transfer molding process,” *J. Compos. Mater.*, vol. 37, no. 17, pp. 1525–1541, 2003.

[182] S. Bickerton, E. M. Sozer, P. \vSimácek, and S. G. Advani, “Fabric structure and mold curvature effects on preform permeability and mold filling in the RTM process. Part II. Predictions and comparisons with experiments,” *Compos. Part Appl. Sci. Manuf.*, vol. 31, no. 5, pp. 439–458, 2000.

[183] S. Bickerton, E. M. Sozer, P. J. Graham, and S. G. Advani, “Fabric structure and mold curvature effects on preform permeability and mold filling in the RTM process. Part I. Experiments,” *Compos. Part Appl. Sci. Manuf.*, vol. 31, no. 5, pp. 423–438, 2000.

[184] Y. R. Kim, S. P. McCarthy, J. P. Fanucci, S. C. Nolet, and C. KOPPERNAES, “Resin flow through fiber reinforcements during composite processing,” *SAMPE Q.*, vol. 22, no. 3, pp. 16–22, 1991.

[185] N. Patel, V. Rohatgi, and L. J. Lee, “Micro scale flow behavior and void formation mechanism during impregnation through a unidirectional stitched fiberglass mat,” *Polym. Eng. Sci.*, vol. 35, no. 10, pp. 837–851, 1995.

[186] Y.-H. Lai, B. Khomami, and J. L. Kardos, “Accurate permeability characterization of preforms used in polymer matrix composite fabrication processes,” *Polym. Compos.*, vol. 18, no. 3, pp. 368–377, 1997.

[187] M. V. Bruschke and S. G. Advani, “RTM: filling simulation of complex three dimensional shell-like structures,” *Sampe Q.*, vol. 23, no. 1, pp. 2–11, 1991.

[188] P. Simacek and S. G. Advani, “A numerical model to predict fiber tow saturation during liquid composite molding,” *Compos. Sci. Technol.*, vol. 63, no. 12, pp. 1725–1736, Sep. 2003.

[189] X. Zeng, L. P. Brown, A. Endruweit, and A. C. Long, “Advanced geometry modelling of 3D woven reinforcements in polymer composites: processing and performance analysis,” 2012.

[190] A. Shojaei, S. Reza Ghaffarian, and S. Mohammad Hossein Karimian, “Three-dimensional process cycle simulation of composite parts manufactured by resin transfer molding,” *Compos. Struct.*, vol. 65, no. 3, pp. 381–390, 2004.

[191] B. W. Grimsley, “Characterization of the Vacuum Assisted Resin Transfer Molding Process for Fabrication of Aerospace Composites,” Virginia Polytechnic Institute and State University, Blacksburg, VA, 2005.

[192] B. W. Grimsley, R. J. Cano, P. Hubert, A. C. Loos, C. B. Kellen, and B. J. Jensen, “Preform Characterization in VARTM Process Model Development,” presented at the 36th International SAMPE Technical Conference, San Diego, CA, 2004.

[193] V. H. Hammond, A. C. Loos, H. B. Dexter, and G. Hasko, “Verification of a two-dimensional infiltration model for the resin transfer molding process,” Virginia Polytechnic Institute and State University, Blacksburg, VA, CCMS‐93‐15, VPI‐E‐93‐09, Aug. 1993.

[194] J. C. Fingerson, A. C. Loos, and H. B. Dexter, “Verification of a Three-Dimensional Resin Transfer Molding Process Simulation Model,” Virginia Polytechnic Institute and State University, Blacksburg, VA, CCMS-95-10, VPI-E-95-04, Sep. 1995.

[195] G. Lebrun, C. D. Rudd, and R. Gauvin, “Laminate Temperature Distributions and Filling Tine Prediction during Non-Isothermal Impregnation of Fibre Preforms,” *J. Reinf. Plast. Compos.*, vol. 14, no. 10, pp. 1069–1080, Oct. 1995.

[196] J. M. Lawrence, V. Neacsu, and S. G. Advani, “Modeling the impact of capillary pressure and air entrapment on fiber tow saturation during resin infusion in LCM,” *Compos. Part Appl. Sci. Manuf.*, vol. 40, no. 8, pp. 1053–1064, 2009.

[197] Charles A. Petty, “Lectures on Transport Phenomena,” presented at the Transport Phenomena, Michigan State University, 15-Jan-2013.

[198] H. C. Brinkman, “A calculation of the viscous force exerted by a flowing fluid on a dense swarm of particles,” *Appl. Sci. Res.*, vol. 1, no. 1, pp. 27–34, 1949.

[199] G. Neale and W. Nader, “Practical significance of Brinkman’s extension of Darcy’s law: coupled parallel flows within a channel and a bounding porous medium,” *Can. J. Chem. Eng.*, vol. 52, no. 4, pp. 475–478, 1974.

[200] J. A. Ochoa-Tapia and S. Whitaker, “Momentum transfer at the boundary between a porous medium and a homogeneous fluid—I. Theoretical development,” *Int. J. Heat Mass Transf.*, vol. 38, no. 14, pp. 2635–2646, 1995.

[201] D. A. Nield, “The limitations of the Brinkman-Forchheimer equation in modeling flow in a saturated porous medium and at an interface,” *Int. J. Heat Fluid Flow*, vol. 12, no. 3, pp. 269–272, 1991.